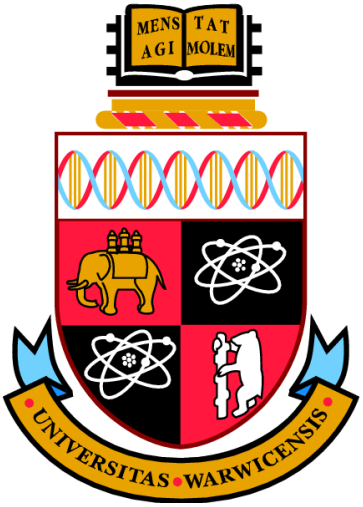

Snoring: A Flow-Structure Interaction

by

Richard Martyn Howell

A thesis submitted in partial fulfilment of the requirements

for the degree of

Doctor of Philosophy in Engineering

University of Warwick, School of Engineering

Fluid Dynamics Research Centre

April, 2006

Contents

List of Figures

List of Tables

Acknowledgments

"Centuries ago the Howeitat came from Hejaz, and their nomad clans prided themselves on being true Bedu. Auda was their master type. His hospitality was sweeping; except to very hungry souls, inconvenient. His generosity kept him always poor, despite the profits of a hundred raids. He had married twenty-eight times, had been wounded thirteen times; while the battles he provoked had seen all his tribesman hurt and most of his relations killed. He himself had slain seventy-five men, Arabs, with his own hand in battle: and never a man except in battle. Of the number of dead Turks he could give no account: they did not register...Auda raided as often as he had opportunity, and as widely as he could...and was careful to be at enmity with nearly all the tribes in the desert, that he might have proper scope for raids...His patience in action was extreme: and he received and ignored advice, criticism, or abuse, with a smile as constant as it was very charming." Seven Pillars of Wisdom, T. E. Lawrence.

I would like to thank Professors Tony Lucey and Peter Carpenter for their unerring support at the unspecified and numerous times when I have asked for their help and advice. I would like to thank my parents for their unending aid through this turbulent time in my life and resisting all my attempts to turn them into amateur snoring experts. My peer group in the Ph.D office has seen many characters pass through in my time here and I would like to thank them all for their almost infinite availability for beverage and chat. I would like to thank the rest of my family and friends for the essential and numerous excursions and distractions they have provided me with. Finally, I am very grateful to the EPSRC for the four years funding they provided me with during the course of this research.

Declaration

All investigations presented in this thesis are my own work except where specific reference has been made to the work of others. No part of this thesis has been submitted to any other university for credit or award. Some of the work presented in this thesis has been published in the following paper:

Howell, R. M., Lucey, A. D. & Carpenter, P. W. 2004 Numerical simulation of a cantilevered flexible plate embedded in an unbounded inviscid flow. In *Proceedings of the 8th international conference on Flow-Induced Vibrations, Paris, France* (edited by F. Axisa and E. de Langre), pp:167-171.

Abstract

A novel method for calculating the linear fluid-structure interaction of a cantilevered flexible surface centrally positioned in an ideal channel flow, incorporating the effects of vorticity shed downstream, is described. The perturbation pressure is modelled using a linearised boundary-element method. The flexible surface deflection is modelled using linearised one-dimensional beam theory. The shed vorticity is modelled using a linearised discrete vortex method. The computational model can therefore be used to conduct numerical experiments where no presupposition of the flexible surface deflection is made. This linear model can accurately capture the onset of instability in this fluid-structure system. The flexible surface is infinitely thin; the upper and lower sides of the surface can therefore be considered stream lines of the flow, with a step jump in pressure between them across the surface. The discontinuity of tangential velocity across the flexible surface generates lift. The flexible surface is therefore modelled by a distribution of vortex singularities with a Kutta condition applied at the surface's trailing edge. The individual models of the flexible surface and the fluid velocity and vorticity, together with the action of the individual hydrodynamic pressure components created when the models are combined to form a single unsteady model, are validated via a series of numerical experiments and by quantitative comparison with an appropriate, previously developed computational model.

Unique, highly detailed investigations into the ideal fluid-structure phenomena observed in numerical experiments conducted over a wide range of mass ratio and inlet velocity are documented. For the first time, detailed numerical investigation of the effect on this fluid-structure interaction of channel walls, a rigid central surface (upstream and adjacent to the flexible surface), unsteady mean flow, the variation of stiffness and damping properties along the flexible surface and the vorticity shed at the trailing edge of the flexible surface have been quantified. Calculations of the critical velocity show good correlation with other published work and examples of the possible application of the unsteady model to different physical fluid-structure phenomena are outlined. Of central importance is the application of the unsteady model to the investigation of the

human snoring phenomenon. Further insight into the operation of two types of snore is made and a new type of snore is discovered, incorporating the effects of inhalation. The numerical experiments demonstrate that the location (on the flexible surface) of the destabilising phase shift between the flexible surface velocity and fluid pressure leading to instability change drastically for a small shift in mass ratio. Coupled with knowledge of further snore mechanisms from other published work, these results show the uniqueness of treatment required to provide effective surgical treatment to individual patients suffering from snoring; furthermore, this highlights the need for more realistic fluid-structure models to be created.

Nomenclature

A	Channel cross-sectional area (m^2)
$[\mathbf{A}]$	Matrix used in solution of perturbation velocity in §3.4.2
B	Flexural rigidity (Nm)
$[\mathbf{B}]$	Matrix used in solution of unsteady velocity potential in §3.4.3
c	Wave speed of the flexible surface (m/s)
c_{fo}	Coefficient of fluid friction
c_m	Length of panel m (m)
$[\mathbf{C}]$	Matrix used in solution of mass point acceleration in §3.4.5
δx	Mass-point spacing (m)
d	Damping coefficient (kg/sm^2)
$\bar{d}$	Non-dimensional damping coefficient (kg/sm^2)
$\dot{D}$	Dissipation rate of energy by the fluid (Nm)
$[\mathbf{D}]$	Matrix used in solution of zero-order vortex strengths in §3.4.5
E	Elastic (Young's) modulus (N/m^2)
E_k	Flexible surface kinetic energy (Nm)
E_s	Flexible surface strain energy (Nm)
E_t	Total energy (Nm)
$\dot{E}_t$	Growth rate of fluid-structure instability (Nm/s)
F_f	Force of the fluid exerted on the flexible surface (N)
F_p	Restorative structural force of the flexible surface (N)
h	Flexible surface thickness (m)
H	Half channel height (m)
$\bar{H}$	Non-dimensional channel height
$\underline{i}$	Horizontal polar co-ordinate
I_{im}	Influence coefficient (influence on i^{th} panel owing to m^{th} panel)
$\underline{j}$	Vertical polar co-ordinate
l	Wall/fluid interface
L	Flexible surface length (m)
L_r	Length scale (m)
$\bar{L}$	Non-dimensional flexible surface length (mass ratio)
M	Discretisation denoter (M panels, etc...)
$\underline{n}$	Unit normal vector (m)

N_b	Number of vortex blobs
p	Surface pressure (N/m^2)
Q	Inspiratory volumetric flow rate (m^3/s)
Re	Reynolds number
t	Time (s)
t_r	Time scale (s)
$\underline{t}$	Unit tangential vector (m)
$\underline{u}$	Total flow velocity (m/s)
$\underline{u}'$	Total perturbation velocity (m/s)
$\bar{U}$	Non-dimensional flow velocity
U_c	Critical flow velocity (m/s)
U_D	Divergence speed (m/s)
U_F	Flutter speed (m/s)
U_∞	Free stream flow-speed (m/s)
$\underline{U}_\infty$	Free stream flow-velocity (m/s)
w	Flexible surface displacement term (m)
w_0	Initial deflection of flexible surface at $t = 0$
w_{max}	Maximum magnitude of deflection of flexible surface at $t = 0$
$\dot{w}$	Flexible surface speed term (m/s)
$\underline{\dot{w}}$	Flexible surface velocity term (m/s)
$\ddot{w}$	Flexible surface acceleration term (m/s^2)
W	Work done by the fluid on the flexible surface (Nm)
$\bar{W}$	Non-dimensional work done by the fluid on the flexible surface
$\dot{W}$	Rate of work done by the fluid on the flexible surface (Nm)
x	Horizontal location (m)
XX	Horizontal distance between influencing point and point of influence (m)
y	Vertical location (m)
YY	Vertical distance between influencing point and point of influence (m)

α	Vortex blob core size (m)
γ	Zero-order vortex singularity strength
δ	Denotes a small change in a property

ζ	Vorticity in the free stream
θ	Panel angle relative to horizontal (rad)
κ	Wave-number (1/s)
λ	First-order vortex singularity strength
ν	Poisson ratio
ξ	Horizontal co-ordinate (m)
π	3.141592654...
ρ	Flexible surface density (kg/m^3)
ρ_f	Fluid density (kg/m^3)
σ	Zero-order source/sink singularity strength
ϕ_i	Discretised velocity-perturbation potential
φ	Angle between influencing point and point of influence (rad)
ψ	Stream function
ω	Angular frequency of oscillation (rad/s) / Vorticity field
Γ	Total vortex singularity strength
Φ	Total velocity-perturbation potential

Superscripts

b	Vortex blob property
D	Downstream half of flexible surface
L	Lower side of flexible surface
N	Normal component
T	Tanegential component
U	Upper side of flexible surface / Upstream half of flexible surface
$'$	Perturbation / Transient property

Subscripts

b	Vortex blob property
cs	Central surface property
i	Discretisation denoter (i^{th} panel, etc...)
m	Discretisation denoter (m^{th} panel, etc...)
p	A point p being influenced
TE	Trailing edge of the flexible surface
w	Channel wall property
xp	Across the flexible surface

Chapter 1

Introduction

1.1 Overview

"Now there was Jim (snoring)*, alarming the whole desert, and yanking the animals out, for miles and miles around to see what in the nation was going on up there; there warn't nobody nor nothing that was as close to the noise as he was, and yet he was the only cretur that wasn't disturbed by it."* Tom Sawyer Abroad, Mark Twain (1894).

The snoring phenomenon: an unfortunate human side effect of evolution; no longer a humorous affliction but a social pest and the precursor of more serious ailments and their subsequent effects on our health. This thesis investigates the pathophysiology of the snoring phenomenon via numerical simulation. Numerical experiments are conducted using a novel fluid-structure model that also provides insight into an area of fluid-structure interactions that demands improved understanding.

Snoring occurs in the human upper airway, specifically in the human pharynx, see figure 1.1. The linear model developed in this thesis is used to conduct numerical experiments on a simplified geometry of the pharynx (see figure 1.2) and utilises the linearised theory of infinitely thin flexible-surfaces, ideal fluids and shed vorticity. Both the linear flexible surface and fluid components of the model are spatially discretised and when

coupled (along with the vorticity model) into a single linearised unsteady model, unsteady numerical-experiments can be conducted. A numerical model of this kind can predict the onset of fluid-structure instabilities that are one route to the generation of audible snores. The models are coded in FORTRAN77 and can be run on a standard PC. All post processing of results was carried out in MATLAB. The separate flexible surface and fluid components of the model are initially validated against well-established results. However, when the components are coupled to produce the unsteady model, only similar results from the published literature are available to compare with. The author sets out a logical investigation into the validity of the unsteady model that suggests the model is at least physically correct for the cases studied. Full validation would require careful experimental work.

This study of snoring belongs to the field of bioengineering, combining (the knowledge of) engineering and medicine. It is hoped that properly validated numerical models can economise on expensive or highly complex *in vivo* experiments and be used to determine correct treatment for individual patients. On a personal note, the author was surprised at the extent of passion exhibited in the response of people who discovered he was investigating the snoring phenomenon. The number of offers of various family members, friends and partners for study was unprecedented. Although humorous, this points to the stressful effect snoring has on our everyday lives. It also highlights the dangerous effect snoring may have on those who cannot escape the burden of a snorer when faced with a stressful situation; for example, when astronauts are enclosed in a small space for a considerable length of time (Balint and Lucey, 2003). The following section of this chapter details current knowledge on the snoring phenomenon: its pathogenesis, characteristics, side affects, treatments and published models. This information is used in later chapters to set up suitable numerical experiments that investigate further the pathophysiology of snoring.

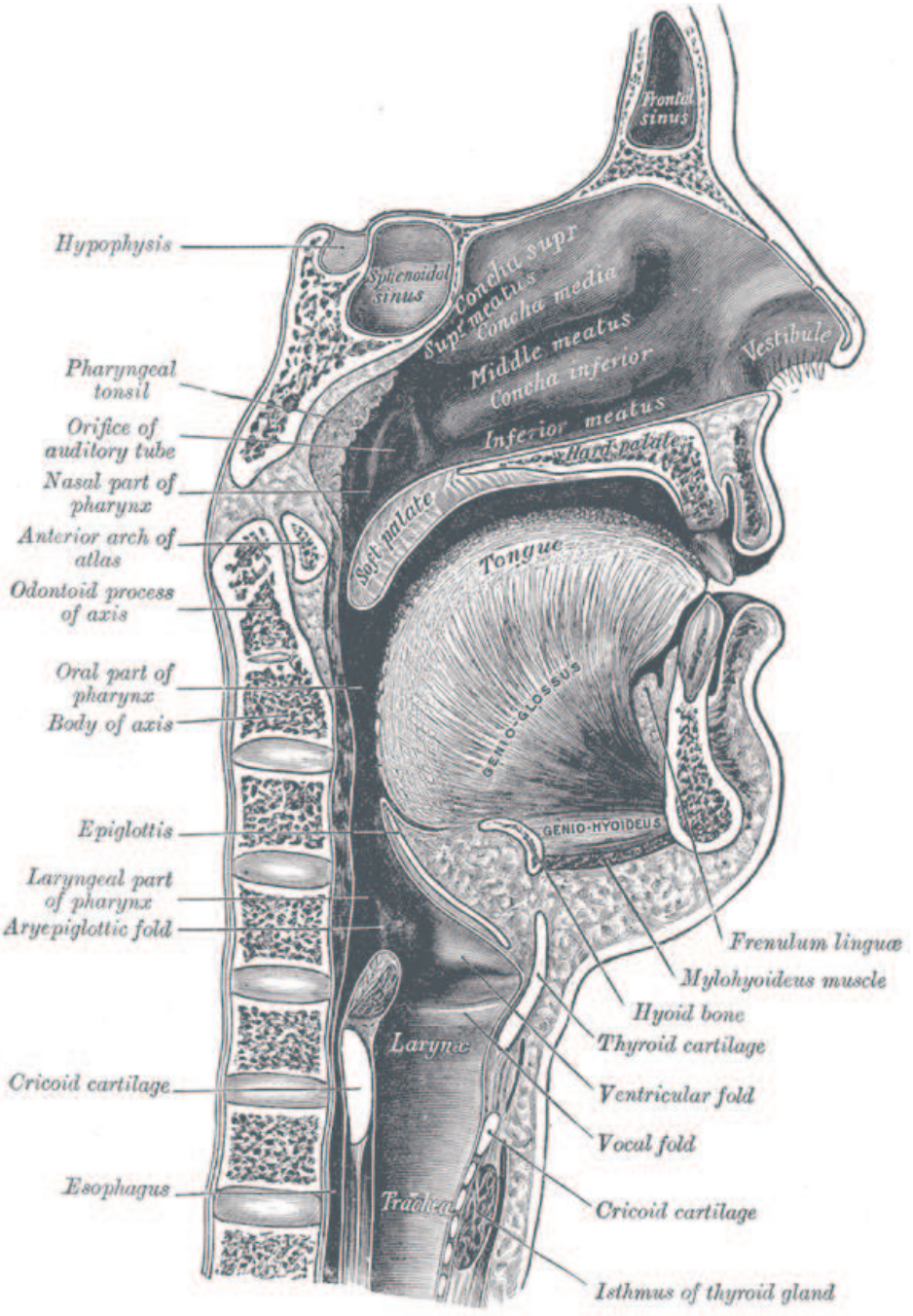

Figure 1.1: Saggital view of the human skull and neck (from Gray (1936)).

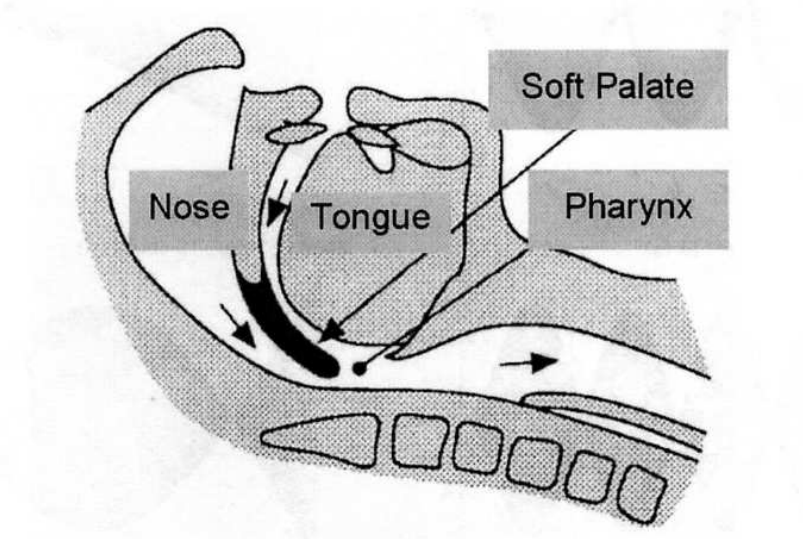

(a) The human upper-airway (adapted from Aurégan and Depollier (1995)).

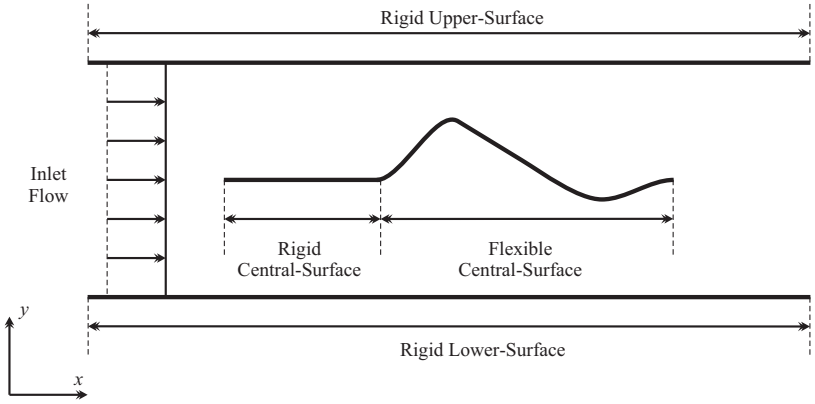

(b) Simplification of pharynx to be modelled numerically.

Figure 1.2: The flow-structure geometry of interest in this thesis.

1.2 The Snoring Phenomenon

1.2.1 The Upper Airway

The upper airway, see figure 1.1, extends from the external entrance of the nares and oral cavity to the junction between the oesophagus and the tracheal airway. The upper airway can be categorised into three anatomical regions:

- **nasal cavity**: extending from the external nares to the posterior nasal concha;
- **oral cavity**: extending from the lips to the tip of the soft palate;
- **pharynx**: extending from the posterior nasal concha to the glottis of the larynx.

These can all be included in the respiratory system along with the trachea, the bronchus, bronchioles and lungs. The pharynx (approximately $0.12\text{m} - 0.14\text{m}$ long) can be further subdivided into three regions:

- **nasopharynx**: extends from the posterior nasal concha to the tip of the soft palate;
- **oropharynx**: extending from the caudal margin of the soft palate to the base of the tongue;
- **laryngopharynx**: extending from the base of the tongue to the larynx.

Further description of the upper airway and the palate and their functions can be found respectively in Appendices §A.1 and §A.2, along with a short glossary of several of the medical terms used in this thesis in Appendix §A.3.

1.2.2 Pathophysiology of Snoring

Snoring is the acoustic manifestation of the vibration of soft flexible-tissues in the upper airway, specifically during sleep. As one inspires, the inspiratory flow speed, U_∞,

increases. This leads to an increased Reynolds Number, Re, and hence increasingly perturbed flow through the region. Subsequently, pressure fluctuates rapidly and initiates flow-induced structural instabilities (FISI) within the soft tissues. At a critical flow velocity these tissue vibrations will be strong enough, provided the frequency is in human auditory range, to manifest as the sound of snoring. Tissue structures involved in the production of snoring are the soft palate, uvula and the pharyngeal walls and to a lesser extent the tonsils and the base of the tongue. Martin (2002) and Amatoury (2004) both reason that soft tissues exist in the upper airway as an engineering compromise has been made in human evolution between the upper airway's rôles of deglution and aspiration. If the only function of the upper airway was to peristaltically pass masticated food on its journey to the stomach, the soft tissues would be far more pliable. On the other hand, if the upper airway had only to facilitate the passage of air to the lungs, the tissues would be rigid. In fact, the upper airway must do both and so its mechanical properties are somewhere in between. There are a multitude of physical attributes that define a snorer. These can generally be divided into two classes of pathophysiological mechanism: abnormally soft upper airway tissues and abnormally high U_∞, as outlined in figure 1.3 below. Snoring will occur in the former class at low U_∞ values. To demonstrate the process in the latter class of generating abnormally high U_∞, consider the inspiratory

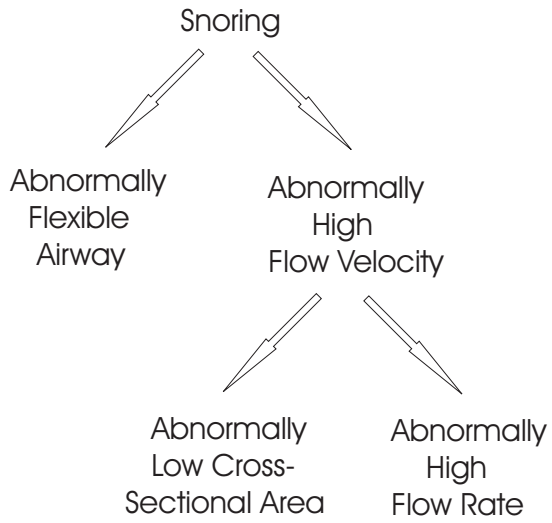

Figure 1.3: Pathophysiology of snoring.

volumetric flow rate, Q, of a human. Q is equated as

$$Q = U_\infty A, \tag{1.1}$$

where A is the averaged cross-sectional area of the upper airway. Q is maintained at a constant level by the body. Therefore, as again shown in figure 1.3, U_∞ can be abnormally high via two mechanisms:

- **abnormally small** A: usually referred to as high upper-airway resistance. The cross-section of a snorer's upper-airway is likely to be either circular or slightly elliptical in nature with the narrowing predominantly at the tongue base and hyoid bone level (Schwab *et al.*, 1995). Other physical features could be a receding chin, enlarged tonsils and small degree of mouth opening;
- **abnormal** Q **required**: owing to poor ventilation, increased lung capacity, hypoxia or hypocapnia.

The physical attributes described above lead to snoring via a single pathophysiological mechanism. During sleep, the *patency* of the upper airway reduces and leads to the production of snoring via all three mechanisms; this process will now be described. Amatoury (2004) defines patency as the upper airway's tendency to narrow and hence cause partial or complete airway obstruction, further saying that in normal sleeping subjects, airway patency increases significantly when compared with the awake state. Amatoury states that airway patency is chiefly determined by the balance between the activity of the *respiratory muscles* (the chest wall and diaphragm; these generate inspiratory negative pressure within the upper-airway lumen), and the *upper-airway dilator muscles* (that act to oppose upper-airway collapse). The limited rigidity the upper airway does have is partly maintained by dilator muscle tension rather than the inherent physical properties of its tissues. Therefore during sleep when dilator muscle activity falls and these supporting muscles relax, the upper airway becomes soft (abnormally flexible) and narrows (abnormally small A). Therefore, the work involved in breathing is augmented leading to an increased activation of the diaphragm and chest-wall muscles.

This increased activation leads to a greater suction pressure on the upper airway (and therefore, abnormally high U_∞). Alongside the hypotonia of the dilator muscles and the drop in intraluminal pressure, a greater pressure is exerted inwards on the upper airway which increases the likelihood of further collapse and the possibility of snoring initiation. Other physical factors that lead to snoring combining several or all of the pathophysiological mechanisms mentioned above are age, gender, alcohol consumption, a relatively long soft palate, obesity, behavioral state and nasal congestion. Snoring is more likely to occur during the inspiration period of the respiratory phase, as an abnormally high U_∞ leads to increased negative pressure in the upper airway (to create a pressure difference such that air can flow into the lungs), greater intraluminal pressure and therefore a high susceptibility to collapse. Upper-airway narrowing during sleep may not involve the complete pharynx but may be limited to specific segments. Narrowing is facilitated by head and neck position and also sleeping in the supine position, where gravitational forces acting on the soft tissues of the upper airway, especially the tongue and soft palate, force them to collapse, falling back towards the posterior pharyngeal wall.

1.2.3 Acoustic Properties of Snores

As there are several mechanisms that govern snoring and many physical factors that influence the phenomenon, it follows there will be several different types of snores. By measuring the acoustic properties of snores, it is possible to distinguish and categorise snores into different types. Snoring generates acoustic noise via the vibration, and hence compression and rarefaction, of adjacent mediums; the bones of the ear detect these vibrations. Amatoury (2004) describes how snoring acoustic characteristics are defined by comparing the upper airway to a guitar. Increasing the stiffness of a guitar string increases the sound frequency produced. Frequency can also be altered by placing a finger on the string to change the length. Similarly, increasing the stiffness or reducing the length of the soft palate will increase the acoustic oscillation frequency of the snore produced. Also, the more massive a string, the lower the acoustic frequency produced

and hence the more mass in the upper airway the lower the snore frequency. Sound intensity is proportional to the strength of the picking; in a snorer, it is proportional to the strength of inspiration. A loud snorer can produce a sound of 85 dB though its intensity in a regular snorer is usually around $50 - 60$ dB (Schoenstein, 1997). A study by Miyazaki *et al.* (1998) found that snores generated at different locations in the upper airway had characteristic frequency ranges. When a snore initiates, the site of the snore can be identified using several pressure transducers; frequency values can then be assigned to particular sites. Sites of snores and their respective characteristic sound frequencies were: soft palate 102.8 ± 34.9 Hz, the tonsil/tongue 331.7 ± 144.8 Hz, the soft palate/tongue 115.7 ± 58.9 Hz and larynx ~ 250 Hz. Beck *et al.* (1995) acoustically grouped snores into simple- and complex-waveform types. Complex-waveform snores were characterised by a repetitive, equally spaced train of sound waves that began with a large deflection followed by a decaying amplitude wave. In the frequency domain, there was a peak power surrounded by smaller equally spaced peaks. Simple-waveform snores exhibited a shape in the time domain close to that of a sine wave with slight deflections such that there was almost no sign of secondary internal oscillations. Therefore in the frequency domain there was a dominating single peak followed by one or two much smaller peaks. Beck *et al.* suggested that complex-wave form snores are produced from complete momentary closure of the upper airway, developing tissue vibrations as a result of the slam when the walls meet to be followed by a rapid popping when the airway reopens. Simple-waveform snores therefore represented oscillations of the upper airway wall (or other associated structures) about a base point without reaching absolute closure. Expiratory snores have also been measured by Perez *et al.* (1993) and are found to have a higher fundamental frequency and wider spaced harmonics. Perez *et al.* suggested that this was due to a change in the source of vibration to the tonsil.

1.2.4 Pathology of Snoring

Apart from the obvious social infraction, snoring is the precursor and progenitor of several other diseases. Amatoury (2004) describes that snoring is one of many sleep

disorders that come under the heading of sleep-disordered breathing (SDB). The SDB spectrum can be separated into two broad categories:

- those associated with abnormalities of central respiratory drive;
- those associated with obstruction and narrowing of the upper airway.

Sleep disorders in the first category are known as central sleep-apnœa. Snoring comes in the second category. Also in this second category are:

- upper-airway-resistance syndrome (UARS): frequent arousals from sleep due to increase in upper-airway resistance;
- hypopnœa: partial obstruction of the upper airway coupled with a drop in tidal volume;
- obstructive sleep-apnœa: characterised by repeated obstruction of the upper airway leading to periods of complete cessation of airflow, associated with continued inspiratory efforts, oxygen desaturation and frequent arousals from sleep.

Obstructive sleep apnœa and hypopnœa are closely related and therefore are referred to under one name as obstructive sleep apnœa-hypopnœa (OSAH). An individual with UARS or OSAH will almost certainly exhibit snoring. A snorer has a greater likelihood of developing one of the more serious disorders listed above than a non-snorer. These disorders and snoring in particular have been linked to cardiovascular disease (CVD). CVD is disease of the heart and blood vessels. It includes all diseases of the circulatory system such as myocardial infarction (heart attack). One CVD is cerebrovascular disease which usually refers to stroke (cerebral infarction) and transient ischaemic attacks (strokes that are relatively mild). During stroke, blood to the brain is cut off or significantly reduced, reducing oxygen supply and thus killing brain cells. The main pathophysiological mechanism leading to CVD is clogging of the arteries due primarily to atherosclerosis. Artherosclerosis manifests as plaque-like material building up in arteries. The causes of this build-up are not understood although there are several theories. One theory reasons

that the plaque build-up is a reaction to injury (Ross, 1986). Amatoury (2004) proposes that damage to the carotid artery due to snoring vibration over several years could lead to artherosclerosis. CVD can also be caused by hypertension. Hypertension refers to abnormally high blood pressure in an individual, even when at rest. Snoring has been related to hypertension in several studies, for example see Bixler *et al.* (2000).

1.2.5 Treatment of Snoring

It has been shown that there are many types of snore. Also, the parts of the body involved are by no means simple in construction. The soft palate which plays a large part in all types of snores has a highly complex muscular structure, blood supply and nerve system (see §A.2 for further description of the soft palate). It therefore follows there will be no singular or simple cure for all types of snoring. Despite being a well known condition, treatments are still rudimentary and unsophisticated. Commercial appliances developed to treat sleeping breathing disorders aim to keep the oral and nasal airways open (Lowe, 2000). The main surgical procedure to treat snoring, uvulopalatopharyngoplasty, concentrates on reducing flutter of the soft palate. Ellis *et al.* (1993) explain that this operation removes a large section of the soft palate and that although it is a successful operation, it is also a drastic one with attendant morbidity and mortality. They executed a new procedure, *palate stiffening*, where part of the soft palate is removed with a laser. The scar tissue that forms over the wound following the operation is stiffer than the original skin, making the soft palate less susceptible to flutter. Other treatments for snoring include the application of constant-positive airway-pressure via a face mask whilst sleeping, nose clips to keep the nostrils open and the removal of mucous membrane from the inside of the nose. The sophistication of snoring treatments will increase with quality of the research conducted into its pathophysiology. To that end, Armstrong *et al.* (2003) have developed an optical-coherence tomography system that can be used to monitor upper-airway size, shape and function during sleep. Coupling this information with a fluid-structure numerical model of the upper airway yields a powerful tool in the investigation into treatments for snoring. Such numerical models

that have been published are now described.

1.2.6 Models of the Snoring Phenomenon

Several studies have been published that model different parts of the upper airway and are related to the snoring phenomenon. In general, they focus on explaining the occurrence of instabilities which lead to snoring. Gavriely and Jensen (1993) carried out analytical and experimental investigations of the snoring phenomenon. Experimental results found typical snoring sounds with frequencies in the region of 30 to 100 Hz. They created an analytical lumped parameter model of a piston on one surface of a fixed channel. Using this simple model they determined that instability was dependent on, in order of importance: a) flow rate; b) length, diameter and elastance of the collapsible segment; and c) the resistance of the upper airway and the fluid density. Aurégan and Depollier (1995) used analytical linearised-theory to model a flexible surface in a simplified resistance-model of a channel, also carrying out an experimental analysis. Their model showed that snoring was controlled by two parameters, one related to soft-palate characteristics and the other related to flow conditions and discovered two types of snore termed *pure* and *apnœic* snores. Pure snorers generated snores through the instability of the soft palate. Apnœic snorers generated snores through the opening and closing of the oropharynx. They argued a non-linear model was required to model the abrupt large pressure changes, resulting from the closing of the pharyngeal channel, that lead to sound production. Huang has conducted several studies. Huang (1995) modelled palatal snoring analytically and experimentally using a cantilevered flexible surface in an unbounded flow. He found a specific flutter speed accompanied by a specific mode shape for the range of different flexible surfaces studied. Huang *et al.* (1995) described three different types of snoring: a) palatal with one airway open; b) palatal with both airways open; and c) pharyngeal snoring. In an experimental model of palatal snoring, they found the model palate lost stability due to flutter. Huang and Ffowcs Williams (1999) showed how neuromechanical forces changed the patency of the airway when oxygen levels were too low. They used a similar lumped-mass parameter model to Gavriely and Jensen with

the addition of a spring modelling the airway response to oxygen levels. They found that if the time of the response was delayed, as during sleep, the reactive stiffening of the airway could cause instability rather than stability. Aittokallio *et al.* (2001) analytically modelled the upper airway with a flow in a flexible channel with the interesting addition of time-dependent Q, wall stiffness and muscle tone. Analytical results produced output Q at the exit of the laryngopharynx similar to those seen in snorers. Balint (2001) and Balint and Lucey (2005) numerically modelled a flexible surface in a viscous channel flow at low Re. With both airways open, the flexible surface lost stability by flutter, but with one airway closed the flexible surface lost stability by divergence. In the latter case, when damping was included it promoted divergence by facilitating the formation of a critical deformation shape. However, for low values of damping at flow speeds below divergence onset, flutter can exist. At higher flow speeds a combination of flutter and divergence instability mechanisms can be responsible for oscillatory growth.

1.3 Summary

From the information presented in this chapter, it is proposed that the snoring phenomenon is a disease with serious side-effects and there is a need for better treatments to alleviate its causes. It has been shown that there are many pathophysiological mechanisms that cause snoring and, therefore, there are several different types of snore. Moreover, snore generation occurs in the human pharynx, a highly complex part of the human anatomy. It follows that there is no simple, single cure for any one patient and any treatment must be tailored to the individual. With the advent of real-time measuring techniques of the upper airway of snorers during sleep, there is a need for computational models that can interpret the measured data to ascertain the type of snoring occurring in the individual and allow the testing and optimisation of a treatment based on the individual's case. Such a model is described in this thesis; how it extends the results of previous models is described in the next chapter.

Chapter 2

Literature Review

This chapter examines existing literature on fluid-structure interaction phenomena and methods of modelling these phenomena relevant to this thesis. Each section covers a different topic and the main findings and key remaining questions are summarised in the final section; this provides an opportunity to describe the novel academic contribution made by this thesis.

2.1 Flow-Induced Structural Instabilities

When a fluid and structure interact, instabilities can occur. This subject area contains a variety of academic problems. Early studies by Rayleigh (1879, 1945) considered how flags flapped in wind; Gray (1936) considered the use dolphins made of their flexible skin to enhance their movement in water. The latter study was taken to the experimental stage by Kramer (1960a,b) who measured substantial drag reduction on a submersible covered with a flexible coating. This sparked a large amount of academic interest into flows over flexible surfaces, seminal works being conducted by Benjamin (1960, 1963) and Landhal (1962). From these studies a pattern began to emerge as to the types of flow-induced structural-instabilities (FISI) that could be generated. There are many excellent reviews of this area of academic work, for instance Carpenter (1990). Using

the description by Huang (1998), the main types of instability can be divided into three groups:

- Class A: the flexibility-modified Tollmien-Schlichting instability (TSI);
- Class B: the travelling-wave flutter (TWF);
- Class C: the static divergence and Kelvin-Helmholtz instability.

The fundamental sources of these instabilities are, respectively, fluid viscosity, vorticity gradient and fluid inertia. Structural damping has a destabilising effect on class A waves but a stabilizing role on class B waves. For elucidation on TWF in flexible surfaces see Carpenter and Garrad (1986), Gad-el-Hak (1986) and Lucey and Carpenter (1995). This subject area now incorporates several other geometries: a flexible surface in an unbounded flow, a flexible surface in a channel flow and flow in a flexible channel. Research into flexible channels has roots in the nuclear industry, for examples see Païdoussis (1966a,b). Larose and Grotberg (1997) described the link between these geometries as the similar ways the introduction of damping, a finite length to the structure or the presence of fluid viscosity can all be destabilising. Kornecki (1978) reviewed FISI in these different geometries and these were also recently summarised by Païdoussis (1998, 2004). The next geometry to be studied would be to couple a flexible surface and a flexible channel flow. In general, these different geometrical cases are modelled using linearised ideal-flow theory coupled with linear flexible surface-models. There are exceptions with examples of viscous fluid work by Carpenter and Garrad (1985, 1986) and non-linear walls being included by Lucey *et al.* (1997). Most work is analytical and based on the use of the Galerkin method, first utilised by Weaver and Unny (1970). Again, there are some exceptions. Lucey and Carpenter (1992a) have utilised panel methods to discretise the solution space. Their model and that of Noguchi *et al.* (1995) is similar to that created for the research in this thesis. Panel methods originated in the aerospace industry, a detailed description of these found in the work of Hess and Smith (1966). A large amount of research was conducted in the aerospace industry on aeroelastic instabilities and was summarised in several seminal texts by Fung (1955), Bisplinghoff *et al.*

(1957) and Scanlan and Rosenbaum (1960); importantly, the work of Dowell (1975) paid particular attention to the aeroelastic properties of plates. The subject remains topical, with articles appearing in the popular science press (for examples, see New Scientist (1997, 1999, 2000)). Examples of commercial FISI packages are given in the work by Knight *et al.* (2001), who describe a methodology using a commercial CFD code coupled with an independently developed two- and three-dimensional structural solver and Berry *et al.* (1999), who used the commercial structural solver ABAQUS to model the dynamics of the soft palate. Theoretical research in general has not utilised commercial software because it is interested in the initiation of the instabilities and therefore simplified linear models are used. Once *unit effects* are understood, the incorporation of further effects such as viscosity can be made, though the usual next step would be to make initial linear models non-linear.

2.1.1 Flapping Flags

Flags flap. Consider a flag in a mild breeze where the airflow is laminar. The flag is a flexible object that bends easily and stretches with difficulty. Huber (2000) asks: why does the flag flap in an unstable motion (*flag flutter*) and not extend straight out in the direction of the breeze parallel to the streamlines? Rayleigh (1879), who likened the problem to that of Kelvin-Helmholtz instability, predicted that any perturbation to the flag or the breeze would lead to flag flutter. Thoma (1939) showed that the mass of the flag had an important rôle to play in the formation of flag flutter. Stearman (1959) studied the problem experimentally and theoretically, finding a critical velocity, U_c; above this fluid velocity the flag would enter into unstable oscillations owing to a particular type of instability. Taneda (1968) obtained experimental results showing that when the flag did not flutter, von Karmán-like vortices were shed from the trailing edge; when the flag did flutter, the flow separated from the surface, accompanied by a large eddy wake and the *Kutta condition* seemingly not being satisfied. Referring to Houghton and Carpenter (2003), the Kutta condition states that a stagnation point should be present at the trailing edge of any lifting body of arbitrary shape and finite length; in the case

of an infinitely thin or cusped trailing edge, it is sufficient to require that the velocities above and below the surface be equal at the trailing edge. This condition ensures that fluid flow does not occur from one side of the trailing edge to the other. Essentially, Balint and Lucey (2005) describe that the deforming flag is a variable-lift thin aerofoil and the Kutta condition reflects the (changing) lumped bound-vorticity that is the sum of the spatially-distributed vorticity located in the boundary layers on the upper and lower sides of the flag. The Kutta condition holds for linear deformations of the flag, but for larger oscillations additional fluid forces are such that the Kutta condition maybe violated, as in the observations of Taneda detailed above. Datta and Gottenberg (1975) showed that their derived governing equation of a flag, approximated as a cantilevered flexible surface, in an air flow was similar to that of a suspended fluid-conveying pipe; this similarity remained valid in the non-linear case. Recently, Rayleigh's original idea was contradicted by Zhang *et al.* (2000), who discovered a stable oscillation at U_c, a *steady state*,[1] of a flapping flag, modelled by a filament in a thin-film flow. Also, when instability was observed, it was not caused by vorticity shed from a flag pole as would be the case with a flag; the instability was initiated by the dynamic interaction of the filament's tension, elastic rigidity and mass with the fluid flow. When the steady-state oscillation occurred, filament mass had come into balance with fluid mass, while the elastic energy of the filament balanced the kinetic energy of the fluid. In this thesis the fluid is modelled as an ideal fluid *i.e.* a fluid that is inviscid, irrotational and incompressible. If the flexible surface is initially flat, no instability occurs as observed in the experiments of Zhang *et al.* FISI can still occur but the model requires a *kick* in the form of an initial deflection of the flexible-surface or an applied pressure perturbation. This shows that the kick in the experiments of Zhang *et al.* was provided by the viscosity and compressibility of the flow and the flow's ability to rotate.

[1] This oscillation is also known as a *neutrally stable* state or a *limit cycle*.

2.1.2 Flutter and Divergence

The critical velocity, U_c, is the velocity at which the fluid forces and the structural forces of the flexible-surface come into balance and a steady-state oscillation is observed. Above this velocity a particular type of FISI will occur. Flexibility-modified-TSI cannot occur in an ideal fluid-structure interaction because of the absence of viscosity. Therefore, two types of FISI remain that can occur; these are flutter and divergence. If the instability observed above U_c is of the divergence type, U_c can be rewritten as U_D; similarly, if the instability observed above U_c is of the flutter type, U_c can be rewritten as U_F. Balint (2001) describes that during divergence, the aerodynamic forces and moments exceed the restorative forces of the flexible surface. As the surface displacement increases, local fluid velocity increases owing to the increased curvature of the surface and, if in a channel, the reduced cross-sectional flow area. Consequently the aerodynamic forces increase too, leading to significant surface displacements. Divergence is considered a quasi-static instability. Flutter, conversely, is regarded as a dynamic instability. Unsteady flow dynamics cause phase shifts between the flexible surface velocity and the fluid pressure away from the ninety degrees neutral state. The phase shift occurs as fluid pressure is not solely proportional to flexible surface curvature but is also affected by the finite length of the structure (Lucey and Carpenter, 1993) and the hydrodynamic damping, inertia and viscous effects of the surrounding fluid. This phase shift provides a mechanism for the surface to extract energy from the flow, allowing constructive or destructive interference between the two and thus the fluid can either destabilise or dampen the surface's motion. Structural damping may influence this mechanism by slowing down the displacement growth or even reversing it. Kornecki *et al.* (1976) described some of the intriguing aspects of the aeroelastic instabilities of panels; the type of instability, whether static or dynamic, depends both on the surface-end conditions and on the Mach number. For example, if a two-dimensional panel is simply supported or clamped at both edges it undergoes divergence in subsonic flow, but flutters in supersonic flow; conversely, a cantilevered panel clamped at one end and free at the other flutters in subsonic flow and undergoes divergence in supersonic flow. Qualitatively, these results

may be explained by noting that at supersonic Mach numbers, the principal aerodynamic pressure contribution is proportional to the panel slope, while at subsonic Mach numbers the leading term in the expression for aerodynamic pressure is proportional to curvature. The rôle of the edge conditions of the panel in determining flutter or divergence is analogous to that for tubes with internal flow.

2.2 Flexible Surfaces in an Unbounded Flow

This particular flow-structure case can be modelled by moving the channel walls shown in figure 1.2(b) *far away*, so that they have no effect on the flexible surface pressure distribution. This is approximately achieved when the half channel height H is greater than the flexible surface length L. General phenomena observed and parameters used in their measurement in this particular flow-structure interaction are now described before specific research is reviewed. In this thesis, as the fluid is modelled as an ideal fluid, a non-dimensional length parameter, $\bar{L}$ (this is often referred to as the *mass ratio*) is utilised instead of using Re to distinguish between result regimes. It is defined as the ratio of fluid mass to flexible surface mass, as shown in the following definition

$$\bar{L} \equiv \frac{\rho_f L}{\rho h}. \tag{2.1}$$

If the fluid was viscous, $\bar{L}$ would still be required to be calculated; Re describes the relation of fluid inertia forces to fluid viscous forces and thus describes which flow regime is currently applied, whereas $\bar{L}$ describes the relation between the fluid mass and structural mass in the coupled system and which of these is dominant. As $\bar{L}$ changes owing to, for example, the change between air and water or between long and short flexible surfaces in the flow-structure system, so the nature of the observed FISI change. For a flexible surface of low $\bar{L}$ ($\bar{L} \leq 1$), it is difficult to induce instability in the flexible surface. The fluid-structure system is equivalent to, for example, a piece of sheet metal in an airflow; the flexible surface mass is large relative to the fluid mass and therefore U_c is high with the flexible surface retaining its original deflected shape and oscillation frequency. Although the flexible surface does lose stability due to divergence, the critical

divergence and flutter speeds are so similar that only the flutter instability is observed. As $\bar{L}$ increases ($\bar{L} > 1$) instability of the flexible surface becomes easier to induce. There are several reasons for this phenomenon:

- as ρ_f increases, the fluid exerts a greater distributed force;
- as L increases, the area of flexible surface flush to the fluid is larger, therefore overall fluid weight (and therefore force) applied to the flexible surface is larger;
- as L increases, if gravity is accounted for, moments applied by the force owing to both the fluid and flexible surface weight are larger about the fixed end;
- as L increases, greater flexible surface curvature is possible and the flexible surface is therefore more susceptible to fluid lift forces.

Also as $\bar{L}$ increases, oscillation frequency and U_c reduce, asymptoting to a constant value. The flexible surface can now be observed to diverge at a critical flow speed well below that of the critical flutter speed owing to the greater lift force of the fluid. As the flow velocity is increased towards that of the critical flutter speed local buckling of the flexible surface is seen, as observed in flag flutter or on the skin of swimming mammals, see figure 2.1. There is a question of inconsistency at the same value of $\bar{L}$; for instance, a bridge and a submarine may have the same $\bar{L}$, but surely instabilities can be induced in the bridge at a lower free stream velocity than a submarine? Therefore, a non-dimensionalised velocity, $\bar{U}$, is utilised which varies with fluid mass, flexible surface mass and stiffness and is defined as

$$\bar{U} \equiv \frac{\rho_f}{\rho h} \frac{1}{\sqrt{\frac{B}{\rho h}}} \underline{U}_\infty, \tag{2.2}$$

where ρ, h and B are respectively the density, thickness and flexural rigidity of the flexible-surface. Therefore, although the bridge and submarine would have the same non-dimensionalised U_c, $\underline{U}_\infty$ would have to be considerably higher for the submarine owing to its relatively higher flexural rigidity. This non-dimensional scheme was also utilised by Crighton and Oswell (1991), Lucey (1998) and Lucey *et al.* (2003). Datta

and Gottenberg (1975) obtained experimental and simple, but qualitatively correct, analytical results for a flexible strip hanging vertically in a flow for $\frac{1}{6} \leq \bar{L} \leq 2$. Higher U_c was observed in experiments than was predicted by analytical results. It was observed that smaller-amplitude oscillations preceded U_c, but were not consistently observable in the experiments. Increasing strip width and thickness caused U_c to rise. Bending stiffness only played a significant role for $L \leq 10b$, where b was the flexible surface width. Kornecki *et al.* (1976) analysed linear flexible surfaces with different end conditions in an ideal fluid. Results indicated that the experimental flexible surface was somewhat stiffer than the ideal theoretical one assumed in the calculations. Shayo (1980) extended the work of Kornecki *et al.* and showed that two-dimensional analysis could yield an underestimate of the critical velocity of finite-width panels. Shayo also demonstrated that the wake at the downstream trailing-edge of a cantilevered flexible surface became of increasing importance as $\bar{L}$ increased. Huang (1995) investigated $0.1 \leq \bar{L} \leq 1.2$ with

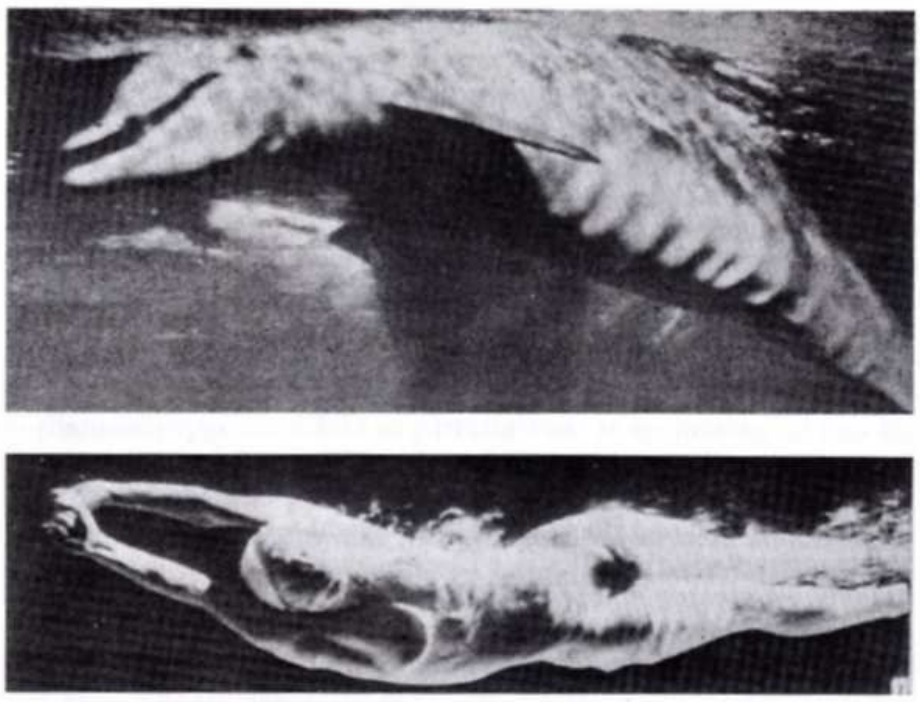

Figure 2.1: Local buckling in the skin of a *delphinidae* (top photograph) and a *homo sapiens* (bottom photograph) (both adapted from Aleyev (1977)).

an analytical model and experimental work. The analytical model used a linear analysis of flexible surface motion with *in vacuo* modes, represented by a truncated sum of orthogonal functions, used to approximate the deformation of the fluid-loaded flexible surface. The flow was modelled as an ideal fluid and included viscous effects through a Kutta condition at the free trailing-edge. Qualitative observations of experimental results identified a flutter instability due to gradual build-up of vibration, then a sudden occurrence of large-amplitude vibration; no static divergence was found. A unique U_c existed provided flow speed was increased slowly. The experimental trend of U_c agreed with that of analytical results showing a strong dependence on $\bar{L}$ below $\bar{L} = 0.3$. Above this value, U_c was constant or increasing slowly up to $\bar{L} = 1$. Mild stationary vibrations were found before the final advance of flow velocity to U_c was made; these mild vibrations were interpreted as the steady state. Bottlenecks were observed in the deflection envelopes close to the theoretically predicted position; the bottleneck was observed to shift upstream when the flow speed was increased, as theory predicted. Theoretical prediction of eigen-vibration as a combination largely consisting of the first two *in vacuo* modes was confirmed. This *Huang flutter* was caused by the finiteness of the flexible surface yielding aerodynamic forces that were out of phase with its motion. Quantitative observations of experimentally measured U_c showed they were higher than the theoretically predicted values. Huang explained that if flow velocity was increased very slowly, flutter actually occurred far beyond the anticipated critical speed for the steady state. Also, structural non-linearities such as dry friction and residual strains may exist that, in effect, set up an initial barrier to instability initiation and a definite activation energy may then be required to break through this barrier.

Yamaguchi *et al.* (2000a,b) studied in detail the region $0.1 \leq \bar{L} \leq 100$ with a numerical model and an extensive set of experiments. The bound vorticity, shed vorticity and tension caused by fluid friction, c_{fo}, were modelled. For all values of $\bar{L}$, the flexible surface deflection peaks would move downstream, whereas pressure waves travelled *upstream*. Three regions were observed with their own distinct types and mechanisms of instability. These were: $\bar{L} < 1.4$; $1.4 \leq \bar{L} \leq 20$; and $\bar{L} > 20$. For $\bar{L} < 1.4$, numerically

predicted oscillation modes and frequencies were near to those of the second eigenmode *in vacuo*. U_c fell with increasing $\bar{L}$ and the effect of c_{fo} was negligibly small. The authors surmised that in experiments the flexible surface was ordinarily in the form of the second eigenmode and not the first mode in accordance with the numerical result. For $1.4 \leq \bar{L} \leq 20$ experimental data of U_c were in a widely scattered band. It was found that a higher discretisation was required for high $\bar{L}$ to capture the introduction of higher eigenmode shapes into the critical flutter mode. The oscillation modes deviated from those *in vacuo*, the macroscopic modes resembling those of the third eigenmode equivalent or higher. The pressure distributions had more peaks than the oscillation modes. Experimental data suggested that actual sheet tension tended to increase with $\bar{L}$, as numerical results with higher c_{fo} better predicted the trend of the widely spread data. Such increases in the drag (and therefore friction) coefficient in fluid flow with increasing $\bar{L}$ have often been reported for fluttering flags and clothes. Possible causes for the phenomenon might be attributed to increases in the surface amplitude, flow separation from the surface and generation of vortices. For $\bar{L} > 20$, experimental data were few in number, but showed higher-order modes emerging for increasing $\bar{L}$. The effect of c_{fo} was marked in this region, affecting the mode shape of oscillation drastically. The ripples present on the flexible surface reflected those of the pressure distribution, suggesting that the waves were bending modes caused by the action of the fluid pressure. On the other hand, the longer and greater waves on the sheet were considered to be caused by skin friction. As c_{fo} was increased, the distance travelled by waves on the sheet decreased for a single oscillation. The speed of the waves were below that of $\underline{U}_\infty$. Greater c_{fo} shifted the major part of the sheet motion toward the trailing edge, possibly because of the greater restorative force toward the leading edge owing to the fixed end.

A cantilevered filament in a soap-film flow was studied experimentally by Zhang *et al.* (2000) who found two different steady states. The second undulating one is normally seen in potential-flow analysis but the first, where the filament becomes outstretched and a von Karmán street is ejected at the free end, is not. Yadykin *et al.* (2001) created a non-linear incompressible flow-structure model; the structure (a strip) had no damping

and was of finite width. Gravity and tangential fluid forces increased the strip tension and thereby reduced flutter amplitude. With increasing strip length, the sensitivity of the strip to flutter at pre-U_c velocities decreased and amplitude and frequency of the strip at U_c also reduced. They found that the introduction of non-linear terms into the flow-structure interaction was destabilising compared to the linear case. The oscillations at pre-U_c damped out though there was no damping in the structural model; the damping was provided by the aerodynamic model radiating energy to infinity along the wake behind the strip. The process from initial disturbance to steady state took twelve seconds and the amplitude of the wave increased towards the free edge. Fitt and Pope (2001) extended the work of Shayo (1980) on a cantilevered flexible surface in an ideal flow by deriving numerical solutions to the governing integral-equations and were able to simulate the flutter instability. Watanabe *et al.* (2002a,b) investigated $0.1 \leq \bar{L} \leq 100$ with two numerical models and a set of experiments. Flow visualisations showed flow patterns similar to those seen in potential flow and good agreement was found between Navier-Stokes and potential-flow models for the prediction of the form of the critical mode. Similar trends but poor agreement was found between experimental values and potential-flow analysis predictions of the magnitude of critical velocity. Experimental hysteresis was found, such that U_c was lower if measured by lowering from a velocity above U_c. It was found that flutter instability was governed by artificially-generated damping induced by a difference between lift values at different mass points along the flexible surface. As $\bar{L}$ was increased, different eigenmodes were found to be the main constituent of the observed flutter. Flow visualisation of experimental flexible surface motion showed good agreement with that predicted by the numerical models. Zhu and Peskin (2002) numerically modelled the experiments of Zhang *et al.* using the viscous *immersed-boundary method* to model the flexible surface and the flow; they were able to numerically recreate the steady-state and flutter oscillations observed in the experiments. Lemaitre *et al.* (2004) conducted physical experiments and also generated analytical results on the motion of vertically hanging flexible surfaces in an air flow in the range $0.1 \leq \bar{L} \leq 20$. Their tests confirmed the similarity between hanging pipes conveying fluid and hanging ribbons. For both experiments and the analytical model, U_c depended

strongly on length for short ribbons and weakly on length (a constant) for long ribbons. Asymptotic values of U_c were well predicted for long ribbons of the same material but not for ribbons made of different materials. Argentina and Mahadevan (2005) utilised thin-aerofoil and thin-plate theory to analytically model a cantilevered flexible surface in an ideal flow and were able to model three-dimensional and viscous boundary layer effects; these effects were found to raise the critical velocity.

2.3 Flexible Surfaces in a Channel Flow

Now the walls in figure 1.2(b) are brought close to the flexible surface. Initially consider the case where the central-surface is removed. From Massey (1995), the steady Bernoulli equation for an ideal fluid is

$$p + \frac{1}{2}\rho_f v^2 \quad = \quad constant, \tag{2.3}$$

that shows the greater the velocity of the fluid, the smaller the pressure within the fluid. This phenomenon leads to the Bernoulli effect; if a channel's walls taper, to conserve mass the flow velocity must increase as cross-sectional area decreases; therefore pressure decreases where the walls are relatively closer together. The central surface is now reintroduced into the channel. The distance of one wall from the central surface is H, the half-channel height. This is non-dimensionalised using the flexible surface length to give $\bar{H}$ (the channel ratio) defined as

$$\bar{H} \quad \equiv \quad \frac{H}{L}. \tag{2.4}$$

As the walls are moved relatively closer to the central surface, where the central flexible-surface constricts the passage owing to its deflection, pressure drops. This effect is balanced on the opposite side of the flexible surface where the pressure will increase as the channel here is relatively wide. The pressure difference across the surface is therefore increased; it would therefore be expected that the proximity of rigid channel-walls to the central surface is destabilising and would cause U_c of the flexible surface to fall. Aurégan and Depollier (1995) investigated $0.006 \leq \bar{L} \leq 0.02$ for $0.03 \leq \bar{H} \leq 0.8$ with

an analytical model and a set of experiments. The analytical model represented flexible surface deformation by orthogonal beam-functions and the flow-structure system was solved using the Galerkin technique; flexible surface-curvature effects were neglected. The length of the flexible surface was found to be of the same order as the vibration wavelength. Both theory and experiment showed the flexible surface lost stability in the form of flutter. This *channel flutter* was caused by the flexible surface alternately increasing and decreasing the half-channel width above and below it. The resulting forces from the ensuing Bernoulli-effect were out of phase with the surface motion. As the walls were moved apart U_c rose and was found to asymptote to a constant value. Conversely, U_c fell as $\bar{L}$ increased over the range studied. Guo and Païdoussis (2000) developed an analytical model of this flow-structure interaction and investigated $0 \leq \bar{L} \leq 1000$ for $0.1 \leq \bar{H} \leq 5$. The analytical model was similar to Aurégan and Depollier (1995) with the effects of stream curvature included. Clamped-free surfaces lost stability by single-mode flutter usually in the second mode; surfaces with fixed ends lost stability due to *divergence*, simply because of the magnitude of the destabilising aerodynamic forces. The trend of U_c made S-shaped jumps as $\bar{L}$ was increased that were caused by the increase in order of the eigenmodes constituting the critical flutter mode. Also, U_c rose and was found to tend asymptotically towards a constant as $\bar{H}$ tended to infinity ($\bar{H} \geq 1$ being a reasonable approximation for $\bar{H} = \infty$).

Balint (2001) and Balint and Lucey (2005) created a non-linear finite-element method to model a viscous channel flow interacting with a linear flexible-surface. The range $378 \leq Re \leq 1512$ (for $\bar{L} = 0.4$ and $\bar{H} = 1.2$) was investigated. Flexible surface stability was lost due to flutter with most of the energy transfer occurring in the upstream half of the surface. Instability set in beyond a critical Re when this energy transfer exceeded the rate of surface-energy dissipation due to material damping. Partial-blockage effects in the channel were not implicated in the flutter-instability generation. Thus, the instability mechanism was similar to Huang flutter for an unbounded fluid domain. Although Huang used a potential-flow solution, it was the enforcement of the Kutta condition that effectively generated the phase shifts. Balint and Lucey described that the phase shift

was generated by the action of the viscous boundary layers, further noting that the observed phase-shift-flutter type of instability is well-known in laminar boundary-layer flow over compliant coatings as the afore-mentioned travelling-wave flutter. Like the observed flutter, the critical Re for travelling-wave flutter is fundamentally dependent upon the level of damping in the compliant-coating material. When one airway was blocked, the principal means of destabilisation was divergence which set in at a flow speed beyond which the magnitude of the fluid-pressure force exceeded the restorative structural forces in the flexible surface. Structural damping promoted pure divergence by facilitating the formation of a critical-mode shape. However, Balint and Lucey described that for very low values of damping at flow speeds below that of divergence onset, flutter may exist and at higher flow speeds a combination of flutter and divergence instability mechanisms can be responsible for oscillatory growth. In such cases, the surface deformation largely comprised fluctuating combinations of both first and second modes of flexible surface deformation. The divergence instability found owed itself to the high hydrodynamic stiffness, dependent on flow speed as opposed to Re, caused by partial blockage to the upper channel in a predominantly one-sided flow.

Epstein *et al.* (1995) created an analytical model of two-dimensional infinitely long flexible surfaces in duct flow. It was noted that as the duct walls were moved relatively further away from the flexible surface, U_c rose and asymptoted to a constant value. However, when the flexible surface width was very much greater than the distance of the duct walls from the flexible surface, the duct walls had little effect on U_c. Yamaguchi *et al.* (2000a,b) used the method of images to calculate the effect of walls on their finite cantilevered flexible surface in an inviscid flow. They found that at $\bar{H} = 0.75$, U_c was reduced by 17%. Tanida (2001) analytically modelled the effect of channel walls and an inlet on a cantilevered flexible surface for $0.25 \leq \bar{H} \leq 2.5$. The movement of the surface was specified *a priori*. The channel walls were found to increase the lift of a previously isolated aerofoil. It was also found that if walls were relatively close to the flexible surface, U_c was lowered, whereas the introduction of an rigid inlet-length upstream and adjacent to the flexible surface was stabilising, thus increasing U_c. Wu and Kaneko

(2004) analytically modelled linear and non-linear viscous channel flow interacting with a non-linear flexible surface. A wide range of $\bar{H}$ were studied in the linear regime and one case for relatively close walls was studied in the non-linear regime. When walls were relatively close to the flexible surface, a wide steady state region was found similar to Yadykin *et al.* (2001), with upper and lower values of U_c. Below the lower U_c, the flexible surface oscillations decreased in amplitude owing to positive fluid-damping; the upper value of U_c demarked the onset of violent flutter. The amplitude of oscillation in the steady state was determined by initial conditions. As walls were moved further away from the flexible surface, upper and lower U_c rose and asymptoted to constant values at the same rate. The FISI were not changed significantly when the walls were moved relatively closer to the flexible surface.

2.4 Motivation

The model that is developed in this thesis captures the onset of FISI while displacements are still linear for the interaction of a flexible surface and an ideal channel flow. How the model developed in this thesis extends the work on this fundamental problem of flow-structure interaction is now examined. The most advanced work referred to in the literature review on the inviscid flow-structure interaction to be modelled in this thesis is that of Guo and Païdoussis (2000). Their work does not address the following open questions

1. investigation into fluid-structure phenomena via detailed analysis of the interaction between applied fluid-pressure and flexible-surface velocity along the flexible surface;

2. the effect of a rigid-inlet surface upstream and adjacent to the flexible surface and the effect of the singularity at its leading edge;

3. the effect of the variation of stiffness and damping properties along the length of the flexible surface;

4. the effect of an unsteady free-stream flow;

5. the effect of shed vorticity from the trailing edge of the flexible surface;

6. the effect of not presupposing the deflection of the flexible-surface;

7. the effect of spatial variation of the bounding channel geometry;

8. the effect of flexible channel walls;

9. the effect of non-linear fluid and flexible-surface models.

The derivation of the numerical model addresses open question 1. as it allows detailed analysis of the applied fluid-pressure and flexible-surface velocity; this gives physical insight into the many fluid-structure phenomena and instabilities observed in the fluid-structure interaction modelled in this thesis. The derivation of the numerical model presented in this thesis allows its application to open questions 2. to 4. and detailed results are presented in later chapters. With reference to open question 5., as the flexible surface moves, the bound vorticity of the flexible surface changes. To conserve vorticity, vortices equal in strength to the negative change of the bound vorticity between time steps must be shed from the trailing edge of the flexible surface. The derivation of

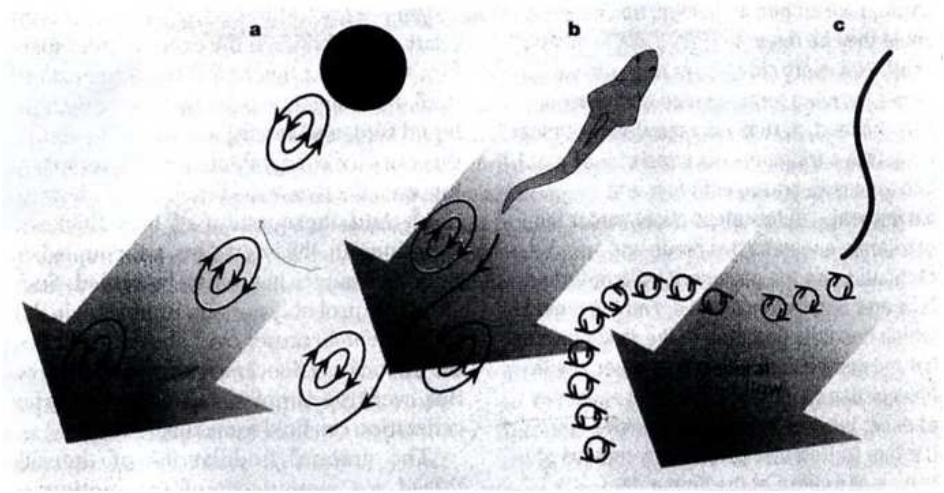

Figure 2.2: Ejection of vortices from bodies in a free-stream flow: (a) a stationary cylinder; (b) a swimming fish; (c) a thread (adapted from Huber (2000)).

the numerical model developed in this thesis captures this effect. The illustration in figure 2.2, adapted from Huber (2000), depicts how vortices are shed behind different bodies in fluid flow. Zhang *et al.* (2000) postulate that the undulations of the silk thread in their experiments, see figure 2.2(c), are reminiscent of the motion of slender-bodied organisms, such as swimming fish. An undulating silk-thread produces a narrow band of clockwise vortices when it moves to the right and of anti-clockwise vortices when it moves to the left. However, swimming fish cast off counter-rotating vortices, see figure 2.2(b), inducing a jet-like flow between the two rows of vortices; the momentum carried off by this jet is in turn related to the forward thrust on the fish. The latter case is more akin to the Karmán vortex streets shed from a cylinder, see figure 2.2(a). Discrete-vortex methods are utilised to numerically model these shed vortices and are described in many texts including the works of Chorin (1973), Ghoniem and Cagnon (1987), Sarpkaya (1989) and Lewis (1991). With reference to open question 6., the numerical model developed in this thesis is similar to the model developed by Balint (2001) in that the movement of the flow and structure is solely determined by the physics of the system and the deflection of the structure is not presupposed. These assumptions ensure physically realistic numerical experiments are conducted. The model of Guo and Païdoussis (2000) makes a presupposition of flexible-surface shape following the utilisation of the Galerkin method. Although this is an excellent simplification of the complex problem, it has been argued, see Lucey *et al.* (1997), that this approximation only allows the accurate modelling of static instabilities. With reference to open questions 7. to 9. the numerical model presented in this thesis facilitates the extension to non-linear fluid and flexible surface models and the incorporation of flexible channel walls, as described in the final chapter of this thesis. As noted at the beginning of this chapter, the next geometry to be investigated in this field of research is that of a flexible surface in a flow through a flexible-channel. The most advanced viscous-fluid work referred to in the literature review on the flow-structure interaction to be modelled in this thesis is that of Balint (2001) and Balint and Lucey (2005). The work described in this thesis seeks to extend their work by

- highlighting the effect of viscosity on this flow-structure interaction;
- conducting far more detailed numerical experiments as the model presented in this thesis is far more computationally inexpensive and therefore requires relatively low computational power to operate effectively.

Further motivation for this work is provided by the general applicability of this model to many physical flow-structure interactions and the knowledge this provides, most notably in this study to that of human snoring. It is proposed that this model can simulate many of the dominant fluid-structure properties of the snoring phenomenon in the human pharynx. The model can therefore be used to perform realistic numerical experiments to investigate the pathophysiology of snoring; with the development of real-time *in-vivo* measuring techniques of the physical attributes of sleeping patients, numerical models such at the one presented in this thesis can be used as a powerful tool to identify the particular cause(s) of snoring in an individual and tailor treatment to the patient concerned. The numerical model can also be applied to the research of other similar physical situations, such as the development of paper manufacture, sail technology and convertible-car roofs (for examples see Yamaguchi *et al.* (2000a), Fiddes and Gaydon (1996) and Knight *et al.* (2001) respectively).

Chapter 3

Theory

The flow-structure system and co-ordinate axes are as shown in figure 3.1. The mechanics of the disturbed system may be represented by an equation of motion of the form

$$[\mathrm{L}]w = -\delta p\left(\ddot{w}, \dot{w}, w\right), \tag{3.1}$$

subject to initial values, inlet conditions, rigid-wall boundary-conditions and flexible-surface edge-conditions. [L] is a differential operator on the vertical flexible-surface displacement, w. δp is the pressure perturbation due to the disturbances to the free-stream flow, $\underline{U}_{\infty}$, and is composed of hydrodynamic stiffness, damping and inertia. Initially in this chapter, the separate linearised flexible surface, velocity and vorticity models are described; the method of coupling these models into the final linearised unsteady model (that can accurately capture the onset of instability in this fluid-structure system) is then illustrated. Finally, diagnostic tools for the interpretation of unsteady results are introduced and the unsteady model is non-dimensionalised.

3.1 The Flexible Surface Model

The flexible surface is discretised into a number of mass points, $i = 1, 2, \ ..., N$, as illustrated in figure 3.2, where, for the purposes of numerical simulation, the various mechanical properties are lumped together.

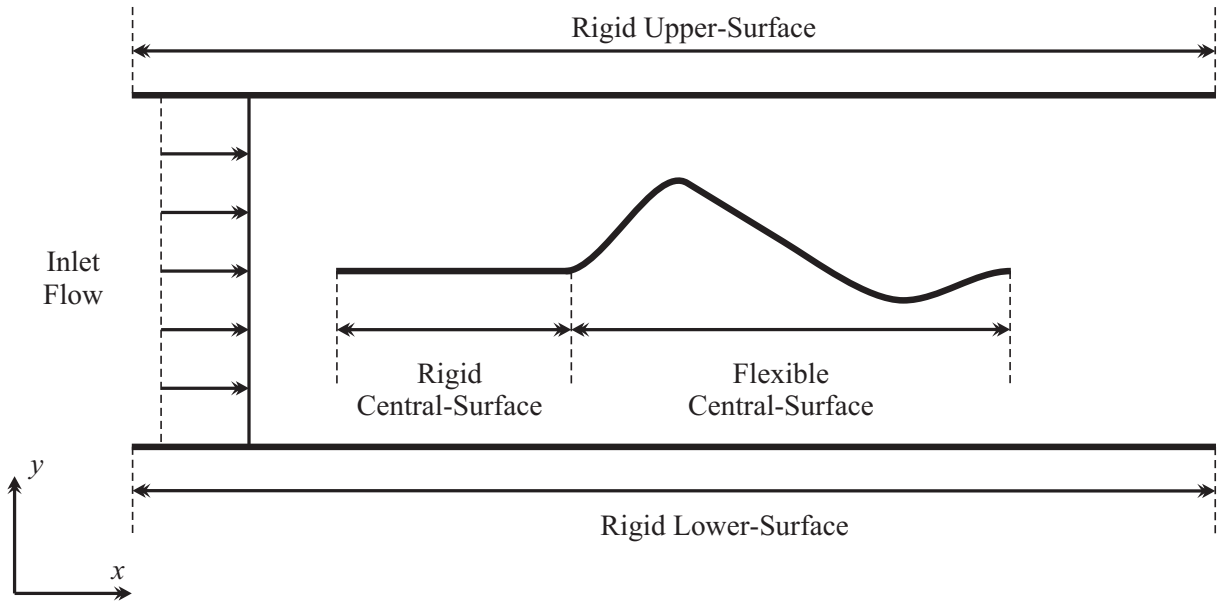

Figure 3.1: Flow-structure system and co-ordinate axes.

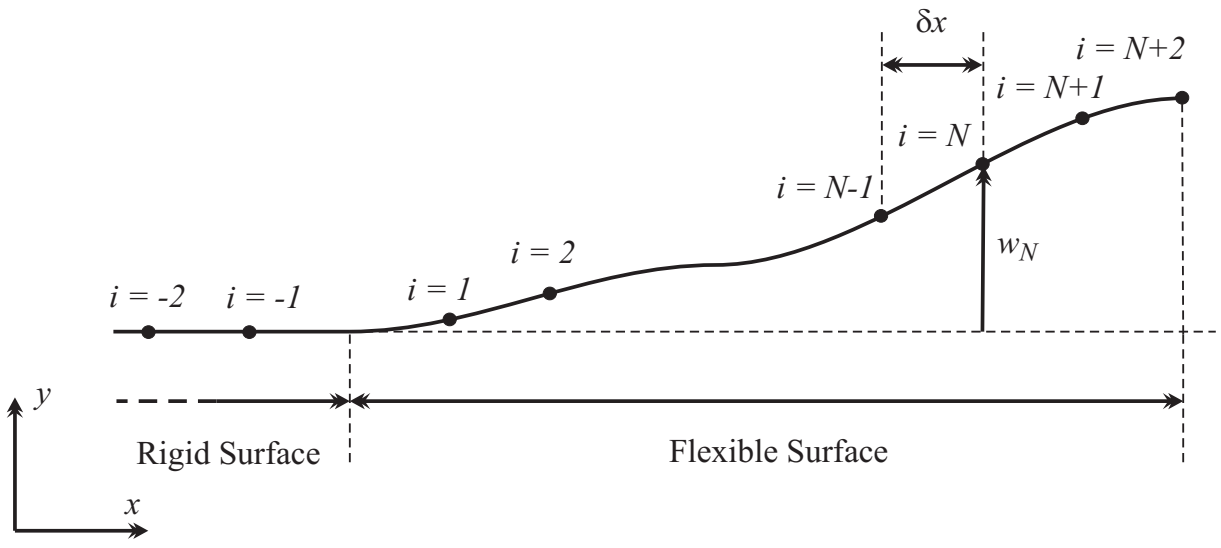

Figure 3.2: Flexible surface discretisation.

3.1.1 General Formulation

The linearised flexible-surface model uses small-deflection plate theory to model the movement of the surface. Balint (2001) details that the specific form of (3.1) (derived from Newton's Second Law) for a thin, elastic flexible-surface is

$$\rho h\ddot{w} + d\dot{w} + B\nabla^4 w = -\delta p, \tag{3.2}$$

where ρ, h and B are respectively the density, thickness and flexural rigidity of the flexible-surface.[1] The flexural rigidity is related to the elastic modulus, E, and the Poisson ratio, ν, as follows

$$B = \frac{Eh^3}{12\left(1-\nu^2\right)}. \tag{3.3}$$

The flexible surface is considered infinitely wide and thus two-dimensional; this leads to a correction in the calculation of the flexural rigidity (the term $1-\nu^2$) as there is no possibility of plane strain in the flexible-surface. Also, the flexible surface is assumed to be thin; therefore it deforms purely by bending and does not experience shear or the effect of its own weight. Balint further shows that the spatially discretised, finite difference form of (3.2) at subsequent time steps for the i^{th} nodal displacement can be written as

$$\begin{aligned} \ddot{w}_i^t &= \frac{1}{\rho h}\left(-\delta p_i^t - B\nabla^4 w_i^t - d\dot{w}_i^t\right), \\ \ddot{w}_i^{t+\delta t} &= \frac{1}{\rho h}\left(-\delta p_i^{t+\delta t} - B\nabla^4 w_i^{t+\delta t} - d\dot{w}_i^{t+\delta t}\right). \end{aligned}$$

Summing the above equations, and rearranging for $\ddot{w}_i^{t+\delta t}$, obtains

$$\ddot{w}_i^{t+\delta t} = \frac{1}{\rho h}\left(-(\delta p_i^t + \delta p_i^{t+\delta t}) - B(\nabla^4 w_i^t + \nabla^4 w_i^{t+\delta t}) - d(\dot{w}_i^t + \dot{w}_i^{t+\delta t})\right) - \ddot{w}_i^t. \tag{3.4}$$

Balint shows that the centred finite-difference operator at mass point i is given by

$$\nabla^4 w_i = \frac{6}{\delta x^4} w_i - \frac{4}{\delta x^4}\left(w_{i-1} + w_{i+1}\right) + \frac{1}{\delta x^4}\left(w_{i-2} + w_{i+2}\right), \tag{3.5}$$

[1] In the absence of damping and mass, (3.2) is sometimes known as *Lagrange's Equation*, for example see Szilard (1974). It is extended to this dynamic form using *d'Alembert's principle*.

where δx is the mass-point spacing. In addition, Balint shows that the basis equations for the motion of any mass point of the discretised flexible-surface can be written in the form of

$$\left\{\dot{w}_i^{t+\delta t}\right\} \approx \left\{\dot{w}_i^t\right\} + \delta t \frac{\left\{\ddot{w}_i^t + \ddot{w}_i^{t+\delta t}\right\}}{2}, \tag{3.6}$$

$$\left\{w_i^{t+\delta t}\right\} \approx \left\{w_i^t\right\} + \delta t \frac{\left\{\dot{w}_i^t + \dot{w}_i^{t+\delta t}\right\}}{2}, \tag{3.7}$$

using a simplified predictor-corrector method formulation, as detailed in Ferziger (1998). Therefore the system of equations to be solved (in finite-difference form) to obtain the displacement, velocity and acceleration of mass points on a flexible surface is defined above.

3.1.2 Boundary Conditions

At the extreme ends of the flexible surface, boundary conditions are enforced. Mass-point numbering for the upstream and downstream ends of the flexible surface is shown in figure 3.2, where mass points $i = N + 1$, $i = N + 2$, $i = -1$ and $i = -2$ represent dummy mass points used in the boundary-condition calculations. At the upstream end, a *clamped-end* condition is enforced. The first boundary-condition mass point, w_{-1}, is therefore stationary ($w_{-1} = 0$). In addition, the tangent of the deformed rod between w_{-1} and w_{-2} is zero; in mathematical terms, this boundary condition can be described as

$$\frac{\partial w_{-\frac{1}{2}}}{\partial x} = 0. \tag{3.8}$$

Since

$$\frac{\partial w_{-\frac{1}{2}}}{\partial x} = \frac{w_{-1} - w_{-2}}{\delta x} = 0,$$

the first derivative results in

$$w_{-2} = w_{-1} = 0. \tag{3.9}$$

At the downstream end a *free-end* condition is enforced; therefore, it is assumed that the bending moment and the shear force is zero at the final mass-point, w_N

$$\frac{\partial^2 w_N}{\partial x^2} = \frac{\partial^3 w_N}{\partial x^3} = 0.$$

Applying zero bending moment at w_N

$$\frac{\partial^2 w_N}{\partial x^2} = \frac{w_{N+1} - 2w_N + w_{N-1}}{\delta x^2} = 0,$$

the second derivative results in

$$w_{N+1} = 2w_N - w_{N-1}. \tag{3.10}$$

Applying zero shear stress at w_N

$$\frac{\partial^3 w_N}{\partial x^3} = \frac{w_{N+2} - 3w_{N+1} + 3w_N - w_{N-1}}{\delta x^3} = 0,$$

the third derivative results in

$$w_{N+2} = 3w_N - 2w_{N-1}. \tag{3.11}$$

3.1.3 Natural Frequencies

The natural frequencies of oscillation *in vacuo* are known as the eigenfrequencies of oscillation. For each eigenfrequency, there is an associated eigenmode shape given by an eigenfunction. From Nowacki (1963), for a cantilevered free beam, the n$^{\text{th}}$ eigenfunction, w_n^*, is given by

$$w_n^* = C\left[U(\lambda_n x) - \frac{S(\beta_n)}{T(\beta_n)} V(\lambda_n x)\right], \tag{3.12}$$

where C is an amplitude scaling constant and the functions $S(\beta_n)$, $T(\beta_n)$, $U(\lambda_n x)$ and $V(\lambda_n x)$ are defined as

$$\begin{aligned} V(\lambda_n x) &= \frac{\sinh(\lambda_n x) - \sin(\lambda_n x)}{2}, \\ U(\lambda_n x) &= \frac{\cosh(\lambda_n x) - \cos(\lambda_n x)}{2}, \\ T(\beta_n) &= \frac{\sinh(\beta_n) + \sin(\beta_n)}{2}, \\ S(\beta_n) &= \frac{\cosh(\beta_n) + \cos(\beta_n)}{2}, \end{aligned}$$

where L is the length of the flexible surface and $\lambda_n = \beta_n / L$; β_n are the solutions to the transcendental equation

$$\cosh \beta_n \cos \beta_n + 1 = 0.$$

For a cantilevered free beam, $\beta_1 = 1.875,\ \beta_2 = 4.694,\ \beta_3 = 7.855,\ \beta_4 = 10.996,\ \beta_5 = 14.137...\ \beta_n = (2n-1)\pi/2$. Using (3.12), the first six eigenmodes are depicted in figure 3.3. The corresponding angular frequencies of oscillation for the eigenmodes are given by

$$\omega_n \quad = \quad \frac{\beta_n^2}{L^2}\sqrt{\frac{B}{\rho h}}. \tag{3.13}$$

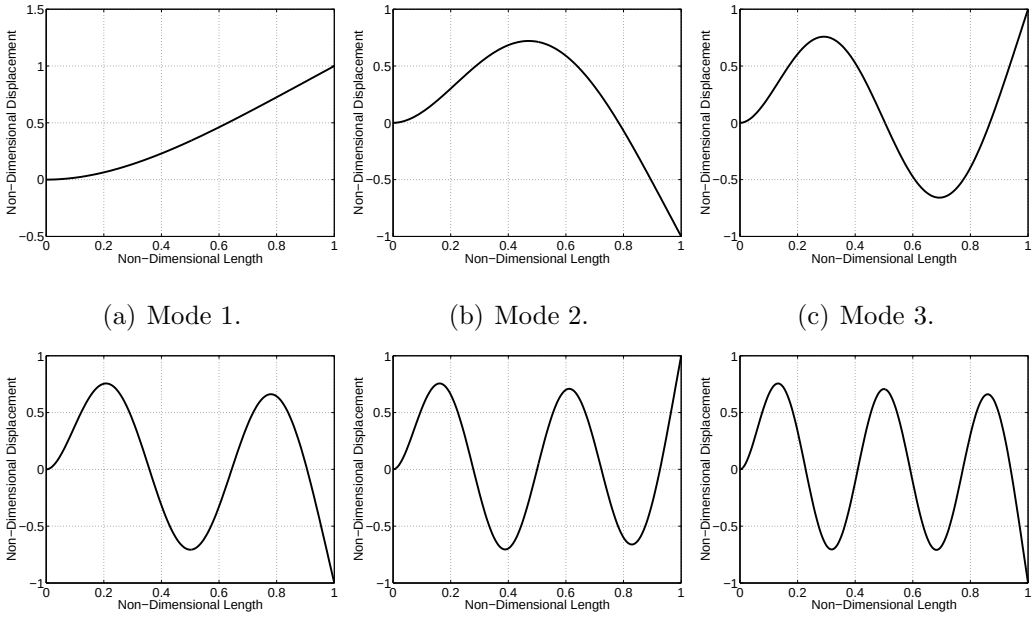

(a) Mode 1. (b) Mode 2. (c) Mode 3.

(d) Mode 4. (e) Mode 5. (f) Mode 6.

Figure 3.3: First six natural eigenmodes of vibration for a cantilevered free plate; two hundred flexible-surface mass-points.

3.2 The Velocity Model

Ideal fluids are modelled using potential-flow theory. This theory is fully described in many texts, prominently in that of Lamb (1932). To compute the unsteady hydrodynamic-pressures due to arbitrary surface disturbances in the modelled flow-structure system the velocity model presented below applies potential flow theory via a boundary-integral or panel method. Panel methods are based on the surface distribution of singularity-elements embedded in an infinite flow field and are well known in the aerospace industry; their derivation and applications are documented in the seminal article of Hess and Smith (1966). Nevertheless, some details of how this method was adapted for the current linear problem are noted below.

3.2.1 General Formulation

This initial general description is for the special case of a non-lifting surface; it is based on that of Lucey (1989) and Lucey and Carpenter (1992a). A flow field existing in the presence of a body of arbitrary shape may be defined by $\underline{u}$ where

$$\underline{u} = \underline{U}_\infty + \underline{u}'. \tag{3.14}$$

$\underline{U}_\infty$ represents the free-stream flow and $\underline{u}'$ is the perturbation velocity due to the presence of the body. Assuming the perturbation field to be potential, one may write

$$\underline{u}' = \nabla\Phi, \tag{3.15}$$

and if the flow is incompressible, the flow field is determined by the solution of Laplace's equation

$$\nabla^2\Phi = 0, \tag{3.16}$$

subject to the boundary conditions everywhere on the body surface (in two dimensions, an infinitely wide line), l. Disturbances to the free-stream flow are characterised by the velocity-perturbation potential, $\Phi(x, y, t)$; this function can be found by spreading a

singularity distribution over the wall/flow boundary and then applying the condition of zero-flux across the (moving) wall/flow interface. Thus

$$\nabla\Phi.\underline{n} + \underline{U}_\infty.\underline{n} = \underline{\dot{w}}.\underline{n}, \tag{3.17}$$

where $\underline{n}$ is an outward-pointing normal vector and $\underline{\dot{w}}$ is the velocity of the moving surface. This boundary condition represents the inadmissibility of fluid migration through the surface. For this general derivation (the special case of a non-lifting surface) the singularities chosen as solutions to Laplace's equation are source(-sink) lines. Referring to figure 3.4(a), the perturbation potential is therefore

$$\Phi(\underline{r}_p) = \frac{1}{2\pi}\int_l \sigma(\underline{r}) \ln|\underline{r}_p - \underline{r}|d\xi, \tag{3.18}$$

where $\underline{r}_p$ is the location of any point in the infinite space away from or on the wall and $\underline{r}$ is the locus vector of the wall which maps out the wall/fluid interface, l. The source strength function is denoted $\sigma(\underline{r})$ and is distributed over the surface defined by the locus of $\underline{r}$. When the point p lies on the surface l, special care must be taken in evaluating the integral as $\underline{r} \to \underline{r}_p$. Substitution of (3.18) into (3.17) leads to the following equation which defines the source strength distribution

$$\frac{1}{2}\sigma(\underline{r}_p) + \frac{1}{2\pi}\frac{\partial}{\partial n_p}\left\{\int_{\substack{l \\ \underline{r}_p \neq \underline{r}}} \sigma(\underline{r}) \ln|\underline{r}_p - \underline{r}|d\xi\right\} + \underline{U}_\infty.\underline{n}_p = \underline{\dot{w}}_p.\underline{n}_p, \tag{3.19}$$

where the singularity at $\underline{r}_p = \underline{r}$ seen in (3.18) has been properly treated. The surface is now modelled as a collection of M panels (*i.e.* line segments), see figure 3.4(b); if the source strength is assumed constant over each panel, then, referring to figure 3.4(c), the previous equation becomes

$$\frac{1}{2}\sigma_i + \sum_{m=1}^{M}\sigma_m\left\{\frac{1}{2\pi}\int_{\substack{\text{panel } m \\ i\neq m}} \frac{\partial}{\partial n_i}(\ln|\underline{r}_i - \underline{r}_m|)d\xi_m\right\} + \underline{U}_\infty.\underline{n}_i = \underline{\dot{w}}_i.\underline{n}_i, \tag{3.20}$$

for $i = 1, 2, ..., M$, where

$$\underline{\dot{w}}_i \;=\; 0\underline{i} + \dot{w}_i\underline{j}\;,\;\; \underline{n}_i \;=\; -\sin\theta_i\underline{i} + \cos\theta_i\underline{j}. \tag{3.21}$$

θ_i is the angle between panel i and the horizontal; ξ_m is measured from the panel origin, the *control point*, and ranges between $-\frac{c_m}{2} \leq \xi_m \leq \frac{c_m}{2}$, where c_m is the length of panel

m. It is now noted that (3.20) represents a set of M linear equations for the unknowns σ_m. The terms in the braces in (3.20) are recognised as being *influence coefficients*; these are constructed into an $(M \times M)$ matrix that is written as $I_{im}^{N\sigma}$, denoting the normal influence on the perturbation velocity on panels i due to the source distributions on panels m. The system may be solved by inverting $I_{im}^{N\sigma}$; the result for $\{\sigma_m\}$ can then be used to determine the perturbation potential on the surface using the appropriately discretised form of (3.18). Subsequently, through the use of the unsteady Bernoulli equation, the pressure on the surface may be found. Lucey (1989) describes that the influence coefficients are dependent solely upon the interface geometry and that evidently in the unsteady problem this geometry changes. Thus at every time step of the evolving disturbance the influence coefficients would have to be recalculated and a possibly large matrix would have to be inverted in the solution of the linear system; both of these requirements would be computationally expensive. This together with the fact that the representation of the surface mechanics is confined to the linear regime, suggests that a more economical variant of the boundary-element technique be used. A linear version was developed by Lucey that requires the sources on each panel to be presumed to lie in the plane $y = 0$ and not on the displaced surface (similar to thin-aerofoil theory) as shown in figure 3.4(c). In further simplification, the second-order terms in angles, displacements and flow-speed perturbations are neglected and the boundary condition is applied at the undisturbed position. The consequences of these assumptions are that the geometry-dependent influence-coefficients remain unchanged throughout the motion, needing only to be calculated once. Lucey (1989) investigated the limitations of the linear method and found it an excellent approximation of the non-linear method in the linear-displacement regime. The perturbation potential ϕ_i, at each panel i may be found using the discretised form of (3.18)

$$\begin{aligned} \phi_i &= \sigma_i \left\{ \frac{c_i}{2\pi} \ln \left| \frac{c_i}{2} \right| - \frac{c_i}{2\pi} \right\} + \sum_{m=1}^{M} \sigma_m \left\{ \frac{1}{2\pi} \int_{\substack{\text{panel } m \\ i \neq m}} \ln |\underline{r}_i - \underline{r}_m| d\xi_m \right\}, \\ &= \sum_{m=1}^{M} I_{im}^{\phi\sigma} \sigma_m, \end{aligned} \tag{3.22}$$

and, from this potential, the perturbation tangential-velocity $u_i^{T'}$, is given by

$$\begin{aligned} u_i^{T'} &= \sum_{m=1}^{M} \sigma_m \left\{ \frac{1}{2\pi} \int_{\substack{\text{panel } m \\ i \neq m}} \frac{\partial}{\partial \xi_i} \left(\ln |\underline{r}_i - \underline{r}_m| \right) d\xi_m \right\}, \\ &= \sum_{m=1}^{M} I_{im}^{T\sigma} \sigma_m, \end{aligned} \tag{3.23}$$

where $\partial/\partial\xi_i$ represents differentiation in the direction tangential to the orientation of the panel i; $I_{im}^{T\sigma}$ denotes the tangential influence on the perturbation velocity on panels i due to the source distributions on panels m and $I_{im}^{\phi\sigma}$ denotes the influence on the perturbation potential on panels i due to the source distributions on panels m. The total tangential-velocity u_i^T, is therefore

$$u_i^T = \underline{U}_\infty . \underline{t}_i + u_i^{T'} \tag{3.24}$$

where $\underline{t}_i$, referring to figure 3.4(c), is the tangential unit-vector on panel i. Having established the perturbation tangential velocities, use of the Bernoulli equation yields the hydrodynamic-stiffness pressure when steady boundary conditions are employed. Furthermore, the use of results from (3.22) and (3.23) and employing dynamic boundary conditions, together with the full, unsteady Bernoulli equation, yields all the pressure terms imposed on the moving surface.

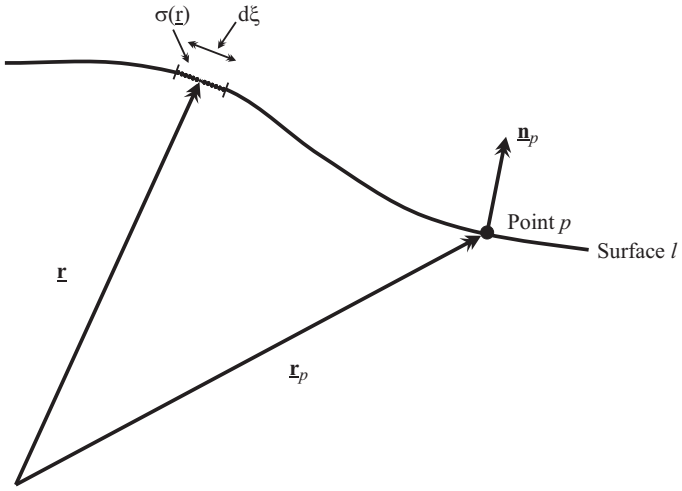

(a) Vector set-up.

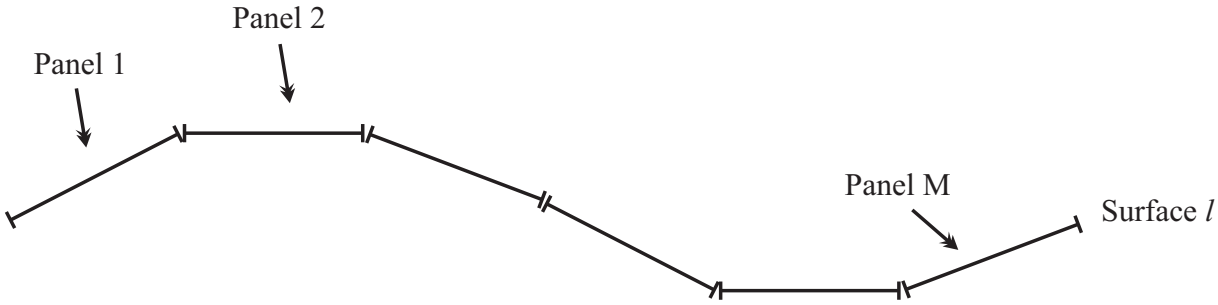

(b) Surface l discretisation.

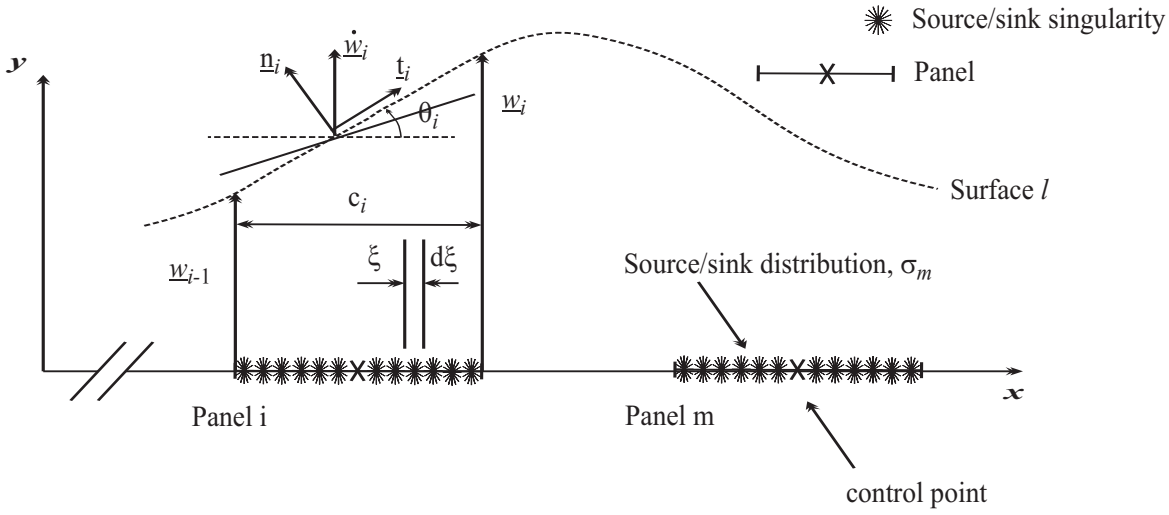

(c) Panel set-up.

Figure 3.4: Panel method definitions.

3.2.2 Application to Present Geometry

As noted, the derivation in the previous subsection was for the special case of a non-lifting surface. In modelling the flow-structure interaction to be studied in this thesis, re-illustrated in figure 3.5(a), this formulation is extended so that

- the central-surface is modelled by a single-layer distribution of first-order vortex singularities;
- each channel wall is modelled by a single-layer distribution of zero-order source/sink singularities.

This distribution is illustrated in figure 3.5(b) and the reasons for selecting this distribution are as follows

- Central surface: The centre surface has flow along its top and bottom sides. The nature of this particular flow-structure interaction is such that the flow will always be faster in either the upper or lower channel. Physically, there is a discontinuity in tangential velocity across the central surface and it is therefore a *lifting surface* and must generate vorticity. A vortex singularity is suited to this situation as it can increase velocity above the surface and decrease velocity below the surface (or *vice-versa*) simultaneously. The author notes that two layers of singularities could be used to model the central surface but that this would add thickness to the surface and greatly alter the flow-structure interaction. Also, this would lead to difficulty in applying the correct pressure difference across the mass points of the flexible surface in the coupled flow-structure model;
- Channel walls: It is assumed that there is no flow on the exterior of the channel. There is therefore no discontinuity in tangential velocity across the channel walls and these are therefore *non-lifting surfaces*. This situation can be physically modelled by source/sink singularities, which will be positive where the flow is fast and negative where the flow is slow.

As this is a linear method, the singularity strengths can be added via the principle of superposition, thus (3.20) becomes

$$\begin{aligned}\frac{1}{2}\sigma_i &+ \sum_{m=1}^{M_w}\sigma_m\left\{\frac{1}{2\pi}\int_{\substack{\text{panel } m\\ i\neq m}}\frac{\partial}{\partial n_i}(\ln|\underline{r}_i-\underline{r}_m|)d\xi_m\right\}\\ &+ \sum_{m=1}^{M_{cs}}\gamma_m\left\{\frac{1}{2\pi}\int_{\substack{\text{panel } m\\ i\neq m}}\frac{1}{r}\frac{\partial}{\partial\varphi_m}\varphi_m d\xi_m\right\}\\ -\frac{c_i}{2\pi}\lambda_i &+ \sum_{m=1}^{M_{cs}}\lambda_m\xi_m\left\{\frac{1}{2\pi}\int_{\substack{\text{panel } m\\ i\neq m}}\frac{1}{r}\frac{\partial}{\partial\varphi_m}\varphi_m d\xi_m\right\}+\underline{U}_\infty.\underline{n}_i=\underline{\dot{w}}_i.\underline{n}_i,\end{aligned}\qquad(3.25)$$

where γ_m and λ_m denote a zero-order and first-order vortex distribution respectively. There are M_w wall panels and M_{cs} central-surface panels and φ_m is the angle between panel m and panel i. It is known that higher-order boundary-integral methods, that admit variations of singularity strength over a given panel and/or allow for panel curvature, provide a substantial enhancement of the basic method. Hess (1973) discusses the theory of such methods and specifically develops a test case demonstrating the improvements offered. In this case, if a zero-order vortex method were solely used, this would lead to an *ill-conditioned* normal influence-matrix, with all terms on the leading diagonal being equal to zero (as a zero-order vortex-singularity has no normal influence on itself). On inversion, this leads to a correct but oscillatory solution for perturbation velocity and potential.[2] First-order vortices are therefore additionally employed that do have a normal influence on themselves. The first-order method developed in the present work neglects surface curvature and therefore the total-vortex strength on panel m, Γ_m, is equated as

$$\Gamma_m=\gamma_m+\lambda_m\xi_m.\qquad(3.26)$$

There are $M=M_w+M_{cs}$ panels and the satisfying of (3.17) leads to the solution of σ_m and γ_m singularities. The λ_m singularities lead to M_{cs} further unknowns. $M_{cs}-1$ equations are provided by the boundary condition of vortex-strength continuity between panels. This is enforced by equating vortex strength at panel ends

$$\gamma_m+\lambda_m\frac{c_m}{2} \;=\; \gamma_{m+1}-\lambda_{m+1}\frac{c_{m+1}}{2}.\qquad(3.27)$$

[2]Katz and Plotkin (2001) describe how this can be corrected by shifting the panel control point away from the centre of the panel.

The M_{cs}^{th} equation is provided by the *Kutta condition*, described in §2.1.1. This is enforced by equating the vortex gradient at the trailing edge (TE) to zero

$$\gamma_{TE} + \lambda_{TE}\frac{c_{TE}}{2} = 0. \tag{3.28}$$

Viscous effects are implicit through the Kutta condition. This singularity distribution and form of Kutta condition has been used after experimenting with many other combinations; this form of first-order method is advantageous as the system is not over-determined and no normal-velocity boundary condition has to be dropped to apply the Kutta condition. To solve for the singularity strengths, the normal influence-coefficients in (3.25) are arranged into one large normal influence-matrix I_{im}^{N}, that also includes the boundary conditions in (3.27) and (3.28), see figure 3.6(a). This matrix is inverted and the calculation of the singularity strengths is shown in figure 3.6(b). Respectively, the tangential velocity-perturbations and perturbation potentials are given by

$$u_i^{T'} = \sum_{m=1}^{M_w} I_{im}^{T\sigma}\sigma_m + \sum_{m=1}^{M_{cs}} I_{im}^{T\gamma}\gamma_m + \sum_{m=1}^{M_{cs}} I_{im}^{T\lambda}\lambda_m, \tag{3.29}$$

$$\phi_i = \sum_{m=1}^{M_w} I_{im}^{\phi\sigma}\sigma_m + \sum_{m=1}^{M_{cs}} I_{im}^{\phi\gamma}\gamma_m + \sum_{m=1}^{M_{cs}} I_{im}^{\phi\lambda}\lambda_m. \tag{3.30}$$

Appendices §B.1 and §B.2 detail respectively the derivations of the normal and tangential perturbation-velocity influence-coefficients and perturbation potential influence-coefficients.

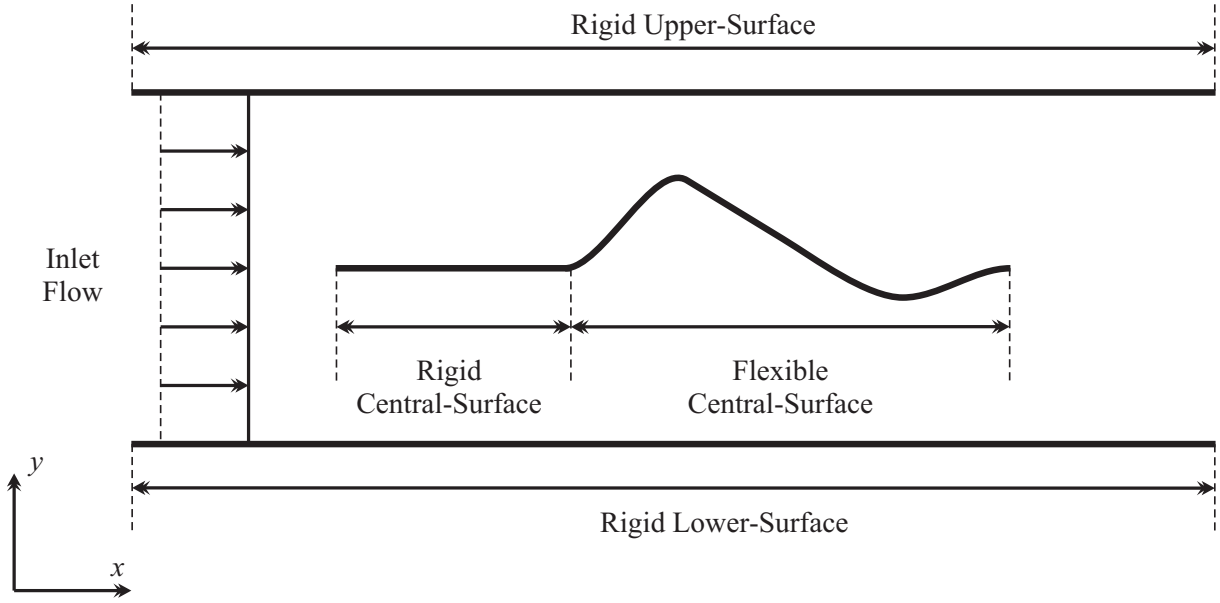

(a) Flow-structure interaction to be modelled.

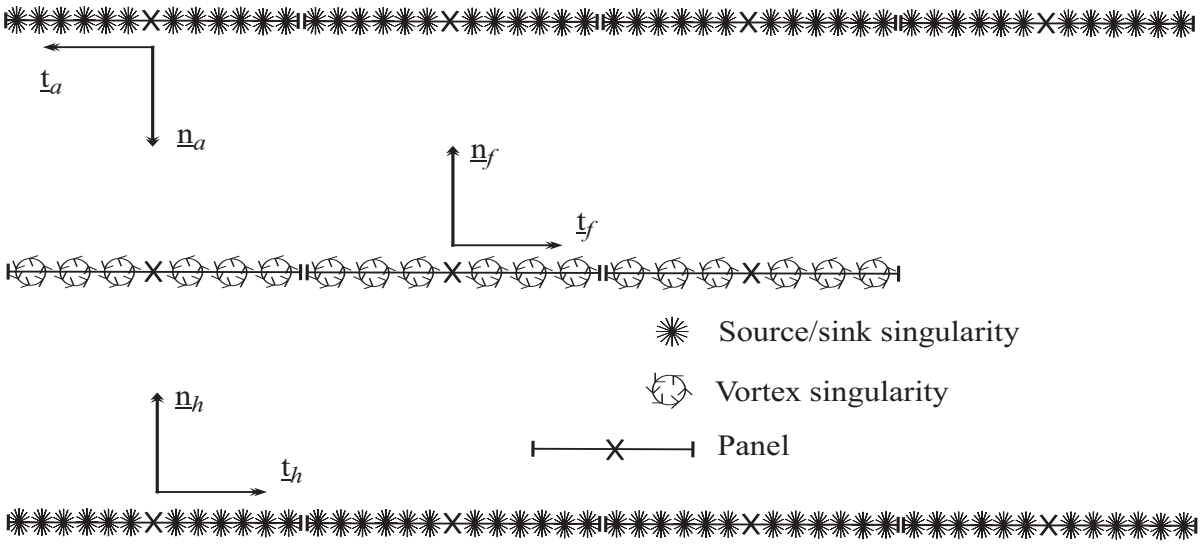

(b) Structure discretisation and singularity distribution.

Figure 3.5: Application of panel method to present geometry.

$$\left[\begin{array}{ccccc|ccccc|ccccc}
0 & I_{1,2}^{N\gamma} & \cdots & \cdots & I_{1,M_{cs}}^{N\gamma} & \frac{c_1}{2\pi} & I_{1,2}^{N\lambda} & \cdots & \cdots & I_{1,M_{cs}}^{N\lambda} & \frac{1}{2} & I_{1,2}^{N\sigma} & \cdots & I_{1,M_w}^{N\sigma} \\
I_{2,1}^{N\gamma} & \ddots & & & \vdots & I_{2,1}^{N\lambda} & \ddots & & & \vdots & I_{2,1}^{N\sigma} & \ddots & & \vdots \\
\vdots & & & \ddots & I_{M-1,M_{cs}}^{N\gamma} & \vdots & & & \ddots & I_{M-1,M_{cs}}^{N\lambda} & \vdots & & \ddots & I_{M-1,M_w}^{N\sigma} \\
I_{M,1}^{N\gamma} & \cdots & \cdots & I_{M,M_{cs}-1}^{N\gamma} & 0 & I_{M,1}^{N\lambda} & \cdots & \cdots & I_{M,M_{cs}-1}^{N\lambda} & \frac{c_{M_{cs}}}{2\pi} & I_{M,1}^{N\sigma} & \cdots & I_{M,M_w-1}^{N\sigma} & \frac{1}{2} \\
\hline
1 & 1 & 0 & \cdots & 0 & \frac{c_1}{2\pi} & \frac{c_2}{2\pi} & 0 & \cdots & 0 & 0 & \cdots & \cdots & 0 \\
0 & 1 & 1 & & \vdots & 0 & \frac{c_2}{2\pi} & \frac{c_3}{2\pi} & & \vdots & \vdots & \ddots & & \vdots \\
\vdots & & \ddots & \ddots & \vdots & \vdots & & \ddots & \ddots & \vdots & \vdots & & \ddots & \vdots \\
\vdots & & & 1 & 1 & \vdots & & & \frac{c_{M_{cs}-1}}{2\pi} & \frac{c_{M_{cs}}}{2\pi} & \vdots & & & \vdots \\
0 & \cdots & \cdots & \cdots & 1 & 0 & \cdots & \cdots & \cdots & \frac{c_{M_{cs}}}{2\pi} & 0 & \cdots & \cdots & 0
\end{array}\right]$$

(a) Construction of I_{im}^N.

$$\left\{\begin{array}{c} \gamma_1 \\ \vdots \\ \gamma_{M_{cs}} \\ \cdots \\ \lambda_1 \\ \vdots \\ \lambda_{M_{cs}} \\ \cdots \\ \sigma_1 \\ \vdots \\ \sigma_{M_w} \end{array}\right\} = \left[I_{im}^N\right]^{-1} \left\{\begin{array}{c} \underline{\dot{w}}_m \cdot \underline{n}_m - \underline{U}_\infty \cdot \underline{n}_m \\ \cdots \\ 0 \end{array}\right\}$$

(b) Solution for singularity strengths.

Figure 3.6: Execution of the panel method.

3.3 The Vorticity Model

The velocity model calculates the *bound vorticity* of the central surface. As the flexible part of the central-surface moves, the bound vorticity of the flexible-surface changes. To conserve vorticity a vortex must be shed at the trailing edge of the flexible central-surface with strength equal to the negative change in bound vorticity. This *shed vorticity* is modelled via a *discrete-vortex method* detailed below. Chorin (1973) shows that the vorticity-transport equation reduces for a two-dimensional potential-flow to the form

$$\frac{D\zeta}{Dt} = 0, \tag{3.31}$$

where ζ is the vorticity in the free-stream. This condition states the circulation of the system cannot change in time; therefore the individual discrete vortices (vortex blobs) that are shed at the trailing edge of the flexible surface and conserve the change in bound vorticity cannot change in strength either along their trajectory. The change in bound vorticity will be greatest at the first time step, resulting in a relatively large *starting-vortex* (Lewis, 1991). As the flow now contains vorticity, the unsteady Bernoulli equation is no longer valid. However, the correct governing pressure equation, as derived by Cafolla (1997), is shown to be approximately the same as the unsteady Bernoulli equation close to the flexible surface, as the shed vorticity is downstream of the flexible surface's trailing edge. Therefore using the unsteady Bernoulli equation as the governing pressure equation is a good approximation in the present case.

3.3.1 General Formulation

In two dimensions, the definition of vorticity is

$$\zeta = \frac{\partial v}{\partial x} - \frac{\partial u}{\partial y}, \tag{3.32}$$

where u and v are components of the free-stream velocity. These components can be expressed in terms of the stream function ψ

$$u = \frac{\partial \psi}{\partial y} \quad \text{and} \quad v = -\frac{\partial \psi}{\partial x}, \tag{3.33a, b}$$

these terms satisfying mass continuity

$$\frac{\partial u}{\partial x} + \frac{\partial v}{\partial y} = \frac{\partial^2 \psi}{\partial x \partial y} - \frac{\partial^2 \psi}{\partial y \partial x} = 0.$$

Inserting (3.33a) and (3.33b) into (3.32) obtains the Poisson equation

$$\frac{\partial^2 \psi}{\partial x^2} + \frac{\partial^2 \psi}{\partial y^2} \;=\; \nabla^2 \psi \;=\; -\zeta. \tag{3.34}$$

The vorticity field is modelled by a superposition of vortex blobs

$$\zeta \;=\; \underline{\omega}(\underline{x}, t) \;=\; \sum_{m=1}^{N_b} f_{\alpha_m}(\underline{r}_m)\underline{\omega}_m, \tag{3.35}$$

where $\underline{r}_m$ is the vector between blob m and any chosen point in the flow, N_b is the number of blobs and $f_{\alpha_m}(r_m)$ and α_m denote the *core function* and the *core size* of blob m respectively. For two-dimensional flows, vorticity has only one component, γ_m^b, and (3.35) becomes

$$\omega(\underline{x}, t) \;=\; \sum_{m=1}^{N_b} f_{\alpha_m}(\underline{r}_m)\gamma_m^b. \tag{3.36}$$

Inserting (3.36) into (3.34) leads to the relation

$$\nabla^2 \psi \;=\; -\omega(\underline{x}, t) \;=\; -\sum_{m=1}^{N_b} f_{\alpha_m}(\underline{r}_m)\gamma_m^b.$$

Deriving the left-hand side in radial form and noting that ψ depends only upon r

$$\frac{1}{r}\frac{\partial}{\partial r}\left(r\frac{\partial \psi}{\partial r}\right) \;=\; -\sum_{m=1}^{N_b} f_{\alpha_m}(\underline{r}_m)\gamma_m^b. \tag{3.37}$$

Integrating gives

$$r\frac{\partial \psi}{\partial r} \;=\; -\sum_{m=1}^{N_b} \gamma_m^b \int_0^{r_m} \underline{r}_m f_{\alpha_m}(\underline{r}_m) dr.$$

Referring to figure 3.7, substituting $r_m = \alpha_m \xi$ and noting blob velocity, $\underline{u}^b$, is equal to the negative change in the stream function with distance leads to the result

$$\underline{u}^b \;=\; -\frac{\partial \psi}{\partial r} \;=\; \sum_{m=1}^{N_b} \frac{\gamma_m^b \alpha_m^2}{\underline{r}_m} \int_0^{\xi} \xi f_{\alpha_m}(\xi) d\xi.$$

The velocity induced at a point p by a blob m is therefore equated as

$$\underline{u}_p^b = \gamma_m^b \alpha_m^2 \left(-\frac{\bar{y}_m}{r_m^2}, \frac{\bar{x}_m}{r_m^2} \right) \int_0^\xi \xi f_{\alpha_m}(\xi) d\xi, \tag{3.38}$$

The core function is now chosen. It is defined as

$$f_{\alpha_m}(r_m) = \frac{1}{\alpha_m \pi} f\left(\frac{r_m}{\alpha_m} \right),$$

where f is the *cut-off function* (where $f \to 0$ as $r \to \infty$). Choosing Gaussian vortices to model the cut-off function, the core function becomes

$$f_{\alpha_m}(r_m) = \frac{1}{\alpha_m \pi} e^{-\frac{r_m^2}{\alpha_m^2}}, \tag{3.39}$$

Inserting (3.39) into (3.38) leads to the discretised form for the blob velocity

$$\begin{aligned}
\underline{u}_p^b &= \frac{\gamma_m^b \alpha_m}{\pi} \left(-\frac{\bar{y}_m}{r_m^2}, \frac{\bar{x}_m}{r_m^2} \right) \int_0^\xi \xi e^{-\xi^2} d\xi, \\
&= \frac{\gamma_m^b \alpha_m}{2\pi} \left(-\frac{\bar{y}_m}{r_m^2}, \frac{\bar{x}_m}{r_m^2} \right) \left[1 - e^{-\xi^2} \right]_0^\xi \\
&= -\gamma_m^b \alpha_m \frac{\bar{y}_m}{2\pi r_m^2} \left(1 - e^{-\frac{r_m^2}{\alpha_m^2}} \right) \underline{i} + \gamma_m^b \alpha_m \frac{\bar{x}_m}{2\pi r_m^2} \left(1 - e^{-\frac{r_m^2}{\alpha_m^2}} \right) \underline{j} \\
&= u_p^{Tb} \underline{i} + u_p^{Nb} \underline{j}
\end{aligned} \tag{3.40}$$

3.3.2 Present Model

The model is linearised, so the shed position of the blobs is at the trailing edge ($x = L, y = 0$) and the blobs only move in x. Therefore, blob position is not affected by the flexible-surface or other blobs. Assuming that the effects on blob position due to the central rigid-surface and channel wall singularity distributions and the blob reflections in the channel walls will be small, blobs therefore convect only with free-stream velocity in the x direction and are calculated explicitly

$$x_i^b|^{t+\delta t} = x_i^b|^t + U_\infty \delta t. \tag{3.41}$$

Further to this assumption, the effect of a blob on the central rigid-surface and channel-wall normal velocity is also considered small and therefore neglected, the blobs therefore

only affect the normal velocity on the flexible-surface. For completeness, the effect that the blobs would have on the tangential perturbation velocity in a non-linear model is included in all further derivations in this chapter. If the number of blobs present in the free stream becomes excessive, a *cut-off length* will be enforced, removing blobs that have travelled over two flexible-surface lengths from the trailing edge of the flexible surface. Justification for this approximation has been given by Basu *et al.* (1992). The individual blob-strengths γ_m^b are assumed, to conserve vorticity, to equal the negative difference between the sum of the vortex strengths along the flexible surface calculated using the panel method, at adjacent time steps

$$\gamma_m^b\Big|^t \;=\; -\left(\sum \gamma_m^t - \sum \gamma_m^{t-\delta t}\right). \tag{3.42}$$

Blob strength will be the summation over several time-steps until the change in vorticity alters polarity. Blobs with a strength below an empirically determined minimum strength will be negated to avoid unnecessary computation. The individual blob strengths are assumed to remain unchanged with time. Finally, it is noted that core size α_m will be the same for all blobs.

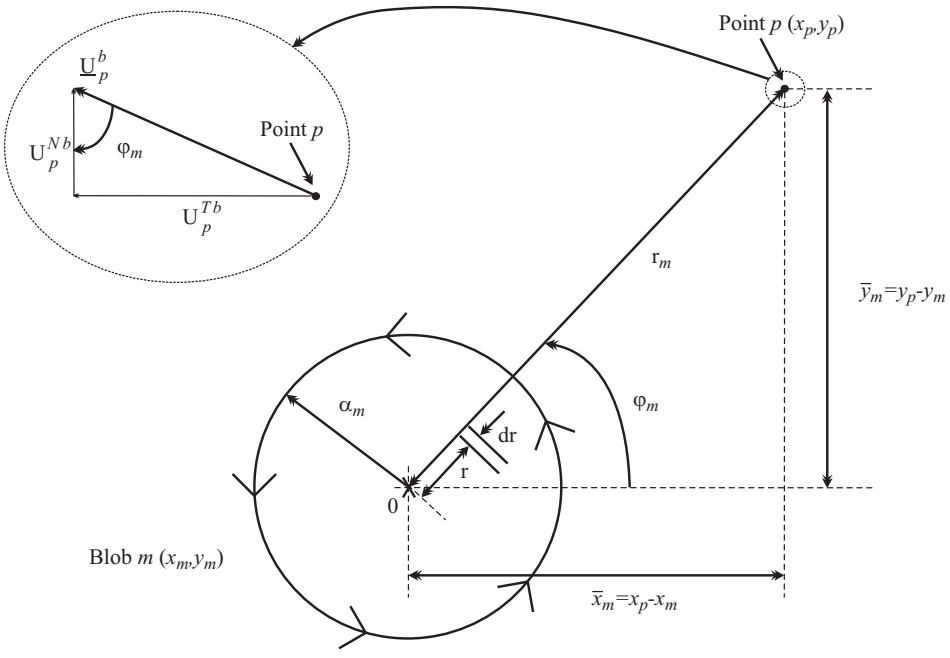

Figure 3.7: Discrete-vortex method set-up.

3.4 The Unsteady Model

3.4.1 Statement of the Unsteady Pressure Equation

The linearised flexible surface, velocity and vorticity models are now linked into one linearised unsteady model that can accurately capture the onset of instability in this fluid-structure system. The panel method has been shown to generate a flow solution that can deliver values of perturbation potential and subsequently perturbation tangential velocities at the control point of each panel. These are to be used in the unsteady Bernoulli equation

$$p + \frac{1}{2}\rho_f \underline{u}.\underline{u} + \rho_f \frac{\partial \phi}{\partial t} \;=\; F(t), \tag{3.43}$$

where the function of time $F(t)$ is usually a constant, but has become temporal as the free-stream flow has been considered unsteady. Far away from the surface the flow is undisturbed and therefore $\underline{u} = (U_\infty, 0)$; following a streamline from this point to the surface leads to the result $\underline{u} = (U_\infty + u^{T'} + u^{Tb}, u^{N'} + u^{Nb})$, where $u^{T'}$ and $u^{N'}$ are the tangential and normal components respectively of the perturbation velocity on the surface. After discretisation and linearisation of (3.43), see §B.4.1, the perturbation pressures *across* the centre surface, denoted by the subscript xp, at a time t are then calculated as

$$\delta p_i\big|_{xp} \;=\; 2\left(p_i - p_\infty\right) \;=\; -2\rho_f U'_\infty \left(u_i^{T'} + u_i^{Tb}\right) - \rho_f \frac{\partial \Phi_i}{\partial t}\Big|_{xp}, \tag{3.44}$$

where ρ_f is the free-stream fluid-density, U'_∞ denotes the variation of the x-component of the free-stream velocity with time and the suffix i denotes any panel control point in the application of the panel method. Negative perturbation pressure implies an upward force on that panel.

3.4.2 Tangential Perturbation-Velocity Calculation

Referring to (3.29), the tangential perturbation velocity at control point i is equal to

$$\left\{u_i^{T'}\right\} \;=\; \left[I_{im}^{T\gamma}\right]\{\gamma_m\} + \left[I_{im}^{T\sigma}\right]\{\sigma_m\}, \tag{3.45}$$

where the first-order vortices have been negated as they give the variation of vortex strength over a panel; this is not required in this calculation. The calculation of $u_i^{T'}$ necessitates the calculation of singularity strengths at each time step; this operation is similar to the panel-method operation shown in figure 3.6(b) with the inclusion of an unsteady free-stream flow and the velocities induced by the shed vorticity. Changes to the panel-method operation are derived in §B.4.2 and result in the equation shown in figure 3.8(a). In figure 3.8(b), it is shown how the inverted normal influence-coefficients are retrieved for each singularity, leading to the following calculation for the required individual singularity strengths

$$\{\gamma_i\} = \left[I_{im}^{N\gamma}\right]^{-1}\left\{\dot{w}_m + U'_\infty\theta_m + u_m^{Tb}\theta_m - u_m^{Nb}\right\}, \tag{3.46}$$

$$\{\sigma_i\} = \left[I_{im}^{N\sigma}\right]^{-1}\left\{\dot{w}_m + U'_\infty\theta_m + u_m^{Tb}\theta_m - u_m^{Nb}\right\}. \tag{3.47}$$

Inserting (3.46) and (3.47) into (3.45), the final calculation for the tangential perturbation-velocity is

$$\begin{aligned}\left\{u_i^{T'}\right\} &= \left[I_{im}^{T\gamma}\left[I_{im}^{N\gamma}\right]^{-1} + I_{im}^{T\sigma}\left[I_{im}^{N\sigma}\right]^{-1}\right]\left\{\dot{w}_m + U'_\infty\theta_m + u_m^{Tb}\theta_m - u_m^{Nb}\right\}, \\ &= [\mathbf{A}]\left\{\dot{w}_m + U'_\infty\theta_m + u_m^{Tb}\theta_m - u_m^{Nb}\right\}. \end{aligned} \tag{3.48}$$

3.4.3 Unsteady Velocity-Potential Calculation

Referring to (3.30), the change in velocity potential across the centre surface with respect to time at panel i is equal to

$$\left\{\frac{\partial\phi_i}{\partial t}\right\}_{xp} = \left[I_{im}^{\phi\gamma}\right]_{xp}\left\{\frac{\partial\gamma_m}{\partial t}\right\} + 2\left[I_{im}^{\phi\sigma}\right]\left\{\frac{\partial\sigma_m}{\partial t}\right\}, \tag{3.49}$$

noting that the velocity-potential influence-coefficients remain constant with time. The calculation of the unsteady singularity-strengths is similar to that shown in figure 3.8(a); the calculation is altered by taking the time derivative of the boundary-condition vector, the full derivation shown in §B.4.3, which results in the formulation shown in figure 3.8(c). Inserting the result shown in figure 3.8(c), after the matrices have been retrieved in similar fashion to figure 3.8(b), into (3.49) leads to a calculation for the unsteady velocity

potential similar to the tangential velocity perturbation in (3.48)

$$\begin{aligned}\left\{\frac{\partial \phi_i}{\partial t}\right\}_{xp} &= \left[2I_{im}^{\phi\sigma}\left[I_{im}^{N\sigma}\right]^{-1} + I_{im}^{\phi\gamma}\big|_{xp}\left[I_{im}^{N\gamma}\right]^{-1}\right] \\ &\quad \left\{\ddot{w}_m + U'_\infty\dot{\theta}_m + \dot{U}'_\infty\theta_m + u_m^{Tb}\dot{\theta}_m + \dot{u}_m^{Tb}\theta_m - \dot{u}_m^{Nb}\right\} \\ &= [\mathbf{B}]\left\{\ddot{w}_m + U'_\infty\dot{\theta}_m + \dot{U}'_\infty\theta_m + u_m^{Tb}\dot{\theta}_m + \dot{u}_m^{Tb}\theta_m - \dot{u}_m^{Nb}\right\}. \qquad (3.50)\end{aligned}$$

To obtain the unsteady velocity potential *across* the central-surface, the source contribution is multiplied by a factor of 2. The vortex contribution already calculates the cross-surface value owing to the way the vortex velocity-potential influence-coefficients are constructed. This construction is illustrated in the following operation

$$\begin{aligned}\left[I_{im}^{\phi\gamma}\right]_{xp}\left\{\frac{\partial \gamma_m}{\partial t}\right\} &= \left[I_{im}^{\phi\gamma}\big|_{i=m}^{U} + I_{im}^{\phi\gamma}\big|_{YY=0}^{U,\varphi=0} + I_{im}^{\phi\gamma}\big|_{YY=0}^{U,\varphi=\pi}\right]\left[I_{im}^{N\gamma}\right]^{-1} \\ &\quad \left\{\ddot{w}_m + U'_\infty\dot{\theta}_m + \dot{U}'_\infty\theta_m + u_m^{Tb}\dot{\theta}_m + \dot{u}_m^{Tb}\theta_m - \dot{u}_m^{Nb}\right\} \\ &+ \left[I_{im}^{\phi\gamma}\big|_{i=m}^{L} + I_{im}^{\phi\gamma}\big|_{YY=0}^{L,\varphi=0} + I_{im}^{\phi\gamma}\big|_{YY=0}^{L,\varphi=\pi}\right]\left[I_{im}^{N\gamma}\right]^{-1} \\ &\quad \left\{-\ddot{w}_m - U'_\infty\dot{\theta}_m - \dot{U}'_\infty\theta_m - u_m^{Tb}\dot{\theta}_m - \dot{u}_m^{Tb}\theta_m + \dot{u}_m^{Nb}\right\}\end{aligned}$$

$$\begin{aligned}&= \left[I_{im}^{\phi\gamma U} - I_{im}^{\phi\gamma L}\right]\left[I_{im}^{N\gamma}\right]^{-1}\left\{\ddot{w}_m + U'_\infty\dot{\theta}_m + \dot{U}'_\infty\theta_m + u_m^{Tb}\dot{\theta}_m + \dot{u}_m^{Tb}\theta_m - \dot{u}_m^{Nb}\right\} \\ &= \left[I_{im}^{\phi\gamma}\big|_{xp}\left[I_{im}^{N\gamma}\right]^{-1}\right]\left\{\ddot{w}_m + U'_\infty\dot{\theta}_m + \dot{U}'_\infty\theta_m + u_m^{Tb}\dot{\theta}_m + \dot{u}_m^{Tb}\theta_m - \dot{u}_m^{Nb}\right\}, \qquad (3.51)\end{aligned}$$

where the subscripts $i = m$ and $YY = 0$ stand for coincidence of panels and all panels are considered horizontal with respect to the influencing panel respectively; the superscripts U, L, $\varphi = 0$ and $\varphi = \pi$ stand for upper and lower sides of the central surface and when panels are at 0 or π radians to the influenced panel. It is noted that for the lower side of the flexible-surface calculation the unit vector has swapped polarity. The derivation of these influence-coefficients is described in §B.2.2 and §B.2.3.

$$\left\{\begin{array}{c}\gamma_1\\ \vdots\\ \gamma_{M_{cs}}\\ \cdots\\ \lambda_1\\ \vdots\\ \lambda_{M_{cs}}\\ \cdots\\ \sigma_1\\ \vdots\\ \sigma_{M_w}\end{array}\right\} = \left[I_{im}^N\right]^{-1}\left\{\begin{array}{c}\dot{w}_m + U'_\infty\theta_m + u_m^{Tb}\theta_m - u_m^{Nb}\\ \cdots\\ 0\end{array}\right\}$$

(a) Solution for steady singularity strengths.

$$\left\{\begin{array}{c}\gamma_1\\ \vdots\\ \gamma_{M_{cs}}\\ \cdots\\ \lambda_1\\ \vdots\\ \lambda_{M_{cs}}\\ \cdots\\ \sigma_1\\ \vdots\\ \sigma_{M_w}\end{array}\right\} = \left[\begin{array}{cc}\left[I_{im}^{N\gamma}\right]^{-1} & \left[BC^{\gamma}\right]^{-1}\\ \left[I_{im}^{N\lambda}\right]^{-1} & \left[BC^{\lambda}\right]^{-1}\\ \left[I_{im}^{N\sigma}\right]^{-1} & 0\end{array}\right]\left\{\begin{array}{c}\dot{w}_m + U'_\infty\theta_m + u_m^{Tb}\theta_m - u_m^{Nb}\\ \cdots\\ 0\end{array}\right\}$$

(b) Retrieval of I_{im}^{N-1} matrices.

$$\left\{\begin{array}{c}\gamma_1\\ \vdots\\ \gamma_{M_{cs}}\\ \cdots\\ \lambda_1\\ \vdots\\ \lambda_{M_{cs}}\\ \cdots\\ \sigma_1\\ \vdots\\ \sigma_{M_w}\end{array}\right\} = \left[I_{im}^N\right]^{-1}\left\{\begin{array}{c}\ddot{w}_m + U'_\infty\dot{\theta}_m + \dot{U}'_\infty\theta_m + u_m^{Tb}\dot{\theta}_m + \dot{u}_m^{Tb}\theta_m - \dot{u}_m^{Nb}\\ \cdots\\ 0\end{array}\right\}$$

(c) Solution for unsteady singularity-strengths.

Figure 3.8: Execution of the unsteady model.

3.4.4 Pressure Components

Inserting (3.48) and (3.50) into (3.44) and rearranging obtains the results

$$\begin{aligned}\{\delta p_i\}_{xp} &= \underbrace{\rho_f \left(U'_\infty [\mathbf{A}] \left\{ U'_\infty \theta_m + u_m^{Tb} \theta_m \right\} - [\mathbf{B}] \left\{ \dot{U}'_\infty \theta_m + \dot{u}_m^{Tb} \theta_m \right\} \right)}_{Hydrodynamic\ Stiffness} \\ &\quad + \underbrace{\rho_f U'_\infty [\mathbf{A}] \left\{ \dot{w}_m - u_m^{Nb} \right\}}_{Hydrodynamic\ Damping\ I} - \underbrace{\rho_f [\mathbf{B}] \left\{ U'_\infty \dot{\theta}_m + u_m^{Tb} \dot{\theta}_m \right\}}_{Hydrodynamic\ Damping\ II} \\ &\quad - \underbrace{\rho_f [\mathbf{B}] \left\{ \ddot{w}_m - \dot{u}_m^{Nb} \right\}}_{Hydrodynamic\ Inertia} \qquad (3.52) \\ &= \left\{ \delta p'_i - \rho_f [\mathbf{B}] \left\{ \ddot{w}_m \right\} \right\}, \qquad (3.53)\end{aligned}$$

where the definition of $\delta p'_i$ is evident from the two forms of the right-hand sides above. The descriptive terms in (3.52) refer to the effects the fluid has via components of the pressure term on the fluid-structure system.[3] The *hydrodynamic stiffness* term (also known as the *centrifugal* term) is proportional to flexible-surface slope. This term refers to the fluid mass attempting to retain its shape like a solid and is the pressure exerted when the flexible surface deflects the fluid; this pressure term is the main component of the total pressure that leads to the divergence instability. The *hydrodynamic damping* terms (also known as the *coriolis* or *gyroscopic* terms) are proportional to the rate of change of slope of the flexible surface and the surface velocity. These terms refer to the stabilising or destabilising effect of the fluid movement on the flexible-surface, moving into or out of phase with the flexible-surface motion and are the main components of the total pressure leading to the flutter instability. The *hydrodynamic inertia* term (also known as the *added mass* term) is proportional to the acceleration of the flexible-surface. This term refers to the effective additional mass created by the need to accelerate fluid where the surface is accelerated. It is important to note that this is the only pressure term that exists when the free-stream velocity is reduced to zero.

[3] Applied mathematicians refer to these terms collectively as *added mass*.

3.4.5 Computational Model Formulation

In order to couple the flexible surface, velocity and vorticity computational models together, the representation of hydrodynamic pressure arrived at in §3.4.4 is introduced into the governing equation, introduced at the beginning of this chapter, along with the appropriate flexible-surface equations of the finite-difference scheme described in §3.1 that determine the surface motion. The coupled wall/flow system is therefore assembled by introducing (3.53) and the discretised form of (3.2) into the right-hand and left-hand sides of (3.1) respectively, giving the result

$$\begin{aligned} \rho h \left\{\ddot{w}_i\right\} + d\left\{\dot{w}_i\right\} + B\nabla^4 \left\{w_i\right\} &= -\left\{\delta p_i\right\} \\ &= \left\{-\delta p_i' + \rho_f \left[\mathbf{B}\right]\left\{\ddot{w}_m\right\}\right\}. \end{aligned} \tag{3.54}$$

This equation is rearranged to collect all the acceleration terms to the left-hand side

$$\underbrace{\left[1 - \frac{\rho_f}{\rho h}\mathbf{B}\right]}_{I_{im}^{\phi'}} \left\{\ddot{w}_m\right\} = \frac{1}{\rho h}\left\{-\delta p_i' - d\dot{w}_i - B\nabla^4 w_i\right\},$$

leading to the surface acceleration being determined by

$$\begin{aligned} \left\{\ddot{w}_i\right\} &= \left[I_{im}^{\phi'-1}\right]\frac{1}{\rho h}\left\{-\delta p_m' - d\dot{w}_m - B\nabla^4 w_m\right\} \\ &= \left[\mathbf{C}\right]\left\{-\delta p_m' - d\dot{w}_m - B\nabla^4 w_m\right\}. \end{aligned} \tag{3.55}$$

In the matrix $[\mathbf{C}]$ the flexible-surface and fluid inertias have been lumped together. The average change in acceleration in time is therefore

$$\frac{\left\{\ddot{w}_i^t + \ddot{w}_i^{t+\delta t}\right\}}{2} = \left[\mathbf{C}\right]\left\{-\delta p_m'^t - d\left\{\dot{w}_m^t\right\} - \frac{1}{2}B\nabla^4\left\{w_m^t + w_m^{t+\delta t}\right\}\right\}, \tag{3.56}$$

where only the stiffness term is averaged in time on the right-hand side as the change in pressure and flexible-surface velocity are considered small. Rewriting (3.6) and (3.7)

$$\left\{\dot{w}_m^{t+\delta t}\right\} = \left\{\dot{w}_m^t\right\} + \delta t\frac{\left\{\ddot{w}_m^t + \ddot{w}_m^{t+\delta t}\right\}}{2}, \tag{3.57}$$

$$\left\{w_m^{t+\delta t}\right\} = \left\{w_m^t\right\} + \delta t\frac{\left\{\dot{w}^t + \dot{w}^{t+\delta t}\right\}}{2}, \tag{3.58}$$

it can now be seen that (3.56), (3.57) and (3.58) represent the means for an implicit solution procedure to be implemented, using Gauss-Siedel sweeps (as detailed in Gerald and Wheatley (1989)), over the internal mass points, to yield converged values of acceleration, velocity and displacement for every mass point at each time step in the evolution of the disturbed system. The formulation for the acceleration term in (3.56) was chosen as the acceleration is relatively large and it ensures numerical stability of the solution, even when the fluid density is high. The use of only $\delta p'^{t}$ in the flexible-surface acceleration solution (*i.e.* the flexible-surface pressure is not calculated at each iteration) makes the application of the normal-velocity boundary condition an *explicit* solution. Combined with the implicit solution for the flexible-surface dynamics, the overall method is therefore *semi-implicit*. These expressions have been used to create two computational models. An initial-geometry computational model calculates the matrices [**A**], [**B**] and [**C**] in (3.48), (3.50) and (3.56) respectively; these matrices are stored to be used when required. The subsequent unsteady computational model is executed as follows: Suppose the motion is started by a given surface deflection w_i^t, at time $t = t_0$. The values of $\dot{w}_i^t$, $\ddot{w}_i^t$, $\dot{w}_i^{t+\delta t}$ and $\ddot{w}_i^{t+\delta t}$ will be set to zero. Then:

1. evaluate $\delta p_i'^{t+\delta t}$ (including effect of blobs after first time-step);
2. evaluate $\partial\Gamma/\partial t$ and shed a new blob (after first time-step, re-evaluate position of blobs);
3. evaluate $w_i^{t+\delta t}$;
4. the value of $w_i^{t+\delta t}$ is used to estimate $(\ddot{w}_i^t + \ddot{w}_i^{t+\delta t})/2$;
5. the value of $(\ddot{w}_i^t + \ddot{w}_i^{t+\delta t})/2$ is used to estimate $\dot{w}_i^{t+\delta t}$;
6. the value of $\dot{w}_i^{t+\delta t}$ is used to estimate $w_i^{t+\delta t}$;
7. the final three steps are repeated until convergence for these terms is achieved.

After sufficient iterations have been executed to satisfy the prescribed convergence criteria, the values at time $t + \delta t$ are transferred into arrays w_i^t, $\dot{w}_i^t$ and $\ddot{w}_i^t$ and the process

repeated for a new iteration cycle to determine variables at the next time-step. At each time-step converged values of w_i, $\dot{w}_i$ and $\ddot{w}_i$ may be dumped into an output file for any or all of the mass-points, i. To calculate pressure values at the flexible-surface mass points (that lie between control points), the average of adjacent panel perturbation velocities and velocity-potentials must be taken; this is executed by averaging the matrices [**A**], [**B**] and [**C**] in i and m. It is noted that the influence coefficients used in the construction of [**A**], [**B**] and [**C**] are further subdivided into the effect individual surfaces have on the flexible surface. It is also noted that as the vortex and source influence-coefficient matrices collapse into the matrices [**A**], [**B**] and [**C**], the unsteady computational time for this flow-structure interaction is unexpectedly the same as for a zero-order singularity distribution on an isolated flexible surface. Finally, it is noted that a fourth matrix [**D**] is required that stores $\left[I_{im}^{N\gamma}\right]^{-1}$; this is used at each time step to calculate the zero-order vortex singularity strengths. This enables the calculation of the change in bound vorticity between time steps.

3.5 Fluid-Structure Phenomena

As the fluid and structure interact, work is done and this work can be measured in the form of energy. The type of energy expended or created can be used to interpret what types of flow-structure phenomena are present in the results produced by the unsteady model. The energy equation is derived from (3.2), restated below

$$\rho h\ddot{w} + d\dot{w} + B\nabla^4 w = -\delta p. \tag{3.59}$$

Balint and Lucey (2005) show that multiplying (3.59) by $\dot{w}$ and integrating over the flexible-surface length, $\int_0^L dx$, obtains the result

$$\frac{d}{dt}\Bigg(\underbrace{\frac{1}{2}\rho h\int_0^L \dot{w}^2 dx}_{E_k} + \underbrace{\frac{1}{2}B\int_0^L w_{,xx}^2 dx}_{E_s}\Bigg) = \underbrace{\int_0^L (-\Delta p)\,\dot{w} dx}_{\dot{W}} - \underbrace{d\int_0^L \dot{w}^2 dx}_{\dot{D}}, \tag{3.60}$$

where E_s and E_k are the strain and kinetic energies of the flexible surface respectively; $\dot{W}$ and $\dot{D}$ are the rate of work done by the fluid and the dissipation rate of energy by

the flexible surface respectively. The total energy E_t can be calculated as

$$E_t \;=\; E_s + E_k. \tag{3.61}$$

As $\underline{U}_\infty$ is increased, a number of fluid-structure phenomena are encountered. Initially consider the *steady-state* oscillation where, over a large period of time, the flexible surface oscillates in a similar shape with no increase or decrease in overall amplitude and the total energy remains constant; the fluid-structure system is stable. In terms of energy, this oscillation is defined as

$$\int_{t_s}^{t} E_t dt \;=\; constant, \tag{3.62}$$

where t_s is at the start of the stable oscillation. This oscillation occurs at a critical free-stream velocity, U_c; above U_c, the system is unstable. As described in §2.1.2, the fluid-structure instabilities possible in this system are *divergence* and *flutter*. These instabilities occur at their own characteristic, critical free-stream velocities, U_D and U_F respectively. For an infinitely thin one-dimensional flexible-surface of infinite-length embedded in a two-dimensional potential flow, the critical divergence and flutter speeds are

$$U_D \;=\; \left(\frac{B\kappa^3}{2\rho_f}\right)^{\frac{1}{2}} \qquad \text{and} \qquad U_F \;=\; U_D\sqrt{1+\frac{2\rho h}{\rho_f \kappa}}, \tag{3.63a, b}$$

where κ is the wavenumber of the initial disturbance to the flow-structure system. The derivations of these critical velocities are presented in §B.5. These velocities only apply quantitatively to infinite-length flexible surfaces, but qualitatively they remain valid for finite flexible surfaces. As divergence is a *static* instability, the solution for U_D is calculated when the angular velocity of flexible-surface oscillation is zero. It manifests itself when the structural forces of the flexible-surface, F_p, are outweighed by the destabilising forces of the fluid, F_f. F_p and F_f are defined as

$$F_f \;=\; \int_0^L (-\Delta p) dx \qquad \text{and} \qquad F_p \;=\; B\int_0^L w_{,xxxx} dx. \tag{3.64a, b}$$

For divergence E_t rises monotonically whereas flutter is characterised by an oscillatory rise in E_t with time. This rise is equivalent to a sustained growth in the deflection of

the flexible surface and therefore the solution for U_F is calculated at the point where the flexible surface deflection begins to grow. The flutter instability occurs when there is constructive interference between the fluid-dynamic forces and the elastic and inertial forces of the flexible surface; this constructive interference is signified by a positive value of $\dot{W}$. It is important to note that as divergence is a static instability and flutter is a dynamic instability, flexible surface damping has different affects on these instabilities: Although damping can slow the growth rate of the divergence instability above U_D, it cannot affect the magnitude of U_D as divergence occurs when the flexible surface is stationary; however, damping can decrease or increase the magnitude of U_F as the surface is moving when flutter occurs.

3.6 Non-Dimensional Ratios.

The purpose of a non-dimensional scheme is to reduce the system to one with as few control parameters as possible. The unsteady model was non-dimensionalised using the method of Crighton and Oswell (1991) including further adaptations by Lucey (1998). The system equation is constructed by combining the beam and unsteady Bernoulli equations ((3.2) and (3.44))

$$\rho h\frac{\partial^2 w}{\partial t^2} + d\frac{\partial w}{\partial t} + B\frac{\partial^4 w}{\partial x^4} \;=\; -\delta p \;=\; 2\rho_f U_\infty \frac{\partial \phi}{\partial x} + \rho_f \frac{\partial \phi}{\partial t}\Big|_{xp}. \tag{3.65}$$

The non-dimensional form of individual properties, denoted by a bar (*e.g.* $\bar{\phi}$), are obtained by dividing or multiplying by a length scale, L_r, and a time scale, t_r; hence

$$x = \bar{x}L_r,\; w = \bar{w}L_r,\; t = \bar{t}t_r,\; U_\infty = \bar{U}\frac{L_r}{t_r},\; \phi = \bar{\phi}\frac{L_r^2}{t_r},$$

where L_r and t_r have the units of metres and seconds respectively. Placing the non-dimensional properties into (3.65) gives

$$\rho h\frac{L_r}{t_r^2}\frac{\partial^2 \bar{w}}{\partial \bar{t}^2} + d\frac{L_r}{t_r}\frac{\partial \bar{w}}{\partial \bar{t}} + B\frac{1}{L_r^3}\frac{\partial^4 \bar{w}}{\partial \bar{x}^4} \;=\; 2\rho_f \bar{U}\frac{L_r^2}{t_r^2}\frac{\partial \bar{\phi}}{\partial \bar{x}} + \rho_f \frac{L_r^2}{t_r^2}\frac{\partial \bar{\phi}}{\partial \bar{t}}\Big|_{xp},$$

and rearranging gives

$$\frac{\rho h}{\rho_f}\frac{1}{L_r}\frac{\partial^2 \bar{w}}{\partial \bar{t}^2} + \frac{d}{\rho_f}\frac{t_r}{L_r}\frac{\partial \bar{w}}{\partial \bar{t}} + \frac{B}{\rho_f}\frac{t_r^2}{L_r^5}\frac{\partial^4 \bar{w}}{\partial \bar{x}^4} \;=\; 2\bar{U}\frac{\partial \bar{\phi}}{\partial \bar{x}} + \frac{\partial \bar{\phi}}{\partial \bar{t}}\Big|_{xp}. \tag{3.66}$$

Choosing

$$L_r = \frac{\rho h}{\rho_f}, \qquad t_r = \frac{(\rho h)^{\frac{5}{2}}}{\rho_f^2 B^{\frac{1}{2}}} \qquad \text{and} \qquad \bar{d} = d\frac{(\rho h)^{\frac{3}{2}}}{\rho_f^2 B^{\frac{1}{2}}}, \tag{3.67a, b, c}$$

(3.66) becomes

$$\frac{\partial^2 \bar{w}}{\partial \bar{t}^2} + \bar{d}\frac{\partial \bar{w}}{\partial \bar{t}} + \frac{\partial^4 \bar{w}}{\partial \bar{x}^4} \;=\; 2\bar{U}\frac{\partial \bar{\phi}}{\partial \bar{x}} + \frac{\partial \bar{\phi}}{\partial \bar{t}}\Big|_{xp}. \tag{3.68}$$

There are now two control parameters that govern the system response, $\bar{U}$ and $\bar{d}$, where $\bar{U}$ is equal to

$$\bar{U} = U_\infty \frac{(\rho h)^{\frac{3}{2}}}{\rho_f B^{\frac{1}{2}}} \left(= \; U_\infty \frac{t_r}{L_r} \right) \tag{3.69}$$

Two further control parameters are the non-dimensional length, $\bar{L}$, and non-dimensional channel height, $\bar{H}$ (introduced in §2.2 and §2.3 respectively)

$$\bar{L} \;=\; \frac{\rho_f L}{\rho h} \;=\; \frac{L}{L_r} \qquad \text{and} \qquad \bar{H} \;=\; \frac{H}{L}. \tag{3.70a, b}$$

When plotting results

$$\bar{x} \;=\; \frac{x}{L},\; \bar{w} \;=\; \frac{w}{w_{max}},\; \bar{E}_t(t) \;=\; \frac{E_t(t) - E_t(0)}{E_t(0)} \;\text{ and }\; \bar{\delta p} \;=\; \frac{\delta p}{\rho_f U_\infty^2}, \tag{3.71a, b, c, d}$$

where w_{max} is the magnitude of the maximum initial deflection of the flexible surface. It is noted that negative energies could be observed owing to the nature of the non-dimensional form of E_t.

Chapter 4

Validation of the Computational Model

This chapter details the validation of the separate flexible surface, velocity and vorticity computational models and their combination into a final unsteady model, utilising the theory described in the previous chapter. Only the results of the velocity model are steady. Programming integrity was tested by recreating all models in an *MS EXCEL* spreadsheet and comparing results for a test case. Linear theory is applied and so only linear displacements are modelled. The size of the initial deflection of the flexible surface was kept well within linear bounds, with the ratio of maximum initial displacement to flexible-surface length, w_{max}/L, kept at 1/1000000 for all numerical experiments; thus when an instability occurs later in unsteady-model numerical experiments, the resulting oscillation will still be in the linear regime ($\frac{1}{100}$) for several oscillations. It is noted that this will also keep the effect of surface curvature on the central-surface pressure distribution constant between numerical experiments. The presented results have been non-dimensionalised utilising the scheme introduced in §3.6 except in special cases such as, for example, when the conducted experiment is *in vacuo* where $\rho_f = 0$. The central feature of the present work is that the surface geometry will not be known *a priori*. Additionally, interest here also lies in representing hydrodynamic damping which is, partially, surface-slope dependent. For these reasons throughout the application of the

method, although the described formulation makes no restriction on the length of any panel, the surface is discretised into an array of panels of equal length.

4.1 Flexible Surface Model Validation

The geometry for the numerical experiments is shown again in figure 4.1 and the discretised flexible-surface is re-illustrated in figure 4.2. Initial validation is carried out on an isolated flexible surface; referring to figure 4.1, the flexible-surface is isolated by moving the channel walls *far away* from the central surface and reducing the rigid central-surface length to zero. Furthermore, *in-vacuo* and undamped conditions are enforced. Referring to the discretised beam equation

$$\rho h \ddot{w}_i + d\dot{w}_i + B\nabla^4 w_i = -\delta p_i, \tag{4.1}$$

this is equivalent to $\delta p = d = 0$. Arbitrary properties of the flexible surface are: $E = 7 \times 10^7$ N/m^2, $\rho = 2100$ kg/m^3, $h = 5 \times 10^{-4}$ m, and $L = 1.355$ m. The flexible surface requires an energy source to initiate oscillations; one method of providing this energy source is to deflect the flexible surface into an arbitrary shape at $t = 0$. By choosing the initial deflection to be in the form of a fundamental eigenmode (see figure 4.3), a harmonic oscillation is produced. The flexible surface model is initially validated by plotting the resulting oscillations for initial deflections in the form of the first six eigenmodes; these are shown in figure 4.4. The figure shows the flexible-surface deformation plotted for a sequence of time steps after the flexible-surface has been released from the applied deformation. It can be seen in the figure that the flexible-surface retains its eigenmode shape over the cycle of oscillation and recovers its original amplitude. From these oscillations, the angular-frequencies of oscillation, ω_n (where n is the eigenmode number), can be calculated by, referring to figure 4.5, plotting the displacement in time of one mass point and calculating its period from the graph produced. To further validate the flexible surface model, these numerically predicted values of ω_n were compared

to those calculated theoretically, using

$$\omega_n = \frac{\beta_n^2}{L^2}\sqrt{\frac{B}{\rho h}}, \tag{4.2}$$

where: $\beta_1 = 1.875$, $\beta_2 = 4.694$, $\beta_3 = 7.855$, $\beta_4 = 10.996$, $\beta_5 = 14.137...$ $\beta_n = (2n-1)\pi/2$. The comparison between numerical experiment and theory is shown in table 4.1; the results show agreement between theory and numerical experiment with a discretisation of fifty mass-points producing results of similar accuracy to results produced using a discretisation of two-hundred mass-points. The introduction of damping and pressure terms into the beam equation was then assessed. Results are shown in figure 4.6 where the displacement of a single mass-point in time is plotted for different beam conditions; initially consider figures 4.6(a), (b) and (c), where all oscillations were initiated by an eigenmode 2 deflection. The *in vacuo* oscillation illustrated in figure 4.6(a) serves as a reference; figure 4.6(b) shows the effect of the introduction of damping and the oscillations are seen to gradually damp out for the level of damping chosen; figure 4.6(c) shows the effect of a constant negative pressure being applied across the whole flexible-surface with the same level of damping, the pressure lifting the surface. To show the effect of an initial mode not in the form of a harmonic mode, figure 4.6(d) was produced where the initial deflection was a mode-six sinusoidal-wave; the flexible-surface oscillation becomes perturbed as the surface attempts to oscillate in a harmonic mode shape. It is proposed that these results confirm the integrity of the flexible surface computational model and its implementation.

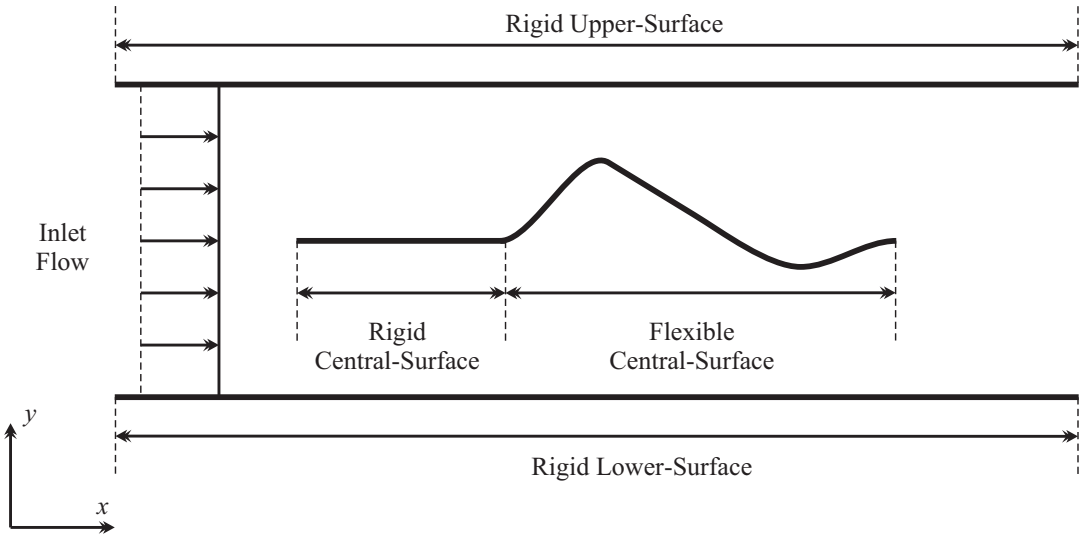

Figure 4.1: The flow-structure geometry modelled.

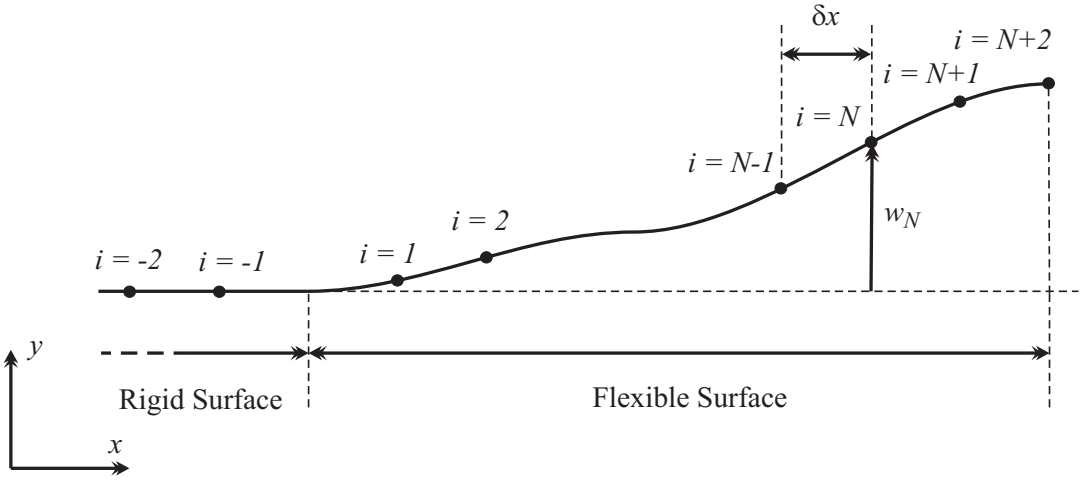

Figure 4.2: Flexible surface discretisation.

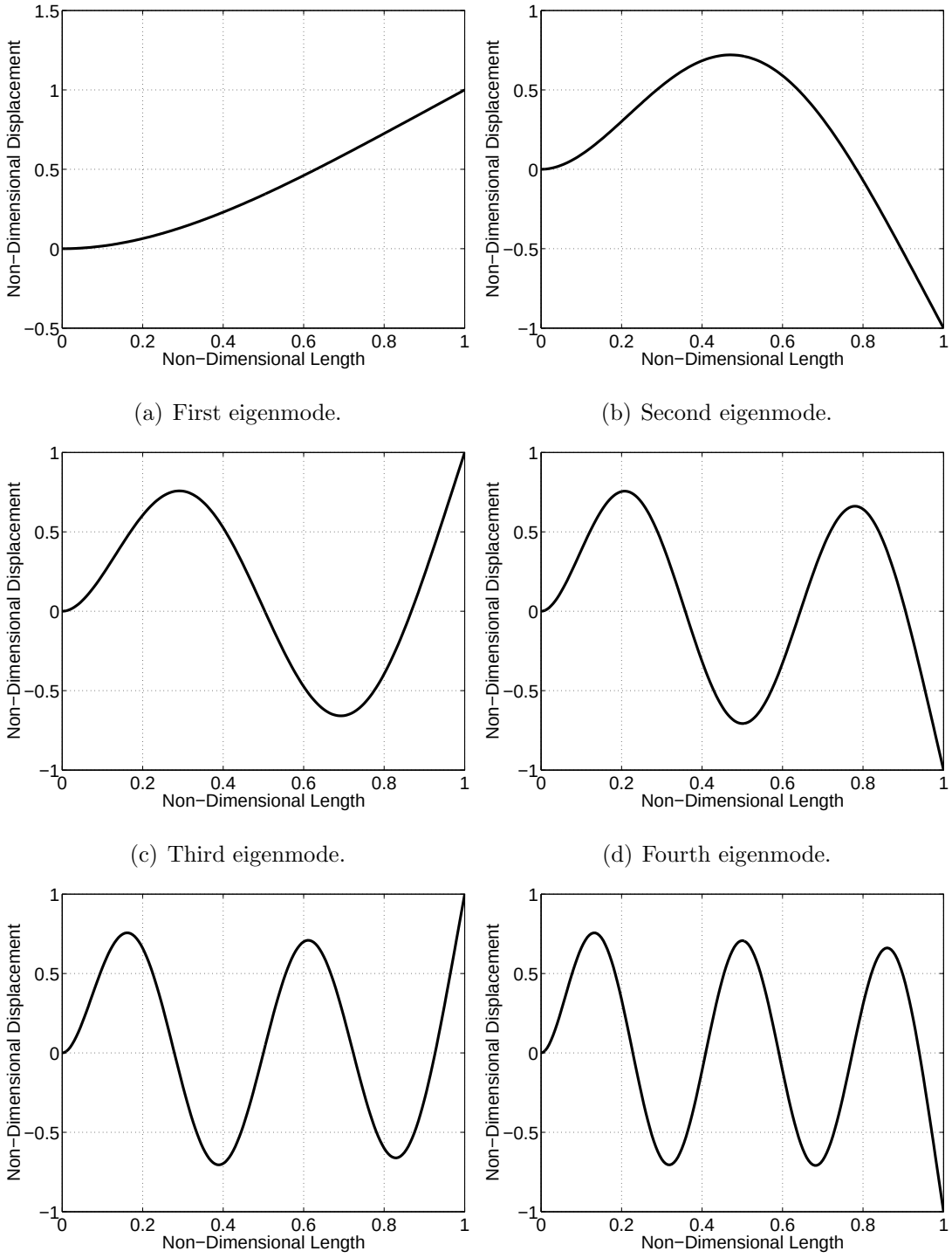

(a) First eigenmode.

(b) Second eigenmode.

(c) Third eigenmode.

(d) Fourth eigenmode.

(e) Fifth eigenmode.

(f) Sixth eigenmode.

Figure 4.3: First six natural eigenmodes of vibration for a cantilevered free flexible surface; two-hundred mass-points.

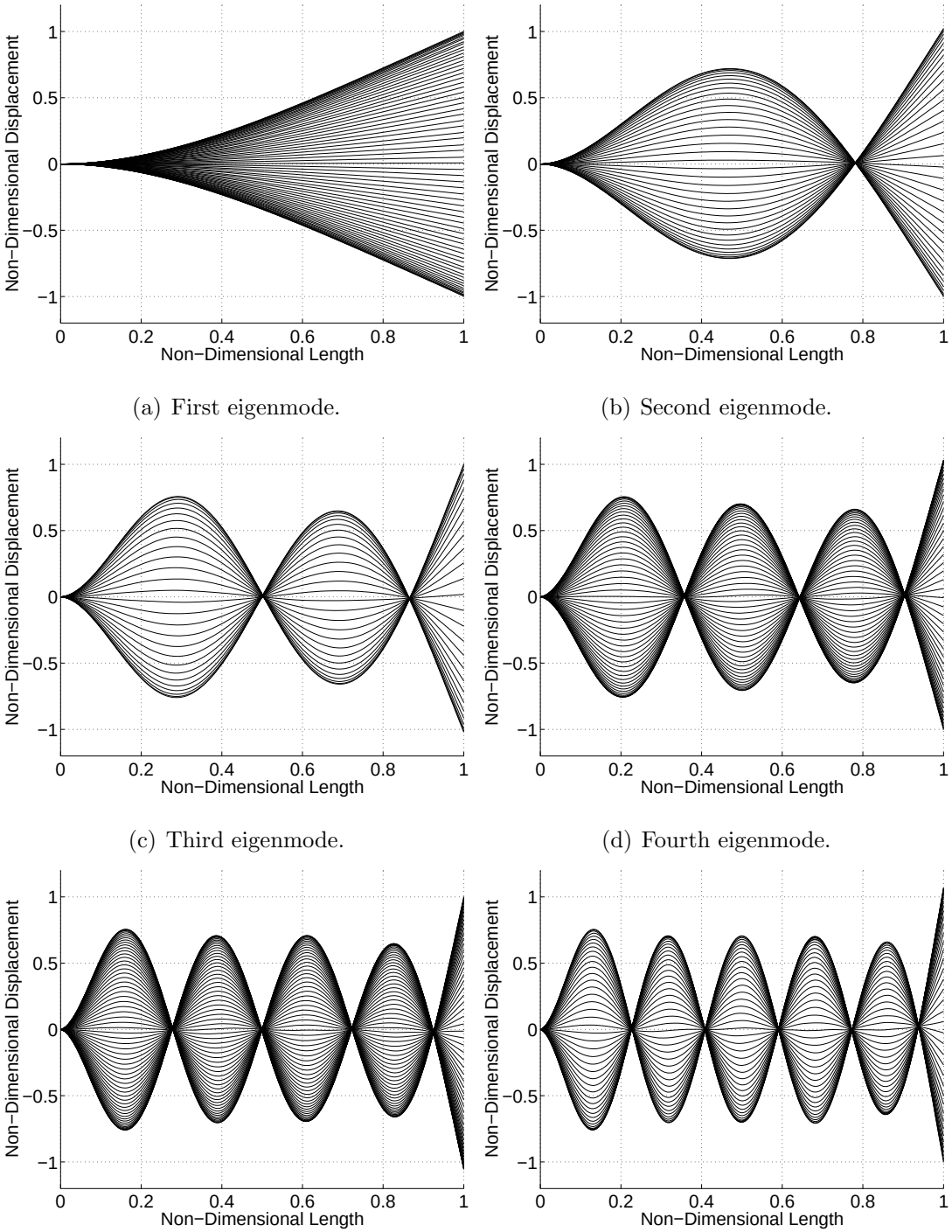

(a) First eigenmode.

(b) Second eigenmode.

(c) Third eigenmode.

(d) Fourth eigenmode.

(e) Fifth eigenmode.

(f) Sixth eigenmode.

Figure 4.4: Flexible-surface oscillations *in vacuo* when initial deflection is of the form of one of the first six eigenmodes of vibration for a cantilevered-free plate; two-hundred mass-points.

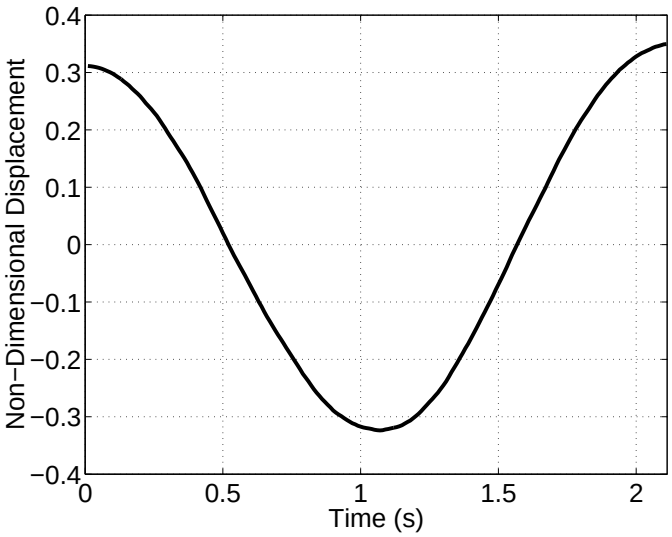

Figure 4.5: Displacement *in vacuo* of mass-point 140 in time; initial deflection is the fourth eigenmode, two-hundred mass-points.

Eigenmode	Theoretical	200 mass-points	50 mass-points
1	133.363 s	133.6 s	134.6 s
2	21.279 s	21.3 s	21.2 s
3	7.599 s	7.58 s	7.6 s
4	3.878 s	3.88 s	3.86 s
5	2.346 s	2.33 s	2.36 s
6	1.570 s	1.57 s	1.58 s

Table 4.1: Theoretical and calculated oscillation periods for *in vacuo* oscillations of the first six eigenmodes for different discretisations; $E = 7\times10^7$ N/m^2, $\rho = 2100$ kg/m^3, $h = 5 \times 10^{-4}$ m, and $L = 1.355$ m.

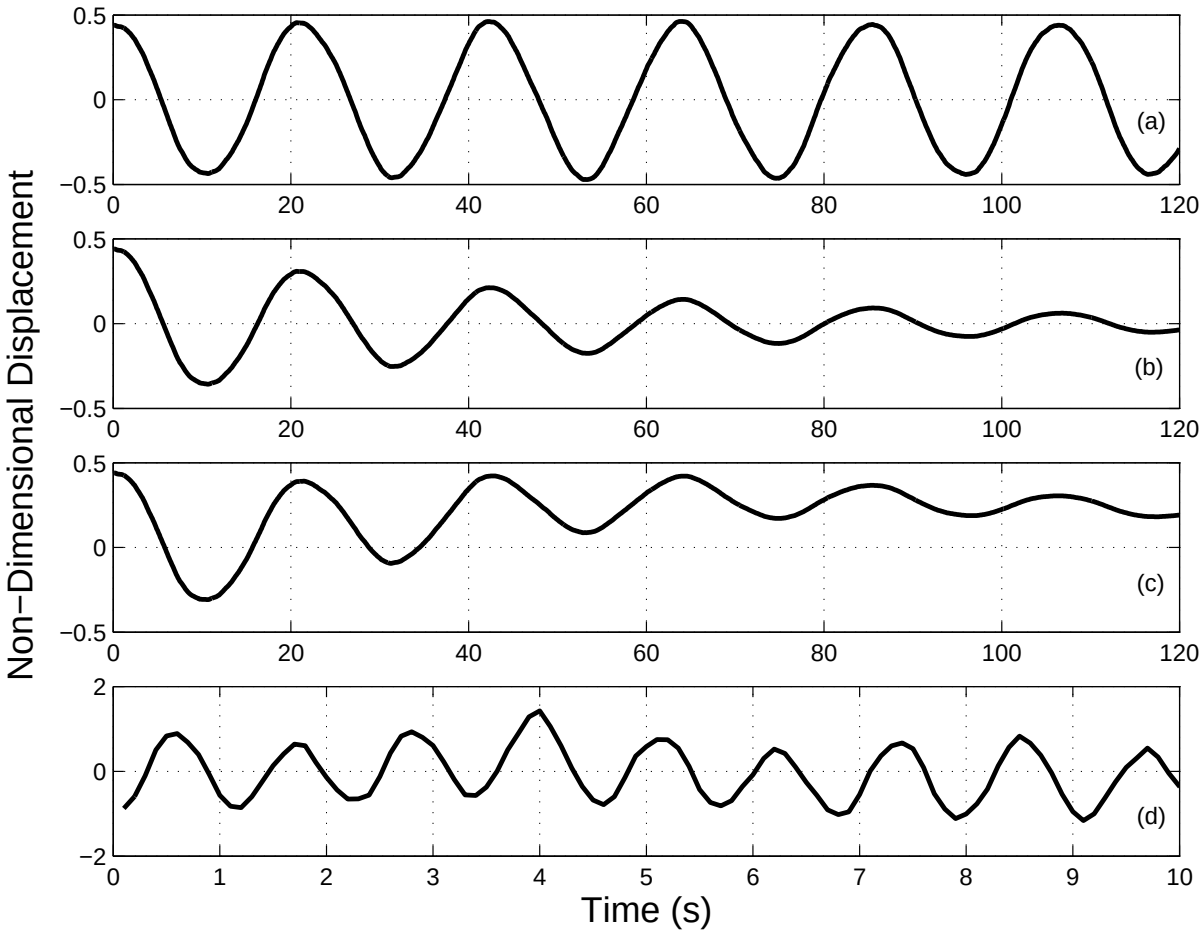

Figure 4.6: Displacement of mass-point 15 in time; fifty mass-points: (a) *in vacuo*, initial deflection is the second eigenmode; (b) *in vacuo* with $d = 0.05$ kg/sm^2, initial deflection is the second eigenmode; (c) $d = 0.05$ kg/sm^2, $\delta p = 5 \times 10^{-8}$ N/m^2, initial deflection is the second eigenmode; (d) *in vacuo*; initial deflection is a sinusoidal wave, $w(x) = A \sin(6\pi x/L)$ where A = 0.00001L .

4.2 Velocity Model Validation

The discretised flow-region geometry is shown again in figure 4.7. Unless otherwise stated, in all numerical experiments the rigid-wall panel control-points are located *in line* with central-surface panel control-points and the wall discretisation required to achieve this is utilised. Pressure is proportional to surface curvature; therefore, if the central flexible-surface is flat, there will be no perturbation to the pressure field owing to the absence of viscosity. Therefore, a perturbation is provided via a linear deflection of the flexible surface. All non-dimensional pressure values plotted in illustrated results are values along the upper surface of the central flexible surface. The initial validation of the velocity model with the rigid walls *far away* from the central surface is quantitative; further validation with rigid walls *close* to the central surface is a logical qualitative validation and is conducted to give confidence in the integrity of this new model.

4.2.1 Absence of Rigid Walls

An initial experiment was carried out to quantitatively validate the calculation of the *hydrodynamic stiffness* part of the pressure equation (3.52), shown again below

$$\begin{aligned}\{\delta p_i\}_{xp} \;=\; & \underbrace{\rho_f \left(U'_\infty \left[\mathbf{A}\right] \left\{ U'_\infty \theta_m + u_m^{Tb} \theta_m \right\} - \left[\mathbf{B}\right] \left\{ \dot{U}'_\infty \theta_m + \dot{u}_m^{Tb} \theta_m \right\} \right)}_{Hydrodynamic\ Stiffness} \\ & + \underbrace{\rho_f U'_\infty \left[\mathbf{A}\right] \left\{ \dot{w}_m - u_m^{Nb} \right\}}_{Hydrodynamic\ Damping\ I} - \underbrace{\rho_f \left[\mathbf{B}\right] \left\{ U'_\infty \dot{\theta}_m + u_m^{Tb} \dot{\theta}_m \right\}}_{Hydrodynamic\ Damping\ II} \\ & - \underbrace{\rho_f \left[\mathbf{B}\right] \left\{ \ddot{w}_m - \dot{u}_m^{Nb} \right\}}_{Hydrodynamic\ Inertia} . \end{aligned} \tag{4.3}$$

The prediction of hydrodynamic stiffness by the velocity model at $\bar{L} = 738$, $\bar{U} = 5.51 \times 10^{-2}$ was halved to enable comparison with the one-sided flow-model prediction of the model developed by Lucey and Carpenter (1992a). To further enable reasonable comparison between the two models, the central flexible surface of length L was deflected as a sinusoidal mode $w(x) = A_n \sin(n\pi x/L)$ where $L = 1$ m and $n = 10$. The flexible surface was therefore effectively of *infinite length*, owing to the high mode deflection,

meaning that the flexible-surface edges and their associated flow disturbances were far away from the centre of the flexible surface, where similar results should be obtained by both methods. A_{10} was set equal to $0.00001L$ to ensure linear assumptions were not violated. The flexible-surface was discretised into 200 panels. The predictions are shown in figure 4.8 and show good agreement. Calculation of the normal-velocity perturbation returned a result of zero, confirming the enforcement of the boundary condition. The pressure was seen to be low (where the velocity was conversely high) at points of high curvature. At the trailing edge, a stagnation point was enforced by the Kutta condition. At the leading edge, singular behaviour was evident in the predicted pressure distribution by the vortex model. This behaviour is predicted by thin-aerofoil theory and was due to the infinite curvature present at the leading edge. Physically in areas of high curvature, such as corners and edges, as there is no viscosity the flow has to travel infinitely fast to not separate; this leads to a singular result. At the leading edge a high pressure would be physically realistic as a stagnation point would be expected at this location. The velocity model was applied to a NACA 2412 aerofoil, detailed in Abbott and von Doenhoff (1959) and illustrated in figure 4.9, to determine whether this effect would also occur if leading-edge curvature were introduced; this would confirm if the velocity model was correctly calculating the magnitude of the pressure at the leading edge of the flexible surface. The resulting pressure distribution is illustrated in figure 4.10, where the square of velocity is plotted so pressure is inversely proportional to magnitudes displayed. The figure shows that with the introduction of leading-edge curvature a large pressure, owing to a stagnation point, does occur. Also, the illustrated result is similar to that of a panel method developed by Houghton and Carpenter (2003) lending further confidence in the validity of the velocity model. Returning to the original flow-structure geometry, general displacements of the flexible surface were made and the resulting pressure distributions are illustrated in figure 4.11, for $\bar{L} = 1$, $\bar{U} = 1$. Again, pressure is low where velocity is high at points of high curvature, at the trailing edge a stagnation point is enforced by the Kutta condition and at the leading edge the singular behaviour is again evident. The velocity model is self consistent and produces identical and opposite pressure distributions when the initial deflections are inverted. It is noted that a stagnation point is only

approximately imposed by the Kutta condition on the second eigenmode deflection; the Kutta condition enforces zero vorticity at the trailing edge and this has not been violated. However, this highlights the relatively high lift potential of the second-eigenmode shape, similar to the camberline of an aerofoil, and hence the greater susceptibility to separation at the trailing edge. Now a rigid central surface is introduced at the leading edge of the central flexible surface. Referring to figure 4.12, as the length of this surface is increased, the singularity is moved away from the flexible surface and the magnitude of the pressure at the leading edge of the flexible surface is substantially reduced. The effect of discretisation on the pressure distribution along the central surface is shown in figure 4.13; the figure shows that discretisations of fifty and two-hundred panels provide similar results for an initial deflection in the form of the second eigenmode. It would be expected that at higher modes and for modelling intricate FISI, a higher discretisation would be required, for example see Yamaguchi *et al.* (2000b).

4.2.2 Rigid Walls *Close* to the Central Surface

We now bring rigid walls *close* to the central surface retaining a symmetrical channel. Initially, we discretise so wall control points line up with central-surface control points. In figure 4.14, flexible-surface pressure distributions are illustrated for various values of $\bar{H}$. The sum of source singularities is very close to zero, and so no fluid is being generated or negated. The figure shows that $\bar{H} = 1$ is a good approximation for $\bar{H} = \infty$. As the walls are moved in closer to the central surface, where the flexible surface constricts the passage the pressure on the central surface drops. This effect is balanced on the opposite side of the central-surface, where the pressure (the exact opposite of that on the upper surface) will increase as the channel here is relatively wide. The pressure difference across the central surface is therefore increased by the proximity of the channel walls. The effect of *channel blockage* is now examined. As the channel walls are brought closer to the flexible surface, figure 4.14 shows that where there is negative curvature in the upper channel the flow has increased in speed. This means that on the opposite side where there is positive curvature, the flow has relatively less speed. This seemingly

spurious result is due to the greater overall blockage in the lower channel, where the flexible surface protrudes further into the channel. As the fluid is incompressible, the narrowest part of the channel sets the maximum flow speed, in a similar fashion to the maximum output of a manufacturing production line. Therefore, the flow has greater speed in the channel that has *least overall blockage* (or, to carry on the manufacturing analogy, greatest output). In figure 4.15 the reduction of wall discretisation and its effect on the flexible-surface pressure distribution is investigated; this is reasonable as the pressure distribution along the walls is not required to be accurate. The figure shows that wall discretisation can be reduced by a third from control-point coincidence levels with no effect on the flexible-surface pressure distribution. Finally, two further effects are noted. First, the effect of the ratio of channel height to *outlet length* (defined as the horizontal distance to the downstream end of the channel, measured from the trailing edge of the flexible surface) has little effect whilst the channel walls extend past the trailing edge of the flexible surface. Second, when the walls are brought closer to the central surface the *aspect ratio* of the channel increases, *i.e.* the inlet and outlet lengths of the channel become relatively longer; this effectively moves the singularity further upstream from the flexible surface with no increase in rigid central-surface length.

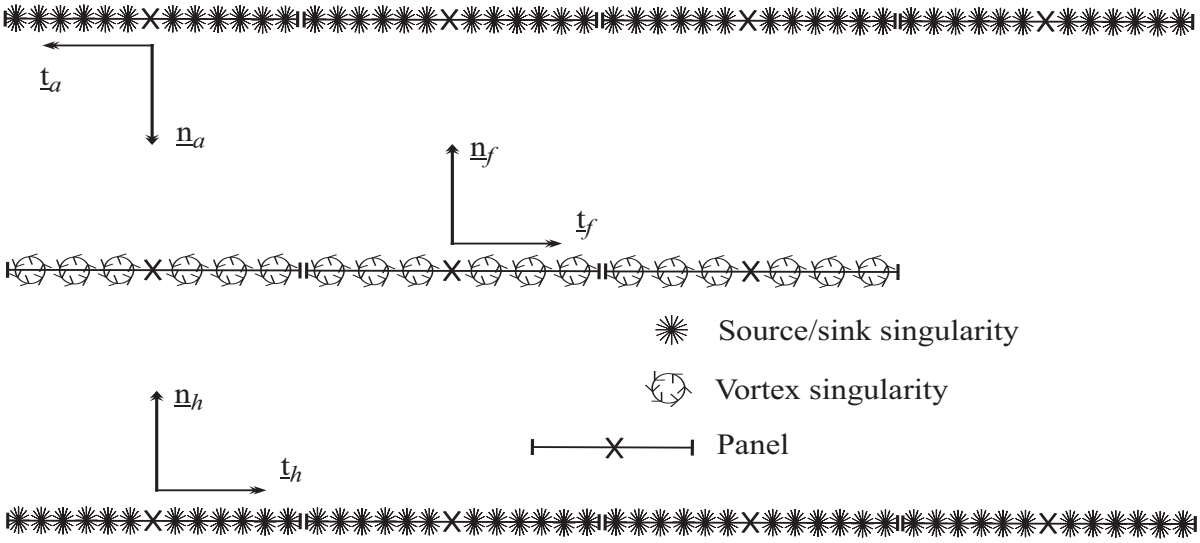

Figure 4.7: Application of panel method to the flow-structure geometry.

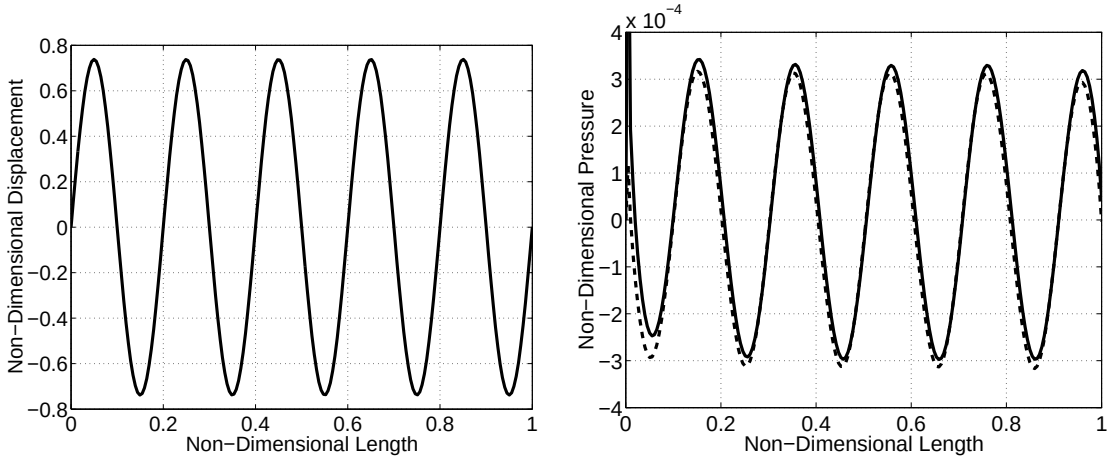

(a) (b)

Figure 4.8: Validation of the prediction of the hydrodynamic stiffness component of the pressure by the velocity model: (a) Initial deflection; (b) Steady pressure distribution: − velocity model, - - model of Lucey and Carpenter (1992a); $\bar{L} = 738,\ \bar{U} = 5.51 \times 10^{-2}$, two-hundred panels.

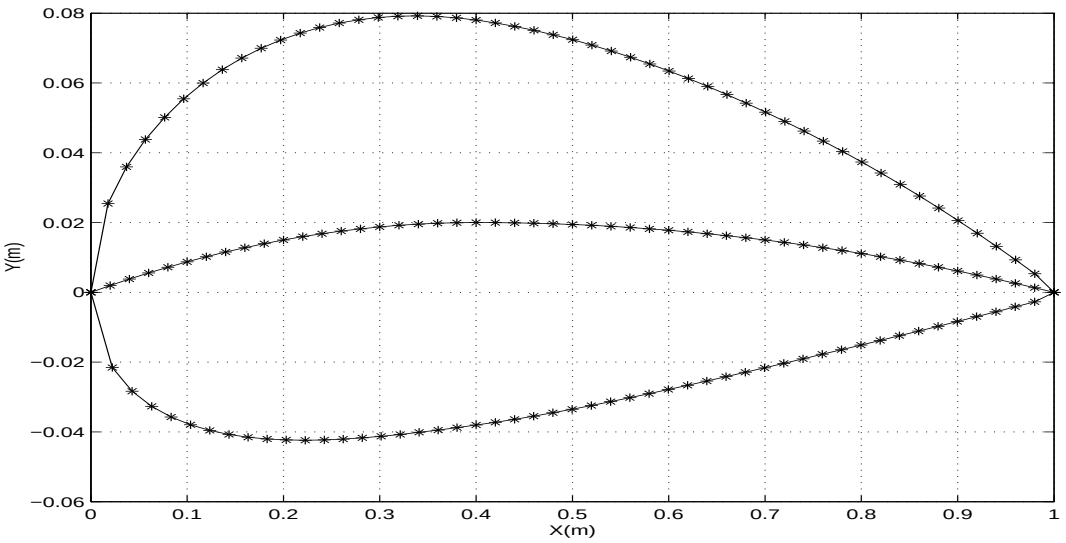

Figure 4.9: NACA 2412 Aerofoil (central line is the chord line).

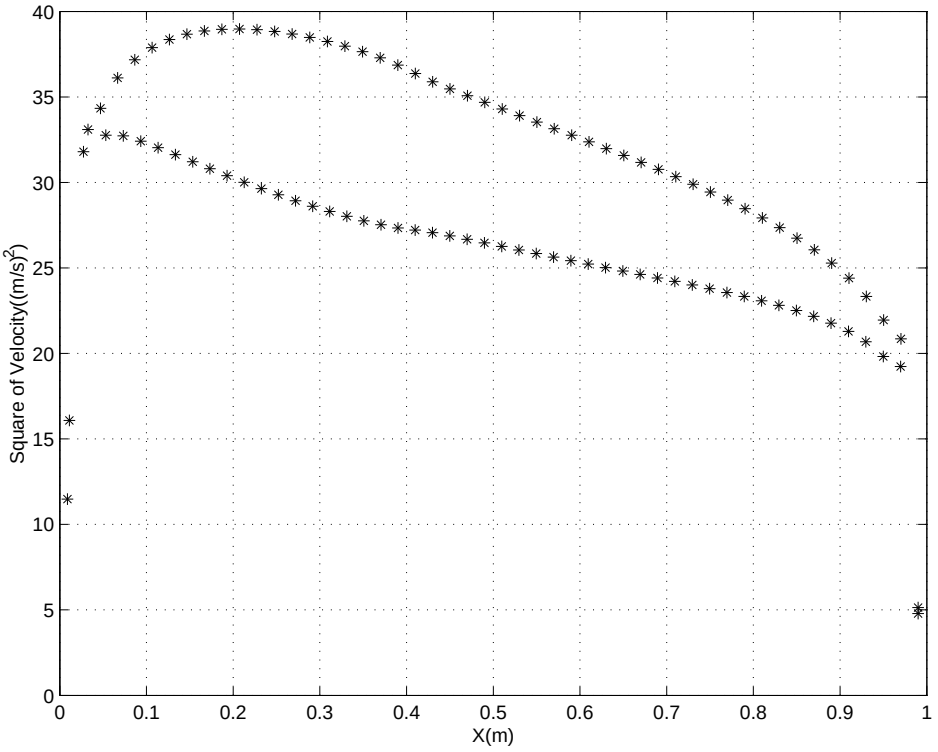

Figure 4.10: Square of velocity calculated over NACA 2412 aerofoil using current velocity model (values plotted are those at panel control points); $\rho_f = 1$ kg/m^3, $U_\infty = 1$ m/s, one-hundred panels.

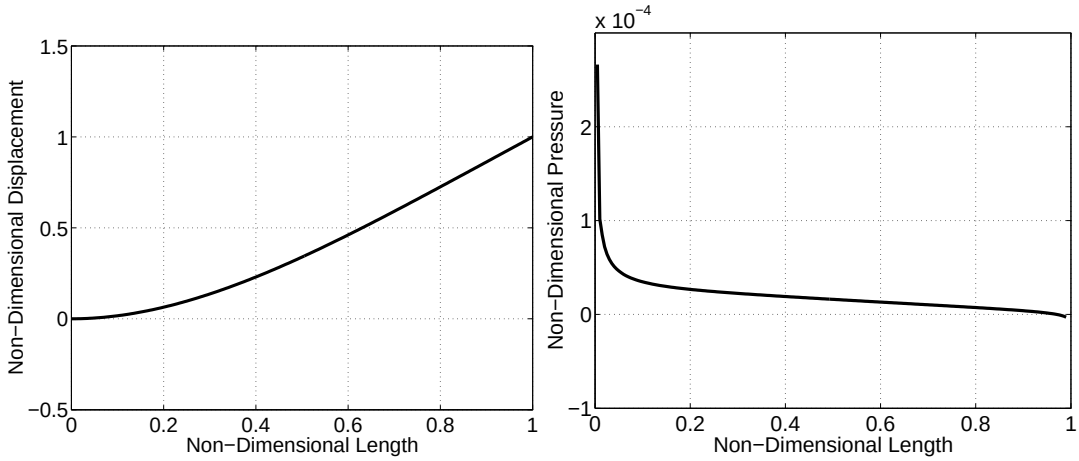

(a) First eigenmode displacement and pressure distribution.

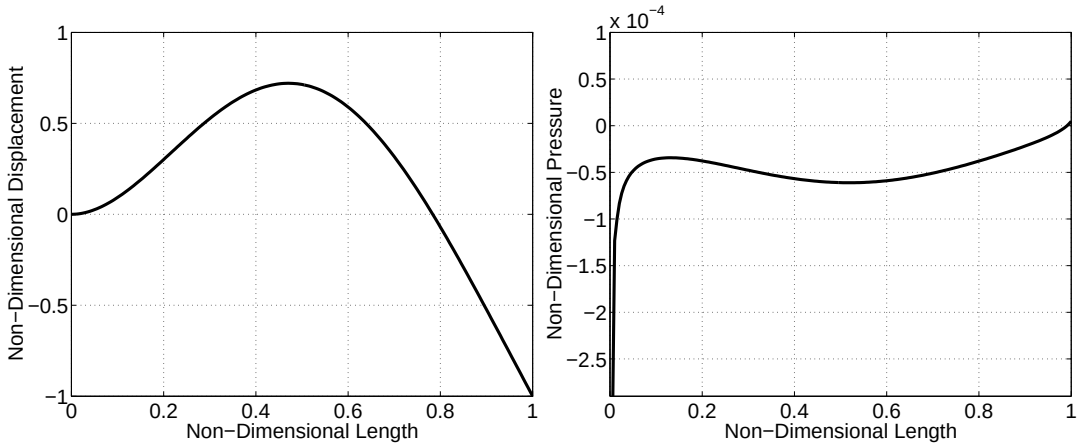

(b) Second eigenmode displacement and pressure distribution.

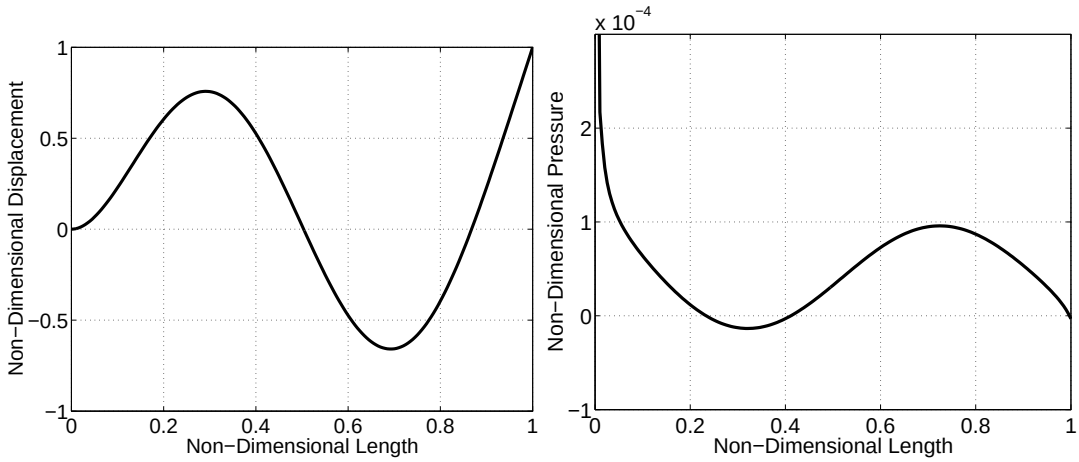

(c) Third eigenmode displacement and pressure distribution.

Figure 4.11: Non-dimensional pressure distributions for first three natural eigenmodes of vibration for a cantilevered-free flexible surface; $\bar{L} = 1,\ \bar{U} = 1$, two-hundred panels.

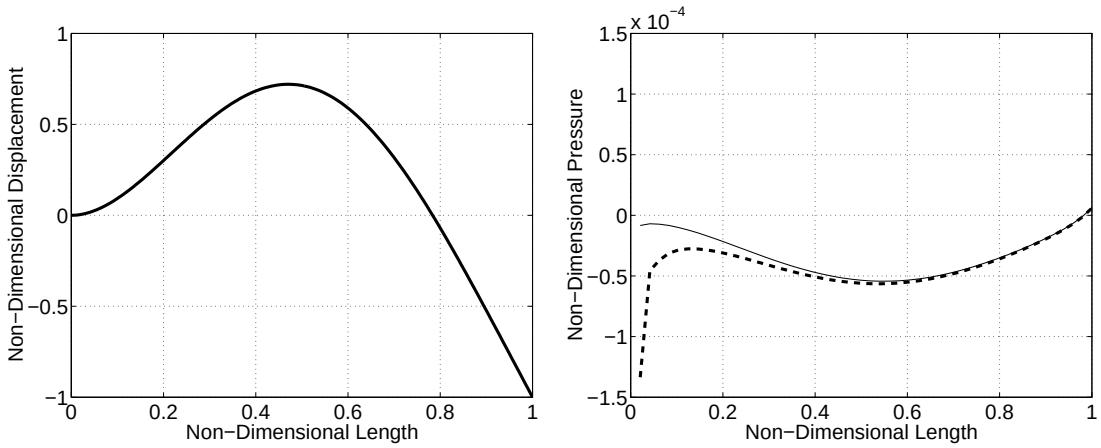

(a) (b)

Figure 4.12: Effect on non-dimensional pressure distribution of rigid central-surface at leading edge of flexible surface deflected as the second eigenmode: (a) initial deflection; (b) pressure distribution: − rigid central surface included, - - rigid central surface absent; $\bar{L} = 1,\ \bar{U} = 1$, 50 flexible-surface panels.

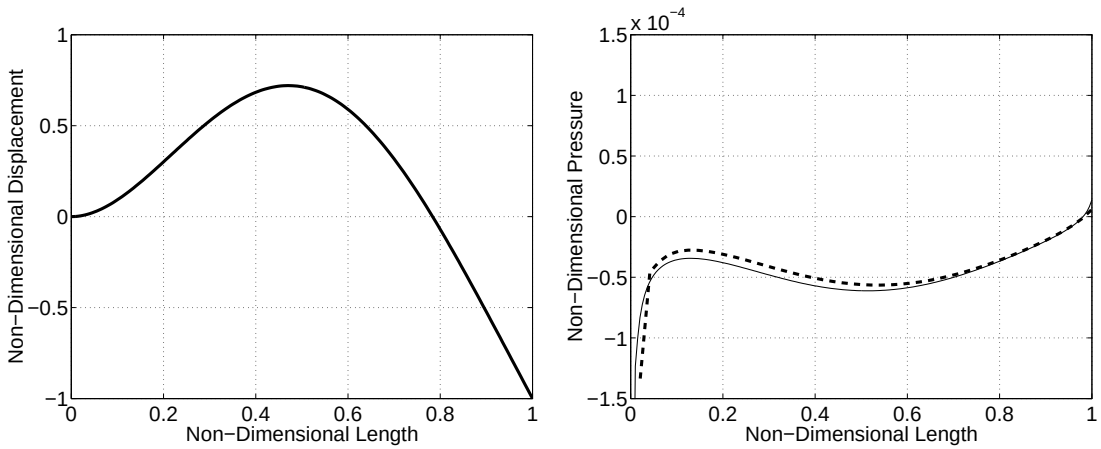

(a) (b)

Figure 4.13: Effect of flexible surface discretisation on the second eigenmode non-dimensional pressure distribution: (a) initial deflection; (b) pressure distribution: − 200 panels, - - 50 panels; $\bar{L} = 1,\ \bar{U} = 1$.

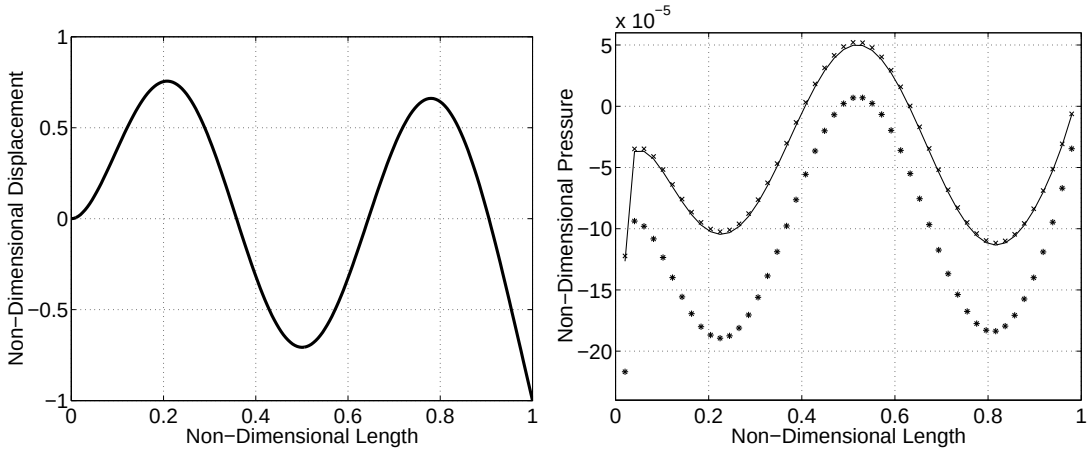

(a) (b)

Figure 4.14: Effect of channel wall proximity on the non-dimensional pressure distribution along the flexible-surface deflected as the fourth-eigenmode: (a) initial deflection; (b) pressure distribution: x $\bar{H} = 10$, - $\bar{H} = 1$, * $\bar{H} = 0.1$; $\bar{L} = 1$, $\bar{U} = 1$.

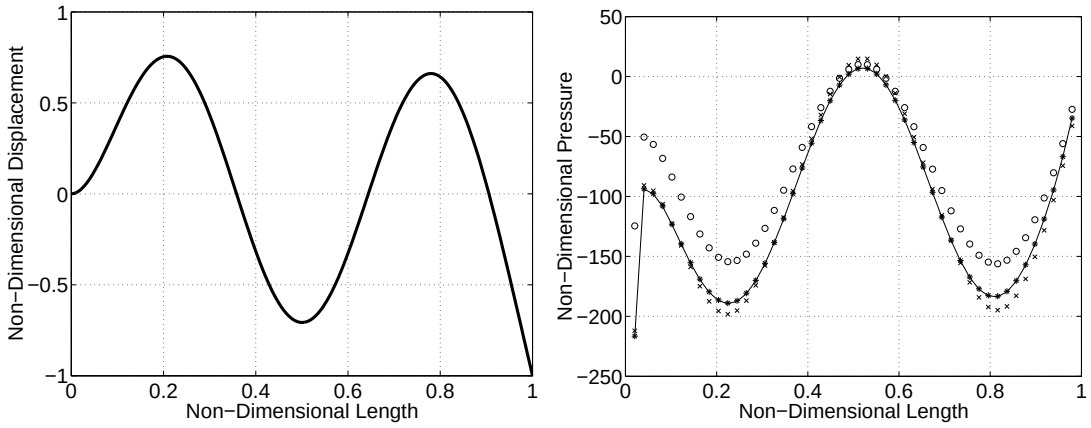

(a) (b)

Figure 4.15: Effect of channel wall discretisation on the non-dimensional pressure distribution along the flexible-surface deflected as the fourth-eigenmode: (a) initial deflection; (b) pressure distribution: − 150 panels, * 50 panels, x 10 panels, o 5 panels; $\bar{L} = 1000$, $\bar{U} = 1$, $\bar{H} = 0.1$.

4.3 Vorticity Model Validation

To quantitatively validate the shed-vorticity computational model, the starting vortex phenomenon was modelled for an aerofoil. In Houghton and Carpenter (2003) it is described that the starting vortex is created as a result of the initial vorticity generated in the free stream that forces a stagnation point to exist at the trailing edge of an aerofoil. An aerofoil was modelled using a zero-order vortex panel-method version of the velocity model described in the previous section, but with no Kutta condition enforced; using a method similar to Lewis (1991) this was captured by a vortex-blob pair released at the trailing edge at every time step, as shown in figure 4.16(a). The upper blob had a strength proportional to the sum of vorticity along the upper surface of the aerofoil ($\Delta\Gamma_a = 0.5\gamma_a^2\delta t$ where γ_a was the total vorticity along the upper surface of the aerofoil), the lower blob being proportional in strength to the distribution of the lower side ($\Delta\Gamma_b = 0.5\gamma_b^2\delta t$). A numerical experiment similar to that carried out by Lewis (1991) was conducted; a NACA 0012 aerofoil at 20^o angle of attack was modelled at $\underline{U}_\infty = 1$ m/s. The resulting wake after fifty time steps (where $\delta t = 0.1$ s) for the present model is shown in figure 4.16(b). The figure shows the formation of the starting vortex has occurred and it was found that the Kutta condition was captured (as the pressure at the trailing edge of the aerofoil was found to be zero at each time step). The capturing of the Kutta condition and the general form of the wake quantitatively validates the numerical implementation of the shed-vorticity model; it also quantitatively validates its coupling with the panel method. To investigate the variation in parameters of the shed vorticity model, a two-dimensional pulsed jet was modelled, illustrated in figure 4.17(a), using blob pairs taking into account their reflections in the wall around the jet orifice and their effect on each other. Fifty blob pairs were released and (in the absence of a free stream velocity) their positions as they convected each other downstream over 250 time steps, where $\delta t = 0.01$ s, were calculated the result shown in figure 4.17(b). Blob properties were then varied to ascertain their effect. Blob strength greater than unity was initially applied and the result of this increase is shown in figure 4.17(c). By comparing this result to that shown in figure 4.17(b) it can be seen that the jet the blobs describe is now more vortical and

convects further downstream than the unit-blob-strength case. Blob core-size is now reduced and the result is shown in figure 4.17(d). By comparing this result to that shown in figure 4.17(b) it can be seen that as the core size is reduced, the blobs travel less distance downstream but also the vorticity has increased. This is a *blob mass effect*, the blob having less mass to rotate and therefore the blob rotates with an increased rate of angular rotation.

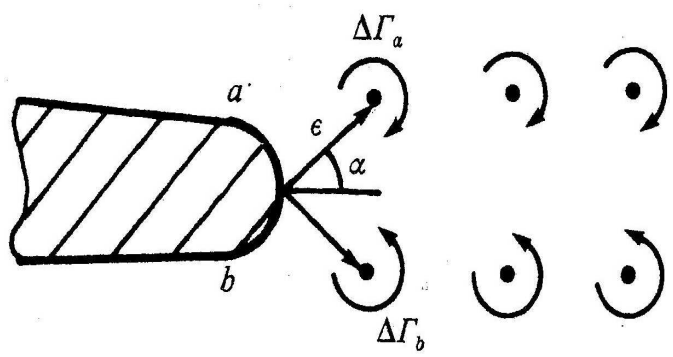

(a) Shed vortices release parameters.

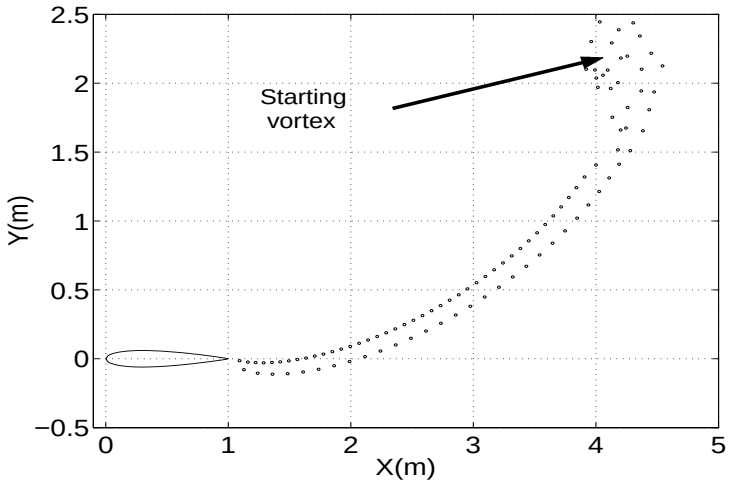

(b) Model of starting vortex.

Figure 4.16: The figure shown in (a) is adapted from Lewis (1991). In (b), the wake behind a NACA 0012 aerofoil at 20^o angle of attack is modelled, each circle representing a vortex blob; parameters were: $U_\infty = 1$ m/s, chord length = 1 m, release parameters were $\epsilon = 5\%$ of chord length and $\alpha = 30^o$, core size $\alpha^b = 3 \times 10^{-4}$ m, 50 time steps, $\delta t = 0.1$ s.

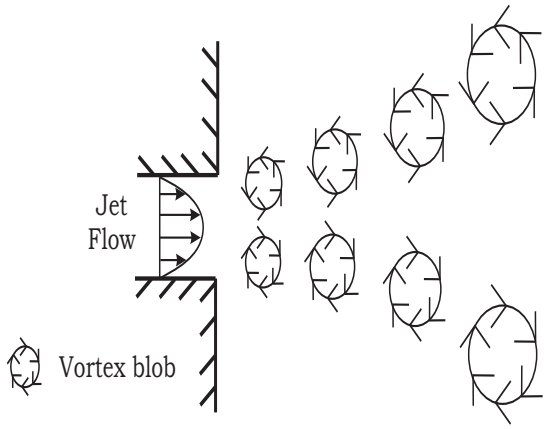

(a) Schematic showing pairs of vortex blobs being ejected from a two-dimensional jet.

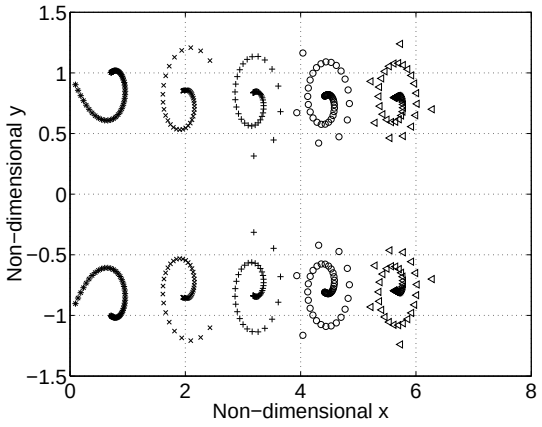

(b) General model.

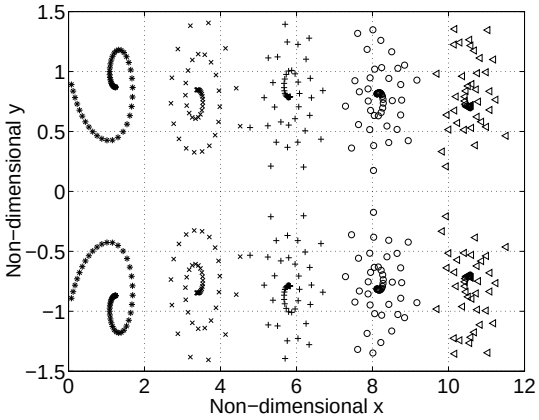

(c) Blob strength = 2 s^{-1}.

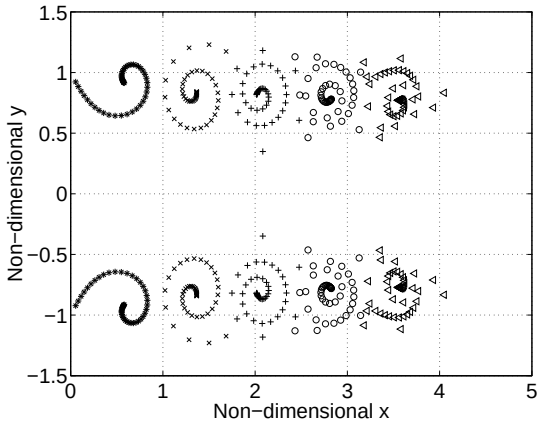

(d) Core size = 0.3 m.

Figure 4.17: Figure illustrating the effect of modifying blob physical parameters on the position of blobs of vorticity after being ejected from a two-dimensional jet at different time steps: $*$ 50 time steps, x 100 time steps, + 150 time steps, $\circ$ 200 time steps, $\triangleleft$ 250 time steps; fifty blob pairs, blob strength (unless otherwise specified) = 1 s^{-1}, core size (unless otherwise specified) = 0.5 m, initial blob pair vertical spacing = 1 m, $\delta t = 0.01$ s, positions calculated using a predictor-corrector method.

4.4 Unsteady Model Validation

Results from a series of numerical experiments that validate the union of the flexible surface, velocity and vorticity models are now presented. Initially, vorticity is not modelled to allow quantitative validation of the hydrodynamic damping and inertia terms in (4.3). This validation is carried out in a similar fashion to §4.2.1, comparison being made with the computational model developed by Lucey and Carpenter (1992a). In these initial numerical experiments, hinged-hinged edge conditions are applied. Thereafter, the effect of clamped-free edge conditions on the oscillation of the flexible surface in the flow-structure system is assessed. A steady-state oscillation is found further validating the model. The set-up of the model for conducting further numerical experiments is described.

4.4.1 Joint Velocity-Flexible Surface Model

This quantitative validation was carried out at $\bar{L} = 738$ and $\bar{U} = 5.51 \times 10^{-2}$. At $t = 0$, the flexible surface of length L was deflected as a sinusoidal mode $w_o = A_n \sin(n\pi x/L)$ where $L = 1$ m and $n = 10$. This deflection provided initial excitation to the flow-structure system. Setting $n = 10$ effectively made the flexible surface infinitely long and $A_{10} = 0.00001L$ ensured linear assumptions were not violated. The fluid had the density of water, 1000 kg/m^3, to demonstrate the computational model's resilience to numerical divergence. The flexible surface was discretised into 200 mass points. Initially consider the hydrodynamic inertia terms in (4.3). By setting $U_\infty = 0$ only the inertia of the fluid contributes to the unsteady pressure. This effect manifests itself as a reduction in the flexible surface's oscillation period owing to the added fluid mass. Inserting the result for flexible-surface pressure from Carpenter and Garrad (1986) into the beam equation yields

$$\delta p = \rho_f \kappa \left(U_\infty - c\right)^2 w, \tag{4.4}$$

where κ and c are the wave number and wave speed of the flexible surface respectively. Rearranging, see §B.6, provides the further result that flexible surface oscillation period is

proportional to $\sqrt{(m_p + m_f)/B}$, where m_p and m_f are respectively the flexible surface mass and the fluid mass. In the present numerical experiment, $m_f >> m_p$ and it is therefore expected that the joint plate-velocity model should have a period of oscillation a factor of $\sqrt{2}$ greater than the model developed by Lucey and Carpenter (1992a) owing to the movement of twice the fluid mass. Periods of oscillation for the two models for $U_\infty = 0$ deduced from figure 4.18 show this relation between the two models is correctly predicted. Now consider the hydrodynamic damping terms in (4.3). Both the present model and that of Lucey and Carpenter should predict similar phase speeds for the movement of the flexible surface. Referring to figure 4.19, a simple calculation of the flexible-surface phase speed in each graph, found by calculating the distance moved between snap-shots of the flexible surface and dividing by the time difference, finds that phase speeds predicted by both models are approximately the same, differing by 10%. The author notes that the relatively large amplitude of oscillation the flexible surface exhibited in the results of the unsteady model in this figure owes to the pressure difference across the surface being twice as large as that of the single-sided model.

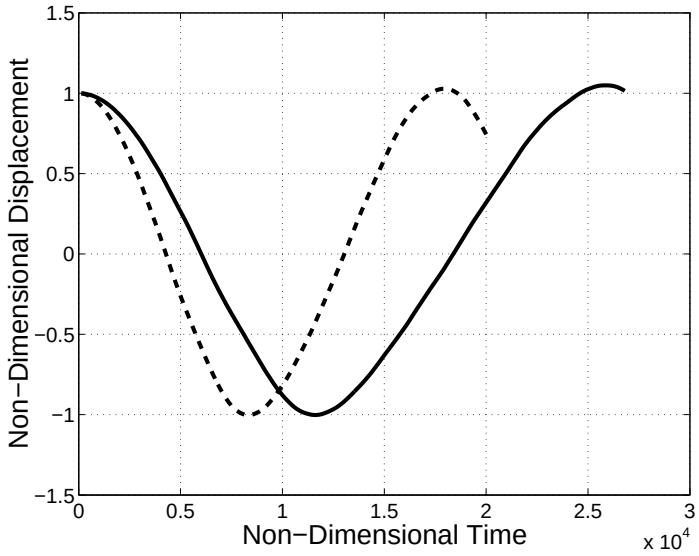

Figure 4.18: Validation of the prediction of the hydrodynamic inertia component of the pressure by the unsteady model, oscillation of mass point at $0.48L$: $-$ present model, $--$ Lucey and Carpenter (1992a); $\bar{L} = 738,\ \bar{U} = 5.51 \times 10^{-2}$, two-hundred mass points.

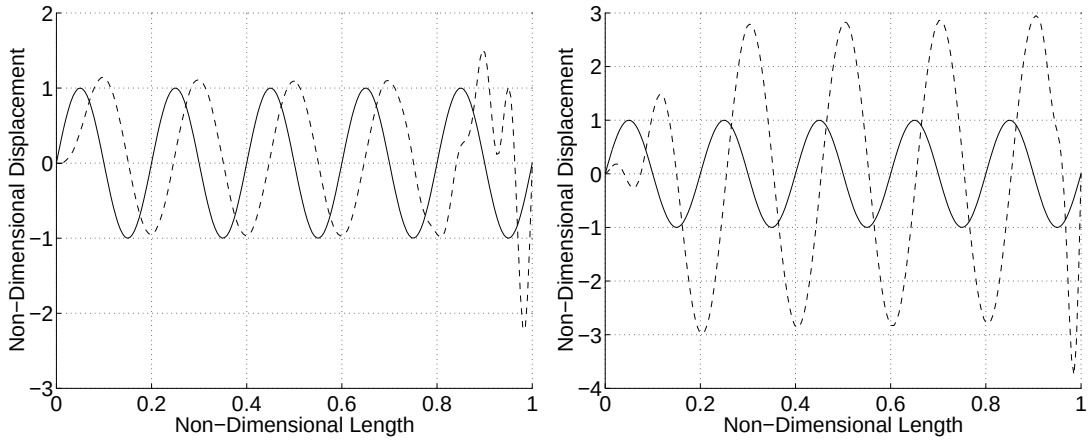

(a) Lucey and Carpenter (1992a).

(b) Present model.

Figure 4.19: Validation of the prediction of the hydrodynamic damping component of the pressure by the unsteady model, oscillation of entire flexible surface: $-$ initial deflection, $--$ deflection after 0.01 s; $\bar{L} = 738,\ \bar{U} = 5.51 \times 10^{-2}$, two-hundred mass points.

4.4.2 The Steady State

As described in §3.5, in a fluid-structure model at some critical velocity U_c, the forces of the fluid and structure will balance and the structure will oscillate in a *steady state*. The form of the oscillation of the flexible surface at U_c is termed the *critical mode*. Published work, for instance Huang (1995), has suggested that in this fluid-structure system when cantilevered-free end conditions are enforced, the critical mode has the overall shape of the second eigenmode.[1] To investigate this phenomenon, initial experiments were conducted with the flexible surface initially deflected in the shape of the second mode; with $\bar{L} = 1$, $\bar{U}$ was varied until U_c was found, the oscillation at this free-stream velocity depicted in figure 4.20(a); figure 4.20(b) shows that average total energy of the flexible surface remained constant with time. The second eigenmode was therefore the critical mode of the system, the *necking* in the oscillation intimating a smaller presence of the first eigenmode. Initiating the numerical experiment with a first-eigenmode initial deflection lead to the same steady-state oscillation as shown in figures 4.20(c) and (d). However, figures 4.21(a) and (b) show an initial quasi-infinite-length surface deflection (the sixth eigenmode) not oscillating in the steady-state oscillation at the critical velocity. These results show that the flexible surface is seemingly oscillating *below* U_c as the total energy is falling. However, it is proposed that U_c has not been measured incorrectly but that the total energy is falling whilst the flexible surface is forming into the critical mode. As the free stream velocity is at the critical level, this transition will be an infinitely long process in time. To further illustrate this point, for the same case $\bar{U}$ was set well above U_c to reduce transient time to the perturbed state. The results, see figures 4.21(c) and (d), show that after a number of steady oscillations of the flexible surface and a fall in total energy, the flexible surface began to deflect into the critical mode and was very unstable, suggesting that $\bar{U}$ was several orders of magnitude above U_c. This was synonymous with the physical experimental results of Huang (1995), where a definite activation energy was required to break through the initial instability barrier of the flexible surface and subsequently a far greater critical velocity of instability onset was measured.

[1] Physically explained by the mode's high curvature and hence increased lift potential.

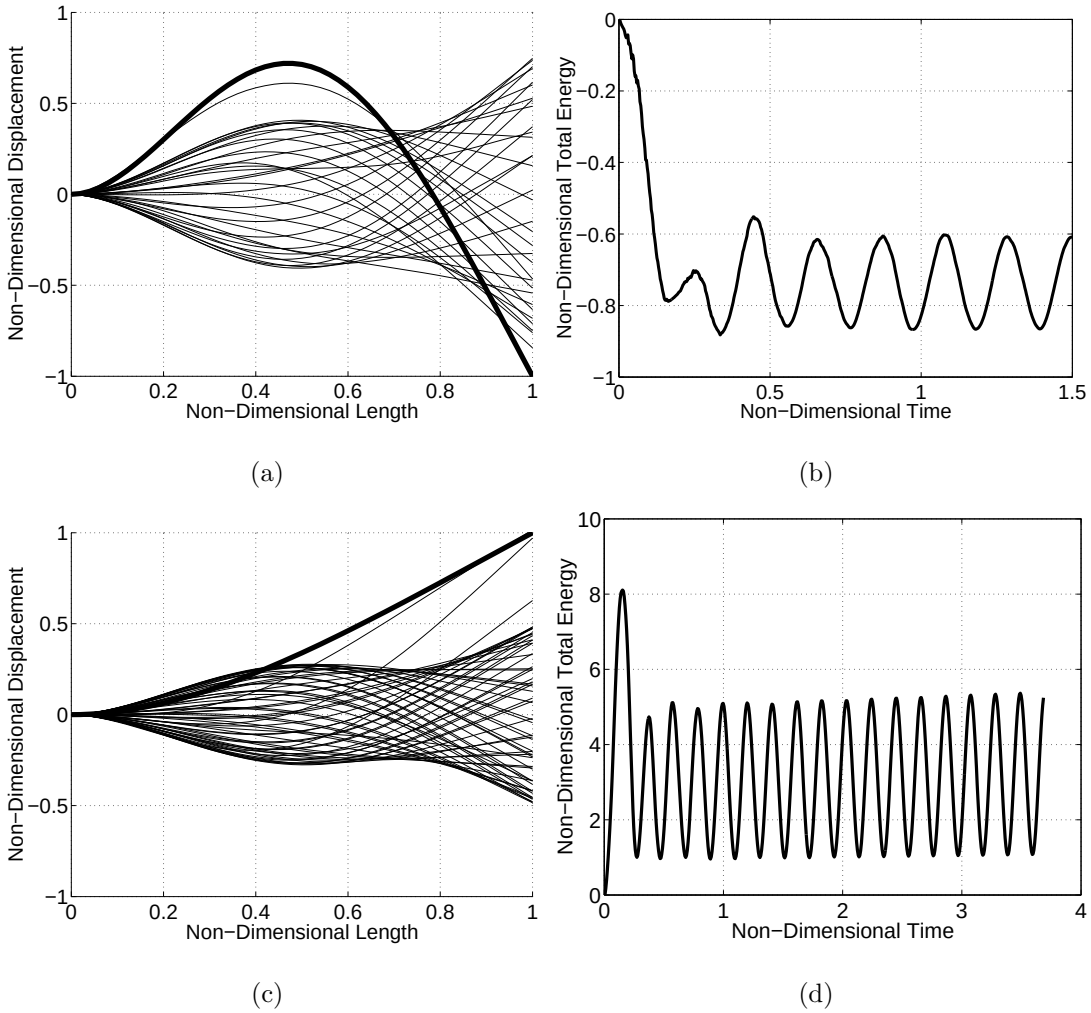

Figure 4.20: Fluid-structure behaviour at critical velocity where (a) and (c) depict the oscillation of the flexible surface (the thick line is the initial deflection) and (b) and (d) are the respective total energies expended: in (a) and (b), $\bar{U} = 5.452$, second eigenmode initial deflection; in (c) and (d), $\bar{U} = 5.452$, first eigenmode initial deflection; fifty mass points, $\bar{L} = 1$.

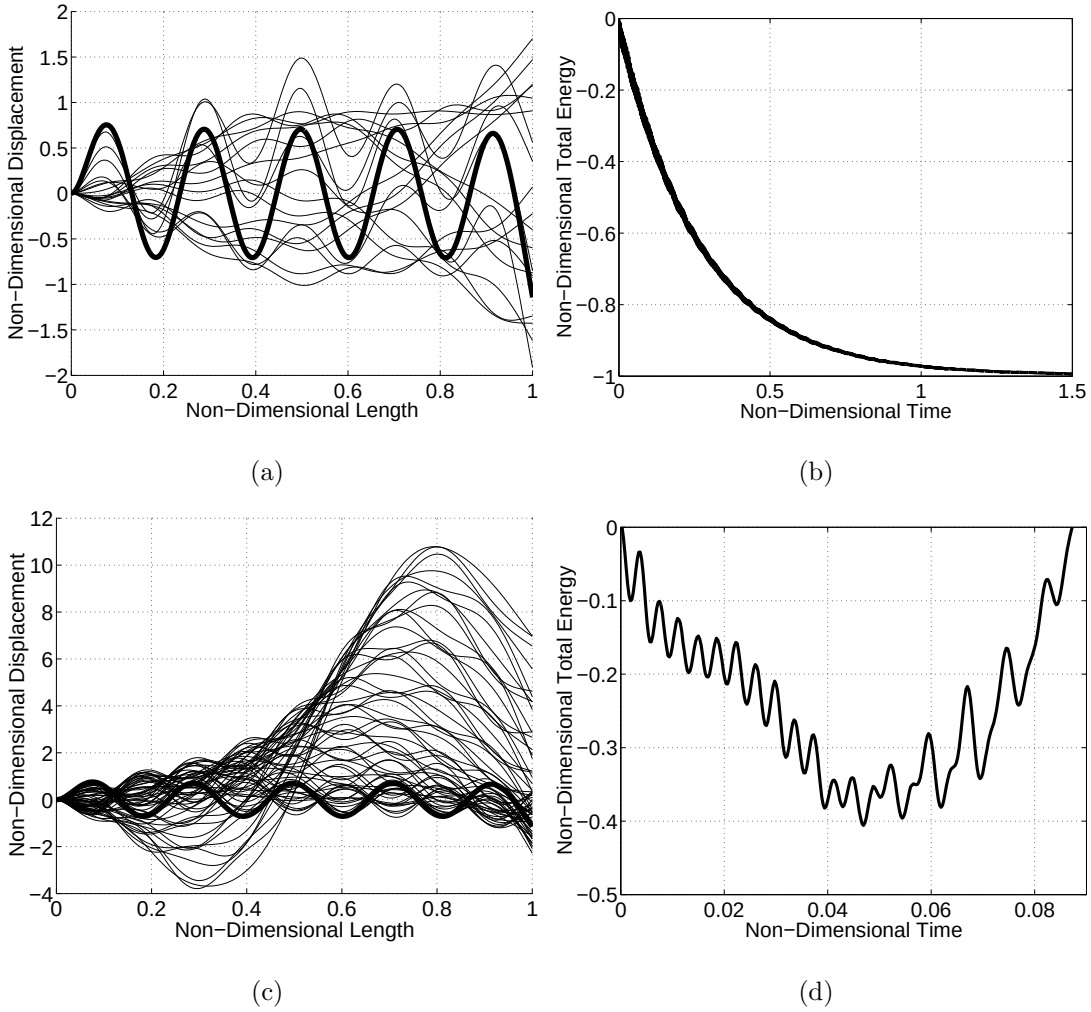

Figure 4.21: Fluid-structure behaviour at critical velocity where (a) and (c) depict the oscillation of the flexible surface (the thick line is the initial deflection) and (b) and (d) are the respective total energies expended: in (a) and (b), $\bar{U} = 5.452$; in (c) and (d), $\bar{U} = 22$; $\bar{L} = 1$, two-hundred mass points, initial deflection is the sixth eigenmode.

4.4.3 Numerical Experiment Setup

Numerical experiments were conducted to establish suitable set-up parameters of the unsteady model for further numerical investigations. The main result required was the measurement of U_c for different $\bar{L}$, obtained by increasing the free-stream velocity until an instability was induced in the fluid-structure system. The ease of measuring U_c was therefore of paramount importance when considering initial excitation to the fluid-structure system. It was therefore important to make the initial excitation to the fluid-structure system similar in shape to the critical mode as this would reduce transient time from $t = 0$ to the steady state, hence facilitating the measurement of U_c. It is proposed that the presented results illustrate that an initial second-eigenmode deflection as the form of initial excitation would yield the lowest transient time to the perturbed state and hence the greatest ease of measuring U_c. Other forms of excitation would take a relatively longer amount of time for oscillations to develop, as observed in figure 4.21, the initial deflection in these experiments being an approximate form of pressure impulse. To determine a suitable level of discretisation, the experiment utilising 50 flexible-surface mass points depicted in figures 4.20(a) and (b) (reshown in figures 4.22(a) and (b)) was repeated using 200 flexible-surface mass points and a smaller time step.[2] The results for the more accurate experiment, see figures 4.22(c) and (d), took a substantially longer computational time to obtain. The results showed the coarser case was more stable and predicted a higher U_c than the finer case, the difference in U_c prediction between the fine and coarse case was approximately 3%. Owing to the reduced discretisation however the computational time of the experiment was significantly reduced, the coarser case's run time approximately one twelfth of the time that it took to run the finer case. Otherwise, the results were in good agreement, confirming that the coarser case produced no numerically generated instabilities. It was proposed that the illustrated discrepancy was an acceptable level of error to incur for the benefit of greatly reduced run time for numerical experiments initially excited using a second-eigenmode deflection.

[2]The ratio of node spacing relative to the time step (an approximate form of the von Neumann number) must be kept within certain limits to allow convergence of the iterative scheme.

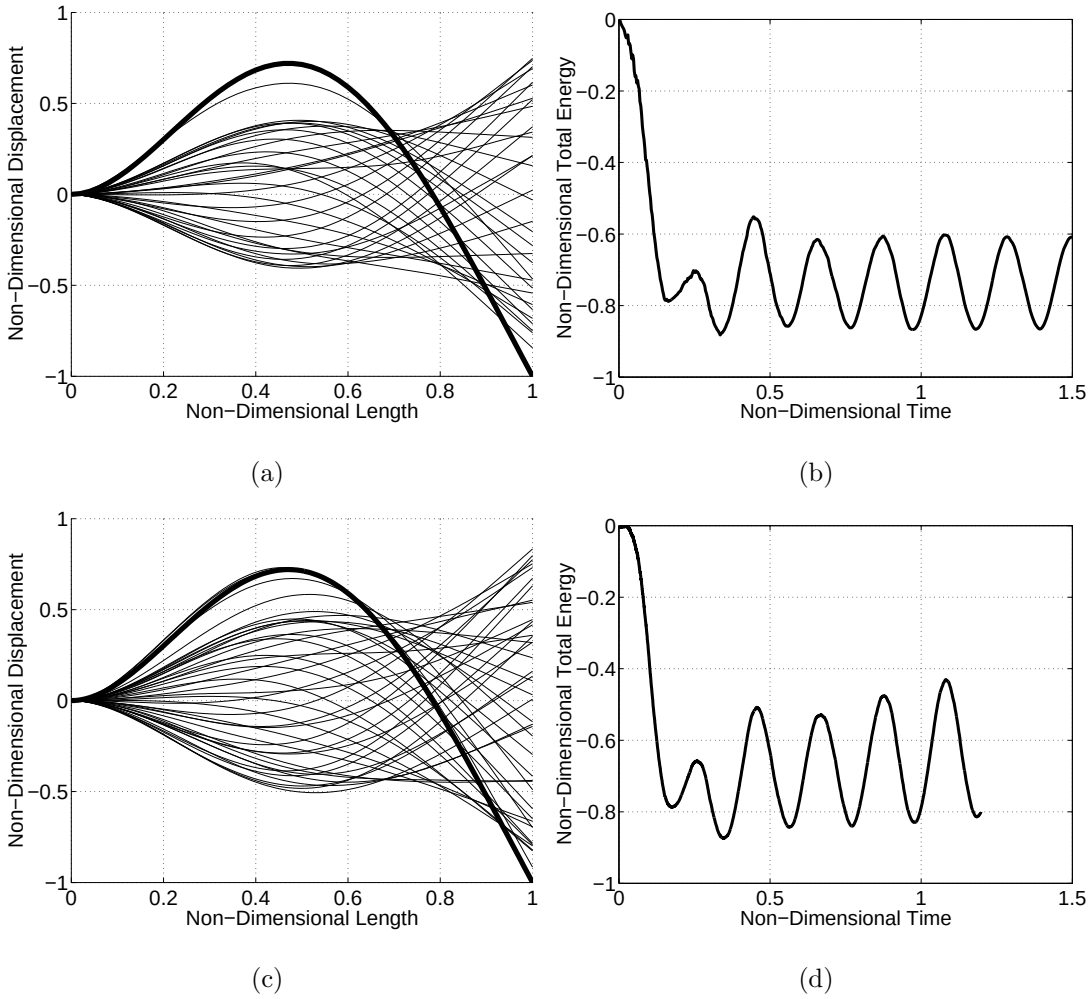

Figure 4.22: Fluid-structure behaviour at critical velocity where (a) and (c) depict the oscillation of the flexible surface (the thick line is the initial deflection) and (b) and (d) are the respective total energies expended: in (a) and (b), $\bar{U} = 5.452$, fifty mass points; in (c) and (d), $\bar{U} = 5.452$, two-hundred mass points; $\bar{L} = 1$, initial deflection is the second eigenmode.

4.5 Summary

It is proposed that the full unsteady model has been validated. There are two effects on the pressure distribution along the flexible surface: flexible-surface curvature and channel blockage. The effect of curvature is kept constant by always using the same ratio of initial deflection to flexible-surface length in experiments. A discretisation of fifty mass points or panels on the flexible surface provides suitable accuracy for unsteady experiments initiated with a low harmonic-mode initial-deflection. The channel walls are far away from the central surface if $\bar{H} \geq 1$. Although the unsteady model has only been quantitatively validated in the absence of channel walls and rigid inlet surface, the velocity model does produce qualitatively correct results with these effects included. Therefore it is proposed that the unsteady model can be used with confidence to generate new results with rigid inlet and channel-wall surfaces included.

Chapter 5

Numerical Experiments

Herein, are presented numerical experiments and new results that give an insight into the phenomena generated by the unsteady system when the fluid and structure interact for a range of $\bar{L}$, $\bar{U}$ and model modifications. The steady-state oscillation for an isolated flexible surface at $\bar{L} = 1$ was described in Chapter 4. First, fluid-structure phenomena at this value of $\bar{L}$ are studied in detail. The effects on these phenomena due to modifications to the unsteady model, *e.g.* the introduction of a rigid central surface, are then investigated. The unsteady model is then used to represent the human snoring phenomenon; realistic oscillation frequencies of the flexible surface and temporally varying free-stream velocity produce unique simulations of this fluid-structure interaction. Finally, fluid-structure phenomena in the range $0.01 \leq \bar{L} \leq 1000$ are investigated and further applications of the unsteady model are discussed. It is noted that when varying $\bar{L}$, ρ_f is varied instead of L and therefore the effect of discretisation is kept constant in all numerical experiments.

5.1 Fluid-Structure Phenomena at $\bar{L} = 1$

Fluid-structure interactions observed at $\bar{L} = 1$ over a range of $\bar{U}$ for an isolated flexible surface are investigated with particular attention paid to U_c, the shape of the steady state

oscillation and the manifestation and mechanism of the observed instability. The effect on these characteristics due to modifications to the unsteady model via the inclusion of rigid channel walls and central surface, variation in flexible surface stiffness and damping and an unsteady free stream velocity are ascertained.

5.1.1 Isolated Flexible-Surface

At $\bar{U} = 0$, see figures 5.1(a) and (b), the flexible surface oscillates in a steady state. Owing to the influence of the fluid inertia its period of oscillation is reduced from that of the *in vacuo* period. As $\bar{U}$ is increased from zero, see figures 5.1(c) and (d), total energy, E_t, begins to fall as the free stream has a damping effect on the amplitude of the flexible surface's oscillation. To explain this damping mechanism, the following proposition is provided: If only the hydrodynamic stiffness component of the fluid pressure was calculated in the unsteady fluid-structure interaction, fluid pressure would then be proportional to flexible surface curvature and therefore ninety degrees out of phase with flexible surface velocity, as was described in §2.1.2. However, owing to the hydrodynamic damping and inertia of the fluid, the effect of the finite length of the flexible surface and the influence of viscous effects captured by the leading-edge singularity and the trailing edge Kutta condition, this phase difference is altered. To investigate the damping mechanism of the fluid, the total fluid work done on the flexible surface at a particular time t_p, $W(t_p)$ $(= \int_0^{t_p} \dot{W}(t)dt)$, at $\bar{U} = 0.28$ is plotted, see figure 5.2; in addition, the total fluid work done on the upstream and downstream halves of the flexible surface are also plotted in the same figure. The plot shows that at this particular $\bar{U}$ there is negative work being done by the fluid on the entire length of the flexible surface; therefore the phase difference between the fluid pressure and the flexible surface velocity is now less than ninety degrees, causing destructive interference between the two and generating the observed damping of the flexible surface motion. (*N.B.* Graphs depicting the total fluid work done can appear to show that negative fluid work is being done when the fluid-structure system is in a steady or unstable state as the area under the graph is negative. This negative area owes to the total fluid work done being cumulatively integrated in

time and in some cases the initial fluid work done is negative and obstructs the motion of the flexible surface. Therefore, it is not the area under the graph but the gradient of the total fluid work done trend that signifies the polarity of fluid work done, a positive gradient indicating positive work.) As further illustration of the damping mechanism and to allow comparison with other fluid-structure interaction described throughout this chapter, figure 5.3 is plotted which shows the magnitude of the fluid pressure and its phase with the flexible surface velocity at different mass points along the flexible surface at $\bar{U} = 0.28$. In figures 5.4(a) and (b) it is shown that as $\bar{U}$ is increased further (therefore also increasing fluid pressure) the damping of the flexible surface oscillation amplitude is also increased. However, as the value of $\bar{U}$ is further increased and approaches U_c, see figures 5.4(c) and (d), the initial fall in E_t ceases and it varies about a constant value; the fluid now has a neutral effect on the oscillation of the flexible surface; the flexible surface again oscillates in a steady state. In figure 5.4(c), the result of §4.4.2 is reshown; using the known eigenmodes detailed in §3.1.3 the energy in the first two modes were calculated to be 33% and 63% respectively, the former evident from the necking at the downstream node point of oscillation. The frequency of the steady state, f, is 3.1×10^{-2} Hz, a fall of 35% from the *in vacuo* oscillation frequency. The author notes that dimensional comparison of frequencies is made as there is no fluid density in the *in vacuo* case and so its value of frequency cannot be non-dimensionalised. The author further notes that the small sizes of oscillation frequency owe to the flexible surface properties selected to achieve a unit value of $\bar{L}$. Above U_c, see figure 5.5, the fluid has a destabilising effect causing the flexible surface to enter into an unstable oscillation; this oscillation is identified as unstable as there is a sustained growth of E_t over the time period of the numerical experiment. As $\bar{U}$ is increased further above U_c, the oscillation increases in amplitude *ad infinitum*. The mechanism by which the fluid and structure interact to cause the observed unsteady oscillation is related to a particular instability type; the unstable oscillation in figure 5.5 is caused by a flutter instability because in this case the introduction of damping raises the value of U_c. The severity of the flutter instability is measured by the instability growth rate (non-dimensional power), $\dot{E}_t$; this is calculated by measuring the gradient of the linear trend generated by plotting the

logarithms of E_t and t (at a value of $\bar{U}$ 0.004% above U_c) when the fluid-structure system has settled into a steadily growing oscillation. The calculated value for $\dot{E}_t$ is 0.084; this value is useful when considered relative to values of $\dot{E}_t$ for other instabilities and is thus of more significance in the following sections. To investigate the mechanism of the flutter instability the total fluid work done on the flexible surface at U_c and $\bar{U} = 6.0$ is plotted, see figure 5.6. The figure shows that although the total fluid work done on the downstream half of the flexible surface defines the overall form of W, transmission of energy into the upstream half of the flexible surface drives the instability, the singularity at the leading edge causing the required increase in phase difference between the wall velocity and fluid pressure. Further illustration of the flutter mechanism is shown in figure 5.7 where, similarly to figure 5.3, the magnitude of the fluid pressure and its phase with the flexible surface velocity is plotted for different mass points along the flexible surface, this time at $\bar{U} = 5.474$ ($\bar{U}$ at 0.004% above U_c). As previously noted, at $\bar{H} = 1$ channel walls have no effect on the pressure distribution over the flexible surface. This knowledge combined with the result showing an upstream driving mechanism to the instability, shows that this instability is similar to *Huang flutter* as described by Huang (1995) and has correspondence with the viscous results of Balint and Lucey (2005), good agreement between the models made possible because of the low mass ratio and therefore flexible-surface forces are far greater than fluid forces. The trend of U_c in the range $0 \leq \bar{L} \leq 1$ is comparable to the results of Huang, see figure 5.8, but not quantitatively as Huang uses a different form of non-dimensional velocity. Both sets of results show an asymptote of U_c to infinity as $\bar{L}$ is decreased, flexible-surface forces increasing relative to fluid forces. Also, as $\bar{L}$ is increased both sets of results show that U_c tends to a constant or rising value rather than a decreasing one, showing that although the fluid forces are increasing relative to the flexible-surface forces, this has no significant effect on the flutter mechanism. Good agreement between the two models lends further confidence to the theoretical approaches used and to the results obtained.

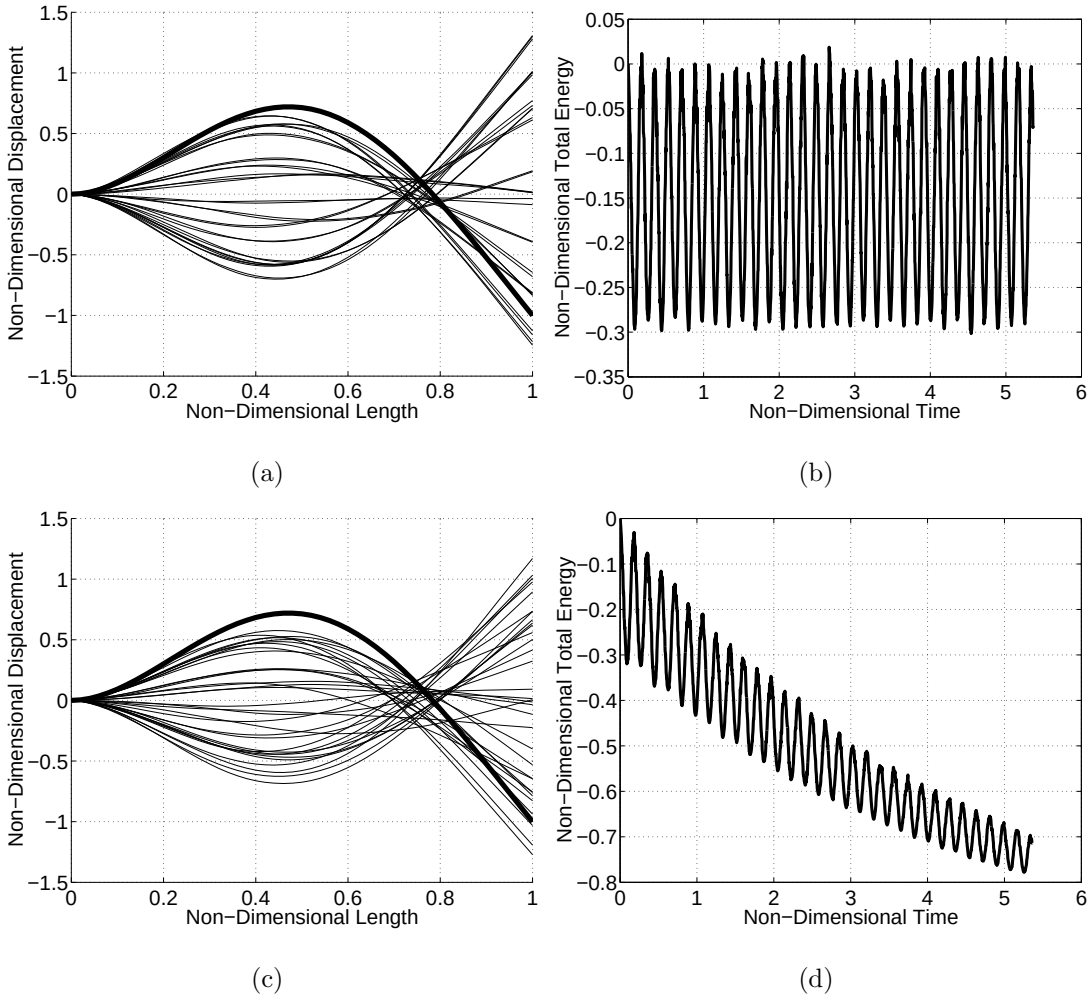

Figure 5.1: Fluid-structure behaviour where (a) and (c) depict the oscillation of the flexible surface (the thick line is the initial deflection) and (b) and (d) are the respective total energies expended: in (a) and (b), $\bar{U} = 0.0$; in (c) and (d), $\bar{U} = 0.28$; $\bar{L} = 1$, $\bar{H} = 1$, fifty mass points, initial deflection is the second eigenmode.

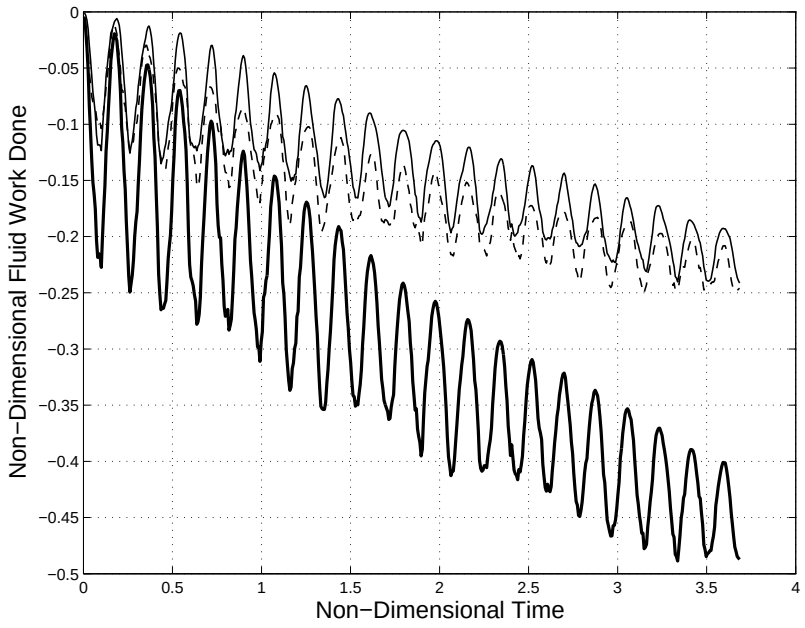

Figure 5.2: Total fluid work done on the whole flexible surface and also on its upstream and downstream halves over a period of several oscillations: −(thin) total fluid work done on upstream half of plate ($\int_0^{t_p} \dot{W}_u(t)dt$), −− total fluid work done on downstream half of plate ($\int_0^{t_p} \dot{W}_d(t)dt$), −(thick) total fluid work done ($\int_0^{t_p} (\dot{W}_u(t) + \dot{W}_d(t))dt$); $\bar{U} = 0.28$, $\bar{L} = 1$, $\bar{H} = 1$, fifty mass points, initial deflection is the second eigenmode.

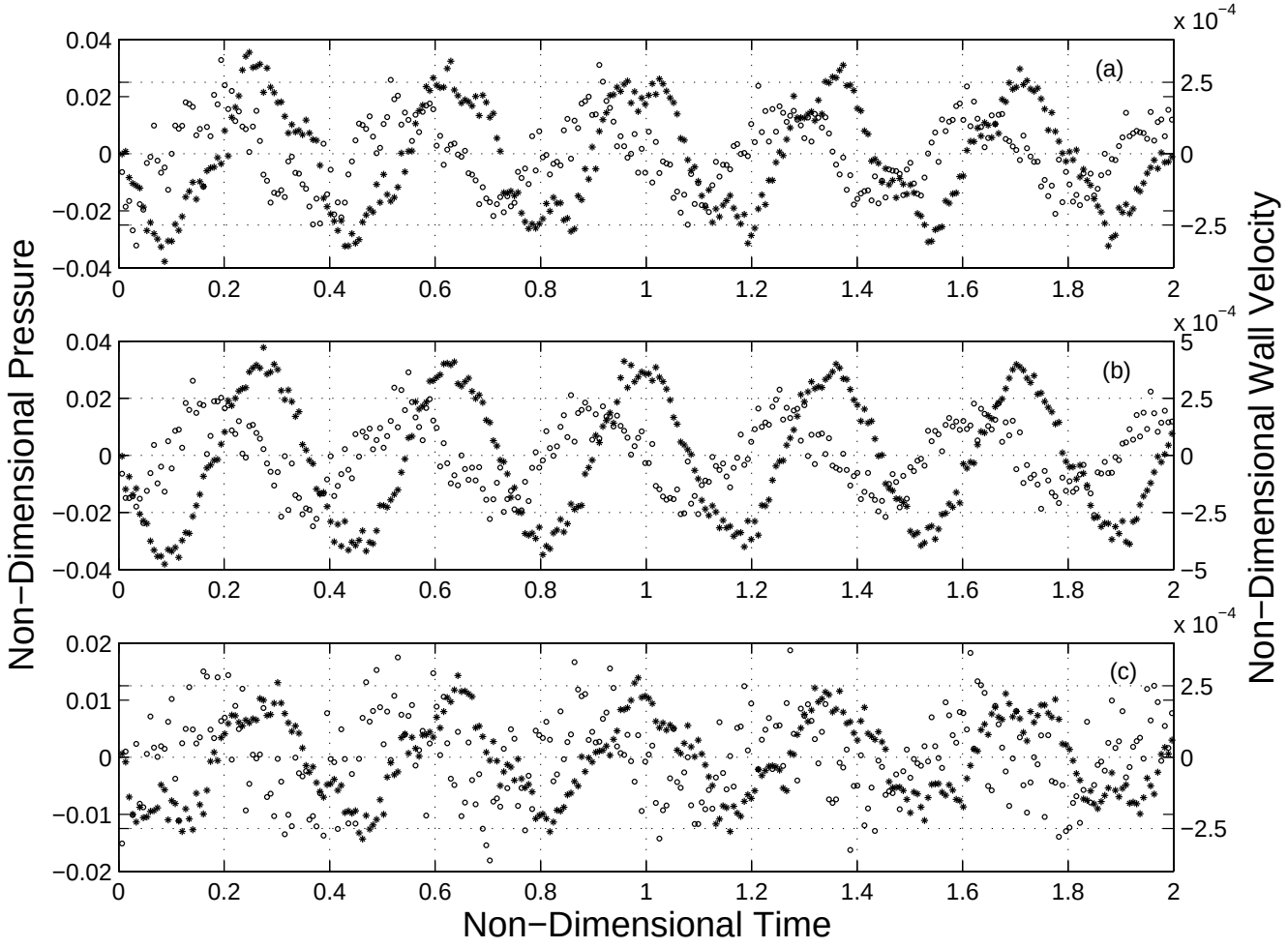

Figure 5.3: Values of non-dimensional flexible-surface velocity and fluid pressure in time at selected mass-points along the flexible-surface length: $\circ$ pressure value, $*$ flexible-surface velocity value; (a) mass-point values at $0.3L$, (b) mass-point values at $0.5L$, (c) mass-point values at $0.7L$; $\bar{U} = 0.28$, $\bar{L} = 1$, $\bar{H} = 1$, fifty mass points, initial deflection is the second eigenmode.

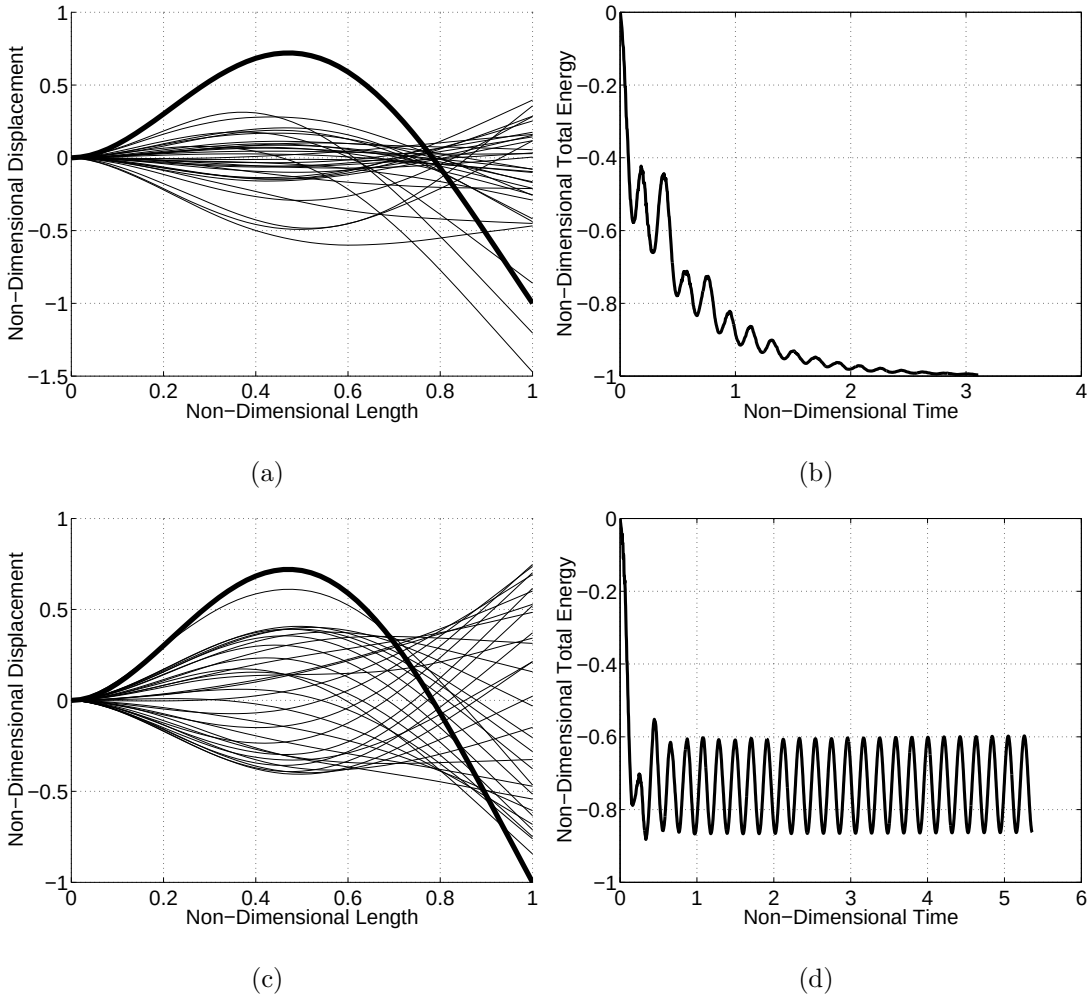

Figure 5.4: Fluid-structure behaviour where (a) and (c) depict the oscillation of the flexible surface (the thick line is the initial deflection) and (b) and (d) are the respective total energies expended: in (a) and (b), $\bar{U} = 2.75$; in (c) and (d), $\bar{U} = 5.452$; $\bar{L} = 1$, $\bar{H} = 1$, fifty mass points, initial deflection is the second eigenmode.

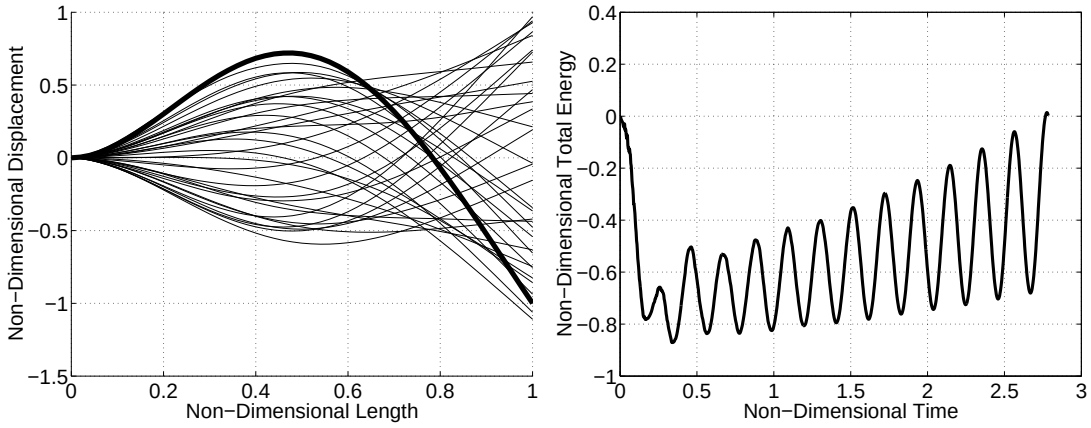

(a) (b)

Figure 5.5: Fluid-structure behaviour where (a) depicts the oscillation of the flexible surface (the thick line is the initial deflection) and (b) is the total energy expended: $\bar{U} = 5.51$, $\bar{L} = 1$, $\bar{H} = 1$, fifty mass points, initial deflection is the second eigenmode.

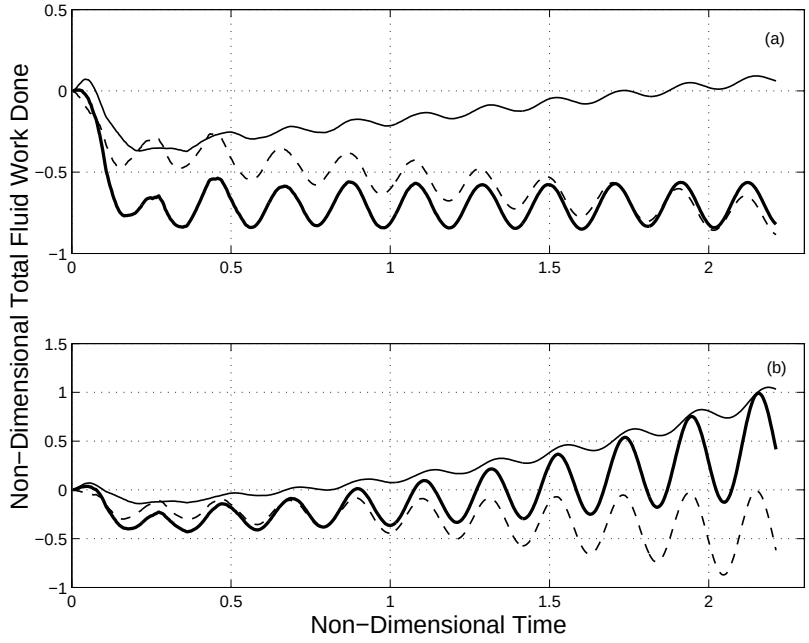

Figure 5.6: Total fluid work done on the whole flexible surface and its upstream and downstream halves over a period of several oscillations: −(thin) work done on upstream half of plate ($\int_0^{t_p} \dot{W}_u(t)dt$), −− work done on downstream half of plate ($\int_0^{t_p} \dot{W}_d(t)dt$), −(thick) total work done ($\int_0^{t_p} (\dot{W}_u(t) + \dot{W}_d(t))dt$); (a) $\bar{U} = U_c = 5.452$, (b) $\bar{U} = 6.0$; $\bar{L} = 1$, $\bar{H} = 1$, fifty mass points, initial deflection is the second eigenmode.

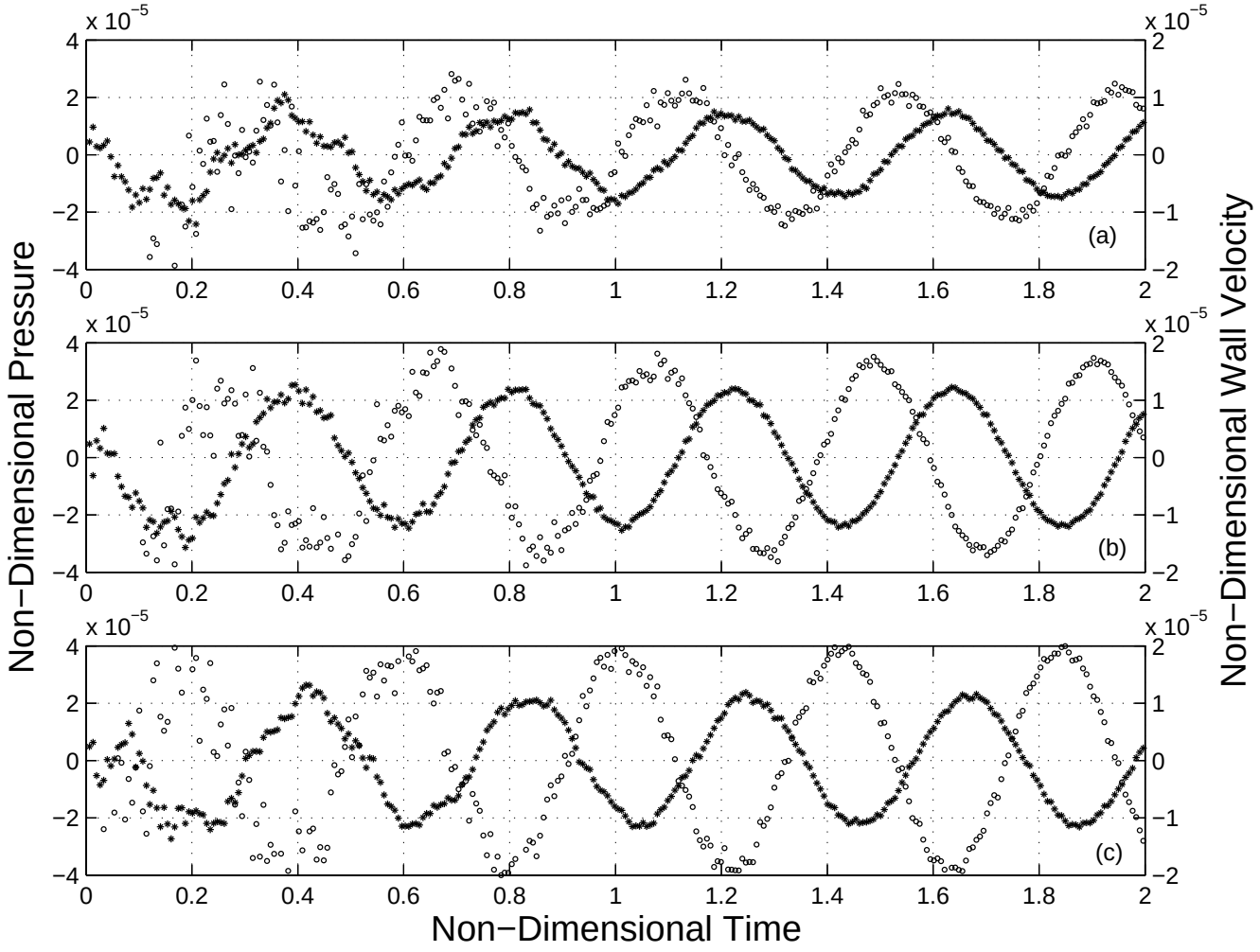

Figure 5.7: Values of non-dimensional flexible-surface velocity and fluid pressure in time at selected mass-points along the flexible-surface length: ∘ pressure value, ∗ flexible-surface velocity value; (a) mass-point values at $0.3L$, (b) mass-point values at $0.5L$, (c) mass-point values at $0.7L$; $\bar{U} = 5.474$, $\bar{L} = 1$, $\bar{H} = 1$, fifty mass points, initial deflection is the second eigenmode.

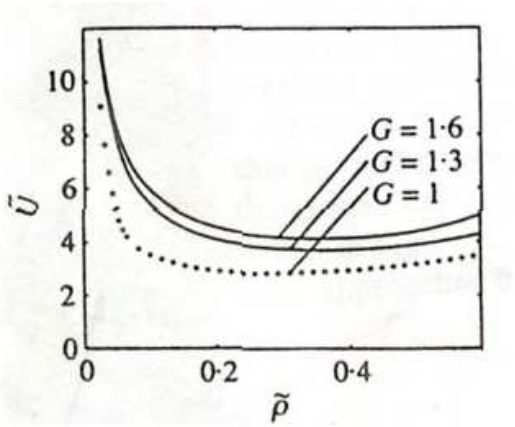

(a) From Huang (1995) ($\tilde{\rho} = 0.5\bar{L}$).

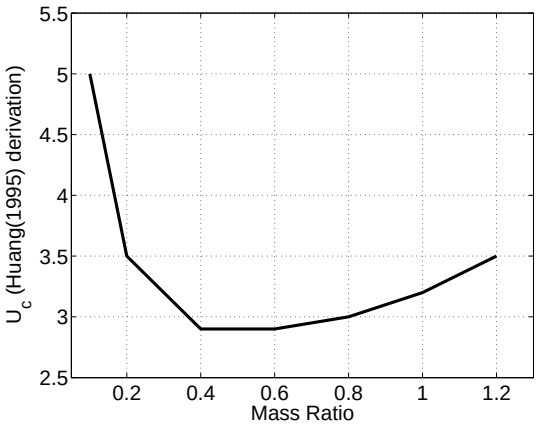

(b) Adapted from Huang (1995).

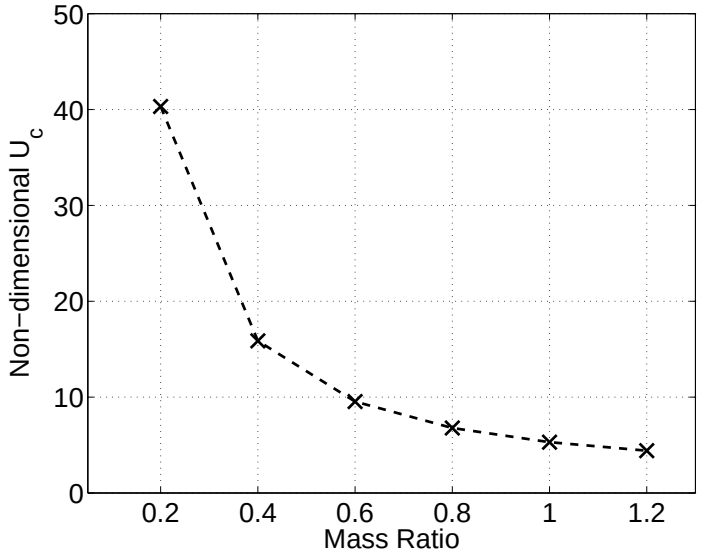

(c) Present model.

Figure 5.8: Trend of non-dimensional U_c for range of $\bar{L}$. Note that Huang's derivation of $\bar{U}$ is different to that presented in this thesis. In (a), G is growth rate with $G = 1$ equivalent to the steady state. In (b), the line $G = 1$ is replotted.

5.1.2 Effect of Unsteady Model Variations

Initially, the effect of the introduction of the vorticity model, validated in §4.3, on the case at $\bar{L} = 1$ studied in the previous sub-section is assessed. The set-up for the present case was described in §3.3.2. In the first experiment the maximum number of blobs that could be retained was modelled (owing to computational restrictions, the maximum number of blobs that could be modelled was 2000, the blob furthest away from the flexible surface being deleted as a new blob was introduced when this maximum was reached). The effect of the shed vorticity model was to slightly dampen the fluid-structure system and thus to cause a small drop in U_c; there was no affect on the instability mechanism or critical mode shape. The dampening phenomenon could occur due to the blob strengths having opposite polarity to the total vorticity of the flexible-surface: When the flexible surface has a cambered shape, similar to the camber line of an aerofoil (as with the second eigenmode), the shed vortices forced the flexible surface towards the horizontal datum, thus dampening the motion. This effect would be the opposite on a first-eigenmode initial deflection. In the second experiment it was possible to capture all the shed vortices by summing the change in bound vorticity over one hundred time steps before releasing a blob (the numerical experiment was run over thirty-thousand time-steps and thus the blobs did not reach the 2000 blob maximum; also, some of the blobs would be deleted as they convected past the cut off length ($L_{cut} = 2L$)). The effect of the shed vorticity in this case was the same on U_c but a drop in the fluid work done was observed, see figure 5.9; as no damping was being applied to the flexible surface, the shed vorticity had thus developed a positive fluid-dampening mechanism. Before assessing the meaning of these results, it is noted that the effect of a large part of the shed vorticity is already captured by the enforced Kutta condition; this shed-vorticity model captures the final component of the shed vorticity owing to the change in bound vorticity as the flexible surface moves. Therefore, the results show that the Kutta condition is a good approximation for the effect of shed vorticity as the effect of the change of bound vorticity that it does not capture in the unsteady case (for linear deflections) is small. A summary of the effects of other variations to the unsteady model parameters on the case at $\bar{L} = 1$ studied in

the previous sub-section are recorded in table 5.1, showing values for U_c, f and $\dot{E}_t$. The values found in the previous sub-section are recorded in the second row of the table. Initially consider the effect of channel walls at $\bar{H} = 0.1$. The new steady-state oscillation

Simulation	U_c	f(Hz)	$\dot{E}_t$
in vacuo	–	4.7×10^{-2}	–
isolated case	5.452	3.1×10^{-2}	0.084
$\bar{H} = 0.1$	5.066	3.1×10^{-2}	0.065
Rigid central-surface, $\bar{H} = 1$	13.22	7.7×10^{-2}	0.740
Rigid central-surface, $\bar{H} = 0.1$	12.28	7.1×10^{-2}	0.360
Stiffness doubled	5.452	4.6×10^{-2}	0.052
Stiffness gradient	6.058	3.6×10^{-2}	0.084
Unit Damping	5.948	3.1×10^{-2}	0.037
Damping gradient	6.058	3.1×10^{-2}	0.110

Table 5.1: Values of U_c, f and $\dot{E}_t$ for observed flutter instabilities determined via numerical experiment for flow-structure interaction of a cantilevered flexible surface embedded in a potential flow for different unsteady model variations; $\bar{L} = 1$, fifty mass points, initial deflection was the second eigenmode.

occurred at a lower U_c, see table 5.1, signifying the destabilising influence of the walls and is of a similar frequency. As the fluid pressure is reduced relative to the isolated case, this has the knock-on effect that $\dot{E}_t$ of the instability is also reduced. The critical mode, see figure 5.10(a), has a wider downstream neck than in the isolated case, see figure 5.4(c). Above U_c, the flexible surface again lost stability owing to flutter; figure 5.10(b) shows that the instability mechanism is now a combination of upstream and downstream fluid work, as opposed to the solely upstream mechanism seen previously in figure 5.6(b). Also, comparing mass point fluid-pressure values with the isolated case at 0.004% above U_c, see figures 5.11 and 5.7, shows that the pressure on the downstream end of the flexible surface has increased. As the walls are affecting the instability mechanism, via the Bernoulli effect, this is therefore *channel flutter* similar to that described by Aurégan

and Depollier (1995) and Guo and Païdoussis (2000). Now consider the effect of a rigid central surface (equal in length to the flexible surface) placed upstream and adjacent to the flexible surface for $\bar{H} = 1$ and 0.1. For both channel-wall geometries, U_c is very much higher than that of the isolated case, see table 5.1, as the system has become more stable owing to the smaller influence of the singularity at the leading edge; the channel walls are again destabilising, this effect manifesting itself as a lower U_c for the $\bar{H} = 0.1$ case. The large increase in U_c has the knock-on effect that $\dot{E}_t$ and f of the observed instabilities is far greater for both cases than the isolated case, see table 5.1, owing to the greater fluid pressure. Also for both cases the critical mode has changed shape, shown in figures 5.12(a) and (c) for $\bar{H} = 1$ and 0.1 respectively, incorporating a greater proportion of higher-order eigenmodes in the deflection than seen in the isolated case, see figure 5.4(c). Pre-empting the results of §5.3.1, as $\bar{L}$ increases the critical mode shape is constituted by eigenmodes of higher order. The increase in the order of the critical mode shape therefore signifies that the introduction of a rigid central surface is equivalent to an increase in $\bar{L}$ and also that as $\bar{L}$ increases, the effect of flexible-surface curvature begins to outweigh the effect of the leading-edge singularity. Also in both cases, a flutter instability is seen again above U_c with an upstream driven mechanism, see figures 5.12(b) and (d), similar to the isolated case, see figure 5.6(a). Therefore the $\bar{H} = 0.1$ case differs from the $\bar{H} = 0.1$ case with no rigid central surface which is half upstream and half downstream driven, see figure 5.10. The effect of walls is seen, however, by comparing mass-point fluid-pressure values for $\bar{H} = 1$ and 0.1 cases at 0.004% above U_c, shown in figures 5.13 and 5.14 respectively, where the walls have made the fluid pressure larger along the length of the flexible surface in the $\bar{H} = 0.1$ case. Now consider the effect of variation of flexible-surface damping and stiffness on an isolated flexible surface. Initially two experiments are carried out, the first with the stiffness doubled and the second with a unit value of $\bar{d}$ introduced. In both cases, instability manifestation and mechanism are unchanged from the isolated case; both variations have stabilising effects manifested as reductions in $\dot{E}_t$ for the stiffness case and U_c for the damping case, see table 5.1. As expected the increase in stiffness raised the steady state frequency. When damping is introduced, a narrow band of velocities for which the unsteady model oscillates in a

steady state is observed, with an upper and lower U_c. Two further experiments are now carried out where stiffness and damping properties are varied linearly from the leading edge along the flexible surface; in the first experiment stiffness was varied as $\frac{3}{2}B \rightarrow B$ (B retaining the value used throughout this chapter thus far) and in the second damping was varied as $\frac{3}{2}\bar{d} \rightarrow \bar{d}$ where $\bar{d} = 1$. Of major note in these experiments is the observation that at U_c, E_t is constant but W is rising as no account is made of the total energy dissipated by the fluid at a particular time t_p, $D(t_p)$ $(= \int_0^{t_p} \dot{D}(t)dt)$; these values for both cases are depicted in figure 5.15. In the case of varying B there is no value of $\bar{d}$ to calculate D; therefore the energy dissipated owes to *flexural damping*. Also, the stiffness gradient caused the value of $\dot{E}_t$ to return to that of the original experiment whereas the damping gradient increased $\dot{E}_t$, see table 5.1. Finally the effect of varying $\bar{U}$ in time on the trend of E_t at U_c for the isolated case at $\bar{L} = 1$, shown again in figure 5.16(a), is investigated. To assist in the determination of the effects of the unsteady free stream, the variation of $\bar{U}$ is initiated when the flexible surface has approximately settled into a steady-state oscillation at $\bar{t} = 0.7$. It is noted that the angular frequencies of oscillation for the flexible surface and E_t for this case are 0.2 rad/s and 0.4 rad/s respectively. For these numerical experiments, it is chosen to vary $\bar{U}$ sinusoidally around U_c, initially with the same frequency of oscillation as that of the flexible-surface steady-state oscillation and with an amplitude of 20% of U_c. As shown in figure 5.16(b), an instability is not initiated for the chosen parameters and a periodic increase then decrease in E_t occurred. However, at twice the oscillation frequency of the flexible-surface (and thus at the same frequency of oscillation of E_t), figure 5.16(c) shows that an unstable oscillation is induced. At four times the oscillation frequency of the flexible surface, see figure 5.16(d), the unstable oscillation is still present but its severity has been reduced.

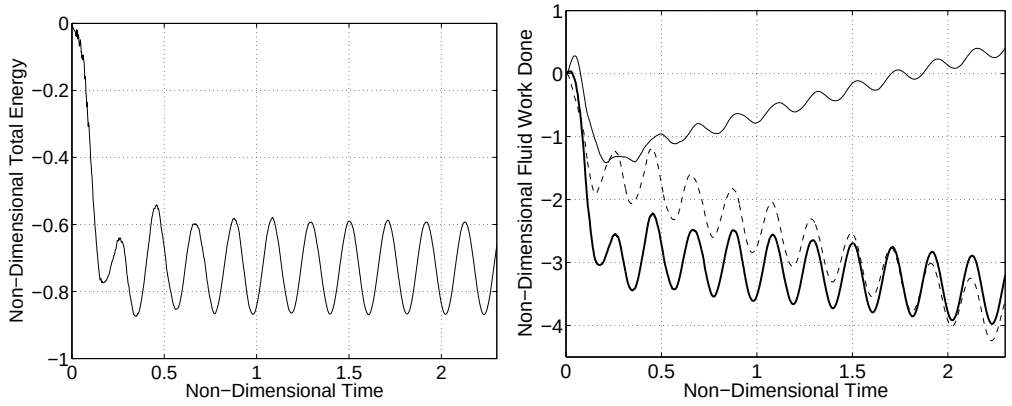

(a) (b)

Figure 5.9: Fluid-structure behaviour at critical velocity where (a) is the total energy expended and (b) is the total fluid work done on the whole flexible surface and also on its upstream and downstream halves: −(thin) total fluid work done on upstream half of plate ($\int_0^{t_p} \dot{W}_u(t)dt$), −− total fluid work done on downstream half of plate ($\int_0^{t_p} \dot{W}_d(t)dt$), −(thick) total fluid work done ($\int_0^{t_p} (\dot{W}_u(t) + \dot{W}_d(t))dt$); $\bar{U} = 5.452$ with shed vorticity included, $\alpha_m = 5.94 \times 10^{-4}$; $\bar{L} = 1$, fifty mass points, initial deflection is the second eigenmode.

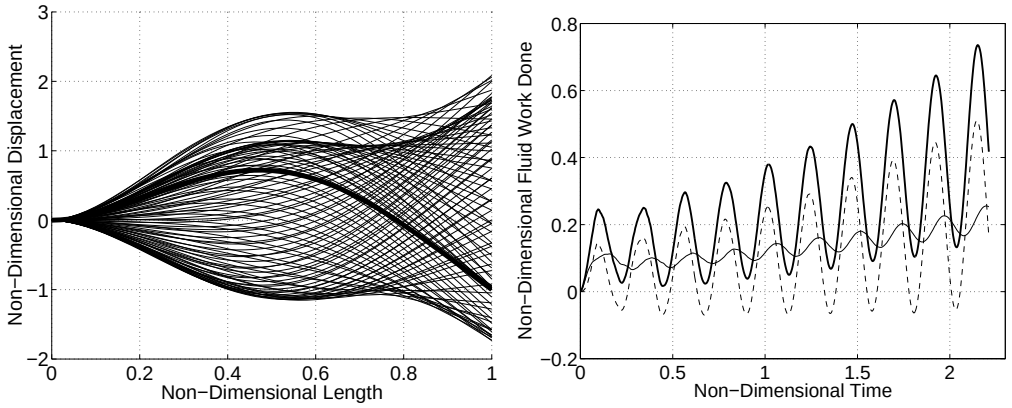

(a) (b)

Figure 5.10: Fluid-structure behaviour where (a) depicts the oscillation of the flexible surface (the thick line is the initial deflection) at the critical velocity and (b) is the total fluid work done on the whole flexible surface and also on its upstream and downstream halves: see figure 5.9 for description; in (a) $\bar{U} = 5.066$; in (b) $\bar{U} = 5.573$; $\bar{L} = 1$, $\bar{H} = 0.1$, fifty mass points, initial deflection is the second eigenmode.

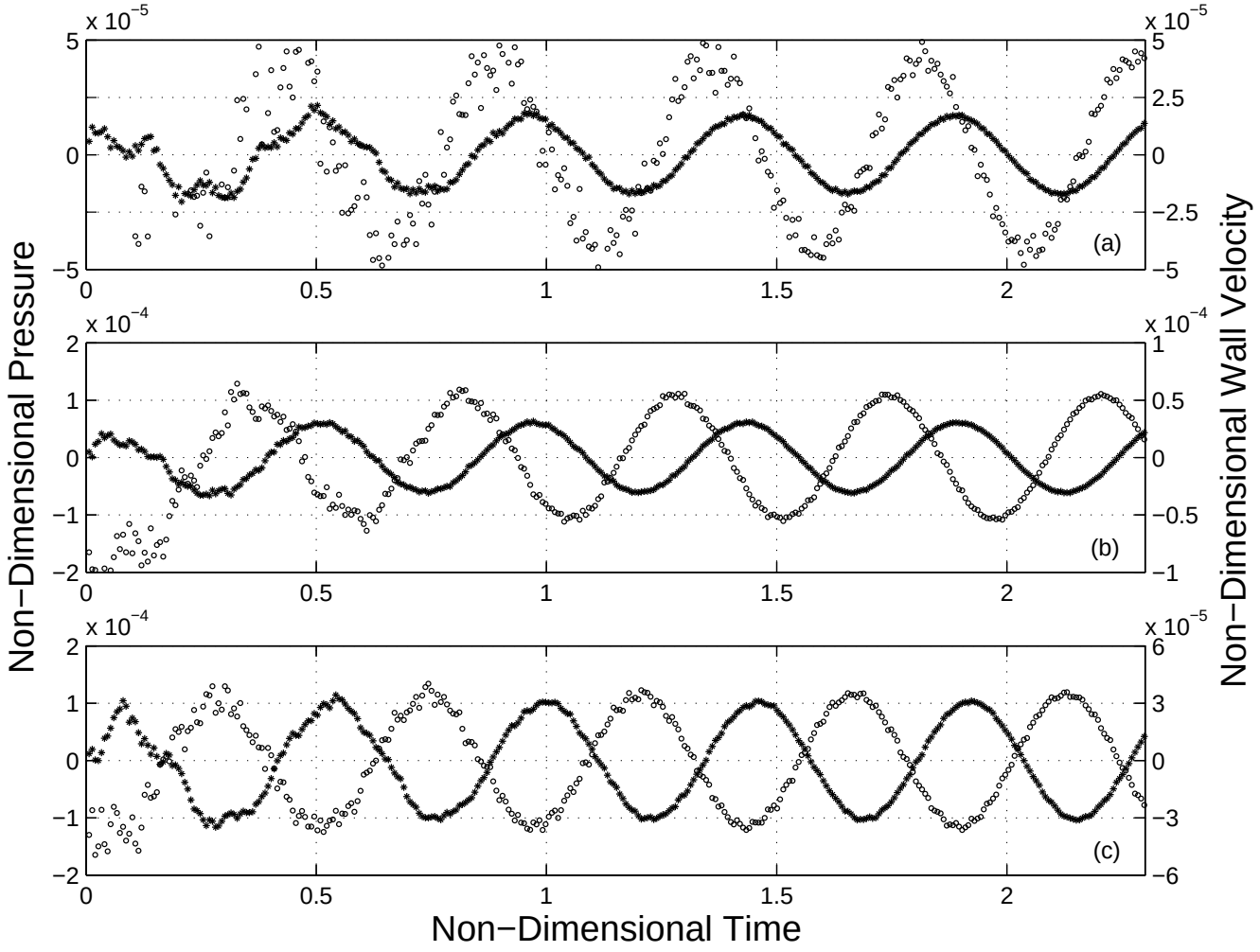

Figure 5.11: Values of non-dimensional flexible-surface velocity and fluid pressure in time at selected mass-points along the flexible-surface length: ∘ pressure value, ∗ flexible-surface velocity value; (a) mass-point values at $0.3L$, (b) mass-point values at $0.5L$, (c) mass-point values at $0.7L$; $\bar{U} = 5.086$, $\bar{L} = 1$, $\bar{H} = 0.1$, fifty mass points, initial deflection is the second eigenmode.

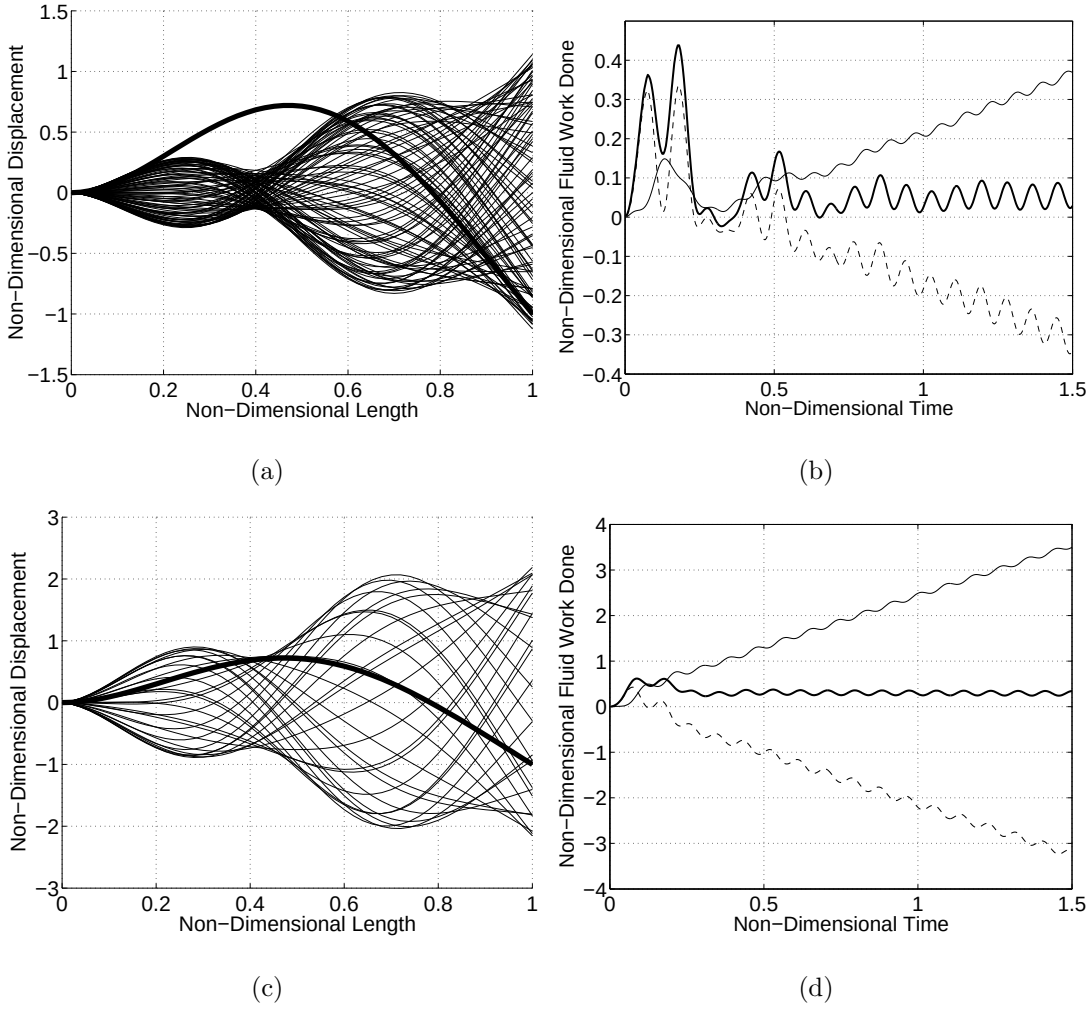

Figure 5.12: Fluid-structure behaviour at critical velocity where (a) and (c) depict the oscillation of the flexible surface (the thick line is the initial deflection; early oscillations have been removed to provide a clearer view of the critical modes) and (b) and (d) are the total fluid work done on the whole flexible surface and also on its upstream and downstream halves: −(thin) total fluid work done on upstream half of plate ($\int_0^{t_p} \dot{W}_u(t)dt$), −− total fluid work done on downstream half of plate ($\int_0^{t_p} \dot{W}_d(t)dt$), −(thick) total fluid work done ($\int_0^{t_p} (\dot{W}_u(t)+\dot{W}_d(t))dt$); (a) and (b) $\bar{U} = 13.22$, $\bar{H} = 1$; (c) and (d) $\bar{U} = 12.28$, $\bar{H} = 0.1$; $\bar{L} = 1$, rigid central-surface, fifty mass points, initial deflection is the second eigenmode.

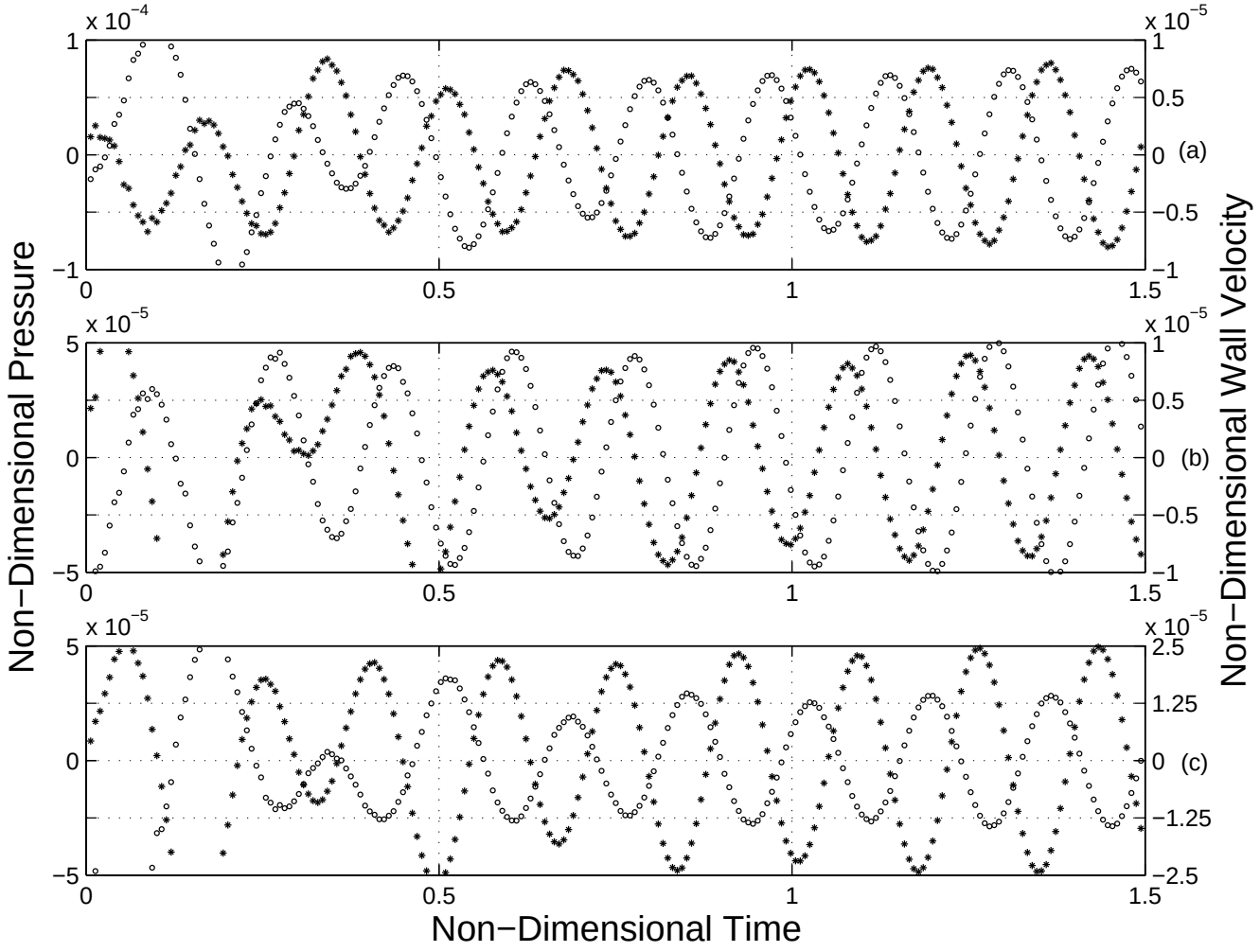

Figure 5.13: Values of non-dimensional flexible-surface velocity and fluid pressure in time at selected mass-points along the flexible-surface length: ∘ pressure value, ∗ flexible-surface velocity value; (a) mass-point values at $0.3L$, (b) mass-point values at $0.5L$, (c) mass-point values at $0.7L$; $\bar{U} = 13.27$, $\bar{L} = 1$, $\bar{H} = 1$, rigid central-surface, fifty mass points, initial deflection is the second eigenmode.

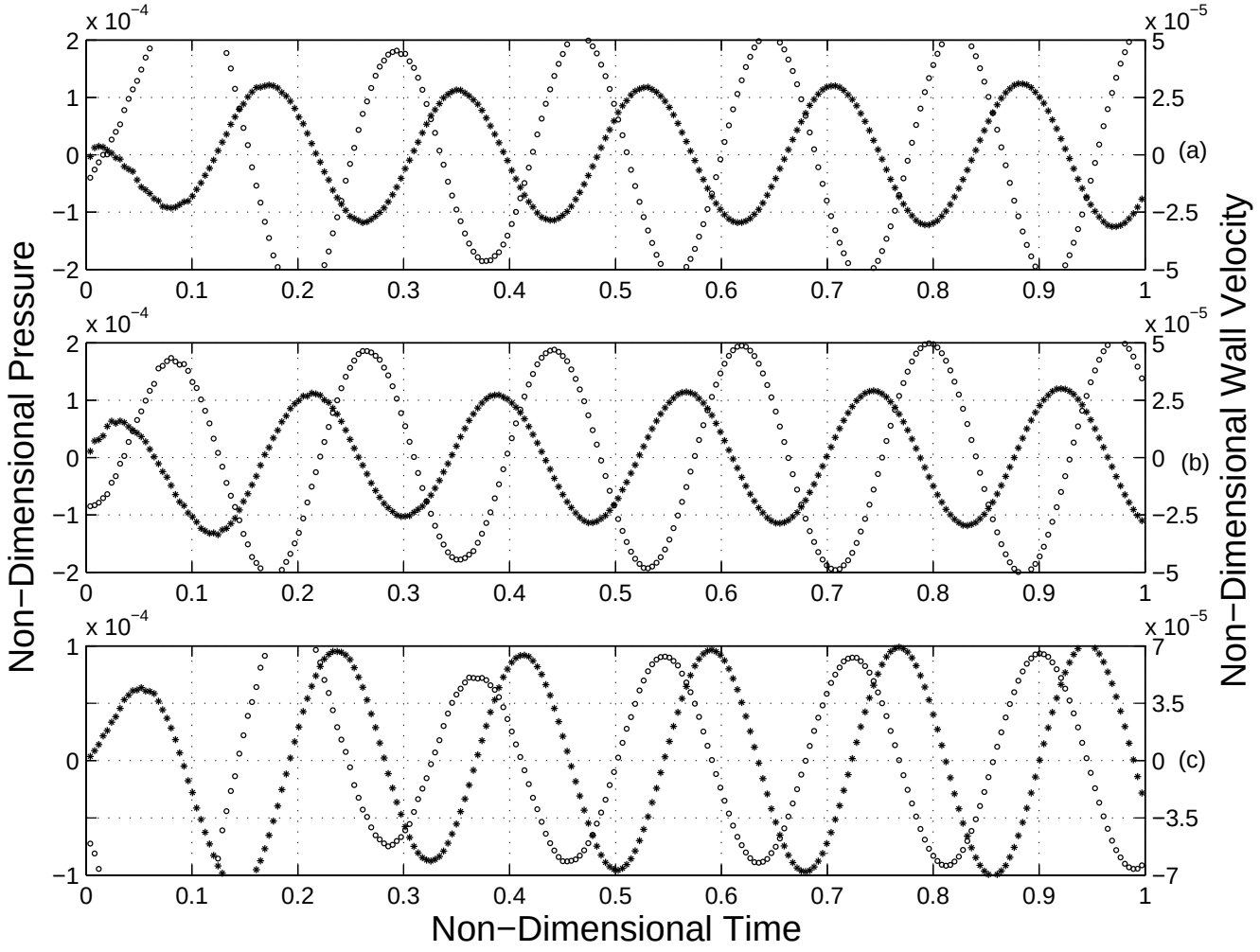

Figure 5.14: Values of non-dimensional flexible-surface velocity and fluid pressure in time at selected mass-points along the flexible-surface length: ∘ pressure value, ∗ flexible-surface velocity value; (a) mass-point values at $0.3L$, (b) mass-point values at $0.5L$, (c) mass-point values at $0.7L$; $\bar{U} = 12.33$, $\bar{L} = 1$, $\bar{H} = 0.1$, rigid central-surface, fifty mass points, initial deflection is the second eigenmode.

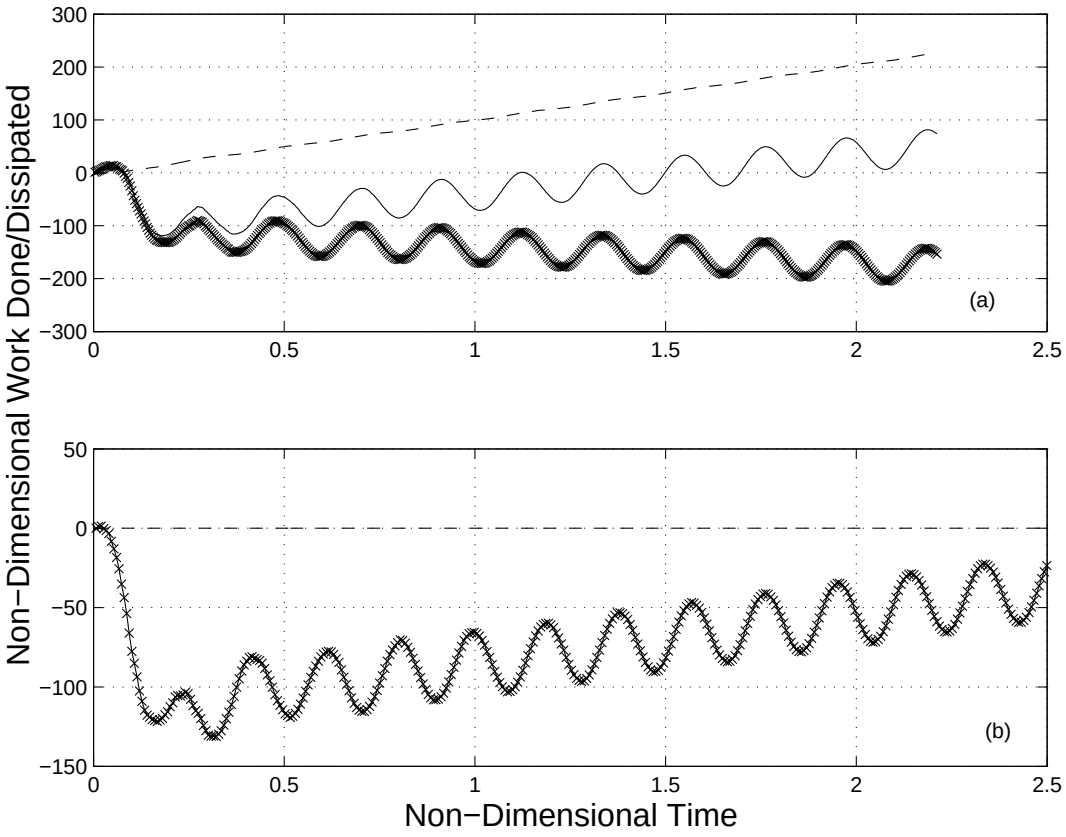

Figure 5.15: Effect of stiffness and damping distributions on the total work done by the fluid on the flexible surface: $-$ total fluid work done on flexible surface $W(t_p)$ $(= \int_0^{t_p} \dot{W}(t)dt)$, $--$ total energy dissipated by the flexible surface $D(t_p)$ $(= \int_0^{t_p} \dot{D}(t)dt)$, $\times$ overall work done $(= \int_0^{t_p} (\dot{W}(t) - \dot{D}(t))dt)$; (a) Damping gradient $(\frac{3}{2}\bar{d} \rightarrow \bar{d}$ where $\bar{d} = 1)$, (b) Stiffness gradient $(\frac{3}{2}B \rightarrow B)$; $\bar{U} = 6.058$, $\bar{L} = 1$, fifty mass points, initial deflection is the second eigenmode.

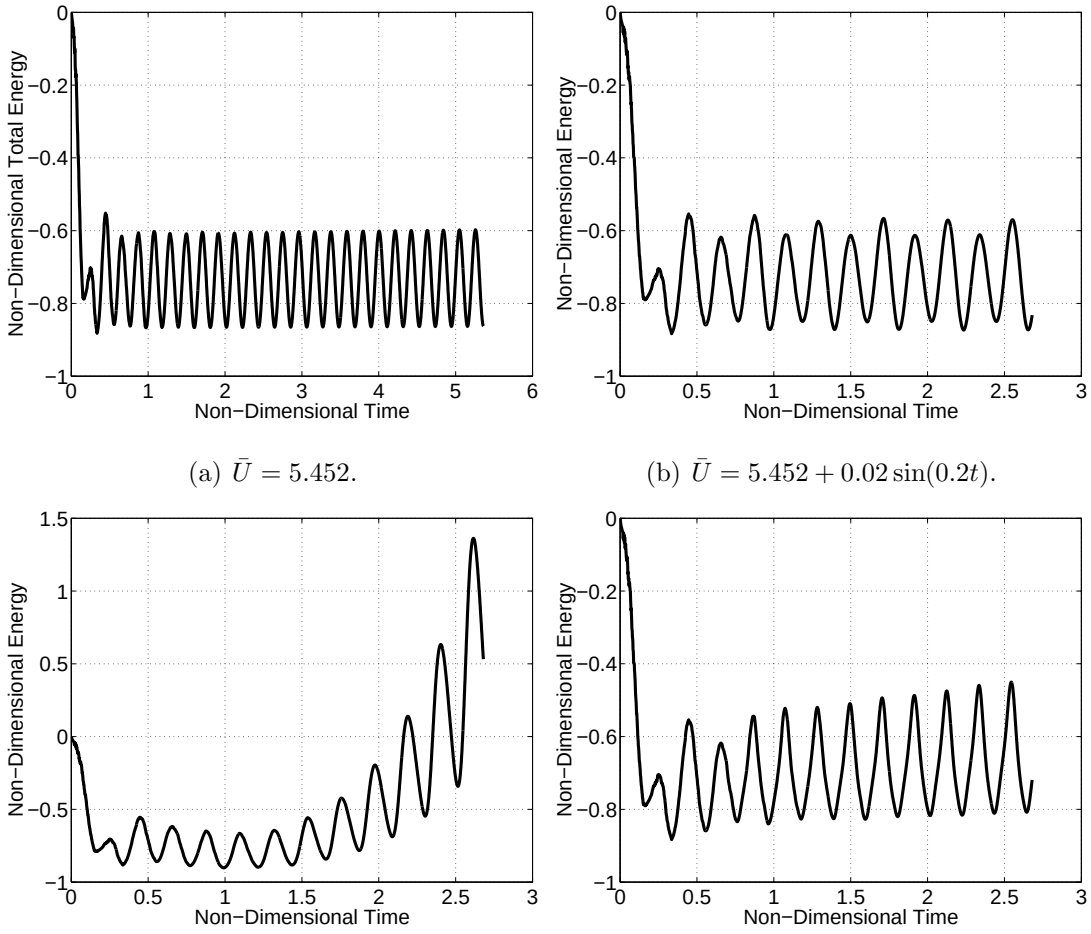

(a) $\bar{U} = 5.452$.

(b) $\bar{U} = 5.452 + 0.02\sin(0.2t)$.

(c) $\bar{U} = 5.452 + 0.02\sin(0.4t)$.

(d) $\bar{U} = 5.452 + 0.02\sin(0.8t)$.

Figure 5.16: Plots of total energy against time showing the effect of unsteady mean flow initiated at $\bar{t} = 0.7$; $\bar{L} = 1$, $\bar{H} = 1$, fifty mass points, initial deflection is the second eigenmode.

5.2 Snore Modelling

The results of numerical experiments that, it is proposed, elucidate information pertaining to the manifestation and mechanism of three types of snore are now presented. Recapping the snoring description presented in the introduction, as one inspires the inspiratory flow velocity, $\underline{U}_\infty$, increases. This leads to increased Re and hence increasingly perturbed flow through the pharyngeal region. Subsequently, pressure fluctuates rapidly and initiates flow-induced structural instabilities (FISI) within the soft tissues. At a critical flow velocity, U_c, these tissue vibrations are strong enough to be manifest as the sound of snoring. In this thesis, palatal snoring is modelled and the inviscid, infinite-Re set of numerical experiments presented in this section complements and extends the work of Balint and Lucey (2005) who conducted low-Re numerical experiments studying the snoring phenomenon. These results compared with those of the previous section also give an insight into how fluid-structure interactions are modified over a small range of mass ratio.

5.2.1 Physical Properties & Dynamics of the Upper Airway

Physical properties of the flexible surface and flow are chosen to enable modelling of the snoring phenomenon. Initially consider the properties of the flexible surface. Typically, snores have a frequency in the range of 30 Hz to 100 Hz (Gavriely and Jensen, 1993); the aim is to recreate this frequency of oscillation *in vacuo* by varying the properties of the flexible-surface model. The soft palate is approximately 0.0085 m in length. Typical Poisson ratios, ν, for stiff and elastomeric materials are 0.2 and 0.5 respectively with most materials having $\nu = 0.\dot{3}$ (Callister, 1994). The palate is composed of many different tissue types. Park and Lakes (1992) and Berry *et al.* (1999) give elastic properties of human tissues present in the soft palate; collagen has an elastic modulus, E, of approximately 1000 MPa with other tissue types having values over a range of 1 MPa to 10^{-5} MPa. As human tissue is a viscoelastic material E increases with rate of loading. Density of human tissue is approximately that of water and the thickness of the soft

palate is approximately 5 mm; this gives a specific mass of 5 kg/m^2. These properties are listed in the second column of table 5.2. When modelling the human upper airway, the authors in Balint and Lucey (2005) used the values listed in the third column of table 5.2, the major difference between the physical case and the numerical model being the specific mass that now has a value of 0.02 kg/m^2. These properties were chosen so that the plate would oscillate at approximately 80 Hz *in vacuo* (when the plate is initially deflected as the second eigenmode); thus when a fluid is introduced, the fluid-structure system should oscillate at values similar to that of average snore frequencies (between $30 - 100$ Hz, see Gavriely and Jensen (1993)). These properties are used in all further numerical experiments in this section. Now consider the flow properties.

Property	Soft Palate	Flexible Surface
Poisson Ratio	$\approx 0.\dot{3}$	$0.\dot{3}$
Elastic Modulus (MPa)	10^{-5} to 1000	880
Density (kg/m^3)	1000	2477
Thickness (m)	0.005	1×10^{-5}
Specific Mass (kg/m^2)	5	0.02

Table 5.2: Human soft-palate properties and those used for the flexible surface in numerical experiments.

Flow rate through the upper airway is dependent upon lung volumes. Tidal volume is the volume of air that moves into and out of the lungs at each breath during normal quiet breathing; this is typically 500 ml (Balint, 2001). Balint and Lucey (2005) note that inspiratory flow rate, Q, varies between 0.0004 m^3/s and 0.0010 m^3/s; when the maximal value of Q is combined with a typical airway hydraulic diameter of 20 mm (half channel height is typically 10 mm) this yields a mean inflow speed of 1.27 m/s. For air, fluid density and kinematic viscosity are respectively 1.2 kg/m^3 and 1.68×10^{-5} m^2/s yielding a typical maximal Re for snoring, based on half channel-height, of 1512. $\bar{L}$ and $\bar{H}$ for the snoring phenomenon are approximately 0.41 and 1.2 respectively. Therefore, flexible surface forces outweigh fluid forces and the channel walls have little effect on the

pressure difference across the soft palate, though it is emphasised that $\bar{H}$ can change drastically during snoring as shall now be intimated. Balint and Lucey (2005) further describe that during inhalation and exhalation, the upper airway and lungs attempt to keep a constant mean value of Q (though Q varies temporally as inspiration begins until mean Q is reached). The throat walls alter cross-sectional area, A, in assisting to keep Q constant during inhalation, $\underline{U}_\infty$ increasing as A decreases (Aurégan and Depollier (1995) note that the tongue and the posterior wall of the pharynx have a typical oscillation period of approximately one second). It should be noted that in some snorers mean Q causes slight collapse of the airway (via the Bernoulli effect) and *flow limitation* to occur, where $\underline{U}_\infty$ continues to increase but with no increase in Q as A continues to reduce (Huang, 1998) (for further description of flow limitation, see Heil and Jensen (2001)). Owing to an enforcement of mean Q and flow limitation, $\underline{U}_\infty$ will increase from start to end of inhalation; it is therefore proposed that in a numerical experiment modelling a snore, the effects of a reduction in A and an increase in $\underline{U}_\infty$ can both be captured by solely increasing $\underline{U}_\infty$ at each time step for the period of inhalation. Aittokallio *et al.* (2001) detail $\underline{U}_\infty$ variations in time for *inspiratory cycles* in humans, typically one inspiration lasting one second over which time $\underline{U}_\infty$ varies from zero to a maximum value with an approximately linear growth rate.

5.2.2 Potential Snores

Three *potential snores* are now modelled. A snore occurs when $\underline{U}_\infty$ passes U_c and is therefore manifested as an unstable oscillation due to a particular type of instability. For the first two types of snore $\underline{U}_\infty$ is kept constant and their properties are recorded in the first two rows of table 5.3. The first type of snore is modelled at $\bar{L} = 0.42$ and $\bar{H} = 1$ with a rigid inlet surface. U_c is 1.45 m/s and $\bar{U}$ has increased from that recorded at $\bar{L} = 1$, compare with table 5.1 and following the trend shown in figure 5.8(c). The critical mode and instability mechanism are shown in figures 5.17(a) and (b) respectively; comparing these with figures 5.12(a) and (b) shows the anticipated lower eigenmode content with lower $\bar{L}$ has occurred and that the upstream driven instability mechanism has remained

unchanged. Furthermore, as the walls have no effect on the instability, this is therefore a snore similar to that identified by Huang (1995) and Balint and Lucey (2005). The second type of snore modelled ($\bar{L} = 0.42$, $\bar{H} = 0.1$) has a critical velocity of 2.34 m/s; again the non-dimensional value of the critical velocity is greater than that at $\bar{L} = 1$. However, at this value of $\bar{L}$ the value of U_c is greater than that of the first snore with $\bar{H} = 1$ showing that the walls have a *stabilising* effect, see table 5.3, compared to having a destabilising effect at $\bar{L} = 1$, see table 5.1. The critical mode shown in figure 5.17(c) has an increased width of neck, similar to figure 5.12(c). However, figure 5.17(d) shows that this snore is *downstream* driven via the constructive interference between flexible surface velocity and fluid pressure at the trailing edge of the flexible surface. This is contrary to the upstream-driven mechanism seen at $\bar{L} = 1$, see figure 5.12(d). This difference is caused by the change in mass ratio *i.e.* the fluid forces are now relatively less than the flexible-surface forces and therefore the singularity at the leading edge has less effect. Therefore, the *aspect ratio* of the channel length relative to the length of the rigid inlet surface has become more important. The downstream forcing mechanism of this second snore is comparable to jumping on a springboard, whereas the upstream forcing mechanism of the first snore is similar to the movement of an unrestricted hosepipe. For the third

Experiment	U_c(m/s)	$\equiv \bar{U}$	f(Hz)	$\dot{E}_t$
Rigid central-surface, $\bar{H} = 1$	1.45	16.4	71.4	0.057
Rigid central-surface, $\bar{H} = 0.1$	2.34	26.5	55.6	0.098
Unsteady $\underline{U}_\infty$, rigid central-surface, $\bar{H} = 0.1$	3.675	42.4	142.9	370.0

Table 5.3: Values of U_c and its equivalent $\bar{U}$, f and $\dot{E}_t$ for observed flutter instabilities determined via numerical experiment for flow-structure interaction of a cantilevered flexible surface embedded in a potential flow for different unsteady model variations; $\bar{L} = 0.42$, fifty mass points, initial deflection was the second eigenmode.

type of snore, unsteady $\underline{U}_\infty$ is applied to model inhalation during sleep for the $\bar{L} = 0.42$ and $\bar{H} = 0.1$ case, the properties of which are shown in the third row of table 5.3. The modelled inhalation lasts for approximately one second, during which time $\underline{U}_\infty$ increases

linearly from zero to a chosen maximum velocity. Therefore, a critical *snore gradient* is found; this is the maximum velocity gradient in time at which the flexible surface is still stable at the end of inhalation, *i.e.* just before a snore occurs. Consequently, as $\underline{U}_\infty$ is increased from zero to the chosen maximum value the whole range of phenomena described in §5.1.1 occur. Therefore before instability onset, flexible-surface velocity and fluid pressure approach zero, as shown in figure 5.18 that depicts the behaviour over the period that culminates in the end of one inhalation, owing to the flexible surface motion being damped by the fluid, similar to the fluid damping phenomenon observed in figure 5.4(a), and fluid pressure being proportional to surface curvature. Therefore, it is to be expected when the maximal value of $\underline{U}_\infty$ is found to be much greater than U_c found for the previous steady snores, the critical gradient occurring when $\underline{U}_\infty$ is increased from zero to 3.675 m/s over one second. This much greater velocity is required to form the flexible surface into the critical mode, shown in figure 5.19(a), similar to the phenomenon observed in the numerical experiment in §4.4.3 where the flexible surface was initially deflected in a shape very dissimilar to the critical mode. The relatively large size of the maximum velocity leads to the oscillation frequency and $\dot{E}_t$ of the snore also being very large, see table 5.3. Although the geometry used is similar to the previous snore, the instability mechanism has changed again, see figure 5.19(b), and is now *upstream driven*. All the snores modelled have a U_c higher than the calculated maximal inspiratory $\underline{U}_\infty$ of 1.27 m/s. It is argued that these are expected results owing to, as previously described, the upper airway's attempt to keep a constant Q, the higher values of U_c therefore taking into account the reduction in A. Furthermore for the second and third snores at $\bar{H} = 0.1$, A has reduced by ten times but U_c has only increased twice and three times respectively. Therefore, it is proposed that in these cases actual maximum inhalation velocity is much higher than 1.27 m/s; this shows how destabilising the Bernoulli effect is for snoring parameters. Also, risk of instability initiation increased if account is made of greater surface curvature.

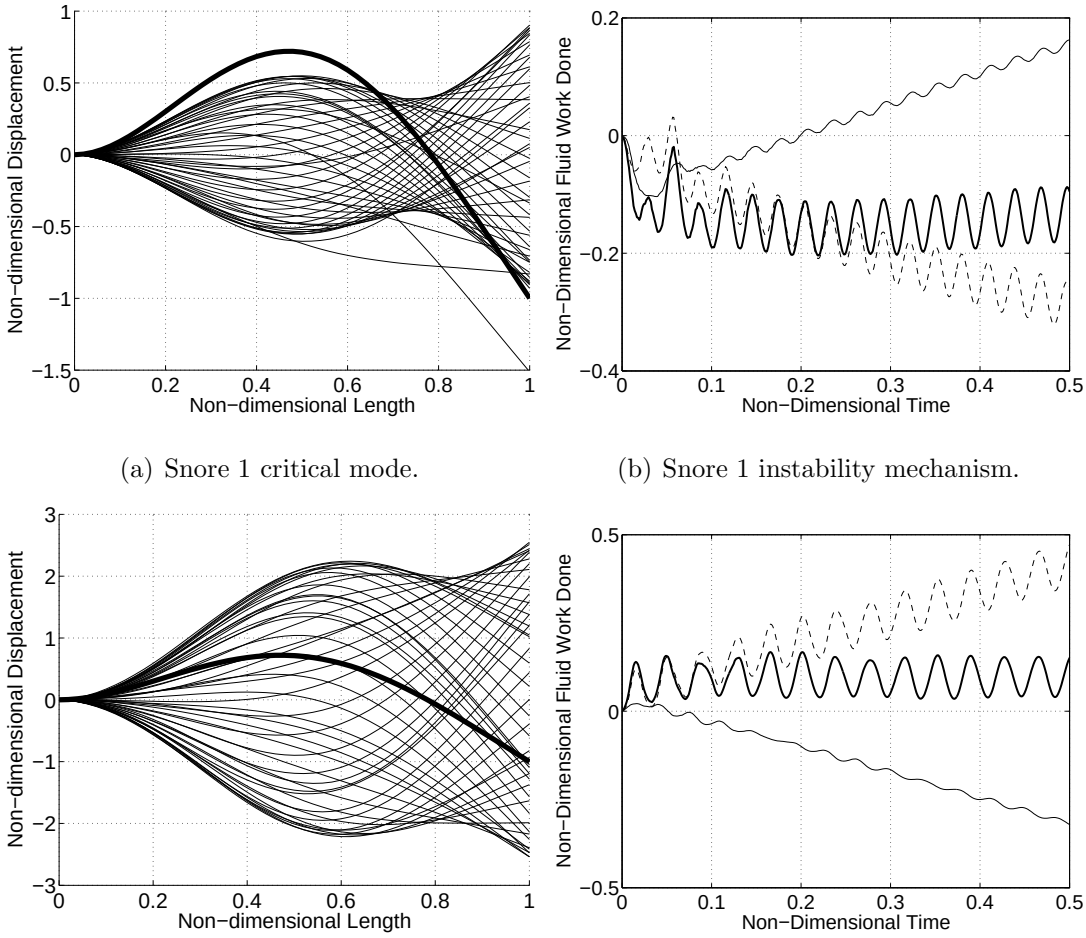

(a) Snore 1 critical mode.

(b) Snore 1 instability mechanism.

(c) Snore 2 critical mode.

(d) Snore 2 instability mechanism.

Figure 5.17: Fluid-structure behaviour at critical velocity where (a) and (c) depict the oscillation of the flexible surface (the thick line is the initial deflection) and (b) and (d) are the total fluid work done on the whole flexible surface and also on its upstream and downstream halves: −(thin) total fluid work done on upstream half of plate ($\int_0^{t_p} \dot{W}_u(t)dt$), −− total fluid work done on downstream half of plate ($\int_0^{t_p} \dot{W}_d(t)dt$), −(thick) total fluid work done ($\int_0^{t_p} (\dot{W}_u(t) + \dot{W}_d(t))dt$); (a) and (b) $U_\infty = 1.45$ m/s, $\bar{H} = 1$; (c) and (d) $U_\infty = 2.34$ m/s, $\bar{H} = 0.1$; $\bar{L} = 0.42$, rigid central surface, fifty mass points, initial deflection is the second eigenmode.

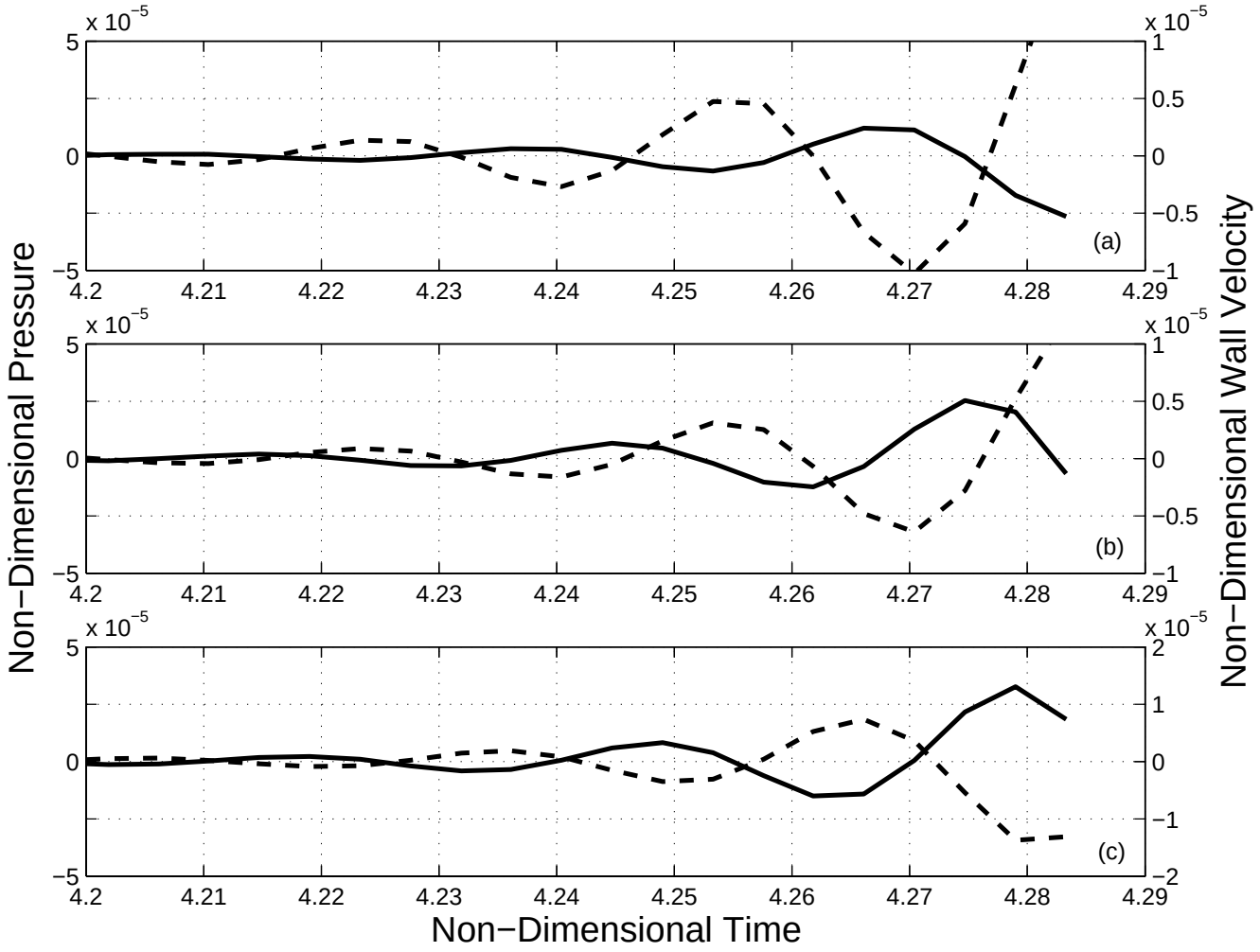

Figure 5.18: Snore 3 values of non-dimensional flexible-surface velocity and fluid pressure in time at selected mass-points along the flexible-surface length: $--$ pressure value, $-$ flexible-surface velocity value, (a) mass-point values at $0.3L$, (b) mass-point values at $0.5L$, (c) mass-point values at $0.7L$; U_∞ increases from zero to 3.675 m/s in one second (approximately one human inhalation during sleep) with only the final 2% of the inhalation depicted, $\bar{L} = 0.42$, $\bar{H} = 0.1$, rigid central surface, fifty mass points, initial deflection is the second eigenmode.

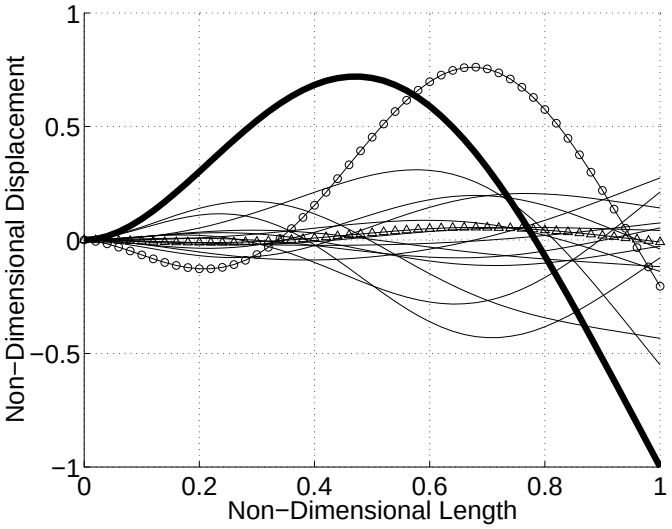

(a) Snore 3 critical mode.

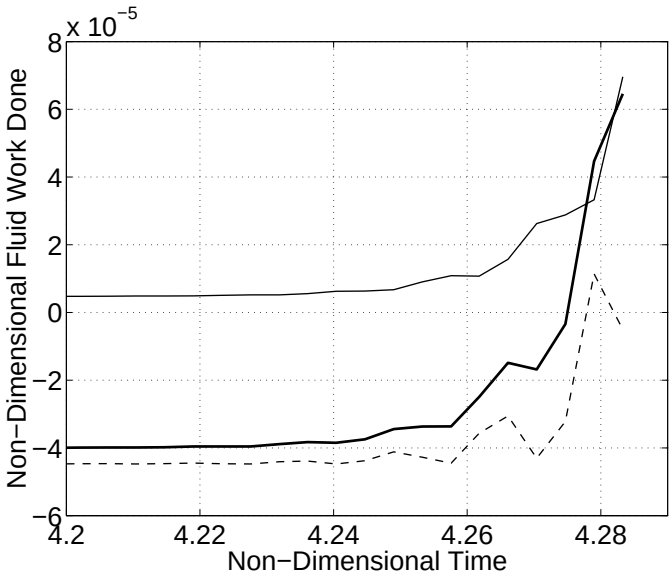

(b) Snore 3 instability mechanism.

Figure 5.19: Fluid-structure behaviour at critical velocity where (a) depicts the oscillation of the flexible surface (the thick line is the initial deflection, $-\triangle$ and $-$O are deflections at $\bar{t} = 4.24$ and 4.28 respectively) and (b) is the total fluid work done on the whole flexible surface and also on its upstream and downstream halves: $-$(thin) total fluid work done on upstream half of plate ($\int_0^{t_p} \dot{W}_u(t)dt$), $--$ total fluid work done on downstream half of plate ($\int_0^{t_p} \dot{W}_d(t)dt$), $-$(thick) total fluid work done ($\int_0^{t_p} (\dot{W}_u(t) + \dot{W}_d(t))dt$); U_∞ increases from zero to 3.675 m/s in one second (approximately one human inhalation during sleep) with only the final 2% of the inhalation depicted, $\bar{L} = 0.42$, $\bar{H} = 0.1$, rigid central surface, fifty mass points, initial deflection is the second eigenmode.

5.2.3 Snore Treatment

The operation of snore treatments described in §1.2.5 are now put into context. Preferable non-surgical treatments, described and compared in detail by Lowe (2000), aim to increase A of the oral and/or the nasal airways, thereby reducing the required $\underline{U}_\infty$ to attain mean Q. If snoring persists, the standard surgical procedure is uvulopalatopharyngoplasty, where the caudal part of the soft palate is removed, thus aiming to increase U_c by lowering the mass ratio as seen in §5.1.1. An alternative idea proposed by Ellis *et al.* (1993) is to stiffen the soft palate, the aim being to increase the U_c required to induce instability. Using knowledge gained in the previous subsection, an attempt to effect a 'cure' on the second steady snore ($\bar{L} = 0.42,\ \bar{H} = 0.1$) is executed. E_t for this snore at U_c is shown in figure 5.20(a). By applying 10% greater stiffness in the upstream area of the flexible surface where the instability mechanism occurs, it is hoped to maximise the reduction in the work done by the fluid on the flexible surface and thus increase the flexible surface's stability. This modification is indeed found to have a stabilising effect, see figure 5.20(b). Unexpectedly, when the stiffness is increased in the downstream half of the flexible surface the effect is *destabilising*, see figure 5.20(c). With such a fine line between successful and unsuccessful treatment, it is argued that treatment will be difficult to apply. This difficulty is compounded by the many different types and mechanisms of snore and several of these are now summarised. Three types of snore with differing instability mechanisms were identified and described in the previous subsection. Aurégan and Depollier (1995) identified two snore instability classifications, *pure* and *apnœic* snores, as described in §1.2.5, due to the flexibility of the soft palate and channel properties respectively. Also described in §1.2.5 was a further type of snore instability, discerned by Balint and Lucey (2005), where one inlet of the airway (oral or nasal) was closed and the flexible surface lost stability to *divergence*. In §1.2.3 several different sites of snore generation in the human upper airway were identified. With so many different types of snore, all with differing instability mechanisms, it therefore follows that there will be different treatments for each type of snore and treatment must be tailored to the individual. This presents a predicament for a surgeon as to what treatment to apply. The development

of the present model can therefore be seen as an essential first step in the elucidation of the underlying mechanisms of different types of snore and the simulated application of proposed treatments. As a result of this research, the ability to tailor treatment to the highly individual needs of patients has been highlighted and clearly shows the usefulness of developing more accurate models in the future.

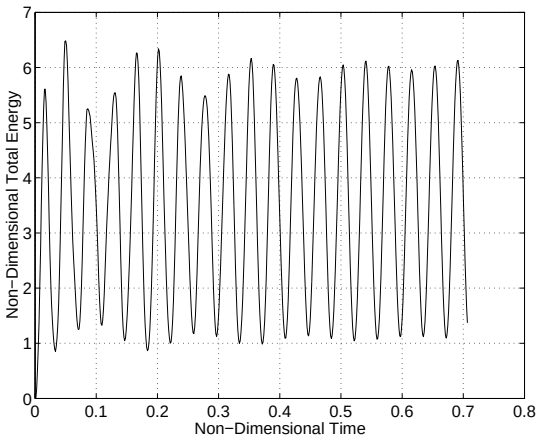

(a) Evenly distributed stiffness.

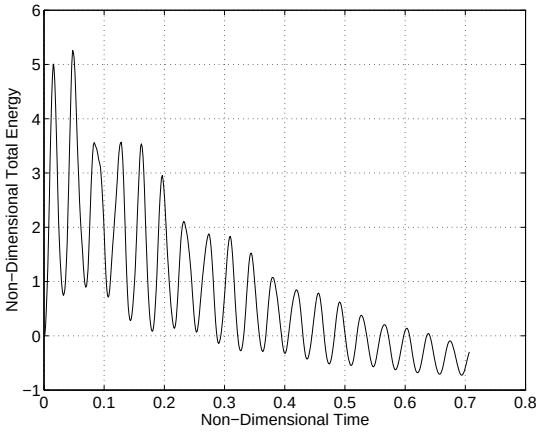

(b) Downstream half of flexible surface has 10% greater stiffness.

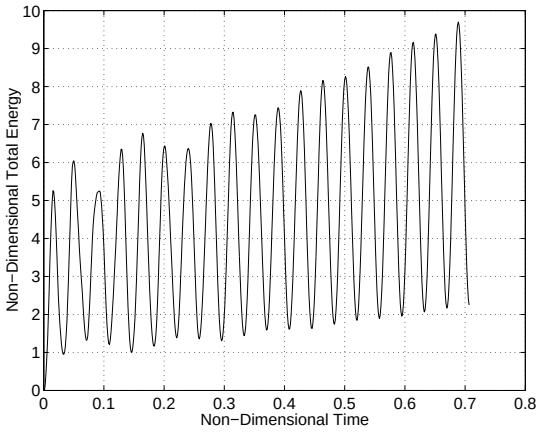

(c) Upstream half of flexible surface has 10% greater stiffness.

Figure 5.20: Plots of total energy against time showing the effect of the variation of flexible-surface stiffness on the stability of the steady state; $U_\infty = 2.34$ m/s, $\bar{L} = 0.42$, $\bar{H} = 0.1$, rigid central surface, fifty mass points, initial deflection is the second eigenmode.

5.3 Further Fluid-Structure Phenomena

Fluid-structure interactions observed at $\bar{L} = 1000$ and $\bar{L} = 0.001$ over a range of $\bar{U}$ for an isolated flexible surface are investigated noting U_c, the shape of the steady-state oscillation and the manifestation and mechanism of the observed instabilities. Comparison with published work is made and further applications of the unsteady model are outlined.

5.3.1 $\bar{L} = 0.001$ to $\bar{L} = 1000$

In the second row of table 5.4 below, the values of U_c, f and $\dot{E}_t$ are recorded for the isolated flexible surface examined at $\bar{L} = 1$. The effect of variations of $\bar{L}$ on these properties are recorded in the other rows of the table. Initially consider fluid-structure

Experiment	U_c	f(Hz)	$\dot{E}_t$
in vacuo	–	4.7×10^{-2}	–
$\bar{L} = 1$	5.452	3.1×10^{-2}	0.084
$\bar{L} = 1000$	1.49×10^{-3}	1.7×10^{-2}	0.120
$\bar{L} = 1 \times 10^{-3}$	1.04×10^{5}	3.6×10^{-2}	0.039

Table 5.4: Values of U_c, f and $\dot{E}_t$ for observed flutter instabilities determined via numerical experiment for flow-structure interaction of a cantilevered flexible surface embedded in a potential flow for variations in $\bar{L}$; fifty mass points, initial deflection was the second eigenmode.

interactions at $\bar{L} = 1000$. At $\bar{U} = 0$, see figures 5.21(a) and (b), the flexible surface oscillated in a steady state. Owing to the influence of the fluid mass, its period of oscillation is reduced from that of the *in vacuo* period. As $\bar{U}$ is increased from zero, see figures 5.21(c) and (d) and figures 5.22(a) and (b), E_t begins to fall as the free stream has a damping effect on the oscillation amplitude of the flexible surface. The fluid damping occurs in equal amounts on the up and downstream halves of the flexible surface, as

shown in figure 5.23. As $\bar{U}$ is further increased, see figures 5.24(a) and (b), fluid pressure forces outweigh flexible-surface forces, the flexible surface lifts and a *semi-divergence* phenomenon is observed. This is divergence as the introduction of damping does not alter the velocity at which the instability occurs; the instability is semi-divergence as the flexible surface falls again after reaching a critical maximum deflection. The instability is caused by positive fluid work done on the whole flexible surface (a larger proportion of this work done on the upstream half), as shown in figure 5.25. Approaching U_c, see figure 5.26, for a second time fluid damping of the flexible surface oscillation amplitude occurs; figures 5.26(a) and (c) show that the flexible-surface oscillation is now constituted by higher-order eigenmodes. The damping is caused by destructive interference on the downstream half of the flexible surface between the mass-point velocity and applied fluid pressure, as shown in figure 5.27. As the value of $\bar{U}$ is further increased and approaches U_c, see figures 5.28(a) and (b), the overall fall in E_t ceases and varies about a constant value, the fluid now having a neutral effect on the flexible-surface oscillation; the flexible surface again oscillates in a steady state. Figure 5.28(a) shows that at this $\bar{L}$ the critical mode is composed of contributions from the first to the fourth eigenmodes inclusive. The value of f is 1.7×10^{-2} Hz, a fall of 64% from the *in vacuo* oscillation frequency and lower than the value of f measured for the $\bar{L} = 1$ case, see table 5.4. Above U_c, see figures 5.28(c) and (d), the fluid has a destabilising effect causing the flexible surface to enter into an unstable oscillation. As $\bar{U}$ is increased further above U_c, the oscillation increases in amplitude *ad infinitum*. The unstable oscillation in figures 5.28(c) and (d) is caused by a flutter instability as the introduction of damping is *destabilising* and *lowers* U_c. As the effect of damping is opposite at $\bar{L} = 1$, acting to stabilise the observed flutter instability, this suggests that there is a critical $\bar{L}$ at which the rôle of damping changes. The calculated value for $\dot{E}_t$ is 0.12, 25% more unstable than the $\bar{L} = 1$ instability, see table 5.4, owing to the increased fluid density. To investigate the mechanism of the flutter instability, W at U_c is plotted, see figure 5.29; in addition, the total fluid work done on the upstream and downstream halves of the flexible surface are also plotted on the same figure. The figure shows that the total fluid work done on the downstream half of the flexible surface drives the instability. Finally, it is noted that the observed phenomenon

of an increase in the order of eigenmodes forming the composition of the critical mode as $\bar{L}$ is increased is similar to the results of Yamaguchi *et al.* (2000a,b) and Watanabe *et al.* (2002a,b); a figure from Watanabe *et al.* (2002b) is shown in figure 5.30 depicting this phenomenon. A consequence of this phenomenon is that the downstream *neck* of the flexible surface oscillation widens as $\bar{L}$ is increased.

Fluid-structure interactions at $\bar{L} = 1 \times 10^{-3}$, shown for $\bar{U} = 0$ and U_c in figure 5.31, are very similar in character to those observed at $\bar{L} = 1$ and the observed instability properties are shown in the final row of table 5.4; the only dissimilarities are the transition from damped to unstable flexible-surface oscillation, which is far more abrupt at $\bar{L} = 1 \times 10^{-3}$, and that $\dot{E}_t$ is less than the $\bar{L} = 1$ instability, see table 5.4, owing to the reduced fluid density.

The trend of U_c over the range $0.1 \leq \bar{L} \leq 1000$ is now compared with that of other published work. Watanabe *et al.* (2002b) collected U_c data from several numerical and experimental studies and, along with their own data, produced the graph shown in figure 5.32(a). The velocity value plotted, U_s^*, has been non-dimensionalised in an alternate way to $\bar{U}$, such that

$$U_s^* = \bar{U}\bar{L}^{\frac{3}{2}}.$$

Further noting that the x-axis variable μ is the inverse of $\bar{L}$, the figure therefore shows that U_c *increases* with $\bar{L}$. This result is not spurious but owes itself to the derivation of U_s^*; this is now a measure of *relative pressure i.e.* as $\bar{L}$ increases, the effect of the fluid pressure forces become relatively large compared to flexible surface restorative forces. In figure 5.32(b), U_c over the range $0.1 \leq \bar{L} \leq 1000$ calculated using the present unsteady model is plotted and shows good correlation with the former figure. Good agreement between the two models lends further confidence to the theoretical approaches used and to the results obtained.

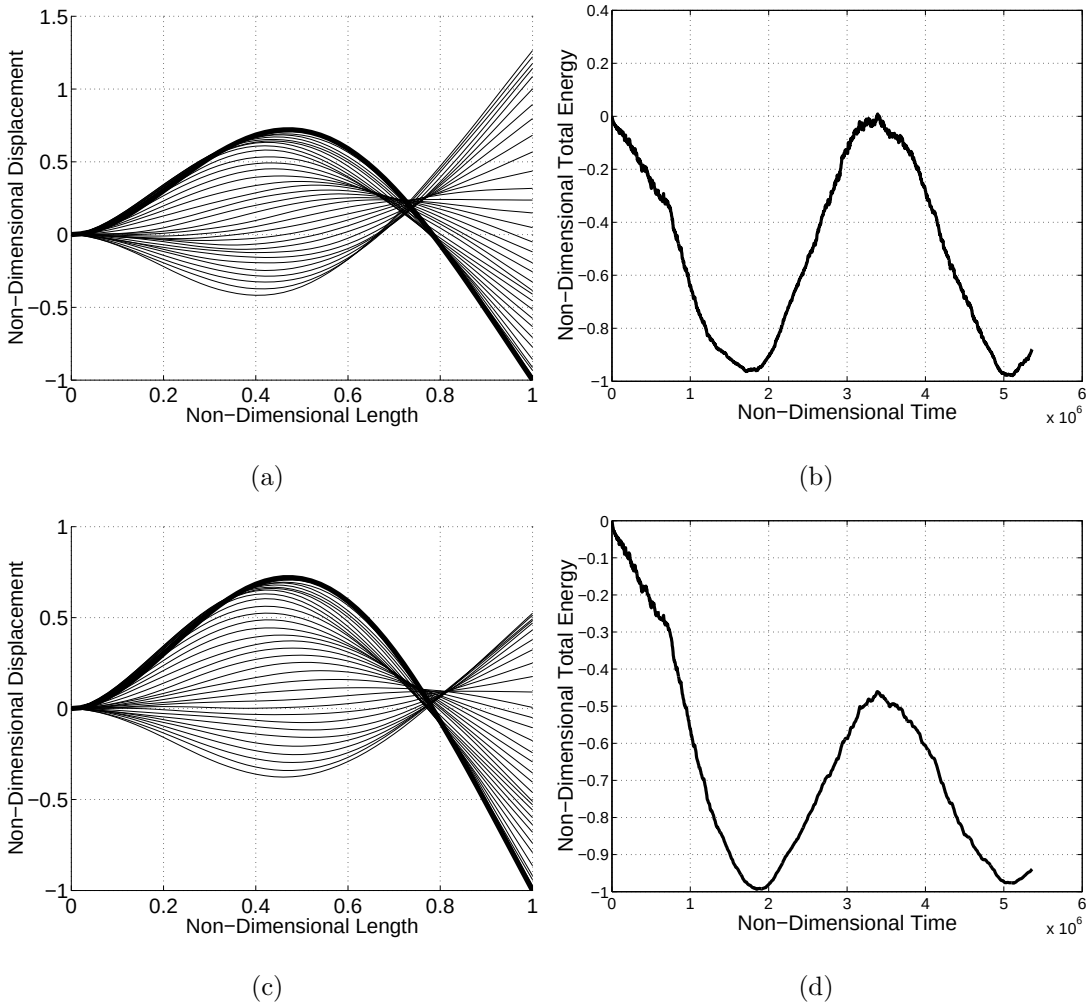

Figure 5.21: Fluid-structure behaviour where (a) and (c) depict the oscillation of the flexible surface (the thick line is the initial deflection) and (b) and (d) are the respective total energies expended: in (a) and (b), $\bar{U} = 0.0$; in (c) and (d), $\bar{U} = 5.51 \times 10^{-5}$; $\bar{L} = 1000$, $\bar{H} = 1$, fifty mass points, initial deflection is the second eigenmode.

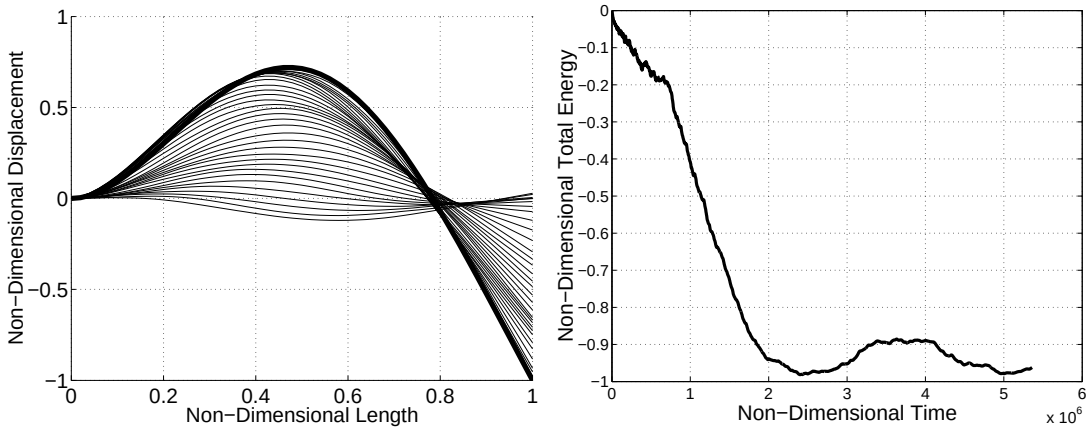

(a) (b)

Figure 5.22: Fluid-structure behaviour where (a) depicts the oscillation of the flexible surface (the thick line is the initial deflection) and (b) is the respective total energies expended: $\bar{U} = 1.1 \times 10^{-4}$, $\bar{L} = 1000$, $\bar{H} = 1$, fifty mass points, initial deflection is the second eigenmode.

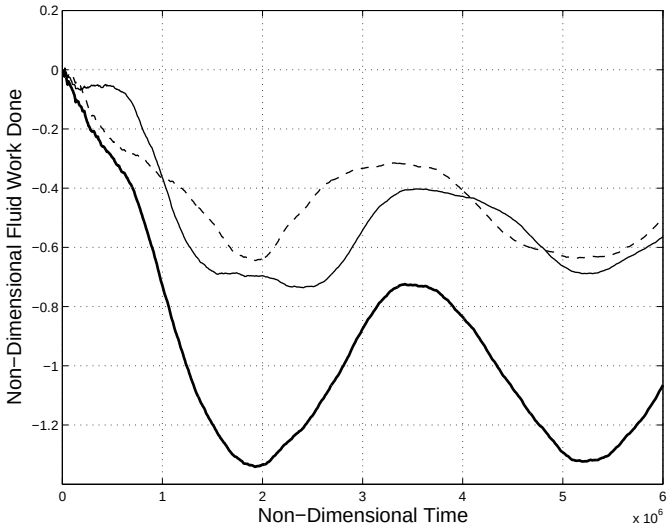

Figure 5.23: Total fluid work done on the whole flexible surface and also on its upstream and downstream halves: $-$(thin) total fluid work done on upstream half of plate ($\int_0^{t_p} \dot{W}_u(t)dt$), $--$ total fluid work done on downstream half of plate ($\int_0^{t_p} \dot{W}_d(t)dt$), $-$(thick) total fluid work done ($\int_0^{t_p} (\dot{W}_u(t) + \dot{W}_d(t))dt$); $\bar{U} = 5.51 \times 10^{-5}$, $\bar{L} = 1000$, $\bar{H} = 1$, fifty mass points, initial deflection is the second eigenmode.

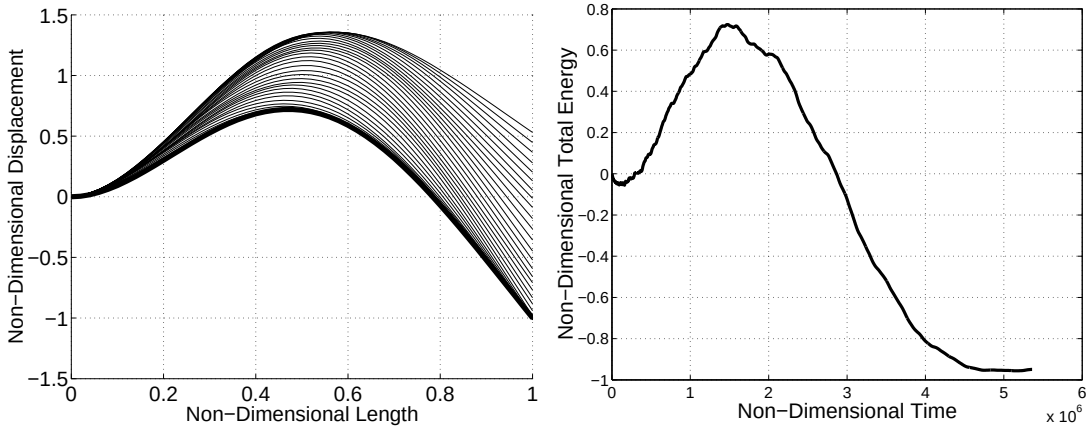

(a) (b)

Figure 5.24: Fluid-structure behaviour where (a) depicts the oscillation of the flexible surface (the thick line is the initial deflection) and (b) is the respective total energies expended: $\bar{U} = 2.75 \times 10^{-4}$, $\bar{L} = 1000$, $\bar{H} = 1$, fifty mass points, initial deflection is the second eigenmode.

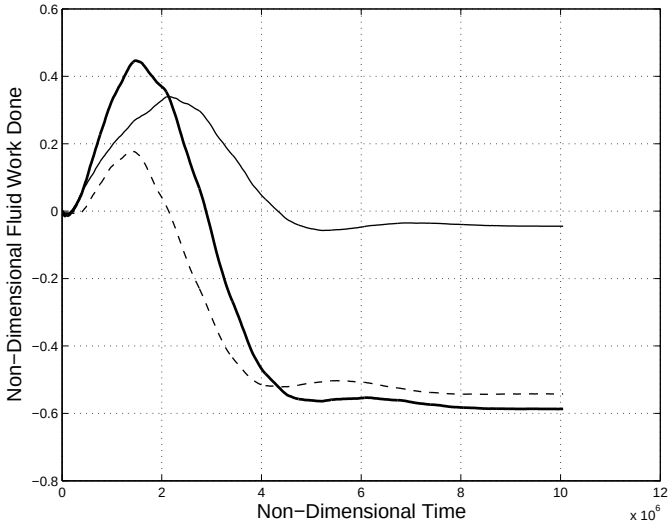

Figure 5.25: Total fluid work done on the whole flexible surface and also on its upstream and downstream halves: −(thin) total fluid work done on upstream half of plate ($\int_0^{t_p} \dot{W}_u(t)dt$), −− total fluid work done on downstream half of plate ($\int_0^{t_p} \dot{W}_d(t)dt$), −(thick) total fluid work done ($\int_0^{t_p} (\dot{W}_u(t) + \dot{W}_d(t))dt$); $\bar{U} = 2.75 \times 10^{-4}$, $\bar{L} = 1000$, $\bar{H} = 1$, fifty mass points, initial deflection is the second eigenmode.

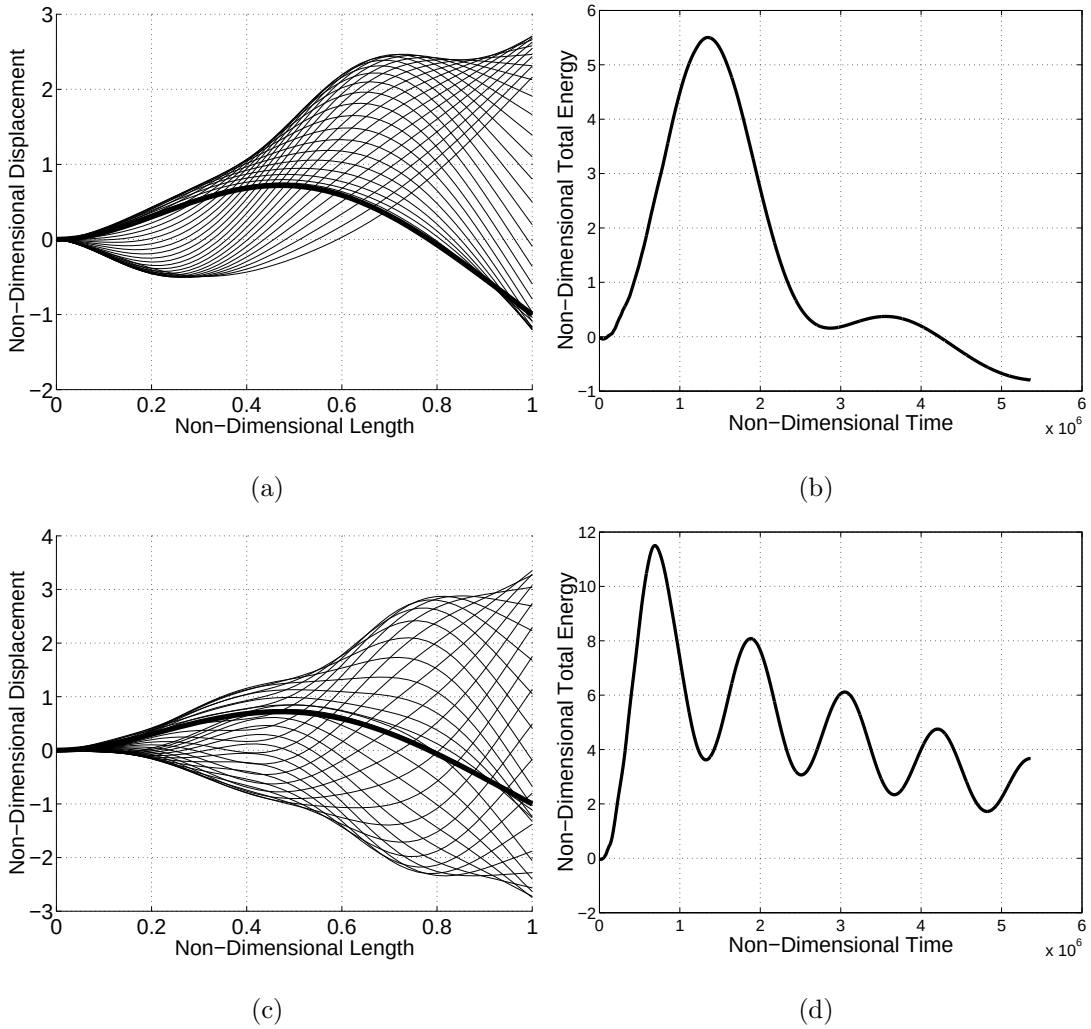

Figure 5.26: Fluid-structure behaviour where (a) and (c) depict the oscillation of the flexible surface (the thick line is the initial deflection) and (b) and (d) are the respective total energies expended: in (a) and (b), $\bar{U} = 5.51 \times 10^{-4}$; in (c) and (d), $\bar{U} = 9.91 \times 10^{-4}$; $\bar{L} = 1000$, $\bar{H} = 1$, fifty mass points, initial deflection is the second eigenmode.

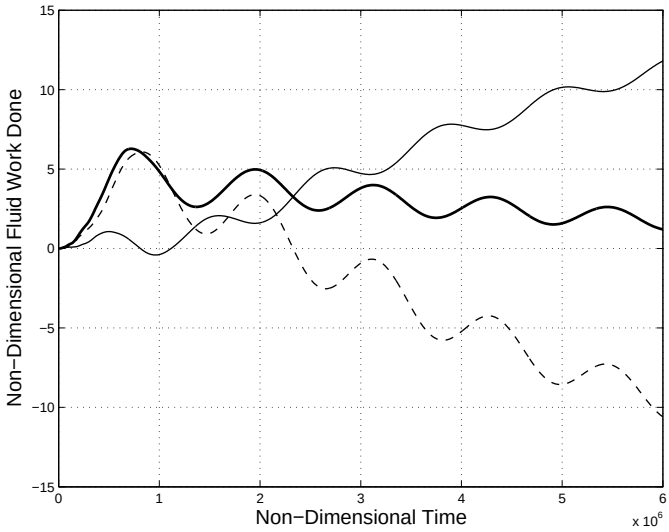

Figure 5.27: Total fluid work done on the whole flexible surface and also on its upstream and downstream halves: $-$(thin) total fluid work done on upstream half of plate ($\int_0^{t_p} \dot{W}_u(t)dt$), $--$ total fluid work done on downstream half of plate ($\int_0^{t_p} \dot{W}_d(t)dt$), $-$(thick) total fluid work done ($\int_0^{t_p} (\dot{W}_u(t) + \dot{W}_d(t))dt$); $\bar{U} = 9.91 \times 10^{-4}$, $\bar{L} = 1000$, $\bar{H} = 1$, fifty mass points, initial deflection is the second eigenmode.

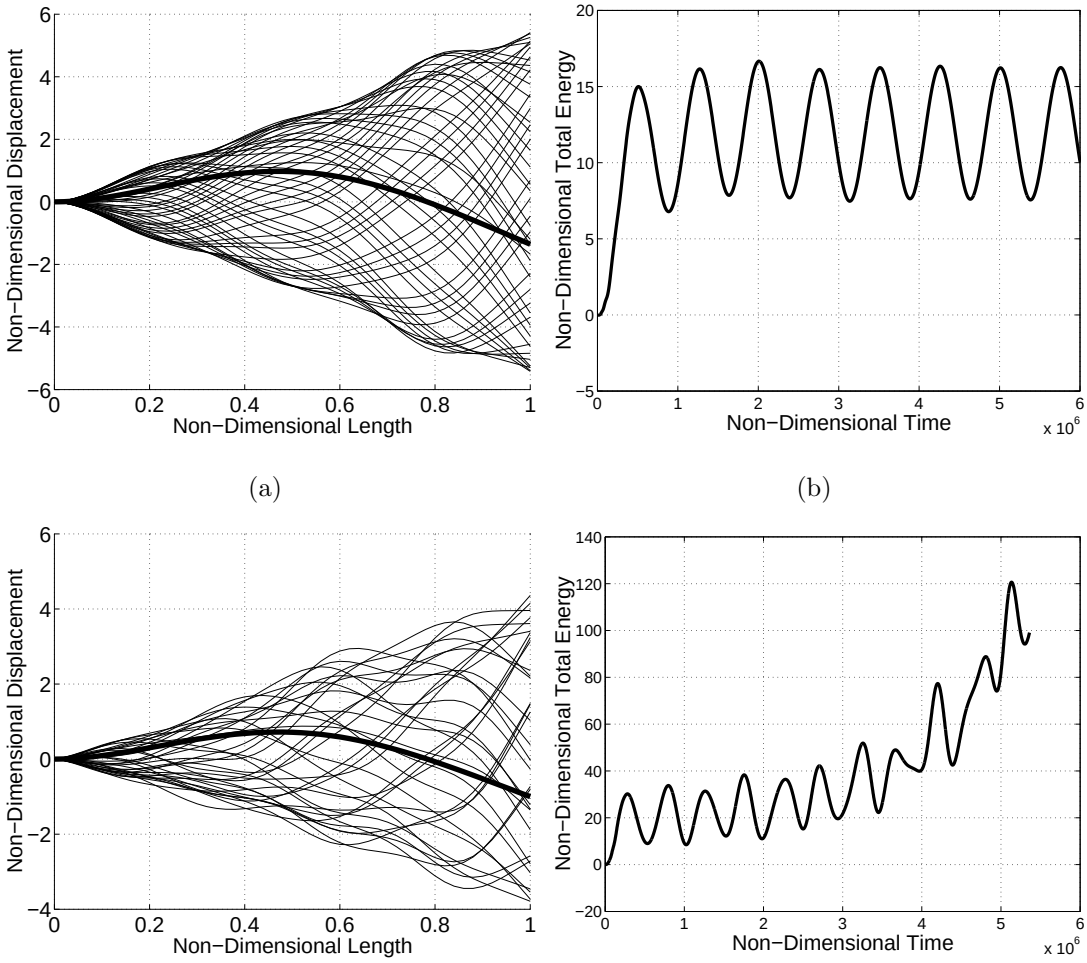

Figure 5.28: Fluid-structure behaviour where (a) and (c) depict the oscillation of the flexible surface (the thick line is the initial deflection) and (b) and (d) are the respective total energies expended: in (a) and (b), $\bar{U} = 1.49 \times 10^{-3}$; in (c) and (d), $\bar{U} = 2.2 \times 10^{-3}$; $\bar{L} = 1000$, $\bar{H} = 1$, fifty mass points, initial deflection is the second eigenmode.

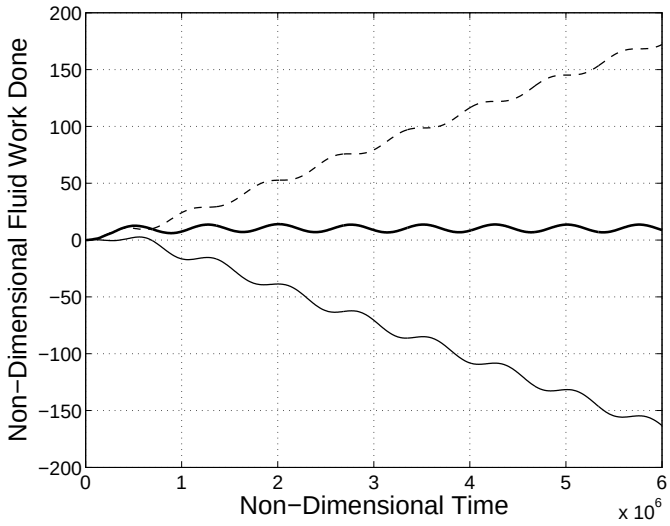

Figure 5.29: Total fluid work done on the whole flexible surface and also on its upstream and downstream halves: −(thin) total fluid work done on upstream half of plate ($\int_0^{t_p} \dot{W}_u(t)dt$), −− total fluid work done on downstream half of plate ($\int_0^{t_p} \dot{W}_d(t)dt$), −(thick) total fluid work done ($\int_0^{t_p} (\dot{W}_u(t) + \dot{W}_d(t))dt$); $\bar{U} = 1.49 \times 10^{-3}$, $\bar{L} = 1000$, $\bar{H} = 1$, fifty mass points, initial deflection is the second eigenmode.

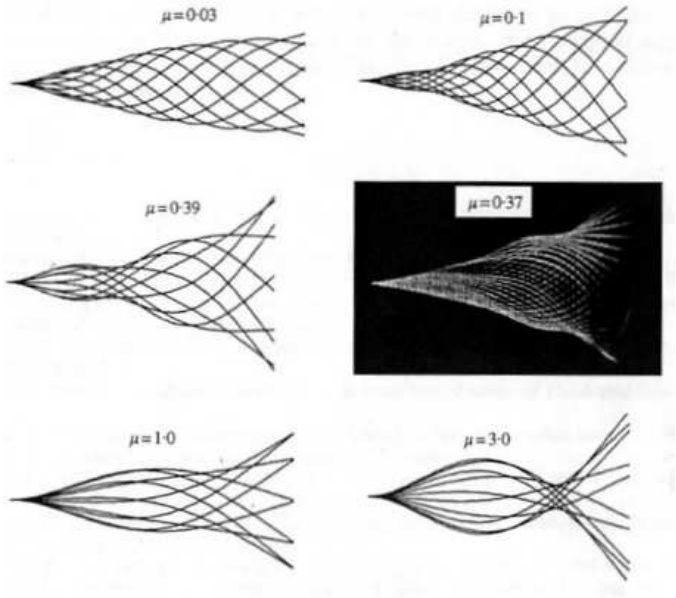

Figure 5.30: Critical modes for different $\bar{L}$, where $\mu = \bar{L}^{-1}$, from Watanabe *et al.* (2002b). Modes were calculated via numerical experiment except for result shown at $\mu = 0.37$ which is an experimental result.

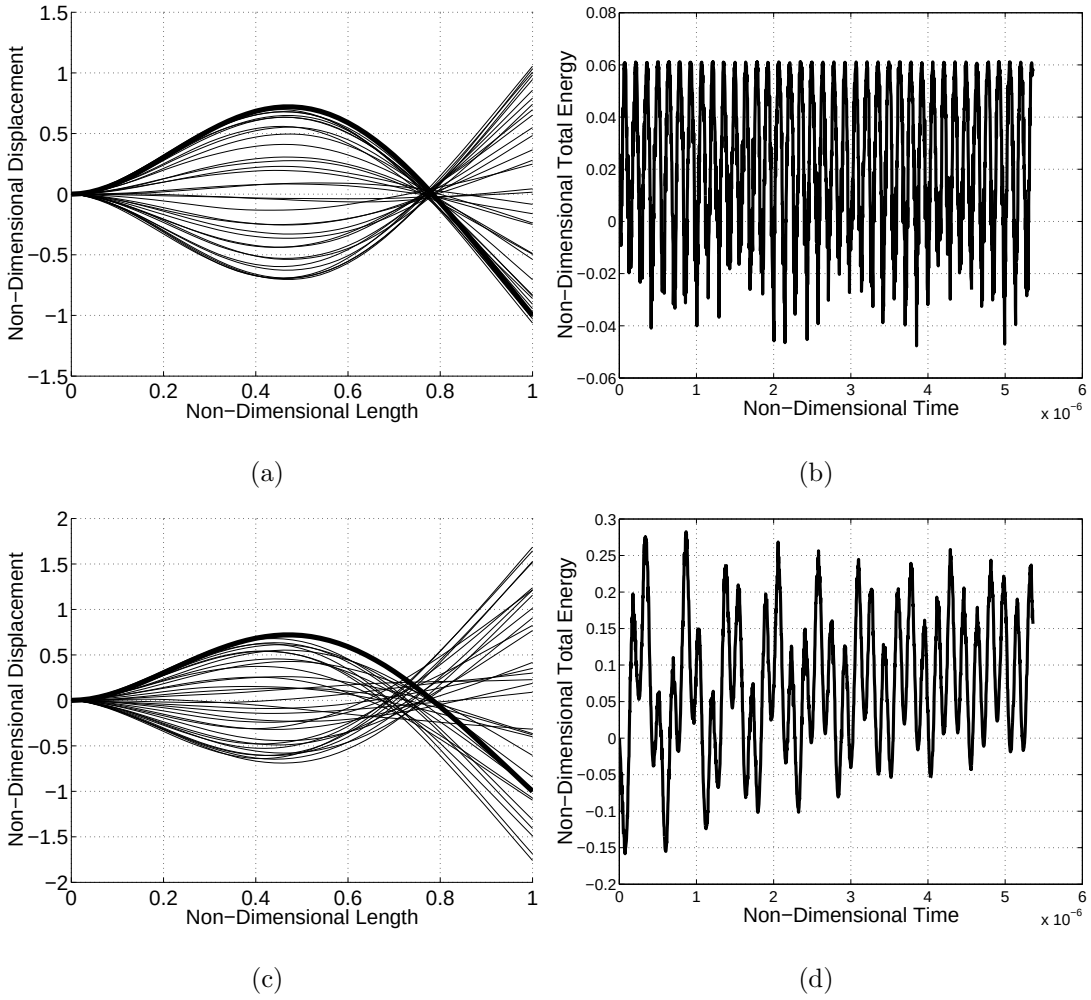

Figure 5.31: Fluid-structure behaviour where (a) and (c) depict the oscillation of the flexible surface (the thick line is the initial deflection) and (b) and (d) are the respective total energies expended: in (a) and (b), $\bar{U} = 0.0$; in (c) and (d), $\bar{U} = 1.04 \times 10^5$; $\bar{H} = 1$, $\bar{L} = 1 \times 10^{-3}$, fifty mass points, initial deflection is the second eigenmode.

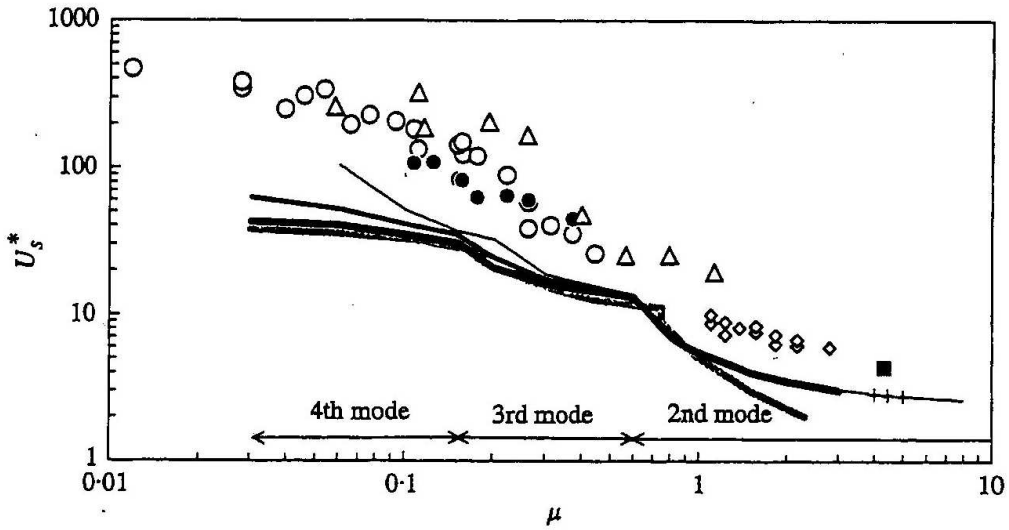

(a) Plot of data from several published studies, from Watanabe *et al.* (2002b). Discretised data are from physical experiments, continuous data are from analytical models.

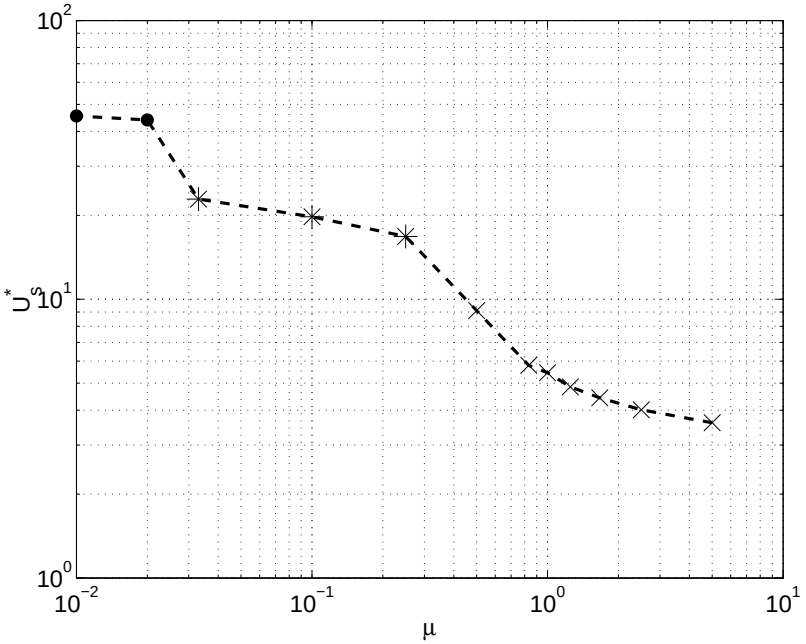

(b) Present unsteady model; different data point markings signify different predominant eigenmodes in form of steady state oscillation: × second eigenmode, ∗ third eigenmode, • fourth eigenmode.

Figure 5.32: U_c at different $\bar{L}$, where $U_s^* = U_c \bar{L}^{\frac{3}{2}}$ and $\mu = \bar{L}^{-1}$.

5.3.2 Further Applications

Following the validation of the unsteady model for a range of mass ratios, three proposed applications of obtained results to fluid-structure phenomena other than snoring that were noted in the literature review are now discussed. Several studies have been referred to that study paper flutter in paper manufacture, see Yamaguchi *et al.* (2000a,b), Watanabe *et al.* (2002a,b) and Wu and Kaneko (2004). As the demand for paper grows and its manufacture speed increases, the velocity of the paper in production also increases and begins to flutter; this causes problems where paper is fed from one roller to the next. One solution highlighted by this work is to somehow trip the paper into a very high mode deflection, causing high activation energy and raising U_c, thus keeping amplitude of oscillation small; the paper is then still able to be fed into the rollers of the next stage of the machine. Applying results to sail technology, it could be argued that tailoring a sail's properties to produce the semi-divergence phenomenon observed at high mass ratios at typical sailing speeds would be advantageous, billowing out a sail rather than fluttering and thus maximising energy transmission from the air into forward speed. A further application is to swimming mammals. As noted in the literature review the shed vorticity from an oscillating, infinitely thin, surface has dissimilar polarity to that of a swimming mammal, the latter more akin to flow around a cylinder (Huber, 2000). However, it is interesting to note the similarity of the critical mode oscillation at $\bar{L} = 1$ to the general mode of propulsion for swimming mammals. Lighthill (1969) describes that the anguilliform mode of propulsion (named after the common eel) can be considered fundamental, a pure undulatory mode of propulsion in which the whole body participates, although amplitude may increase markedly towards the tail. Lighthill further describes that the most important modification to this mode of propulsion is the carangiform mode where undulation of the whole body is inessential and it is confined to the posterior half, or even third, of the body. It is proposed that the study of mass-point velocity and applied fluid pressure, for the critical mode oscillation at $\bar{L} = 1$, would elucidate information pertaining to the swimming mammal's transition of energy to the surrounding fluid to provide itself with forward propulsive motion.

Chapter 6

Conclusions

6.1 Thesis Concept and Motivation

A novel method for calculating the linear fluid-structure interaction of a cantilevered flexible surface centrally positioned in an ideal channel flow, incorporating the effects of vorticity shed downstream, has been described. This linear model can accurately capture the onset of instability in this fluid-structure system. A summary of the motivation section (see §2.4), that described how the model developed in this thesis extends the work on this fundamental problem of flow-structure interaction is now presented. The most advanced work referred to in the literature review on the inviscid flow-structure interaction to be modelled in this thesis is that of Guo and Païdoussis (2000). Their work does not address the following open questions

1. investigation into fluid-structure phenomena via detailed analysis of the interaction between applied fluid-pressure and flexible-surface velocity along the flexible surface;

2. the effect of a rigid-inlet surface upstream and adjacent to the flexible surface and the effect of the singularity at its leading edge;

3. the effect of the variation of stiffness and damping properties along the length of the flexible surface;

4. the effect of an unsteady free-stream flow;

5. the effect of shed vorticity from the trailing edge of the flexible surface;

6. the effect of not presupposing the deflection of the flexible-surface;

7. the effect of spatial variation of the bounding channel geometry;

8. the effect of flexible channel walls;

9. the effect of non-linear fluid and flexible-surface models.

The derivation of the numerical model presented in this thesis allows its application to open questions 1. to 6. and detailed results have been presented. With reference to open questions 7. to 9. the numerical model presented in this thesis facilitates the extension to non-linear fluid and flexible surface models and the incorporation of flexible channel walls, as described in the final section of this chapter. As noted in the literature review (see §2.1), the next geometry to be investigated in this field of research is that of a flexible surface in a flow through a flexible-channel. The most advanced viscous-fluid work referred to in the literature review on the flow-structure interaction modelled in this thesis is that of Balint (2001) and Balint and Lucey (2005). The work described in this thesis has extended their work by

- highlighting the effect of viscosity on this flow-structure interaction;

- conducting far more detailed numerical experiments as the model presented in this thesis is far more computationally inexpensive and therefore requires relatively low computational power to operate effectively.

Further motivation for this work is provided by the general applicability of this model to many physical flow-structure interactions and the knowledge this provides, most notably in this study to that of human snoring.

6.2 Summary of Main Results & Conclusions

Noting the sections in this thesis they were detailed, the main results and conclusions from the numerical experiments that were carried out in this thesis were

1. §4: The individual linearised models of the flexible surface and the fluid velocity and vorticity, together with the action of the individual hydrodynamic pressure components created when the models were combined to form a single linearised unsteady model, were validated via a series of numerical experiments.

2. §5.1.1: Detailed analysis of the fluid-structure phenomena at $\bar{L} = 1$ was carried out for values of non-dimensional velocity, $\bar{U}$, from zero to just above the critical velocity, U_c. A fluid damping mechanism and the flutter instability found above U_c were both investigated. Results for U_c and critical mode shape showed good correlation with the work of Huang (1995). Viscosity was shown to have little effect on the critical mode shape as the form of the critical mode found also showed good correlation with that found by Balint and Lucey (2005).

3. §5.1.2: For the first time, detailed analysis of the effects on this fluid-structure interaction of the variations described in open questions 2. to 5. have been quantified. The main effects of these variations were: a) The proximity of channel walls was destabilising; b) A rigid central surface (upstream and adjacent to the flexible surface) was stabilising and drastically altered the form of the critical mode; c) When a linear gradient of damping along the flexible surface was enforced a narrow band a U_c for which the fluid-structure system was stable was observed. When a linear gradient of stiffness along the flexible surface was enforced a flexural damping mechanism was found; d) An unsteady mean flow was found to be destabilising when it was varied at a critical sinusoidal frequency at U_c; and e) The effect of shed vorticity owing to the change in bound vorticity of the flexible surface was found to be small, thus showing that the Kutta condition is a good approximation for the total shed-vorticity.

4. §5.2.2: Three types of snore were modelled and detailed analysis of these was carried out. The first without the effect of channel walls was again similar to that found by Huang (1995) and Balint and Lucey (2005). The second type with the effect of channel walls was similar to that found by Aurégan and Depollier (1995) and Guo and Païdoussis (2000). The third type of snore had not been previously modelled and incorporated the effects of inhalation. The conducted numerical experiments demonstrated that the location (on the flexible surface) of the destabilising phase shift between the flexible surface velocity and fluid pressure leading to instability would change drastically for a small shift in $\bar{L}$ and numerical model variations.

5. §5.2.3: Using knowledge gained from the investigation of the general fluid-structure interaction, the operation of several types of snore treatment was explained. Application of one treatment, the stiffening of the soft palate, was investigated. Results showed that if treatment were was applied incorrectly it would create a destabilising effect rather than a stabilising one. Coupled with knowledge gained from the previous section and further snore mechanisms from other published work, these results showed the uniqueness of treatment required to provide effective surgical treatment to individual patients suffering from snoring; furthermore, this highlighted the need for more accurate fluid-structure models to be created.

6. §5.3.1: Detailed analysis of the fluid-structure phenomena at $\bar{L} = 0.001$ and 1000 was carried out for values of non-dimensional velocity, $\bar{U}$, from zero to just above the citical velocity, U_c. Two fluid damping mechanisms, a semi-divergence instability and the flutter instability found above U_c were investigated. Results for U_c and critical mode shape showed good correlation with the work of Watanabe *et al.* (2002b).

7. §5.3.2: Using knowledge gained from the investigation of the general fluid-structure interaction, several brief applications of these results to flow-structure interactions seen in paper manufacture, sail technology and swimming mammals was described.

In final conclusion, this thesis has documented a study, via the use of a numerical model, into the onset of flow-induced structural instabilities in the interaction of a flexible surface and an ideal channel flow. The results obtained in this study have been generally applied to several physical cases, most significantly to that of the human snoring phenomenon. Pertinent areas for further work are detailed below.

6.3 Further Research Recommendations

6.3.1 Unsteady Model Development

Further physical understanding of the fluid-structure system was gained when the unsteady model was found to incorrectly model variations in channel geometry, leading to two suggested improvements of the unsteady model. First, when a non-symmetrical channel was applied, the formulation of the unsteady model was found to be incorrect as the proximity of the upper channel wall was found to be more destabilising than that of the lower channel wall. This effect was due to the multiplication of the source singularity distribution's effect on the central surface by a factor of 2 in the source unsteady velocity potential, seen previously in (3.49) and reshown in (6.1) below

$$\left\{\frac{\partial \phi_i}{\partial t}\right\}_{xp} = \left[I_{im}^{\phi\gamma}\right]_{xp}\left\{\frac{\partial \gamma_m}{\partial t}\right\} + 2\left[I_{im}^{\phi\sigma}\right]\left\{\frac{\partial \sigma_m}{\partial t}\right\}. \tag{6.1}$$

This error was due to the pressure on upper and lower sides of the central surface no longer being equal and opposite and can be corrected by having a further separate calculation for the pressure on the lower side of the central surface owing to the source singularities; this would add no further computational time to unsteady model calculations. Secondly, further difficulty was found when modelling a converging channel, specifically in the application of the normal velocity boundary condition on the channel walls. Again, physically incorrect results were obtained, a converging channel found to have a stabilising effect on the fluid-structure system. This error was attributed to the walls being incorrectly modelled by the source singularities as the walls had been transformed into lifting surfaces owing to the applied angle of attack. To model this

effect, it is proposed that the channel walls should be modelled in a similar fashion to the central surface *viz.* with distributions of first-order vortex singularities. These two improvements would then allow actual human pharynx geometries (detailed in Dedouch *et al.* (1999)) to be modelled. Also, it would be feasible to incorporate the effects of induced tension and gravity into the present flexible surface model and extend it to model non-linear effects, see Lucey *et al.* (1997). These extensions would allow more accurate modelling of the characteristics of the human soft palate.

6.3.2 Future Research Direction

A novel and more complex research step would be to introduce the non-linear effects of compliant channel walls into the present fluid-structure system. Much work has been carried out on flexible tubes, for particularly relevant examples see Larose and Grotberg (1997) and Heil and Jensen (2001). A method for the incorporation of infinitely thin flexible channel walls with a viscous fluid model was outlined by Balint (2001), involving a triple-implicit iteration process for flexible surface deflection calculation. Utilising the present ideal fluid model would require the calculation of wall pressure on all three flexible surfaces at each time step, thus resulting in large matrix operations. The modelling of the effects of flow-limitation and wall vibration would allow additional investigation into pharyngeal snoring. This fluid-structure interaction can also be applied to a further medical condition related to snoring known as obstructive sleep apnœa-hypopnœa (OSAH) described in the introductory chapter; Huang (1998) further describes that *"...'sleep apnoea' is defined as a total cessation of breathing for more than ten seconds, causing life-threatening oxygen desaturation. The pathogenesis of apnoea is still a mystery, but it seems reasonable to suggest that the airway collapse is a prelude."* It is noted that in sleep apnœa only one pharyngeal wall collapses and this occurs in the region of the soft palate. The airway's resistance is now proportional to narrowing and collapsibility of the pharyngeal channel, the inclusion of the latter effect resulting in greater inhalation velocity required to reach mean Q. Fluid density and length of collapsible wall also affect the critical velocity at which channel collapse will occur and the rate

of channel collapse. Two further routes of research are then relevant. First, commercial fluid-structure software, such as ADINA, can be utilised now that base effects are understood. The utilisation of a finite element model for the flexural mechanics would thus allow the modelling of the soft palate with its actual elastic properties; these are documented in Berry *et al.* (1999) who show the soft palate to have a value of E varying from 100 kPa at the root of the soft palate to 0.51 kPa at the tip of the uvula. The tissue closest to the root has the highest stiffness as it is composed of mainly tendinous tissue. Secondly, as an alternate step or in conjunction, a non-linear ideal flow and vorticity model could be developed, see Lucey (1989) and Chorin (1973) respectively. The no-flux condition would be strictly applied at the deformed surface and shed vortices would be allowed to move in two dimensions; these would be used in conjunction with the aforementioned non-linear flexible surface model. This non-linear model would require the utilisation of a fast multipole method, see Graps (2000), to execute the increased size of matrix operations required at each time step. One would then expect to see a band of critical velocity for which the unsteady model was in a steady-state, see Zhang *et al.* (2000) and Yadykin *et al.* (2001). Along with their practical applications, both research routes are novel techniques and therefore are of important academic interest. Ultimately the present unsteady model could be extended to three dimensions, see Calladine (1983) and Katz and Plotkin (2001).

References

Abbott, I. H. & von Doenhoff, A. E. 1959 *Theory of Wing Sections.* Dover Edition.

Aittokallio, T., Gyllenberg, M. & Polo, O. 2001 A model of a snorer's upper airway. *Mathematical Biosciences* **170**:79-90.

Aleyev, Yu. G. 1977 *Nekton.* Dr. W. Junk b.v. Publishers.

Amatoury, J. 2004 Snoring energy transmission to the carotid artery, an animal model. Ph.D Thesis, University of New South Wales.

Argentina, M. & Mahadevan, L. 2005 Fluid-flow-induced flutter of a flag. *Proceedings of the National Academy of Sciences of the United States of America* **102**(6):1829-1834.

Armstrong, J. J., Leigh, M. S., Walton, I. D., Zvyagin, A. V., Alexandrov, S. A., Schwer, S., Sampson, D. D., Hillman, D. R. & Eastwood, P. R. 2003 In vivo size and shape measurement of the human upper airway using endoscopic longrange optical coherence tomography. *Optical Express* **11**(15):1817-1826.

Aurégan, Y. & Depollier, C. 1995 Snoring: Linear Stability Analysis and *in vitro* Experiments. *Journal of Sound and Vibration* **188**(1):39-54.

Balint, T. S. 2001 Dynamics of the Upper Airway. Ph.D Thesis, University of Warwick.

Balint, T. S. & Lucey, A. D. 2003 Sleep Disorders in Microgravity (An Engineering Approach). In *Proceedings of the* 54^{th} *International Astronautical Conference, Paper IAC-03-G.1.06.*

Balint, T. S. & Lucey, A. D. 2005 Instability of a cantilevered flexible plate in viscous channel flow. *Journal of Fluids and Structures* **20**(7):893-912.

Basu, A. J., Prabhu, A. & Narasimha, R. 1992 Vortex sheet simulation of a plane "canonical" mixing layer. *Computers and Fluids* **21**(1):1-30.

Beck, R., Odeh, M., Oliven, A. & Gavriely, N. 1995 The acoustic properties of snores. *European Respiratory Journal* **8**:2120-2128.

Benjamin, T. B. 1960 Effects of a flexible boundary on hydrodynamic instability. *Journal of Fluid Mechanics* **9**:513-532.

Benjamin, T. B. 1963 The threefold classification of unstable disturbances in flexible surfaces bounding inviscid flows. *Journal of Fluid Mechanics* **16**:436-450.

Berger, A. J. 1964 *Elementary Human Anatomy.* John Wiley and Sons, Inc., First Edition.

Berry, D. A., Moon, J. B. & Kuehn, D. P. 1999 A finite element model of the soft palate. *Cleft Palate - Craniofacial Journal* **36**(3):217-223.

Bisplinghoff, R. L., Ashley, H. & Halfman, R. L. 1957 *Aeroelasticity.* Addison Wesley, Second Edition.

Bixler, E. O., Vgontzas, A. N., Lin, H. M., Ten Have, T., Leiby, B. E., Vela-Bueno, A. & Kales, A. 2000 Association of Hypertension and Sleep-Disordered Breathing. *Archives of Internal Medicine* **160**:2289-2295.

Black's Medical Dictionary, 1992. Edited by G. Macpherson. A and C Black Ltd., Thirty-seventh Edition.

Cafolla, G. J. 1997 Hydroelastic Instabilities of Compliant Panels. Ph.D Thesis, University of Warwick.

Calladine, C. R. 1983 *Theory of Shell Structures.* Cambridge University Press, First Edition.

Callister, W. D. 1994 *Materials Science and Engineering, An Introduction.* John Wiley and Sons, Third Edition.

Carpenter, P. W. & Garrad, A. D. 1985 The Hydrodynamic Stability of Flow over Kramer-Type Compliant Surfaces. Part 1. Tollmien-Schlichting Instabilities. *Journal of Fluid Mechanics* **155**:465-510.

Carpenter, P. W. & Garrad, A. D. 1986 The Hydrodynamic Stability of Flow over Kramer-Type Compliant Surfaces. Part 2. Flow-Induced Surface Instabilities. *Journal of Fluid Mechanics* **170**:199-232.

Carpenter, P. W. 1990 Status of transition delay using compliant walls. *Viscous drag reduction in boundary layers*, edited by D. M. Bushnell and J. N. Hefner. *Progress in Astronautics and Aeronautics, AIAA* **123**:79-113.

Carpenter, P. W. & Pedley, T. J. (Eds.) 2001 *IUTAM Symposium on flow past highly compliant boundaries and in collapsible tubes; Fluid mechanics and its applications, Volume 72.* Kluwer Academic Publishers.

Chorin, A. J. 1973 Numerical study of slightly viscous flow. *Journal of Fluid Mechanics* **57**(4):785-796.

Crighton, D. G. & Oswell, J. E. 1991 Fluid loading with mean flow. I. Response of an elastic plate to localized excitation. *Philosophical Transactions of the Royal Society of London* A **335**:557-592.

Datta, S. K. & Gottenberg, W. G. 1975 Instability of an elastic strip hanging in an airstream. *ASME: Journal of Applied Mechanics* **42**:195-198.

Dedouch, K., Horáček, J., Vampola, T., Vohradník, M. & Švec, J. 1999 Finite element model of supraglottal vocal tract with consideration of wall impedance. In *3rd International Conference, Engineering Aero-Hydroelasticity,* August 1999.

Dowell, E. H. 1975 *Aeroelasticity of Plates and Shells.* Noordhoff.

Ellis, P. D. M., Ffowcs Williams, J. E. & Shneerson, J. M. 1993 Surgical relief of snoring due to palatal flutter: a preliminary report. *Annals of the Royal College of Surgeons of England* **75**:286-290.

Epstein, R. J., Srinivasan, R. & Dowell, E. H. 1995 Flutter of an infinitely long panel in a duct. *AIAA Journal* **33**(1):109-115.

Ferziger, J. H. 1998 *Numerical Methods for Engineering Application.* John Wiley and Sons Inc., Second Edition.

Fiddes, S. P. & Gaydon, J. H. 1996 A new vortex lattice method for calculating the flow past yacht sails. *Journal of Wind Engineering and Industrial Aerodynamics* **63**:35-59.

Fitt, A. D. & Pope, M. P. 2001 The unsteady motion of two-dimensional flags with bending stiffness. *Journal of Engineering Mathematics* **40**(3):227-248.

Fung, Y. C. 1955 *The Theory of Aeroelasticity.* John Wiley and Sons Inc., First Edition.

Gad-el-Hak, M. 1986 The response of elastic and viscoelastic surfaces to a turbulent boundary layer. *ASME: Journal of Applied Mechanics* **53**:206-212.

Garrad, A. D. & Carpenter, P. W. 1982 A Theoretical Investigation of Flow-Induced Instabilities in Compliant Coatings. *Journal of Sound and Vibration* **85**(4):483-500.

Gavriely, N. & Jensen, O. 1993 Theory and Measurement of Snores. *Journal of Applied Physiology* **74**(6):2828-2837.

Gerald, C. F. & Wheatley, P. O. 1989 *Applied Numerical Analysis.* Addison-Wesley, Fourth Edition.

Ghoniem, A. F. & Cagnon, Y. 1987 Vortex Simulation of Laminar Recirculating Flow. *Journal of Computational Physics* **68**:346-377.

Graps, A. 2000 *N-Body / Particle Simulation Methods.* http://www.amara.com/ papers/nbody.html.

Gray, H. 1918 *Anatomy of the Human Body.* Lea and Febiger, First Edition. Bartleby.com, 2000, http://www.bartleby.com/107/.

Gray, J. 1936 Studies in animal locomotion. VI The propulsive powers of the dolphin. *Journal of Experimental Biology* **13**:192-199.

Guo, C. Q. & Païdoussis, M. P. 2000 Stability of Rectangular Plates with Free Side-Edges in Two-Dimensional Inviscid Channel Flow. *Journal of Applied Mechanics* **67**:171-176.

Heil, M. & Jensen, O. E. 2001 Flows in deformable tubes and channels. In *Proceedings of the IUTAM Symposium on flow past highly compliant boundaries and in collapsible tubes, Warwick, UK* (edited by P. W. Carpenter and T. J. Pedley). *Fluid mechanics and its applications,* **72**:15-49. Kluwer Academic Publishers.

Hess, J. L. 1973 Higher order numerical solution of the integral equation for the two-dimensional Neumann problem. *Computer Methods in Applied Mechanics and Engineering* **2**:1-15.

Hess, J. L. & Smith, A. M. O. 1966 Calculation of potential flow about arbitrary bodies. *Progress in Aeronautical Science* **8**:1-138.

Houghton, E. L. & Carpenter, P. W. 2003 *Aerodynamics for Engineering Students.* Butterworth-Heinemann, Fifth Edition.

Huang, L. 1995 Flutter of Cantilevered Plates in Axial Flow. *Journal of Fluids and Structures* **9**:127-147.

Huang, L., James Quinn, S., Ellis, P. D. M. & Ffowcs Williams, J. E. 1995 Biomechanics of snoring. *Endeavour* **19**(3):96-100.

Huang, L. 1998 Reversal of the Bernoulli effect and channel flutter. *Journal of Fluids and Structures* **12**:131-151.

Huang, L. & Ffowcs Williams, J. E. 1999 Neuromechanical interaction in human snoring and upper airway obstruction. *Journal of Applied Physiology* **86**(6):1759-1763.

Huber, G. 2000 Swimming in Flatsea. *Nature* **408**:777-778.

Katz, J. & Plotkin, A. 2001 *Low-Speed Aerodynamics.* Cambridge University Press, Third Edition.

Kornecki, A., Dowell, E. H. & O'Brien, J. 1976 On the Aeroelastic Instability of Two-Dimensional Panels in Uniform Incompressible Flow. *Journal of Sound and Vibration* **47**(2):163-178.

Kornecki, A. 1978 Aeroelastic and hydroelastic instabilities of infinitely long plates 1. *Solid Mechanics Archives* **3**(4):381-440.

Knight, J. J., Lucey, A. D. & Shaw, C. T. 2001 On the Aerodynamic Loading and Deformation of Convertible Car Roofs. *SAE 2001 World Congress, Detroit, Michigan, March 5-8 2001* **SAE Technical Paper Series:2001-01-1269**.

Kramer, M. O. 1960 The Dolphin's Secret. *The New Scientist* **5 May**, pp. 1118-1120.

Kramer, M. O. 1960 Boundary-Layer Stabilization by Distributed Damping. *Journal of the American Society of Naval Engineers* **72**:25-33; *Journal of the Aero/Space Sciences* **27**:69.

Lamb, Sir H. 1932 *Hydrodynamics.* Cambridge University Press, Sixth Edition.

Landhal, M. T. 1962 On the stability of a laminar incompressible boundary layer over a flexible surface. *Journal of Fluid Mechanics* **13**:609-632.

Larose, P. G. & Grotberg, J. B. 1997 Flutter and long-wave instabilities in compliant channels conveying developing flows. *Journal of Fluid Mechanics* **331**:37-58.

Lemaitre, C., de Langre, E. & Hémon, P. 2004 Instability of a long ribbon hanging in axial flow. *Proceedings of 8th International Conference on Flow-Induced Vibrations*, France, **Paper 57**.

Leonard, A. 1980 Vortex Methods for Flow Simulation. *Journal of Computational Physics* **37**:289-355.

Lewis, R. I. 1991 *Vortex element methods for fluid dynamic analysis of engineering systems.* Cambridge University Press.

Lighthill, J. 1969 Hydrodynamics of aquatic animal propulsion - A survey. *Annual Review of Fluid Mechanics* **1**:413-446.

Lowe, A. A. 2000 Oral Appliances for Sleep Breathing Disorders. In *Principles and Practice of Sleep Medicine.* (edited by M. H. Krger, T. Roth and W. C. Dement). **2**:929-939. Saunders, Third Edition.

Lucey, A. D. 1989 Hydroelastic Instability of a Flexible Surface. Ph.D Thesis, University of Exeter.

Lucey, A.D. & Carpenter, P.W. 1992a A numerical simulation of the interaction of a compliant wall and inviscid flow. *Journal of Fluid Mechanics* **234**:121-146.

Lucey, A. D. & Carpenter, P. W. 1992b A study of the hydroelastic stability of a compliant panel using numerical methods. *International Journal of Numerical Methods for Heat and Fluid Flow* **2**(6):537-553.

Lucey, A. D. & Carpenter, P. W. 1993 On the Difference between the Hydroelastic Instability of Infinite and Very Long Compliant Panels. *Journal of Sound and Vibration* **163**(1):176-181.

Lucey, A.D. & Carpenter, P.W. 1995 Boundary layer instability over compliant walls: Comparison between theory and experiment. *Physics of Fluids* **7**(10):2355-2363.

Lucey, A.D., Cafolla, G. J., Carpenter, P.W. & Yang, M. 1997 The nonlinear hydroelastic behaviour of flexible walls. *Journal of Fluids and Structures* **11**:717-744.

Lucey, A.D. 1998 The Excitation of Waves on a Flexible Panel in a Uniform Flow. *Philosophical Transactions: Mathematical, Physical and Engineering Sciences* **356**(1749):2999-3039.

Lucey, A.D., Sen, P. K. & Carpenter, P.W. 2003 Excitation and evolution of waves on an inhomogeneous flexible wall in a mean flow. *Journal of Fluids and Structures* **18**:251-267.

Martin, P. 2002 *Counting Sheep: On the Science and Pleasures of Sleeps and Dreams.* HarperCollins Publishers, First Edition.

Massey, B. S. 1995 *Mechanics of fluids.* Chapman and Hall, Sixth Edition.

Miyazaki, S., Itasaka, Y., Ishikawa, K. & Togawa, K. 1998 Acoustic analysis of snoring and the site of airway obstruction in sleep related respiratory disorders. *Acta Oto-Laryngologica* **118**(Supplement 537):47-51.

Moore, K. L. & Agur, A. M. R. 1995 *Essential Clinical Anatomy.* Lippincott, Williams and Wilkins, First Edition.

New Scientist Secrets of a perfect skin. (18 January 1997).

New Scientist The Last Word - In a flutter. (18 December 1999).

New Scientist Making Waves. (3 June 2000).

Noguchi, H., Tanaka, H., Tanaka, K., Adachi, T. & Watanabe, Y. 1995 Application of vortex method to analysis of flag flutter. *The 73rd JSME Fall Annual Meeting* pp. 143-144.

Nowacki, W. 1963 *Dynamics of Elastic Systems.* Chapman and Hall, First Edition.

The Oxford English Dictionary, 2005 www.dictionary.oed.com.

Païdoussis, M. P. 1966 Dynamics of flexible slender cylinders in axial flow - Part 1. Theory. *Journal of Fluid Mechanics* **26**(4):717-736.

Païdoussis, M. P. 1966 Dynamics of flexible slender cylinders in axial flow - Part 2. Experiments. *Journal of Fluid Mechanics* **26**(4):737-751.

Païdoussis, M. P. 1998 *Fluid-Structure Interactions, Slender Structures and Axial Flow, Volume 1.* Elsevier Academic Press, First Edition.

Païdoussis, M. P. 2004 *Fluid-Structure Interactions, Slender Structures and Axial Flow, Volume 2.* Elsevier Academic Press, First Edition.

Park, J. B. & Lakes, R. S. 1992 *Biomaterials, An Introduction.* Plenum Press, Second Edition.

Perez-Padilla, J. R., Slawinski, E., Difrancesco, L. M., Feige, R. R., Remmers, J. E. & Whitelaw, W. A. 1993 Characteristics of the snoring noise in patients with and without occlusive sleep apnea. *American Review of Respiratory Disease* **147**(3):635-644.

Rayleigh, Lord 1879 On the instability of jets. *Proceedings of the London Mathematical Society* **10**:4-12.

Rayleigh, Lord 1945 *Theory of Sound, Volumes 1 and 2.* Dover, First American Edition.

Ross, R. 1986 The pathogenesis of atherosclerosis - an update. *New England Journal of Medicine* **314**(8):488-500.

Sarpkaya, T. 1989 Computational Methods with Vortices - The 1988 Freeman Scholar Lecture. *Journal of Fluids Engineering* **111**:5-52.

Scanlan, R. H. & Rosenbaum, R. 1960 *Introduction to the Study of Aircraft Vibration and Flutter.* Macmillan, Second Edition.

Schoenstein, R. 1997 *Stop the Snoring: At Last, End Your Mate's Nocturnal Noise.* Warner Books.

Schwab, R. J., Gupta, K. B., Gefter, W. B., Metzger, L. J., Hoffman, E.A. & Pack, A. I. 1995 Upper airway and soft tissue anatomy in normal subjects and patients with sleep-disordered breathing. Significance of the lateral pharyngeal walls. *American Journal of Respiratory and Critical Care Medicine* **152**(5):1673-1689.

Shayo, L. K. 1980 The stability of cantilever panels in uniform incompressible flow. *Journal of Sound and Vibration* **68**(3):341-350.

Stearman, R. 1959 Small aspect ratio panel flutter. *California Institute of Technology Report* AFOSR-TR 1,59-45.

Szilard, R. 1974 *Theory and Analysis of Plates, Classical and Numerical Methods.* Prentice Hall, First Edition.

Taneda, S. 1968 Waving motions of flag. *Journal of the Physical Society of Japan* **24**:393-401.

Tanida, Y. 2001 Stability of a Soft Plate in Channel Flow (Aerodynamic Aspects of Palatal Flutter). *Japanese Society of Mechanical Engineers* Series B **44**(1):8-13.

Thoma, D. 1939 Why does the flag flutter? Cornell Aeronautical Laboratory translation, 1949. (Translated from *Mitteilungen des Hydraulischen, Institut der Technischen Hochschule, Munich* **9**:30-34.)

Tritton, D. J. 1999 *Physical Fluid Dynamics.* Oxford University Press, Second Edition (reprint).

Twain, M. 1980 *The Adventures of Tom Sawyer; Tom Sawyer Abroad; Tom Sawyer Detective.* (edited by John C. Gerber, Paul Baender and Terry Firkins). University of California Press for the Iowa Center for Textual Studies.

Watanabe, Y., Suzuki, S., Sugihara, M. & Sueoka, Y. 2002a An Experimental Study of Paper Flutter. *Journal of Fluids and Structures* **16**(4):529-542.

Watanabe, Y., Isogai, K., Suzuki, S. & Sugihara, M. 2002b A Theoretical Study of Paper Flutter. *Journal of Fluids and Structures* **16**(4):543-560.

Weaver, D. S. & Unny, T. E. 1970 The Hydroelastic Stability of a Flat Plate. *ASME, Journal of Applied Mechanics* **37**(1):823-827.

Wu, X. & Kaneko, S. 2004 Linear and nonlinear analysis of sheet flutter induced by leakage flow. *Proceedings of the 8th International Conference on Flow-Induced Vibrations,* **Paper 215**.

Yadykin, Y., Tenetov, V. & Levin, D. 2001 The Flow-Induced Vibration of a Flexible Strip Hanging Vertically in a Parallel Flow. Part 1: Temporal Aeroelastic Instability. *Journal of Fluids and Structures* **15**:1167-1185.

Yamaguchi, N., Yokota, K. & Tsujimoto, Y. 2000a Flutter Limits and Behaviours of a Flexible Thin Sheet in High Speed Flow - I: Analytical Method for Prediction of the Sheet Behaviour. *Journal of Fluids Engineering* **122**:65-73.

Yamaguchi, N., Sekiguchi, T., Yokota, K. & Tsujimoto, Y. 2000b Flutter Limits and Behaviours of a Flexible Thin Sheet in High Speed Flow - II: Experimental Results and Predicted Behaviours for Low Mass Ratios. *Journal of Fluids Engineering* **122**:74-83.

Zhang, J., Childress, S., Libchaber, A. & Shelley, M. 2000 Flexible filaments in a flowing soap film as a model for one-dimensional flags in a two-dimensional wind. *Nature* **408**:835-839.

Zhu, L. & Peskin, C. S. 2002 Simulation of a Flapping Flexible Filament in a Flowing Soap Film by the Immersed Boundary Method. *Journal of Computational Physics* **179**:452-468.

Appendices

Appendix A

Medical Information

A.1 The Upper Airway

This section details further information, adapted from the descriptions of Amatoury (2004) and Balint (2001), on the structure and functions of the upper airway (illustrated in figure A.1) that are of relevance to the snoring phenomenon.

A.1.1 Passage of Air

During nasal breathing air first enters through the external nares; these open up into two parallel pathways separated by a cartilaginous septum within the nasal cavity. It is here that air passes through the conduits formed by the complex scroll-like superior, middle and inferior nasal turbinate structures, covered with mucosal epithelium. Inhaled gas exits the nasal cavity via the posterior nasal turbinates and then transits to the nasopharynx. The inferior border of the nasopharynx is defined by the hard and soft palate. The hard palate is a bony structure covered by a mucous membrane and acts as a physical divider of the oral and nasal cavities. It is then that air will pass the soft palate, a section of movable epithelial and skeletal muscle tissue attached to the hard palate, to enter the oropharynx. The inhaled gas traverses the oropharynx into the laryngopharynx before entering the glottis and transiting the laryngeal lumen and

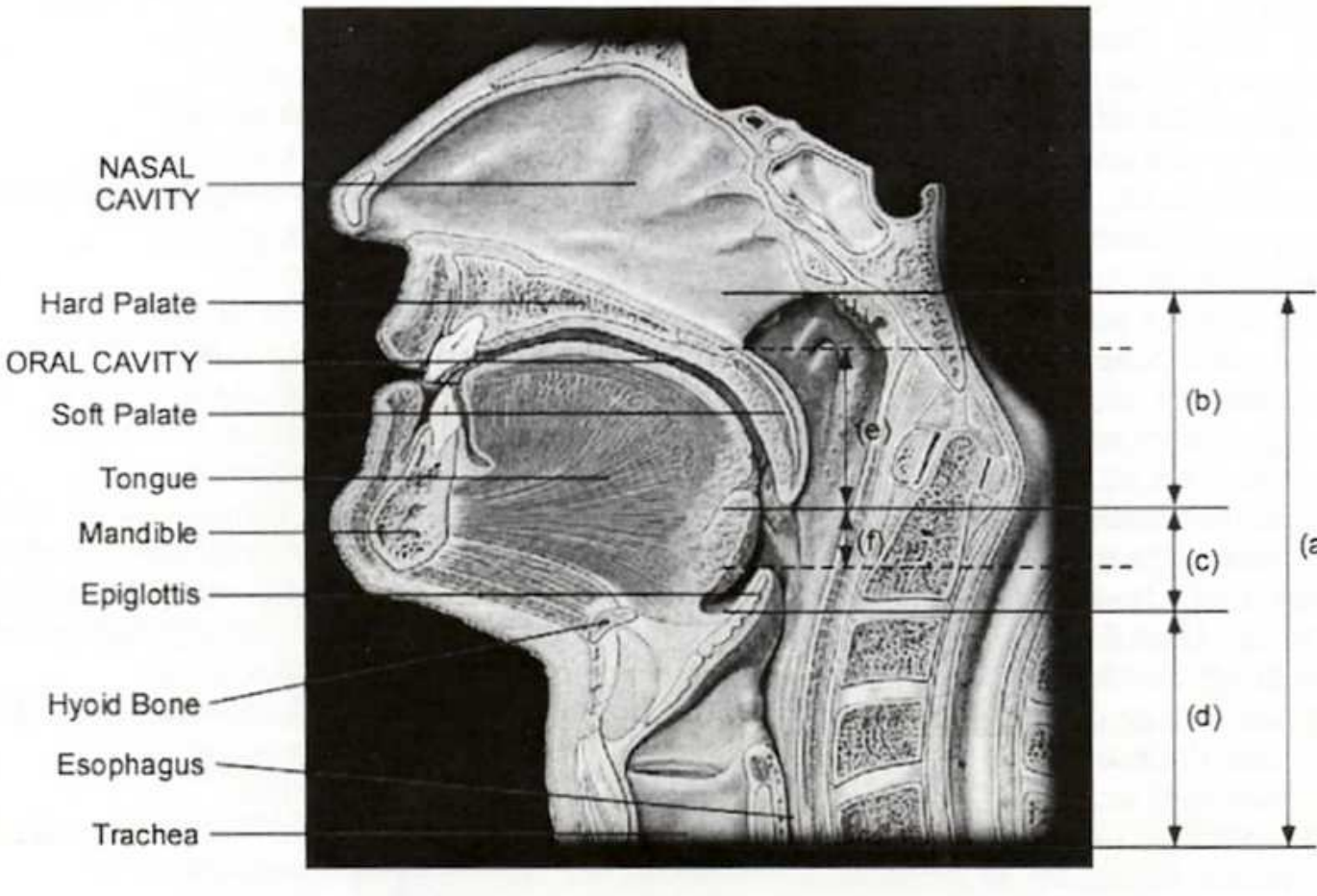

Figure A.1: Saggital view of the human skull and neck: (a) pharynx; (b) nasopharynx; (c) oropharynx; (d) laryngopharynx; (e) retropalatal segment; (f) retroglossal segment (from Amatoury (2004)).

trachea to reach the lungs within the thoracic cavity. Air can also flow to the lungs via the mouth through the oral cavity, passing over the tongue and below the hard and soft palates, before joining the path of nasal air at the oropharynx.

A.1.2 Bone & Tissue Structure

Non-muscular structures in the upper airway include the tonsils, parts of the lateral pharyngeal walls and mobile craniofacial bone structures that determine the airway's size (including the mandible and hyoid bone). The hyoid bone is suspended only by

ligaments and muscles (no bone or cartilaginous connections). These bone structures serve as sites for muscle attachments that permit force transfer to the upper airway walls when the muscles contract, thus modifying the size and stability of the airway. The upper airway is composed of approximately twenty-four muscles that permit changes in the airways configuration via constriction and dilation. The muscles of the upper airway are concentrated in four areas and include those which regulate the movement of the soft palate and uvula (which hangs from the middle border of the soft palate), the tongue, the hyoid apparatus and the posteriolateral pharyngeal walls. Except for the posterior vertebral column, the oropharynx and the caudal part of the nasopharynx have no bone or cartilaginous support and so posses an elastic constitution, resulting in a highly deformable lumen. These are the most deformable regions of the upper airway and hence the most prone to collapse. The most deformable regions are:

- **the retropalatal segment**: the region of the nasopharynx that is posterior to the soft palate, see figure A.1(e);
- **the retroglossal segment**: the area of the oropharynx that is posterior to the base of the tongue, see figure A.1(f).

The anterior wall of retropalatal and retroglossal regions is dominated by the tongue and soft palate, whereas the posterior wall has constrictor muscles (superior, middle and inferior) as the bulk of its construction. These muscles make up a portion of the lateral walls that consist of a complex structural network of other muscles, lymphoid tissue and pharyngeal mucosa. The precise manner in which these muscles interact is complicated and not yet completely understood.

A.1.3 Upper Airway Functions

Of the numerous physiological functions the upper airway performs, its major function is *breathing*, permitting air movement into and out of the lungs (the regulation of both inspiratory and expiratory airflow). During nasal breathing, the hairs lining the nasal

cavity behave as a filter to remove particulate matter. These nasal turbinates further circulate the air around the nasal cavity to warm, filter and humidify the inspired air as it crosses the nasal epithelium. In the nasal cavity, inspired air exposes the olfactory nerves to various aromas from the environment. When airflow increases, breathing becomes oral in addition to nasal. If one was required to breathe at all times the upper airway would be rigid and permanently open. However, the secondary function of the upper airway is *deglutition* and this requires the upper airway to be soft, distensible and collapsible thus allowing the passage of solid and liquid foods while swallowing. The rôle of the soft palate is to move posteriorly against the wall of the pharynx when a person swallows, thereby preventing regurgitation of food into the nasal cavity. Elevation and lowering of the soft palate can also regulate nasal and oral breathing. Other functions of the upper airway are *coughing* and *speech*. Coughing protects the lungs from inhaling foreign objects and clears secretions. The vocal sound known as speech is produced in the larynx within a pair of vocal cords. The larynx is situated in front of the neck above the trachea and is made up of a framework of nine pieces of cartilage bound together by ligaments and muscles lined with mucous membrane.

A.2 The Palate

This section aims to relate the complexity of such a seemingly simple part of the human anatomy. This description of the palate is adapted from Moore and Agur (1995) and Berger (1964). The palate, two views of which are shown in figure A.2, forms the roof of the mouth and the floor of the nasal cavities. The palate consists of two regions: the hard palate (the anterior two-thirds or bony part) and the soft palate (the posterior one-third or fibromuscular part). The hard palate is formed by the palatine process of the maxillae and the horizontal plates of the palatine bones. The incisive foramen is posterior to the central incisor teeth. The incisive canal transmits the nasopalatine nerve and the terminal branch of the sphenopalatine artery. Medial to the third molar tooth the greater palatine foramen pierces the lateral border of the bony palate. The greater

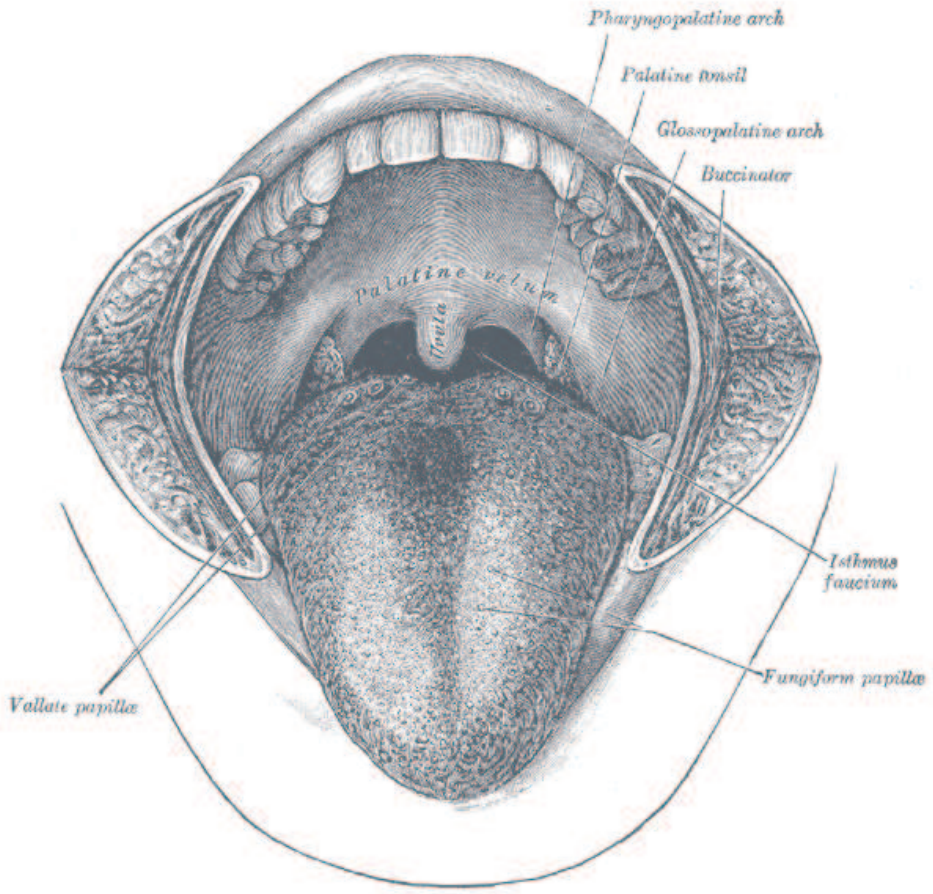

(a) From Gray (1936).

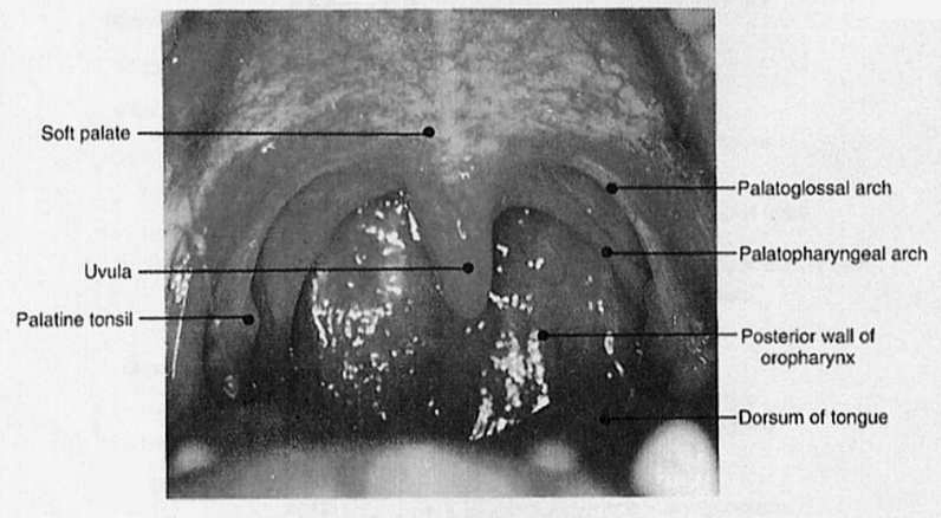

(b) From Moore and Agur (1995).

Figure A.2: Views of the human palate.

palatine vessels and nerve emerge from this foramen and run anteriorly on the palate. The lesser palatine foramina transmit the lesser palatine nerves and vessels to the soft palate and adjacent structures. The soft palate is the posterior fibromuscular part of the palate that is attached to the posterior edge of the hard palate. It extends posterioinferiorly as a curved free margin from which hangs a conical process, the uvula. Laterally the soft palate is continuous with the wall of the pharynx and is joined to the tongue and the pharynx by the palatoglossal and palatopharyngeal arches respectively. The palatine tonsils are two masses of lymphoid tissue, one on each side of the oropharynx. Each is in a tonsillar fossa, bounded by the palatoglossal and palatopharyngeal arches and the tongue. The soft palate is strengthened by the palatine aponeurosis formed by the expanded tendon of the *tensor veli-palatini*. The aponeurosis, attached to the posterior margin of the hard palate, is thick anteriorly and thin posteriorly. The anterior part of the soft palate is formed mainly by the aponeurosis, whereas the posterior part is muscular.

A.2.1 Musculature

Muscles of the soft palate arise from the base of the cranium and descend to the palate. The soft palate may be raised so that it is in contact with the posterior wall of the pharynx. The soft palate can also be drawn inferiorly so that it is in contact with the posterior part of the tongue. The muscles of the soft palate and their independent rôles are:

- *Levator veli-palatini* is a cylindrical muscle that runs inferoanteriorly, spreading out in the soft palate where it attaches to the superior surface of the palatine aponeurosis. It elevates the soft palate during swallowing and yawning;
- *Tensor veli-palatini* is a triangular muscle that passes inferiorly; its tendon hooks around the hamulus of the medial pterygoid plate before inserting into the palatine aponeurosis. It tenses the soft palate and opens the mouth auditory tube during swallowing and yawning;

- *Palatoglossus* is a slender slip of muscle covered with mucous membrane and forms the palatoglossal arch. It elevates the posterior part of the tongue and draws the soft palate onto the tongue;
- *Palatopharyngeus* is a thin flat muscle covered with mucous membrane and forms the palatopharyngeal arch. It tenses the soft palate and pulls the walls of the pharynx superiorly, anteriorly and medially during swallowing;
- *Musculus uvulae* inserts into the mucosa of the uvula. It shortens the uvula and pulls it superiorly.

A.2.2 Blood Supply

The palate has a rich blood supply chiefly from the greater palatine artery on each side, a branch of the descending palatine artery. This artery passes through the greater palatine foramen and runs anteriorly and medially. The lesser palatine artery enters through the lesser palatine foramen and anastomoses with the ascending palatine artery, a branch of the facial artery. The veins of the palate, corresponding and accompanying the branches of the maxillary artery, are tributaries of the pterygoid plexus.

A.2.3 Nervous System

The sensory nerves of the palate are branches of the pterygopalatine ganglion. The greater palatine nerve supplies the gingivae, mucous membrane and glands of most of the hard palate. The nasopalatine nerve supplies the mucous membrane of the anterior part of the hard palate. The lesser palatine nerve supplies the soft palate. The palatine nerves accompany the arteries through the greater and lesser palatine foramina respectively. Except for the *tensor veli-palatini* supplied by the nerve $CN\ V^2$, all muscles of the soft palate are supplied through the pharyngeal plexus of nerves.

A.3 Glossary of Medical Terms

It is anticipated that those who read this thesis will be of an engineering background and therefore it would be of use to have a glossary of the medical terms used. Definitions are adapted from Black's Medical Dictionary (1992), Gray (1918) and The Oxford English Dictionary (2005). It should be noted that although some terms can have several meanings, only the definitions relevant to this thesis are presented. Also, words in italics in definitions are also contained in this glossary.

- **Anastomosis**: term describing the means by which the circulation is carried on when large vessels are narrowed or closed.
- **Anterior**: adjective that describes or relates to the front part of the body, limbs or organs.
- **Aponeurosis**: the white fibrous membrane that serves as an investment for the muscles and covers the skull beneath the scalp.
- **Bronchioles**: term applied to the finest divisions of the bronchus.
- **Bronchus**: (or bronchial tube) name applied to tubes into which the windpipe divides, one going into either lung.
- **Cauda**: a tail or tail-like structure.
- **Concha**: any one of the three turbinated bones of the nose.
- **Diaphragm**: the muscular partition that separates the cavity of the abdomen from that of the chest. It plays the chief part in filling the lungs with air.
- **Epiglottis**: leaf-like piece of elastic cartilage covered with *mucous membrane*, which stands upright between the back of the *tongue* and the *glottis*. In the act of swallowing, it prevents fluids and solids from passing off the back of the *tongue* into the *larynx*.

- **Epithelium**: cellular layer that forms the epidermis of the skin, covers the inner surface of the bowels and forms the linings of ducts and hollow organs. It is part of the *mucous membrane*.
- **Fossa**: term applied to various depressions or holes both on the surface of the body and in internal parts.
- **Gingival**: of or pertaining to the gums.
- **Glottis**: narrow opening at the upper end of the larynx.
- **Hamulus**: hook-like process.
- **Hypocapnia**: a blood tension of carbon dioxide below normal.
- **Hypotonic**: muscles with abnormally reduced tone.
- **Hypoxia**: a blood tension of oxygen below normal.
- **Inferior**: situated below.
- **Larynx**: voice box.
- **Lumen**: the space enclosed by a tubular structure or hollow organ.
- **Lymphoid tissue**: tissue involved in the formation of lymph, lymphocyte and anti-bodies.
- **Margin**: border, strip near edge.
- **Medial**: near the middle of tissue, organ or body.
- **Mucosa**: see *mucous membrane*.
- **Mucous Membrane**: membrane that lines many of the hollow organs of the body. The *epithelium* is part of this along with a basis of fibrous tissue in which blood vessels, nerves and mucous glands lie.
- **Nares**: nostrils

- **Oesophagus**: tube that conveys food and drink from the pharynx down to the stomach.
- **Pharynx**: throat.
- **Plexus**: a network of nerves or vessels.
- **Posterior**: adjective that describes or relates to the rear part of the body, limbs or organs.
- **Septum**: a dividing wall within a structure in the body.
- **Superior**: situated above.
- **Supine**: lying on the back, face upwards.
- **Thorax**: the chest.
- **Tidal volume**: the amount of air that moves into and out of the lungs at each breath during normal, quiet breathing (typically 500 ml).
- **Thoracic Cavity**: the cavity inside the chest.
- **Tongue**: the primary uses of the tongue are: a) to push food between the teeth for mastication and then mould it into a bolus preparatory to swallowing; b) the organ of the sense of taste; and c) to play a part in the production of speech.
- **Tonsils**: have a structure resembling that of a lymphatic gland and play an important rôle in the protective mechanism of the body against infection.
- **Trachea**: windpipe.
- **Turbinates**: a lamina of spongy bone, curled upon itself like a scroll. An individual turbinated bone of the nose is known as a *concha*.

Appendix B

Equation Derivations

B.1 Perturbation-Velocity Influence-Coefficients

These derivations are based upon those in Houghton and Carpenter (2003). Referring to figure B.1(a), the perturbation velocity induced at a point p by a source or a vortex singularity-distribution respectively on panel m is

$$\underline{u}_p^{'\sigma} = u_p^{x\sigma}\underline{t}_m + u_p^{y\sigma}\underline{n}_m, \tag{B.1}$$

$$\underline{u}_p^{'\Gamma} = -u_p^{x\Gamma}\underline{t}_m + u_p^{y\Gamma}\underline{n}_m, \tag{B.2}$$

noting that, following convention, vorticity is positive anticlockwise. The individual vector components of the perturbation velocities are equated as

$$u_p^{x\sigma} = I_{pm}^{x\sigma}\sigma_m, \tag{B.3}$$

$$u_p^{y\sigma} = I_{pm}^{y\sigma}\sigma_m, \tag{B.4}$$

$$u_p^{x\Gamma} = I_{pm}^{x\gamma}\gamma_m + I_{pm}^{x\lambda}\lambda_m, \tag{B.5}$$

$$u_p^{y\Gamma} = I_{pm}^{y\gamma}\gamma_m + I_{pm}^{y\lambda}\lambda_m. \tag{B.6}$$

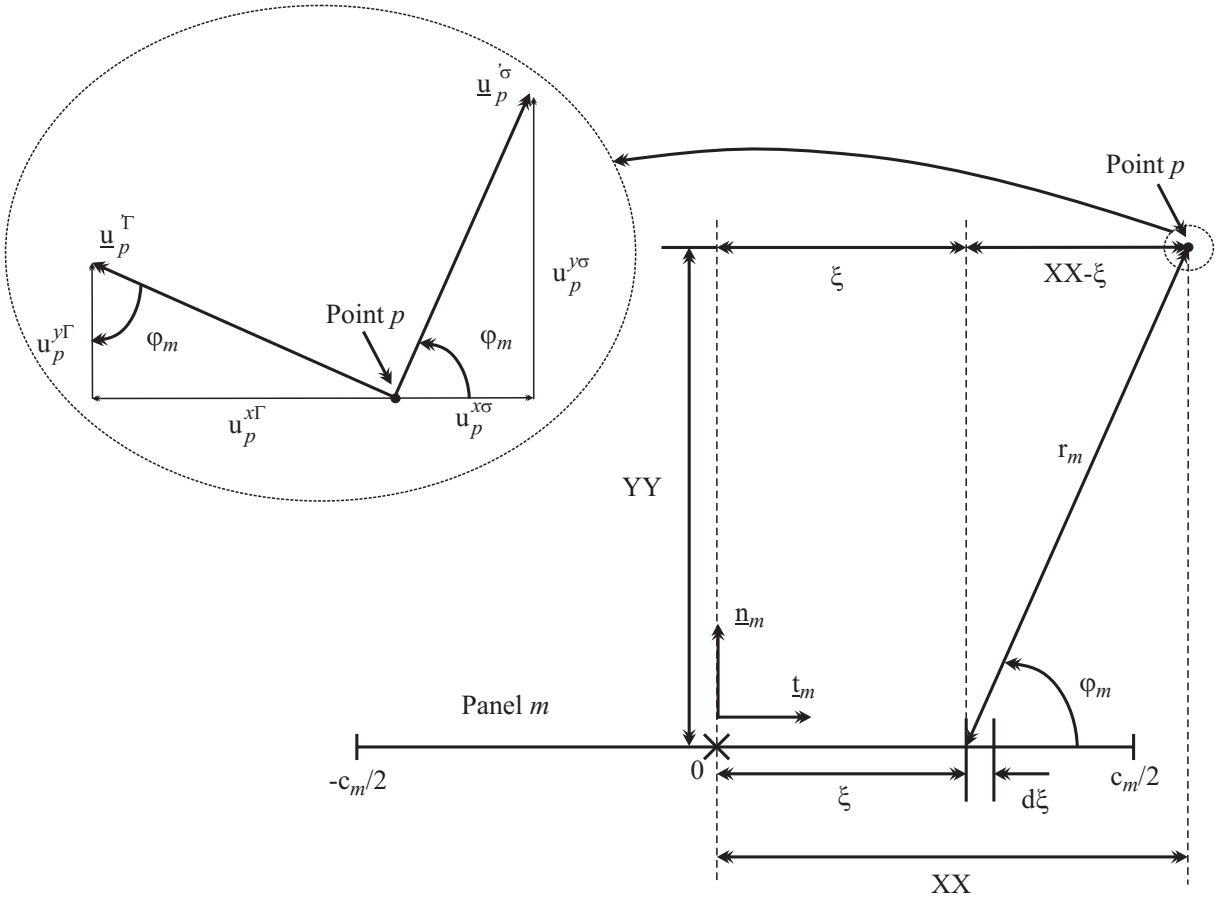

(a) General set-up.

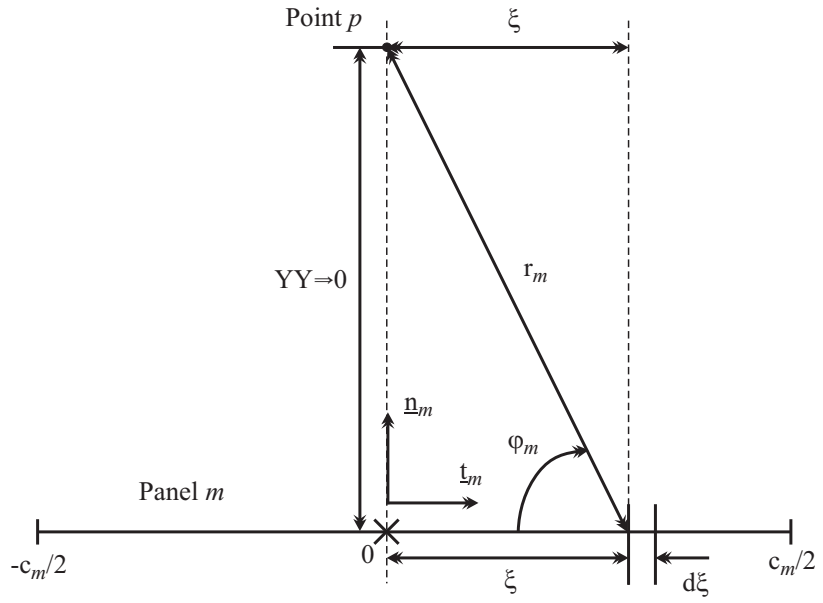

(b) Set-up for calculation of self-induced panel influence-coefficients.

Figure B.1: Set-up of the panel method.

The influence coefficients I^x_{pm} and I^y_{pm} are now derived for the generic panel m. The individual singularity velocities are taken from (3.25), redisplayed below

$$\begin{aligned}\frac{1}{2}\sigma_i &+ \sum_{m=1}^{M_w}\sigma_m\left\{\frac{1}{2\pi}\int_m\frac{\partial}{\partial n_i}(\ln|r-r_\xi|)d\xi_m\right\}+\sum_{m=1}^{M_{cs}}\gamma_m\left\{\frac{1}{2\pi}\int_m\frac{1}{r}\frac{\partial}{\partial\varphi_m}\varphi_m d\xi_m\right\}-\\ \frac{c_i}{2\pi}\lambda_i &+ \sum_{m=1}^{M_{cs}}\lambda_m\xi_m\left\{\frac{1}{2\pi}\int_m\frac{1}{r}\frac{\partial}{\partial\varphi_m}\varphi_m d\xi_m\right\}+\underline{U}_\infty.\underline{n}_i=\underline{\dot{w}}_i.\underline{n}_i.\end{aligned} \tag{B.7}$$

B.1.1 General Influence-Coefficients

Source Influence-Coefficients

$$\begin{aligned}u_p^{x\sigma} &= \frac{\sigma_m}{2\pi}\int_{-\frac{c_m}{2}}^{\frac{c_m}{2}}\frac{1}{r_m}\cos\varphi_m\,d\xi\\ &= \frac{\sigma_m}{2\pi}\int_{-\frac{c_m}{2}}^{\frac{c_m}{2}}\frac{XX-\xi}{r_m^2}d\xi\\ &= \frac{\sigma_m}{2\pi}\int_{-\frac{c_m}{2}}^{\frac{c_m}{2}}\frac{XX-\xi}{(XX-\xi)^2+YY^2}\,d\xi\\ &= \sigma_m\left[-\frac{1}{4\pi}\ln\left|(XX-\xi)^2+YY^2\right|\right]_{-\frac{c_m}{2}}^{\frac{c_m}{2}}\\ &= \sigma_m\left(\left[-\frac{1}{4\pi}\ln\left|(XX-\frac{c_m}{2})^2+YY^2\right|\right]-\left[-\frac{1}{4\pi}\ln\left|(XX+\frac{c_m}{2})^2+YY^2\right|\right]\right)\\ &= I_{pm}^{x\sigma}\sigma_m\end{aligned} \tag{B.8}$$

$$\begin{aligned}u_p^{y\sigma} &= \frac{\sigma_m}{2\pi}\int_{-\frac{c_m}{2}}^{\frac{c_m}{2}}\frac{1}{r_m}\sin\varphi_m\,d\xi\\ &= \frac{\sigma_m}{2\pi}\int_{-\frac{c_m}{2}}^{\frac{c_m}{2}}\frac{YY}{r_m^2}d\xi\\ &= \frac{\sigma_m}{2\pi}\int_{-\frac{c_m}{2}}^{\frac{c_m}{2}}\frac{YY}{(XX-\xi)^2+YY^2}d\xi\\ &= \sigma_m\left[-\frac{1}{2\pi}\tan^{-1}\left(\frac{XX-\xi}{YY}\right)\right]_{-\frac{c_m}{2}}^{\frac{c_m}{2}}\\ &= \sigma_m\left(\left[-\frac{1}{2\pi}\tan^{-1}\left(\frac{XX-\frac{c_m}{2}}{YY}\right)\right]-\left[-\frac{1}{2\pi}\tan^{-1}\left(\frac{XX+\frac{c_m}{2}}{YY}\right)\right]\right)\\ &= I_{pm}^{y\sigma}\sigma_m\end{aligned} \tag{B.9}$$

Zero-order Vortex Influence-Coefficients

$$
\begin{aligned}
u_p^{x\gamma} &= \int_{-\frac{c_m}{2}}^{\frac{c_m}{2}} \frac{\gamma_m}{2\pi r_m}(-\sin\varphi_m)\ d\xi \\
&= -\int_{-\frac{c_m}{2}}^{\frac{c_m}{2}} \frac{\gamma_m YY}{2\pi r_m^2} d\xi \\
&= -\frac{\gamma_m YY}{2\pi}\int_{-\frac{c_m}{2}}^{\frac{c_m}{2}} \frac{1}{(XX-\xi)^2+YY^2} d\xi \\
&= \frac{\gamma_m YY}{2\pi}\left[\frac{1}{YY}\tan^{-1}\left(\frac{XX-\xi}{YY}\right)\right]_{-\frac{c_m}{2}}^{\frac{c_m}{2}} \\
&= \gamma_m\Bigg(\left[\frac{1}{2\pi}\tan^{-1}\left(\frac{XX-\frac{c_m}{2}}{YY}\right)\right]-\left[\frac{1}{2\pi}\tan^{-1}\left(\frac{XX+\frac{c_m}{2}}{YY}\right)\right]\Bigg) \\
&= I_{pm}^{x\gamma}\gamma_m
\end{aligned}
\tag{B.10}
$$

$$
\begin{aligned}
u_p^{y\gamma} &= \int_{-\frac{c_m}{2}}^{\frac{c_m}{2}} \frac{\gamma_m}{2\pi r_m}\cos\varphi_m\ d\xi \\
&= \int_{-\frac{c_m}{2}}^{\frac{c_m}{2}} \frac{\gamma_m(XX-\xi)}{2\pi r_m^2}\ d\xi \\
&= \frac{\gamma_m}{2\pi}\int_{-\frac{c_m}{2}}^{\frac{c_m}{2}} \frac{(XX-\xi)}{(XX-\xi)^2+YY^2}\ d\xi \\
&= \frac{\gamma_m}{2\pi}\left[-\frac{1}{2}\ln\left|(XX-\xi)^2+YY^2\right|\right]_{-\frac{c_m}{2}}^{\frac{c_m}{2}} \\
&= \gamma_m\Bigg(\left[-\frac{1}{4\pi}\ln\left|(XX-\frac{c_m}{2})^2+YY^2\right|\right]-\left[-\frac{1}{4\pi}\ln\left|(XX+\frac{c_m}{2})^2+YY^2\right|\right]\Bigg) \\
&= I_{pm}^{y\gamma}\gamma_m
\end{aligned}
\tag{B.11}
$$

First-order Vortex Influence Coefficients

$$
\begin{aligned}
u_p^{x\lambda} &= \int_{-\frac{c_m}{2}}^{\frac{c_m}{2}} \frac{\lambda_m \xi}{2\pi r_m}(-\sin\varphi_m)\, d\xi \\
&= -\int_{-\frac{c_m}{2}}^{\frac{c_m}{2}} \frac{\lambda_m \xi YY}{2\pi r_m^2} d\xi \\
&= -\frac{\lambda_m YY}{2\pi}\int_{-\frac{c_m}{2}}^{\frac{c_m}{2}} \frac{\xi}{(XX-\xi)^2+YY^2} d\xi \\
&= \frac{\lambda_m YY}{2\pi}\int_{-\frac{c_m}{2}}^{\frac{c_m}{2}} \frac{XX-\xi-XX}{(XX-\xi)^2+YY^2} d\xi \\
&= \lambda_m\left[-\frac{YY}{4\pi}\ln\left|(XX-\xi)^2+YY^2\right| + \frac{XX}{2\pi}\tan^{-1}\left(\frac{XX-\xi}{YY}\right)\right]_{-\frac{c_m}{2}}^{\frac{c_m}{2}} \\
&= \lambda_m\Bigg(\left[-\frac{YY}{4\pi}\ln\left|(XX-\frac{c_m}{2})^2+YY^2\right| + \frac{XX}{2\pi}\tan^{-1}\left(\frac{XX-\frac{c_m}{2}}{YY}\right)\right] \\
&\quad - \left[-\frac{YY}{4\pi}\ln\left|(XX+\frac{c_m}{2})^2+YY^2\right| + \frac{XX}{2\pi}\tan^{-1}\left(\frac{XX+\frac{c_m}{2}}{YY}\right)\right]\Bigg) \\
&= I_{pm}^{x\lambda}\lambda_m
\end{aligned}
\tag{B.12}
$$

$$
\begin{aligned}
u_p^{y\lambda} &= \int_{-\frac{c_m}{2}}^{\frac{c_m}{2}} \frac{\lambda_m \xi}{2\pi r_m}\cos\varphi_m\, d\xi \\
&= \int_{-\frac{c_m}{2}}^{\frac{c_m}{2}} \frac{\lambda_m \xi(XX-\xi)}{2\pi r_m^2}\, d\xi \\
&= \frac{\lambda_m}{2\pi}\int_{-\frac{c_m}{2}}^{\frac{c_m}{2}} \frac{\xi(XX-\xi)}{(XX-\xi)^2+YY^2}\, d\xi \\
&= -\frac{\lambda_m}{2\pi}\int_{-\frac{c_m}{2}}^{\frac{c_m}{2}} \frac{(XX-\xi)^2-(XX-\xi)XX}{(XX-\xi)^2+YY^2}\, d\xi \\
&= -\frac{\lambda_m}{2\pi}\int_{-\frac{c_m}{2}}^{\frac{c_m}{2}} \left(1-\frac{YY^2}{(XX-\xi)^2+YY^2}-\frac{(XX-\xi)XX}{(XX-\xi)^2+YY^2}\right) d\xi \\
&= \lambda_m\left[-\frac{\xi}{2\pi}-\frac{YY}{2\pi}\tan^{-1}\left(\frac{XX-\xi}{YY}\right)-\frac{XX}{4\pi}\ln\left|(XX-\xi)^2+YY^2\right|\right]_{-\frac{c_m}{2}}^{\frac{c_m}{2}} \\
&= \lambda_m\Bigg(\left[-\frac{c_m}{4\pi}-\frac{YY}{2\pi}\tan^{-1}\left(\frac{XX-\frac{c_m}{2}}{YY}\right)-\frac{XX}{4\pi}\ln\left|(XX-\frac{c_m}{2})^2+YY^2\right|\right] \\
&\quad - \left[\frac{c_m}{4\pi}-\frac{YY}{2\pi}\tan^{-1}\left(\frac{XX+\frac{c_m}{2}}{YY}\right)-\frac{XX}{4\pi}\ln\left|(XX+\frac{c_m}{2})^2+YY^2\right|\right]\Bigg) \\
&= I_{pm}^{y\lambda}\lambda_m
\end{aligned}
\tag{B.13}
$$

B.1.2 Self-Induced Panel Influence-Coefficients

This occurs when a panel influences itself; the situation is illustrated in figure B.1(b). YY is reduced to zero in the final steps of all the following derivations.

Source Influence-Coefficients

$$\begin{aligned}
u_p^{x\sigma}\big|_{p=m} &= \frac{\sigma_m}{2\pi}\int_{-\frac{c_m}{2}}^{\frac{c_m}{2}} \frac{1}{r_m}(-\cos\varphi_m)\ d\xi \\
&= \frac{\sigma_m}{2\pi}\int_{-\frac{c_m}{2}}^{\frac{c_m}{2}} \frac{\xi}{r_m^2} d\xi \\
&= \frac{\sigma_m}{2\pi}\int_{-\frac{c_m}{2}}^{\frac{c_m}{2}} \frac{\xi}{\xi^2+YY^2}\ d\xi \\
&= \frac{\sigma_m}{2\pi}\left[\frac{1}{2}\ln\left|\xi^2+YY^2\right|\right]_{-\frac{c_m}{2}}^{\frac{c_m}{2}} \\
&= \frac{\sigma_m}{2\pi}\frac{1}{2}\ln\left|\frac{\frac{c_m^2}{4}+YY^2}{\frac{c_m^2}{4}+YY^2}\right| \\
&= 0
\end{aligned} \tag{B.14}$$

$$\begin{aligned}
u_p^{y\sigma}\big|_{p=m} &= \frac{\sigma_m}{2\pi}\int_{-\frac{c_m}{2}}^{\frac{c_m}{2}} \frac{1}{r_m}\sin\varphi_m\ d\xi \\
&= \frac{\sigma_m}{2\pi}\int_{-\frac{c_m}{2}}^{\frac{c_m}{2}} \frac{YY}{r_m^2} d\xi \\
&= \frac{\sigma_m YY}{2\pi}\int_{-\frac{c_m}{2}}^{\frac{c_m}{2}} \frac{1}{\xi^2+YY^2} d\xi \\
&= \frac{\sigma_m YY}{2\pi}\left[\frac{1}{YY}\tan^{-1}\left(\frac{\xi}{YY}\right)\right]_{-\frac{c_m}{2}}^{\frac{c_m}{2}} \\
&= \frac{\sigma_m}{2\pi}\ 2\tan^{-1}\left(\frac{\frac{c_m}{2}}{YY}\right) \\
&= \frac{\sigma_m}{\pi}\ \tan^{-1}(\infty)
\end{aligned} \tag{B.15}$$

Zero-order Vortex Influence-Coefficients

$$
\begin{aligned}
u_p^{x\gamma}\big|_{p=m} &= \int_{-\frac{c_m}{2}}^{\frac{c_m}{2}} \frac{\gamma_m}{2\pi r_m}(-\sin\varphi_m)\ d\xi \\
&= -\int_{-\frac{c_m}{2}}^{\frac{c_m}{2}} \frac{\gamma_m YY}{2\pi r_m^2} d\xi \\
&= -\frac{\gamma_m YY}{2\pi}\int_{-\frac{c_m}{2}}^{\frac{c_m}{2}} \frac{1}{\xi^2 + YY^2} d\xi \\
&= -\frac{\gamma_m YY}{2\pi}\left[\frac{1}{YY}\tan^{-1}\left(\frac{\xi}{YY}\right)\right]_{-\frac{c_m}{2}}^{\frac{c_m}{2}} \\
&= -\frac{\gamma_m}{2\pi}\ 2\tan^{-1}\left(\frac{\frac{c_m}{2}}{YY}\right) \\
&= -\frac{\gamma_m}{\pi}\ \tan^{-1}(\infty)
\end{aligned}
\tag{B.16}
$$

$$
\begin{aligned}
u_p^{y\gamma}\big|_{p=m} &= \int_{-\frac{c_m}{2}}^{\frac{c_m}{2}} \frac{\gamma_m}{2\pi r_m}(-\cos\varphi_m)\ d\xi \\
&= -\int_{-\frac{c_m}{2}}^{\frac{c_m}{2}} \frac{\gamma_m \xi}{2\pi r_m^2}\ d\xi \\
&= -\frac{\gamma_m}{2\pi}\int_{-\frac{c_m}{2}}^{\frac{c_m}{2}} \frac{\xi}{\xi^2 + YY^2}\ d\xi \\
&= -\frac{\gamma_m}{2\pi}\left[\frac{1}{2}\ln\left|\xi^2 + YY^2\right|\right]_{-\frac{c_m}{2}}^{\frac{c_m}{2}} \\
&= -\frac{\gamma_m}{2\pi}\frac{1}{2}\ln\left|\frac{\frac{c_m^2}{4} + YY^2}{\frac{c_m^2}{4} + YY^2}\right| \\
&= 0
\end{aligned}
\tag{B.17}
$$

First-order Vortex Influence-Coefficients

$$
\begin{aligned}
u_p^{x\lambda}\big|_{p=m} &= \int_{-\frac{c_m}{2}}^{\frac{c_m}{2}} \frac{\lambda_m \xi}{2\pi r_m}(-\sin\varphi_m)\ d\xi \\
&= -\int_{-\frac{c_m}{2}}^{\frac{c_m}{2}} \frac{\lambda_m \xi Y Y}{2\pi r_m^2} d\xi \\
&= -\frac{\lambda_m Y Y}{2\pi} \int_{-\frac{c_m}{2}}^{\frac{c_m}{2}} \frac{\xi}{\xi^2 + YY^2} d\xi \\
&= -\frac{\lambda_m}{2\pi} \left[\frac{1}{2} \ln \left| \xi^2 + YY^2 \right| \right]_{-\frac{c_m}{2}}^{\frac{c_m}{2}} \\
&= -\frac{\lambda_m}{2\pi} \frac{1}{2} \ln \left| \frac{\frac{c_m^2}{4} + YY^2}{\frac{c_m^2}{4} + YY^2} \right| \\
&= 0
\end{aligned}
\tag{B.18}
$$

$$
\begin{aligned}
u_p^{y\lambda}\big|_{p=m} &= \int_{-\frac{c_m}{2}}^{\frac{c_m}{2}} \frac{\lambda_m \xi}{2\pi r_m}(-\cos\varphi_m)\ d\xi \\
&= -\int_{-\frac{c_m}{2}}^{\frac{c_m}{2}} \frac{\lambda_m \xi^2}{2\pi r_m^2}\ d\xi \\
&= -\frac{\lambda_m}{2\pi} \int_{-\frac{c_m}{2}}^{\frac{c_m}{2}} \frac{\xi^2}{\xi^2 + YY^2}\ d\xi \\
&= -\frac{\lambda_m}{2\pi} \left[\xi - YY \tan^{-1}\left(\frac{\xi}{YY} \right) \right]_{-\frac{c_m}{2}}^{\frac{c_m}{2}} \\
&= -\frac{\lambda_m}{2\pi} \left[c_m \right] \\
&= -\lambda_m \frac{c_m}{2\pi}
\end{aligned}
\tag{B.19}
$$

B.1.3 $YY = 0$ Influence-Coefficients

This situation occurs when panels are at the same height above or below the origin as each other, as in the case of a horizontal infinitely-thin surface.

Source Influence-Coefficients

$$\begin{aligned} u_p^{x\sigma}\big|_{YY=0} &= \frac{\sigma_m}{2\pi}\int_{-\frac{c_m}{2}}^{\frac{c_m}{2}} \frac{1}{r_m}\cos\varphi_m \; d\xi \\ &= \frac{\sigma_m}{2\pi}\int_{-\frac{c_m}{2}}^{\frac{c_m}{2}} \frac{1}{XX-\xi} d\xi \\ &= \frac{\sigma_m}{2\pi}\left[-\ln|XX-\xi|\right]_{-\frac{c_m}{2}}^{\frac{c_m}{2}} \\ &= \sigma_m\left(\frac{1}{2\pi}\ln\left|\frac{(XX+\frac{c_m}{2})}{(XX-\frac{c_m}{2})}\right|\right) \\ &= I_{pm}^{x\sigma}\sigma_m \end{aligned} \tag{B.20}$$

$$\begin{aligned} u_p^{y\sigma}\big|_{YY=0} &= \frac{\sigma_m}{2\pi}\int_{-\frac{c_m}{2}}^{\frac{c_m}{2}} \frac{1}{r_m}\sin\varphi_m \; d\xi \\ &= 0 \end{aligned} \tag{B.21}$$

Zero-order Vortex Influence-Coefficients

$$\begin{aligned} u_p^{x\gamma}\big|_{YY=0} &= \int_{-\frac{c_m}{2}}^{\frac{c_m}{2}} \frac{\gamma_m}{2\pi r_m}(-\sin\varphi_m) \; d\xi \\ &= 0 \end{aligned} \tag{B.22}$$

$$\begin{aligned} u_p^{y\gamma}\big|_{YY=0} &= \int_{-\frac{c_m}{2}}^{\frac{c_m}{2}} \frac{\gamma_m}{2\pi r_m}\cos\varphi_m \; d\xi \\ &= \frac{\gamma_m}{2\pi}\int_{-\frac{c_m}{2}}^{\frac{c_m}{2}} \frac{1}{XX-\xi} \; d\xi \\ &= -\frac{\gamma_m}{2\pi}\left[\ln|XX-\xi|\right]_{-\frac{c_m}{2}}^{\frac{c_m}{2}} \\ &= \gamma_m\left(\frac{1}{2\pi}\ln\left|\frac{(XX+\frac{c_m}{2})}{(XX-\frac{c_m}{2})}\right|\right) \\ &= I_{pm}^{y\gamma}\gamma_m \end{aligned} \tag{B.23}$$

First-order Vortex Influence-Coefficients

$$\begin{aligned} u_p^{x\lambda}\big|_{YY=0} &= \int_{-\frac{c_m}{2}}^{\frac{c_m}{2}} \frac{\lambda_m \xi}{2\pi r_m}(-\sin\varphi_m)\ d\xi \\ &= 0 \end{aligned} \tag{B.24}$$

$$\begin{aligned} u_p^{y\lambda}\big|_{YY=0} &= \int_{-\frac{c_m}{2}}^{\frac{c_m}{2}} \frac{\lambda_m \xi}{2\pi r_m}\cos\varphi_m\ d\xi \\ &= \frac{\lambda_m}{2\pi}\int_{-\frac{c_m}{2}}^{\frac{c_m}{2}} \frac{\xi}{XX-\xi}\ d\xi \\ &= -\frac{\lambda_m}{2\pi}\int_{XX+\frac{c_m}{2}}^{XX-\frac{c_m}{2}} \frac{XX-U}{U}\ dU \\ &= -\frac{\lambda_m}{2\pi}\left[XX\ln|U|-U\right]_{XX+\frac{c_m}{2}}^{XX-\frac{c_m}{2}} \\ &= \frac{\lambda_m}{2\pi}\left(XX\ln\left|\frac{XX+\frac{c_m}{2}}{XX-\frac{c_m}{2}}\right| - c_m\right) \\ &= I_{pm}^{y\lambda}\lambda_m \end{aligned} \tag{B.25}$$

B.1.4 Normal and Tangential Influence-Coefficients

The formulation of the overall normal and tangential influence-coefficients I^N_{pm} and I^T_{pm}, is now illustrated. The total perturbation velocity at point p is

$$\underline{u}'_p = u_p^{'T}\underline{i} + u_p^{'N}\underline{j}$$

As an example, consider that there are only distributions of source singularities in the system. Referring to (B.1), the normal component of the total perturbation velocity at a point p is therefore

$$\begin{aligned} u_p^{'N} &= \underline{u}_p^{'\sigma}.\underline{n}_p \\ &= \left(u_p^{x\sigma}\underline{t}_m + u_p^{y\sigma}\underline{n}_m\right).\underline{n}_p \end{aligned}$$

From (B.3) and (B.4)

$$\begin{aligned} u_p^{'N} &= \left(I^{x\sigma}_{pm}\underline{t}_m.\underline{n}_p + I^{y\sigma}_{pm}\underline{n}_m.\underline{n}_p\right)\sigma_m \\ &= I^{N\sigma}_{pm}\sigma_m \end{aligned} \tag{B.26}$$

Similarly for the tangential influence-coefficient $I^{T\sigma}_{pm}$

$$I^{T\sigma}_{pm} = I^{x\sigma}_{pm}\underline{t}_m.\underline{t}_p + I^{y\sigma}_{pm}\underline{n}_m.\underline{t}_p \tag{B.27}$$

B.2 Velocity-Potential Influence-Coefficients

Referring to (B.7) the velocity potential induced at point p is

$$\begin{aligned}\phi_p &= \sum_{m=1}^{M_w}\sigma_m\left\{\frac{1}{2\pi}\int_m \ln|r-r_\xi|d\xi_m\right\}+\sum_{m=1}^{M_{cs}}\gamma_m\left\{\frac{1}{2\pi}\int_m\varphi_m d\xi_m\right\}+\\ &\quad\sum_{m=1}^{M_{cs}}\lambda_m\xi_m\left\{\frac{1}{2\pi}\int_m\varphi_m d\xi_m\right\},\end{aligned}$$

noting that the velocity potential is a scalar quantity (similar, for example, to temperature) and therefore has no x or y components. The individual source and vortex velocity potentials are equated as

$$\phi_p^\sigma = I_{pm}^{\phi\sigma}\sigma_m, \tag{B.28}$$

$$\phi_p^\Gamma = I_{pm}^{\phi\gamma}\gamma_m + I_{pm}^{\phi\lambda}\lambda_m. \tag{B.29}$$

The influence coefficient I_{pm}^{ϕ} is now derived for the generic panel m.

B.2.1 General Influence-Coefficients

Source Influence-Coefficients

$$\begin{aligned}\phi_p^\sigma &= \sigma_m\frac{1}{4\pi}\int_{-\frac{c_m}{2}}^{\frac{c_m}{2}}\ln|(XX-\xi)^2+YY^2|d\xi\\ &= \sigma_m\frac{-1}{4\pi}\int_{XX+\frac{c_m}{2}}^{XX-\frac{c_m}{2}}\ln|U^2+YY^2|dU\\ &= \sigma_m\frac{-1}{4\pi}\left(\left[U\ln|U^2+YY^2|\right]_{XX+\frac{c_m}{2}}^{XX-\frac{c_m}{2}}-\int_{XX+\frac{c_m}{2}}^{XX-\frac{c_m}{2}}U\frac{2U}{U^2+YY^2}dU\right)\\ &= \sigma_m\frac{-1}{4\pi}\left(\left[U\ln|U^2+YY^2|\right]_{XX+\frac{c_m}{2}}^{XX-\frac{c_m}{2}}-2\left[U-YY\tan^{-1}\left(\frac{U}{YY}\right)\right]_{XX+\frac{c_m}{2}}^{XX-\frac{c_m}{2}}\right)\\ &= \sigma_m\Bigg\{-\frac{XX}{4\pi}\left(\ln|\left(XX-\frac{c_m}{2}\right)^2+YY^2|-\ln|\left(XX+\frac{c_m}{2}\right)^2+YY^2|\right)\\ &\qquad+\frac{c_m}{8\pi}\left(\ln|\left(XX-\frac{c_m}{2}\right)^2+YY^2|+\ln|\left(XX+\frac{c_m}{2}\right)^2+YY^2|\right)\\ &\quad-\frac{c_m}{2\pi}-\frac{YY}{2\pi}\left(\tan^{-1}\left(\frac{XX-\frac{c_m}{2}}{YY}\right)-\tan^{-1}\left(\frac{XX+\frac{c_m}{2}}{YY}\right)\right)\Bigg\}\\ &= I_{pm}^{\phi\sigma}\sigma_m\end{aligned} \tag{B.30}$$

Zero-order Vortex Influence Coefficients

$$
\begin{aligned}
\phi_p^{\gamma} &= \gamma_m \frac{1}{2\pi} \int_{-\frac{c_m}{2}}^{\frac{c_m}{2}} \tan^{-1}\left(\frac{YY}{XX-\xi}\right) d\xi \\
&= \gamma_m \frac{1}{2\pi}\left(\left[\xi \tan^{-1}\left(\frac{YY}{XX-\xi}\right)\right]_{-\frac{c_m}{2}}^{\frac{c_m}{2}} - \int_{-\frac{c_m}{2}}^{\frac{c_m}{2}} \xi \frac{YY}{(XX-\xi)^2+YY^2} d\xi \right) \\
&= \gamma_m \frac{1}{2\pi}\left(\left[\xi \tan^{-1}\left(\frac{YY}{XX-\xi}\right)\right]_{-\frac{c_m}{2}}^{\frac{c_m}{2}} - YY \int_{-\frac{c_m}{2}}^{\frac{c_m}{2}} \frac{-(XX-\xi-XX)}{(XX-\xi)^2+YY^2} d\xi \right) \\
&= \gamma_m \frac{1}{2\pi}\left(\left[\xi \tan^{-1}\left(\frac{YY}{XX-\xi}\right)\right]_{-\frac{c_m}{2}}^{\frac{c_m}{2}} \right. \\
&+ \left. YY\left[-\frac{1}{2}\ln\left|(XX-\xi)^2+YY^2\right| + \frac{XX}{YY}\tan^{-1}\left(\frac{XX-\xi}{YY}\right)\right]_{-\frac{c_m}{2}}^{\frac{c_m}{2}} \right) \\
&= \gamma_m \frac{1}{2\pi}\left\{ \left(\left[\frac{c_m}{2}\tan^{-1}\left(\frac{YY}{XX-\frac{c_m}{2}}\right)\right] - \left[-\frac{c_m}{2}\tan^{-1}\left(\frac{YY}{XX+\frac{c_m}{2}}\right)\right]\right)\right. \\
&+ \left(\left[-\frac{YY}{2}\ln\left|(XX-\frac{c_m}{2})^2+YY^2\right| + XX\tan^{-1}\left(\frac{XX-\frac{c_m}{2}}{YY}\right)\right]\right. \\
&\left.\left. -\left[-\frac{YY}{2}\ln\left|(XX+\frac{c_m}{2})^2+YY^2\right| + XX\tan^{-1}\left(\frac{XX+\frac{c_m}{2}}{YY}\right)\right]\right)\right\} \\
&= \gamma_m \left\{ \frac{c_m}{4\pi}\left(\tan^{-1}\left(\frac{YY}{XX-\frac{c_m}{2}}\right) + \tan^{-1}\left(\frac{YY}{XX+\frac{c_m}{2}}\right)\right)\right. \\
&\quad + \frac{YY}{4\pi}\left(\ln\left|(XX+\frac{c_m}{2})^2+YY^2\right| - \ln\left|(XX-\frac{c_m}{2})^2+YY^2\right|\right) \\
&\quad \left. + \frac{XX}{2\pi}\left(\tan^{-1}\left(\frac{XX-\frac{c_m}{2}}{YY}\right) - \tan^{-1}\left(\frac{XX+\frac{c_m}{2}}{YY}\right)\right)\right\} \\
&= I_{pm}^{\phi\gamma}\gamma_m
\end{aligned}
\tag{B.31}
$$

First-order Vortex Influence Coefficients

$$
\begin{aligned}
\phi_p^{\lambda} &= \lambda_m \frac{1}{2\pi} \int_{-\frac{c_m}{2}}^{\frac{c_m}{2}} \xi \tan^{-1}\left(\frac{YY}{XX-\xi}\right) d\xi \\
&= \lambda_m \frac{1}{2\pi}\left(\left[\frac{1}{2}\xi^2 \tan^{-1}\left(\frac{YY}{XX-\xi}\right)\right]_{-\frac{c_m}{2}}^{\frac{c_m}{2}} - \int_{-\frac{c_m}{2}}^{\frac{c_m}{2}} \frac{1}{2}\xi^2 \frac{YY}{(XX-\xi)^2+YY^2} d\xi \right) \\
&= \lambda_m \frac{1}{2\pi}\left(\left[\frac{1}{2}\xi^2 \tan^{-1}\left(\frac{YY}{XX-\xi}\right)\right]_{-\frac{c_m}{2}}^{\frac{c_m}{2}} \right. \\
&- \frac{YY}{2}\left[\xi + \frac{XX^2+YY^2}{YY}\tan^{-1}\left(\frac{XX-\xi}{YY}\right)\right. \\
&\left.\left. - 2XX\left(-\frac{1}{2}\ln\left|(XX-\xi)^2+YY^2\right| + \frac{XX}{YY}\tan^{-1}\left(\frac{XX-\xi}{YY}\right)\right)\right]_{-\frac{c_m}{2}}^{\frac{c_m}{2}} \right) \\
&= \lambda_m \frac{1}{2\pi}\left(\left[\frac{1}{2}\xi^2 \tan^{-1}\left(\frac{YY}{XX-\xi}\right)\right]_{-\frac{c_m}{2}}^{\frac{c_m}{2}} \right. \\
&- \left.\frac{YY}{2}\left[\xi + \frac{YY^2-XX^2}{YY}\tan^{-1}\left(\frac{XX-\xi}{YY}\right) + XX\ln\left|(XX-\xi)^2+YY^2\right|\right]_{-\frac{c_m}{2}}^{\frac{c_m}{2}} \right) \\
&= \lambda_m \frac{1}{2\pi}\left\{ \left(\left[\frac{1}{2}\left(\frac{c_m}{2}\right)^2 \tan^{-1}\left(\frac{YY}{XX-\frac{c_m}{2}}\right)\right] - \left[\frac{1}{2}\left(\frac{c_m}{2}\right)^2 \tan^{-1}\left(\frac{YY}{XX+\frac{c_m}{2}}\right)\right] \right) \right. \\
&- \frac{YY}{2}\left(\left[\frac{c_m}{2} + \frac{YY^2-XX^2}{YY}\tan^{-1}\left(\frac{XX-\frac{c_m}{2}}{YY}\right) + XX\ln\left|(XX-\frac{c_m}{2})^2+YY^2\right|\right] \right. \\
&\left.\left. - \left[-\frac{c_m}{2} + \frac{YY^2-XX^2}{YY}\tan^{-1}\left(\frac{XX+\frac{c_m}{2}}{YY}\right) + XX\ln\left|(XX+\frac{c_m}{2})^2+YY^2\right|\right] \right) \right\} \\
&= \lambda_m \left\{ \frac{c_m^2}{16\pi}\left(\tan^{-1}\left(\frac{YY}{XX-\frac{c_m}{2}}\right) - \tan^{-1}\left(\frac{YY}{XX+\frac{c_m}{2}}\right)\right) \right. \\
&- \frac{YY c_m}{4\pi} - \frac{YY^2-XX^2}{4\pi}\left(\tan^{-1}\left(\frac{XX-\frac{c_m}{2}}{YY}\right) - \tan^{-1}\left(\frac{XX+\frac{c_m}{2}}{YY}\right)\right) \\
&\left. - \frac{YYXX}{4\pi}\left(\ln\left|(XX-\frac{c_m}{2})^2+YY^2\right| - \ln\left|(XX+\frac{c_m}{2})^2+YY^2\right|\right)\right\} \\
&= I_{pm}^{\phi\lambda}\lambda_m
\end{aligned}
\tag{B.32}
$$

B.2.2 Self-Induced Panel Influence-Coefficients

This occurs when a panel influences itself; the situation is illustrated in figure B.1(b). YY is reduced to zero in the final steps of all the following derivations. For vortices, these values are calculated for upper and lower surfaces of a panel separately and the corresponding derivations are denoted by the superscripts U and L respectively; the final influence-coefficient for vortices is assembled in §3.4.3.

Source Influence-Coefficients

$$\begin{aligned}
\phi_p^{\sigma}\big|_{p=m} &= \sigma_m \frac{1}{4\pi}\int_{-\frac{c_m}{2}}^{\frac{c_m}{2}} \ln|\xi^2+YY^2|d\xi \\
&= \sigma_m \frac{1}{4\pi}\left(\left[\xi\ln|\xi^2+YY^2|\right]_{-\frac{c_m}{2}}^{\frac{c_m}{2}} - \int_{-\frac{c_m}{2}}^{\frac{c_m}{2}} \xi\frac{2\xi}{\xi^2+YY^2}dU\right) \\
&= \sigma_m \frac{1}{4\pi}\left(\left[\xi\ln|\xi^2+YY^2|\right]_{-\frac{c_m}{2}}^{\frac{c_m}{2}} - 2\left[\xi - YY\tan^{-1}\left(\frac{\xi}{YY}\right)\right]_{-\frac{c_m}{2}}^{\frac{c_m}{2}}\right) \\
&= \sigma_m \frac{1}{4\pi}\left\{\left(\left[\frac{c_m}{2}\ln\left|(\frac{c_m}{2})^2+YY^2\right|\right] - \left[-\frac{c_m}{2}\ln\left|(\frac{c_m}{2})^2+YY^2\right|\right]\right)\right. \\
&\quad \left.-2\left(\left[\frac{c_m}{2} - YY\tan^{-1}\left(\frac{\frac{c_m}{2}}{YY}\right)\right] - \left[-\frac{c_m}{2} - YY\tan^{-1}\left(\frac{-\frac{c_m}{2}}{YY}\right)\right]\right)\right\} \\
&= \sigma_m \frac{1}{4\pi}\left\{\frac{c_m}{2}\left(\ln\left|(\frac{c_m}{2})^2+YY^2\right| + \ln\left|(\frac{c_m}{2})^2+YY^2\right|\right)\right. \\
&\quad \left.-2c_m - 2YY\left(YY\tan^{-1}\left(\frac{-\frac{c_m}{2}}{YY}\right) - YY\tan^{-1}\left(\frac{\frac{c_m}{2}}{YY}\right)\right)\right\} \\
&= \left(\frac{c_m}{2\pi}\ln\left|\frac{c_m}{2}\right| - \frac{c_m}{2\pi}\right)\sigma_m
\end{aligned} \tag{B.33}$$

Zero-order Vortex Influence-Coefficients

$$\begin{aligned}
\phi_p^{\gamma}\big|_{p=m}^{L} &= \gamma_m \frac{1}{2\pi}\int_{\frac{c_m}{2}}^{-\frac{c_m}{2}} \tan^{-1}\left(\frac{YY}{\xi}\right)d\xi \\
&= \gamma_m \frac{c_m}{4}
\end{aligned} \tag{B.34}$$

$$\begin{aligned}
\phi_p^{\gamma}\big|_{p=m}^{U} &= \gamma_m \frac{1}{2\pi}\int_{-\frac{c_m}{2}}^{\frac{c_m}{2}} \tan^{-1}\left(\frac{YY}{\xi}\right)d\xi \\
&= \gamma_m \frac{1}{2\pi}\left(\left[\xi\tan^{-1}\left(\frac{YY}{\xi}\right)\right]_{-\frac{c_m}{2}}^{\frac{c_m}{2}} - \int_{-\frac{c_m}{2}}^{\frac{c_m}{2}} \xi\frac{-YY}{\xi^2+YY^2}d\xi\right) \\
&= \gamma_m \frac{1}{2\pi}\left(\left[\xi\tan^{-1}\left(\frac{YY}{\xi}\right)\right]_{-\frac{c_m}{2}}^{\frac{c_m}{2}} + YY\left[\frac{1}{2}\ln|\xi^2+YY^2|\right]_{-\frac{c_m}{2}}^{\frac{c_m}{2}}\right) \\
&= \gamma_m \frac{1}{2\pi}\Bigg\{\left(\left[\frac{c_m}{2}\tan^{-1}\left(\frac{YY}{\frac{c_m}{2}}\right)\right] - \left[-\frac{c_m}{2}\tan^{-1}\left(\frac{YY}{-\frac{c_m}{2}}\right)\right]\right) \\
&\quad + \left(\left[\frac{YY}{2}\ln|\frac{c_m^2}{4}+YY^2|\right] - \left[\frac{YY}{2}\ln|\frac{c_m^2}{4}+YY^2|\right]\right)\Bigg\} \\
&= \gamma_m \frac{1}{2\pi}\left(0+\frac{c_m\pi}{2}\right) \\
&= \gamma_m \frac{c_m}{4}
\end{aligned} \tag{B.35}$$

First-order Vortex Influence Coefficients

$$\begin{aligned}
\phi_p^{\lambda}\big|_{p=m}^{U} &= \lambda_m \frac{1}{2\pi}\int_{-\frac{c_m}{2}}^{\frac{c_m}{2}} \xi\tan^{-1}\left(\frac{YY}{\xi}\right)d\xi \\
&= \lambda_m \frac{1}{2\pi}\left(\left[\frac{1}{2}\xi^2\tan^{-1}\left(\frac{YY}{\xi}\right)\right]_{-\frac{c_m}{2}}^{\frac{c_m}{2}} - \int_{-\frac{c_m}{2}}^{\frac{c_m}{2}} \frac{1}{2}\xi^2\frac{-YY}{\xi^2+YY^2}d\xi\right) \\
&= \lambda_m \frac{1}{2\pi}\left(\left[\frac{1}{2}\xi^2\tan^{-1}\left(\frac{YY}{\xi}\right)\right]_{-\frac{c_m}{2}}^{\frac{c_m}{2}} + \frac{YY}{2}\left[\xi - YY\tan^{-1}\left(\frac{\xi}{YY}\right)\right]_{-\frac{c_m}{2}}^{\frac{c_m}{2}}\right) \\
&= \lambda_m \frac{1}{2\pi}\Bigg\{\frac{c_m^2}{8}\left(\left[\tan^{-1}\left(\frac{YY}{\frac{c_m}{2}}\right)\right] - \left[\tan^{-1}\left(\frac{YY}{-\frac{c_m}{2}}\right)\right]\right) \\
&\quad + \frac{YY}{2}\left(\left[\frac{c_m}{2} - YY\tan^{-1}\left(\frac{\frac{c_m}{2}}{YY}\right)\right] - \left[-\frac{c_m}{2} - YY\tan^{-1}\left(\frac{-\frac{c_m}{2}}{YY}\right)\right]\right)\Bigg\} \\
&= \lambda_m \frac{1}{2\pi}\left(\frac{c_m^2}{8}\left[0-\pi\right]\right) \\
&= \lambda_m \frac{c_m^2}{16}
\end{aligned} \tag{B.36}$$

$$\begin{aligned}
\phi_p^{\lambda}\big|_{p=m}^{L} &= \lambda_m \frac{1}{2\pi}\int_{\frac{c_m}{2}}^{-\frac{c_m}{2}} \xi\tan^{-1}\left(\frac{YY}{\xi}\right)d\xi \\
&= \lambda_m \frac{c_m^2}{16}
\end{aligned} \tag{B.37}$$

B.2.3 $YY = 0$ Influence-Coefficients

This situation occurs when panels are at the same height above or below the origin as each other, as in the case of a horizontal infinitely-thin surface. For vortices, these values are calculated for upper and lower surfaces of a panel separately and the corresponding derivations are denoted by the superscripts U and L respectively. Also, each vortex calculation is carried out at $\varphi_m = 0$ radians and $\varphi_m = \pi$ radians; the final influence-coefficient for vortices is assembled in §3.4.3.

Source Influence-Coefficients

The general source influence coefficient reduces to the required infinitely-thin surface form with no further derivation.

Zero-order Vortex Influence-Coefficients

$$\phi_p^{\gamma}\Big|_{YY=0}^{U,\varphi_m=0} = 0 \tag{B.38}$$

$$\begin{aligned}\phi_p^{\gamma}\Big|_{YY=0}^{U,\varphi_m=\pi} &= \gamma_m \frac{1}{2\pi} \int_{-\frac{c_m}{2}}^{\frac{c_m}{2}} \pi d\xi \\ &= \gamma_m \frac{c_m}{2}\end{aligned} \tag{B.39}$$

$$\phi_p^{\gamma}\Big|_{YY=0}^{L,\varphi_m=0} = 0 \tag{B.40}$$

$$\phi_p^{\gamma}\Big|_{YY=0}^{L,\varphi_m=\pi} = \gamma_m \frac{c_m}{2} \tag{B.41}$$

First-order Vortex Influence Coefficients

$$\phi_p^{\lambda}\big|_{YY=0}^{U,\varphi_m=0} = 0 \tag{B.42}$$

$$\begin{aligned}\phi_p^{\lambda}\big|_{YY=0}^{U,\varphi_m=\pi} &= \gamma_m \frac{1}{2\pi}\int_{-\frac{c_m}{2}}^{\frac{c_m}{2}} \pi\xi d\xi \\ &= \gamma_m \frac{1}{2}\left[\frac{1}{2}\xi^2\right]_{-\frac{c_m}{2}}^{\frac{c_m}{2}} \\ &= 0\end{aligned} \tag{B.43}$$

$$\phi_p^{\lambda}\big|_{YY=0}^{L,\varphi_m=0} = 0 \tag{B.44}$$

$$\phi_p^{\lambda}\big|_{YY=0}^{L,\varphi_m=\pi} = 0 \tag{B.45}$$

B.3 Derivation of XX and YY

It is necessary to recalculate the variables XX and YY in terms of the co-ordinate system based on the panel m. Referring to figure B.2, the vector from panel m to point p, $\underline{mp}$, is equated as

$$\underline{mp} = (X_p - X_m)\underline{i} + (Y_p - Y_m)\underline{j},$$

where (X_p, Y_p) and (X_m, Y_m) are the co-ordinates of the point p and the control point of panel m respectively. Therefore XX and YY in terms of the co-ordinate system based on the panel m are

$$\begin{aligned}XX &= \underline{mp}.\underline{t}_m, \\ YY &= \underline{mp}.\underline{n}_m.\end{aligned}$$

The unit vectors on panel m are equated as

$$\begin{aligned}\underline{t}_m &= \cos\theta_m\underline{i} + \sin\theta_m\underline{j}, \\ \underline{n}_m &= -\sin\theta_m\underline{i} + \cos\theta_m\underline{j},\end{aligned}$$

where θ_m is the angle of panel m to the horizontal. Therefore, the final calculations of XX and YY are

$$XX = [(X_i - X_m)\cos\theta_m] + [(Y_i - Y_m)\sin\theta_m]\,, \tag{B.46}$$

$$YY = [(X_i - X_m)(-\sin\theta_m)] + [(Y_i - Y_m)\cos\theta_m]\,. \tag{B.47}$$

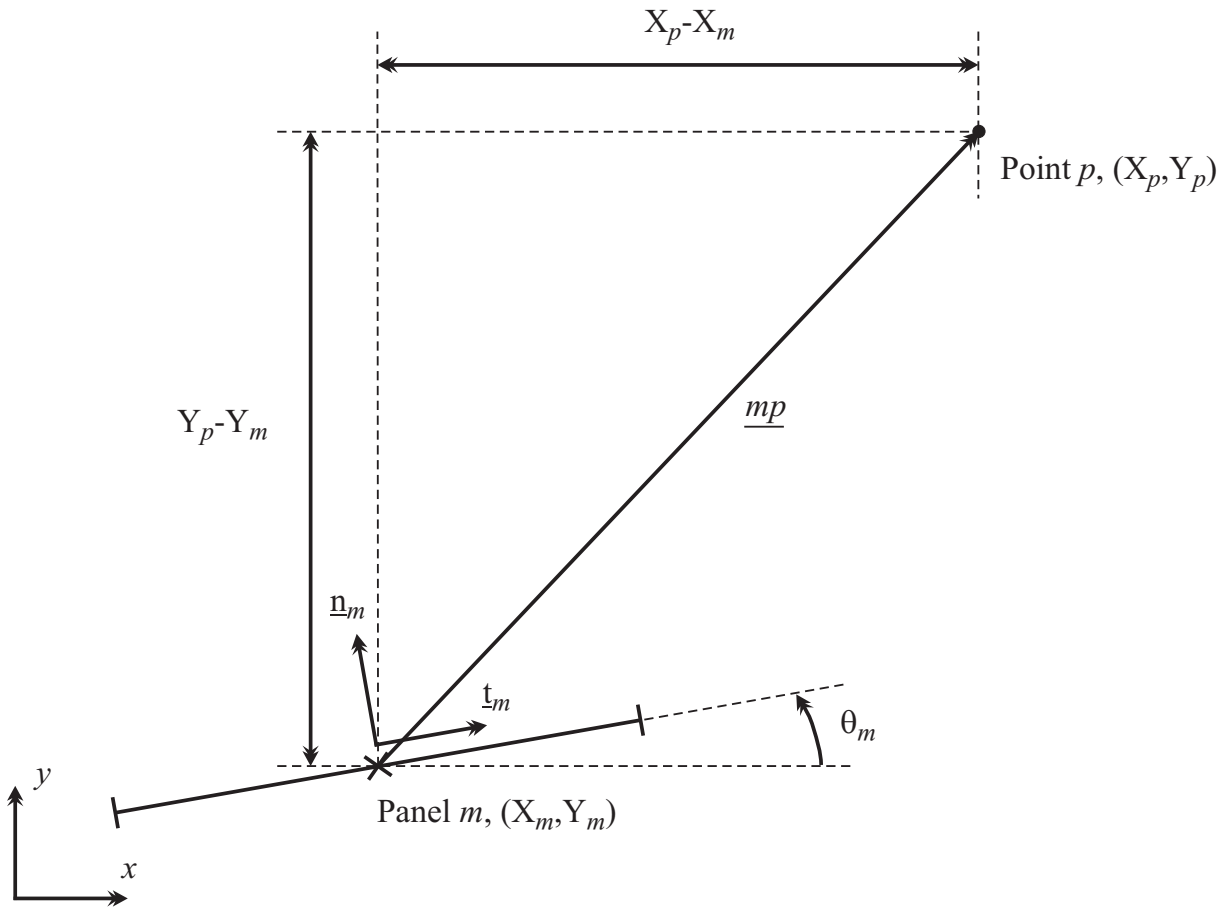

Figure B.2: Calculation of the lengths XX and YY.

B.4 The Unsteady Model

B.4.1 Unsteady Pressure Equation

The flow-structure-system pressure will be governed by the unsteady Bernoulli equation. At a location infinitely far-away from the location of interest, this equation can be written as

$$p'_\infty + \frac{1}{2}\rho_f(\underline{U}_\infty.\underline{U}_\infty) + \rho_f\frac{\partial\Phi_\infty}{\partial t} = F(t), \tag{B.48}$$

noting that with the introduction of a temporally fluctuating free-stream flow, this equation is no longer equal to a constant, but to a function of time $F(t)$; $\underline{U}_\infty$ is assumed to have only an x component

$$\underline{U}_\infty = U'_\infty\underline{i} + 0\underline{j}. \tag{B.49}$$

It is required to find a solution for $F(t)$; the pressure-gradient infinitely far-away, $\partial p'_\infty/\partial x$, will be considered to fluctuate as

$$\frac{\partial p'_\infty}{\partial x} = -\rho_f\Pi\cos\omega_f t, \tag{B.50}$$

where ω_f is the angular velocity of the free stream. From the continuity equation

$$\frac{\partial U'_\infty}{\partial x} = 0. \tag{B.51}$$

Inserting (B.50) and (B.51) into the *momentum equation* neglecting viscosity and body forces (Tritton, 1999)

$$\frac{\partial U'_\infty}{\partial t} + U'_\infty\frac{\partial U'_\infty}{\partial x} = -\frac{1}{\rho_f}\frac{\partial p'_\infty}{\partial x},$$

obtains the result

$$\frac{\partial U'_\infty}{\partial t} = \Pi\cos\omega_f t. \tag{B.52}$$

Integrating (B.50) with distance and (B.52) with time obtains the results

$$p'_\infty = p_\infty - (\rho_f\Pi\cos\omega_f t)\,x, \tag{B.53}$$

$$U'_\infty = U_\infty + \frac{\Pi}{\omega_f}\sin\omega_f t. \tag{B.54}$$

Now solve for $\partial\Phi_\infty/\partial t$. Initially solve for Φ_∞; utilising (B.54) we have

$$\frac{\partial\Phi_\infty}{\partial x} = U_\infty + \frac{\Pi}{\omega_f}\sin\omega_f t, \qquad \frac{\partial\Phi_\infty}{\partial y} = 0,$$

$$\Phi^x_\infty = \underbrace{\left(U_\infty + \frac{\Pi}{\omega_f}\sin\omega_f t\right)x}_{E(x,t)} + F(y,t), \qquad \Phi^y_\infty = G(x,t).$$

As Φ^x_∞ must equal Φ^y_∞, $F(y,t)$ must equal zero and $G(x,t) = E(x,t)$; the final result for Φ_∞ is therefore

$$\Phi_\infty = \left(U_\infty + \frac{\Pi}{\omega_f}\sin\omega_f t\right)x.$$

Differentiating this result with respect to time obtains

$$\frac{\partial\Phi_\infty}{\partial t} = (\Pi\cos\omega_f t)\,x. \tag{B.55}$$

Enter (B.53) and (B.55) into (B.48) to obtain the result for $F(t)$

$$p_\infty - \rho_f(\Pi\cos\omega_f t)\,x + \frac{1}{2}\rho_f(\underline{U}_\infty.\underline{U}_\infty) + \rho_f(\Pi\cos\omega_f t)\,x = F(t),$$

$$p_\infty + \frac{1}{2}\rho_f(\underline{U}_\infty.\underline{U}_\infty) = F(t). \tag{B.56}$$

Consider the pressure at a point m on the flow-region geometry

$$p_m + \frac{1}{2}\rho_f(\underline{u}_m.\underline{u}_m) + \rho_f\frac{\partial\phi_m}{\partial t} = F(t),$$

where $\underline{u}_m$ is the total velocity. Substitute (B.56) for $F(t)$ to calculate the flow-structure-system pressure-equation

$$p_m + \frac{1}{2}\rho_f(\underline{u}_m.\underline{u}_m) + \rho_f\frac{\partial\phi_m}{\partial t} = p_\infty + \frac{1}{2}\rho_f(\underline{U}_\infty.\underline{U}_\infty),$$

$$(p_m - p_\infty\ =)\ \delta p_m = \frac{1}{2}\rho_f(\underline{U}_\infty.\underline{U}_\infty) - \frac{1}{2}\rho_f(\underline{u}_m.\underline{u}_m) - \rho_f\frac{\partial\phi_m}{\partial t}. \tag{B.57}$$

The total velocity is equal to

$$(\underline{\nabla}\Phi_m\ =)\ \underline{u}_m = \underline{U}_\infty + \underline{u}'_m + \underline{u}^b_m,$$

where $\underline{u}'_m$ is the total perturbation velocity due to the singularity distribution and $\underline{u}^b_m$ is the total blob-velocity. The components of these velocities are equal to

$$\underline{u}'_m = u^{T'}_m\underline{i} + \underbrace{u^{N'}_m\underline{j}}_{=0}, \tag{B.58}$$

$$\underline{u}^b_m = u^{Tb}_m\underline{i} + u^{Nb}_m\underline{j}. \tag{B.59}$$

Insert (B.49), (B.58) and (B.59) into (B.57) to derive the final pressure equation

$$\begin{aligned}
\delta p_m &= \frac{1}{2}\rho_f\left(\underline{U}_\infty.\underline{U}_\infty - (\underline{U}_\infty.\underline{U}_\infty + 2\underline{U}_\infty.\underline{u}'_m + 2\underline{U}_\infty.\underline{u}^b_m)\right) - \rho_f\frac{\partial\phi_m}{\partial t}, \\
&= -\rho_f(\underline{U}_\infty.\underline{u}'_m + \underline{U}_\infty.\underline{u}^b_m) - \rho_f\frac{\partial\phi_m}{\partial t}, \\
&= -\rho_f\left((U'_\infty\underline{i} + 0\underline{j})(u^{T'}_m\underline{i} + 0\underline{j}) + (U'_\infty\underline{i} + 0\underline{j})(u^{Tb}_m\underline{i} + u^{Nb}_m\underline{j})\right) - \rho_f\frac{\partial\phi_m}{\partial t}, \\
&= -\rho_f U'_\infty\left(u^{T'}_m + u^{Tb}_m\right) - \rho_f\frac{\partial\phi_m}{\partial t}.
\end{aligned}$$

The pressure acting across the flexible-surface is therefore equal to

$$\delta p_m\big|_{xp} = -2\rho_f U'_\infty\left(u^{T'}_m + u^{Tb}_m\right) - \rho_f\left.\frac{\partial\phi_m}{\partial t}\right|_{xp}. \tag{B.60}$$

B.4.2 Steady Singularity Strengths

The normal influence-coefficient matrix assembly and the solution for the singularity strengths was illustrated in §3.2.2. Taking blob velocity into account, the solution for the singularity strengths becomes

$$\left\{\begin{array}{c}\gamma_1\\ \vdots\\ \gamma_{M_{cs}}\\ \cdots\\ \lambda_1\\ \vdots\\ \lambda_{M_{cs}}\\ \cdots\\ \sigma_1\\ \vdots\\ \sigma_{M_w}\end{array}\right\} = \left\{\begin{array}{c}\Gamma\\ \cdots\\ \sigma\end{array}\right\} = \left[I^N_{im}\right]^{-1}\left\{\begin{array}{c}\underline{\dot{w}}_m.\underline{n}_m - \underline{U}_\infty.\underline{n}_m - \underline{u}^b_m.\underline{n}_m\\ \cdots\\ 0\end{array}\right\}. \tag{B.61}$$

Wall velocity is equated as

$$\underline{\dot{w}}_m = 0\underline{i} + \dot{w}_m\underline{j}. \tag{B.62}$$

The linearised normal unit vector is equated as

$$\begin{aligned} \underline{n}_m &= -\sin\theta_m \underline{i} + \cos\theta_m \underline{j}, \\ &= -\theta_m \underline{i} + 1\underline{j}. \end{aligned} \tag{B.63}$$

Inserting (B.49), (B.59), (B.62) and (B.63) into (B.61) gives the final solution for the singularity strengths

$$\left\{ \begin{array}{c} \Gamma \\ \cdots \\ \sigma \end{array} \right\} = \left[I_{im}^N\right]^{-1} \left\{ \dot{w}_m + U'_\infty \theta_m + u_m^{Tb}\theta_m - u_m^{Nb} \right\}. \tag{B.64}$$

B.4.3 Unsteady Singularity Strengths

Taking the time derivative of (B.61) leads to

$$\frac{\partial}{\partial t}\left\{ \begin{array}{c} \Gamma \\ \cdots \\ \sigma \end{array} \right\} = \left[I_{im}^N\right]^{-1} \frac{\partial}{\partial t}\left\{ \underline{\dot{w}}_m . \underline{n}_m - \underline{U}_\infty . \underline{n}_m - \underline{u}_m^b . \underline{n}_m \right\},$$

$$= \left[I_{im}^N\right]^{-1} \left\{ \underline{\dot{w}}_m . \frac{\partial \underline{n}_m}{\partial t} + \underline{n}_m . \frac{\partial \underline{\dot{w}}_m}{\partial t} - \underline{U}_\infty . \frac{\partial \underline{n}_m}{\partial t} - \underline{n}_m . \frac{\partial \underline{U}_\infty}{\partial t} - \underline{u}_m^b . \frac{\partial \underline{n}_m}{\partial t} - \underline{n}_m . \frac{\partial \underline{u}_m^b}{\partial t} \right\}. \tag{B.65}$$

First, consider the change in free-stream velocity with time

$$\frac{\partial \underline{U}_\infty}{\partial t} = \frac{U_\infty^{'(t+\frac{1}{2}\delta t)} - U_\infty^{'(t-\frac{1}{2}\delta t)}}{\delta t}\underline{i} + 0\underline{j}. \tag{B.66}$$

As $\underline{U}_\infty$ has a prescribed motion its previous and future values are known

$$U_\infty^{'(t+\frac{1}{2}\delta t)} = \frac{U_\infty^{'(t+\delta t)} + U_\infty^{'(t)}}{2}, \tag{B.67}$$

$$U_\infty^{'(t-\frac{1}{2}\delta t)} = \frac{U_\infty^{'(t)} + U_\infty^{'(t-\delta t)}}{2}. \tag{B.68}$$

Inserting (B.67) and (B.68) into (B.66) yields the result

$$\begin{aligned} \frac{\partial \underline{U}_\infty}{\partial t} &= \frac{U_\infty^{'(t+\delta t)} - U_\infty^{'(t-\delta t)}}{2\delta t}\underline{i} + 0\underline{j}, \\ &= \dot{U}'_\infty \underline{i} + 0\underline{j}. \end{aligned} \tag{B.69}$$

Second, consider the change in blob velocity in time

$$\frac{\partial \underline{u}_m^b}{\partial t} = \frac{\partial u_m^{Tb}}{\partial t}\underline{i} + \frac{\partial u_m^{Nb}}{\partial t}\underline{j}. \tag{B.70}$$

Consider one component of the blob velocity

$$\begin{aligned} \frac{\partial u_m^b}{\partial t} &= \frac{u_m^{b(t)} - u_m^{b(t-\delta t)}}{\delta t}, \\ &= \dot{u}_m^b. \end{aligned} \tag{B.71}$$

Only a simple calculation of the blob acceleration is required as the blob dynamics are only affected by the free-stream; when the free-stream does vary, its time-dependent oscillation is regular and of a low frequency. Inserting (B.71) into (B.70) gives the result

$$\frac{\partial \underline{u}_m^b}{\partial t} = \dot{u}_m^{Tb}\underline{i} + \dot{u}_m^{Nb}\underline{j}. \tag{B.72}$$

Third, calculate the unit normal vector change in time. Initially consider the change in unit normal vector with panel angle

$$\frac{\partial \underline{n}_m}{\partial \theta_m} = -\cos\theta_m \underline{i} - \sin\theta_m \underline{j}. \tag{B.73}$$

Now consider the change in panel angle with time

$$\frac{\partial \theta_m}{\partial t} = \frac{\dot{w}_{n+1} - \dot{w}_n}{\delta x} = \dot{\theta}_m. \tag{B.74}$$

Multiplying (B.73) and (B.74) and linearising gives the final result

$$\begin{aligned} \frac{\partial \underline{n}_m}{\partial t} &= -\dot{\theta}_m\left(\cos\theta_m \underline{i} + \sin\theta_m \underline{j}\right) = -\dot{\theta}_m \underline{i} - \dot{\theta}_m\theta_m \underline{j}, \\ &= -\dot{\theta}_m \underline{i} + 0\underline{j}. \end{aligned} \tag{B.75}$$

Finally, calculate the change of wall velocity with time

$$\frac{\partial \dot{\underline{w}}_m}{\partial t} = 0\underline{i} + \ddot{w}_m \underline{j}. \tag{B.76}$$

Inserting (B.49), (B.59), (B.62), (B.69), (B.72), (B.75) and (B.76) into (B.65) gives the final result for the unsteady singularity strengths

$$\frac{\partial}{\partial t}\begin{Bmatrix} \Gamma \\ \cdots \\ \sigma \end{Bmatrix} = \left[I_{im}^N\right]^{-1}\left\{\ddot{w}_m + U'_\infty\dot{\theta}_m + \dot{U}'_\infty\theta_m + u_m^{Tb}\dot{\theta}_m + \dot{u}_m^{Tb}\theta_m - \dot{u}_m^{Nb}\right\}. \tag{B.77}$$

B.5 Divergence & Flutter Speeds

To derive U_D and U_F, it is required to write the system equation (3.65) in terms of the angular velocity, ω, and wave number, κ, of the flexible surface. The flexible-surface displacement in terms of ω and κ has the form

$$w = w_0 e^{i(\kappa x - \omega t)} \ (= w_0 E). \tag{B.78}$$

For w to grow, ω must be complex and its complex part must be positive as

$$\begin{aligned} e^{-i\omega t} &= e^{-i(\omega_R + i\omega_C)t} \\ &= e^{-i\omega_R t} e^{-ii\omega_C t} \\ &= e^{-i\omega_R t} e^{\omega_C t}. \end{aligned} \tag{B.79}$$

Now define the velocity-potential in terms of ω and κ. As a first step, define the flow field using the Laplace equation

$$\nabla^2 \phi = 0.$$

Assume ϕ is of the form

$$\phi = \theta(y) e^{i(\kappa x - \omega t)}.$$

Place this function for ϕ into the Laplace equation (differentiate twice in the x and y direction)

$$\frac{d^2\theta}{dy^2} - \kappa^2 \theta = 0.$$

The general solution of a differential equation of this form is

$$\theta = C e^{\kappa y} + D e^{-\kappa y}.$$

Evaluate the solution so that at $y = \infty$, $\theta = 0$; therefore, $C = 0$ and

$$\phi = D e^{-\kappa y} e^{i(\kappa x - \omega t)} \ (= D e^{-\kappa y} E \ ). \tag{B.80}$$

To solve for D, consider the normal-velocity condition at the wall-flow interface ($y = 0$)

$$\underline{u}^N = \frac{\partial \phi}{\partial y} = \frac{\partial w}{\partial t} + U_\infty \frac{\partial w}{\partial x}.$$

Substituting for w and ϕ using (B.78) and (B.80) respectively

$$-\kappa D E = -i\omega w_0 E + i\kappa U_\infty w_0 E,$$

and D is therefore equal to

$$D = i\frac{w_0}{\kappa}(\omega - \kappa U_\infty). \tag{B.81}$$

Inserting (B.81) into (B.80), the total velocity-potential is therefore

$$\Phi = i\frac{w_0}{\kappa}(\omega - \kappa U_\infty)E. \tag{B.82}$$

To obtain δp in terms of ω and κ, restate the unsteady Bernoulli-equation and substitute for Φ

$$\begin{aligned} \delta p = p - p_\infty &= -\rho_f U_\infty \Phi - \rho_f \frac{\partial \Phi}{\partial t}, \\ -\delta p &= i\rho_f \frac{w_0}{\kappa}(\omega - \kappa U_\infty)(U_\infty i\kappa + [-i\omega])E, \\ &= -\rho_f \frac{w_0}{\kappa}(\omega - \kappa U_\infty)(U_\infty \kappa - \omega)E, \\ -\delta p &= \frac{w\rho_f}{\kappa}(\omega - \kappa U_\infty)^2. \end{aligned} \tag{B.83}$$

Now insert (B.83) into the beam equation (3.2)

$$\rho h \frac{\partial^2 w}{\partial t^2} + B\frac{\partial^4 w}{\partial x^4} = 2\frac{w\rho_f}{\kappa}(\omega - \kappa U_\infty)^2,$$

where the pressure term is multiplied by two as the pressure difference across the flexible-surface is being modelled (the pressure on the upper side of the flexible surface being equal and opposite to that on its lower side). Substitute for w on the left-hand side

$$-\rho h\omega^2 + B\kappa^4 = \frac{2\rho_f}{\kappa}\omega^2 - 4U_\infty \rho_f \omega + 2\rho_f \kappa U_\infty^2.$$

Rearrange the above equation to obtain the final dispersion equation

$$\left(\rho h + \frac{2\rho_f}{\kappa}\right)\omega^2 + \left(-4\rho_f U_\infty\right)\omega + \left(2\rho_f \kappa U_\infty^2 - B\kappa^4\right) = 0. \tag{B.84}$$

Utilise the dispersion equation to obtain U_D (when $\omega = 0$)

$$\begin{aligned} 2\rho_f \kappa U_\infty^2 - B\kappa^4 &= 0, \\ U_D &= \left(\frac{B\kappa^3}{2\rho_f}\right)^{\frac{1}{2}}. \end{aligned} \tag{B.85}$$

Utilise the dispersion equation to obtain U_F: Flutter occurs when the solution for w in (B.78) is growing; as shown in (B.79), this occurs when the complex part of ω is positive. Therefore flutter occurs at the velocity where the complex part of ω changes from negative to positive.

$$\omega = \frac{4\rho_f U_\infty \pm \sqrt{16\rho_f^2 U_\infty^2 - 4\left(\rho h + \frac{2\rho_f}{\kappa}\right)\left(2\rho_f \kappa U_\infty^2 - B\kappa^4\right)}}{2\left(\rho h + \frac{2\rho_f}{\kappa}\right)},$$

$$16\rho_f^2 U_\infty^2 - 4\left(\rho h + \frac{2\rho_f}{\kappa}\right)\left(2\rho_f \kappa U_\infty^2 - B\kappa^4\right) = 0,$$

$$U_F = U_D \sqrt{1 + \frac{2\rho_f}{\rho h \kappa}}. \tag{B.86}$$

B.6 Validation of the Hydrodynamic Inertia Term

Carpenter and Garrad (1986) showed that for a flexible surface with a potential flow along one side

$$\delta p = -\rho_f \kappa \left(U_\infty - c\right)^2 w. \tag{B.87}$$

Enforcing a stationary flow and defining variables

$$U_\infty = 0,\ \kappa = \frac{2\pi}{\lambda},\ c = f\lambda \ \text{ and } \ f = \frac{\omega}{2\pi}. \tag{B.88a, b, c, d}$$

Inserting (B.88a, b, c, d) into (B.87) and rearranging returns the result

$$\delta p = -\rho_f \frac{\lambda}{2\pi} \omega^2 w, \tag{B.89}$$

where λ is the wavelength of a sinusoidal deflection of the flexible surface with hinged-hinged conditions enforced and is equal to

$$\lambda = \frac{2L}{n}, \tag{B.90}$$

where n is the mode number of the deflection. The deflection of the flexible surface can be described as

$$w = w_0 e^{i\omega t} \sin\left(\frac{n\pi x}{L}\right). \tag{B.91}$$

Differentiating (B.91) with respect to time gives

$$\begin{aligned} \dot{w} &= w_0 i\omega e^{i\omega t} \sin\left(\frac{n\pi x}{L}\right), \\ \ddot{w} &= -w_0 \omega^2 e^{i\omega t} \sin\left(\frac{n\pi x}{L}\right). \end{aligned} \tag{B.92}$$

Differentiating (B.91) with respect to horizontal distance gives

$$\begin{aligned} w &= w_0 e^{i\omega t} \sin\left(\frac{n\pi x}{L}\right) \\ \frac{\partial^4 w}{\partial x^4} &= w_0 e^{i\omega t} \left(\frac{n\pi}{L}\right)^4 \sin\left(\frac{n\pi x}{L}\right) \\ &= w_0 e^{i\omega t} \left(\frac{2\pi}{\lambda}\right)^4 \sin\left(\frac{n\pi x}{L}\right). \end{aligned} \tag{B.93}$$

Inserting (B.89), (B.91), (B.92) and (B.93) into the beam equation and cancelling recurring terms returns the result

$$-\rho h\omega^2 + B\left(\frac{2\pi}{\lambda}\right)^4 = \rho_f \frac{\lambda}{2\pi}\omega^2 \tag{B.94}$$

Noting that the pressure difference across a flexible surface with flow on both sides will be twice as great as over a flexible surface with a flow over only one side, respective one sided and two sided angular velocities of oscillation, calculated utilising (B.94), are

$$\omega_{os} = \sqrt{\frac{B\left(\frac{2\pi}{\lambda}\right)^4}{\rho_f \frac{\lambda}{2\pi} + \rho h}} \quad \text{and} \quad \omega_{ts} = \sqrt{\frac{B\left(\frac{2\pi}{\lambda}\right)^4}{\rho_f \frac{\lambda}{\pi} + \rho h}}. \tag{B.95}$$

When the density of the fluid is much greater than the specific mass of the flexible surface ($\rho_f >> \rho h$) the ratio of periods of oscillation is therefore

$$\frac{T_{ts}}{T_{os}} = \frac{\sqrt{\frac{B\left(\frac{2\pi}{\lambda}\right)^4}{\rho_f \frac{\lambda}{2\pi} + \rho h}}}{\sqrt{\frac{B\left(\frac{2\pi}{\lambda}\right)^4}{\rho_f \frac{\lambda}{\pi} + \rho h}}} = \sqrt{\frac{\rho_f \frac{\lambda}{\pi} + \rho h}{\rho_f \frac{\lambda}{2\pi} + \rho h}} \approx \sqrt{2}. \tag{B.96}$$

Appendix C

Additional Material

Excerpt for "The Pickwick Papers (Dickens, 1837)":

"Come, come," said the bustling host, with a natural anxiety to change the conversation,- "What say you to a rubber, Mr. Pickwick?"

"I should like it of all things," replied that gentleman; "but pray don't make up one on my account."

"Oh, I assure you, mother's very fond of a rubber," said Mr. Wardle; "a'nt you, mother?"

The old lady, who was much less deaf on this subject than on any other, replied in the affirmative.

"Joe, Joe!" said the old gentleman; "Joe–damn that–oh, here he is; put out the card-tables."

The lethargic youth contrived without any additional rousing to set out two card-tables; the one for Pope Joan, and the other for whist. The whist-players were Mr. Pickwick and the old lady; Mr. Miller and the fat gentleman. The round game comprised the rest of the company.

The rubber was conducted with all that gravity of deportment and sedateness of demeanour which befit the pursuit entitled "whist"-a solemn observance, to which, as it

appears to us, the title of "game" has been very irreverently and ignominiously applied. The round-game table, on the other hand, was so boisterously merry as materially to interrupt the contemplations of Mr. Miller, who, not being quite so much absorbed as he ought to have been, contrived to commit various high crimes and misdemeanours, which excited the wrath of the fat gentleman to a very great extent, and called forth the good-humour of the old lady in a proportionate degree.

"There!" said the criminal Miller triumphantly, as he took up the odd trick at the conclusion of a hand; "that could not have been played better, I flatter myself;-impossible to have made another trick!"

"Miller ought to have trumped the diamond, oughtn't he, sir?" said the old lady.

Mr. Pickwick nodded assent.

"Ought I, though?" said the unfortunate, with a doubtful appeal to his partner.

"You ought, sir," said the fat gentleman, in an awful voice.

"Very sorry," said the crest-fallen Miller.

"Much use that," growled the fat gentleman.

"Two by honours makes us eight," said Mr. Pickwick. Another hand.

"Can you one?" inquired the old lady.

"I can," replied Mr. Pickwick. "Double, single, and the rub."

"Never was such luck," said Mr. Miller.

"Never was such cards," said the fat gentleman.

A solemn silence: Mr. Pickwick humorous, the old lady serious, the fat gentleman captious, and Mr. Miller timorous.

"Another double," said the old lady: triumphantly making a memorandum of the circumstance, by placing one sixpence and a battered half-penny under the candlestick.

"A double, sir," said Mr. Pickwick.

"Quite aware of the fact, sir," replied the fat gentleman, sharply.

Another game, with a similar result, was followed by a revoke from the unlucky Miller; on which the fat gentleman burst into a state of high personal excitement which lasted until the conclusion of the game, when he retired into a corner, and remained perfectly mute for one hour and twenty-seven minutes; at the end of which time he emerged from his retirement, and offered Mr. Pickwick a pinch of snuff with the air of a man who had made up his mind to a Christian forgiveness of injuries sustained. The old lady's hearing decidedly improved, and the unlucky Miller felt as much out of his element as a dolphin in a sentry-box.

- Additional information for Vorticity model: Comments on the starting vortex should refer to Houghton and Carpenter (2003), who describe that this phenomenon in some part owes to the free stream forcing the stagnation point on the upper surface of a lifting body to the trailing edge of that body. An initial blob vector diagram similar to that shown in figure 3.4(a) should be included in the development of the blob equations; the vector $\underline{r}$ is then defined as $|\underline{r} - \underline{r}_p|$. Blob unit vectors are then defined in a similar way to the linear panel-method and remain constant with time. The blob release co-ordinates remain at the trailing edge of the flexible surface; however, this is because the free-stream convects the released blob to its correct position of $U_\infty \delta t$ before its influence is calculated on the panel method solution. Therefore, the maximum blob core size, if the blob is not to overlap the trailing edge of the flexible surface, is $U_\infty \delta t$. Using a panel method with a fixed Kutta condition, the wake is correctly modelled at the first step; therefore, the initial change in bound vorticity to be captured by the shed vorticity model occurs between the first and second time steps (*i.e.* there is no effect from the blobs until the second time step). Finally, it should be noted that the affect of the blobs is not calculated on the velocity potential.

- A summary figure for §5.3.1 is shown in figure C.1, collating all the data shown in figure 5.32, taken from Watanabe *et al.* (2002b), and converting it to show $\bar{U}$ and $\bar{L}$ values using the relation in (5.1) and noting that $\bar{L} = 1/\mu$.

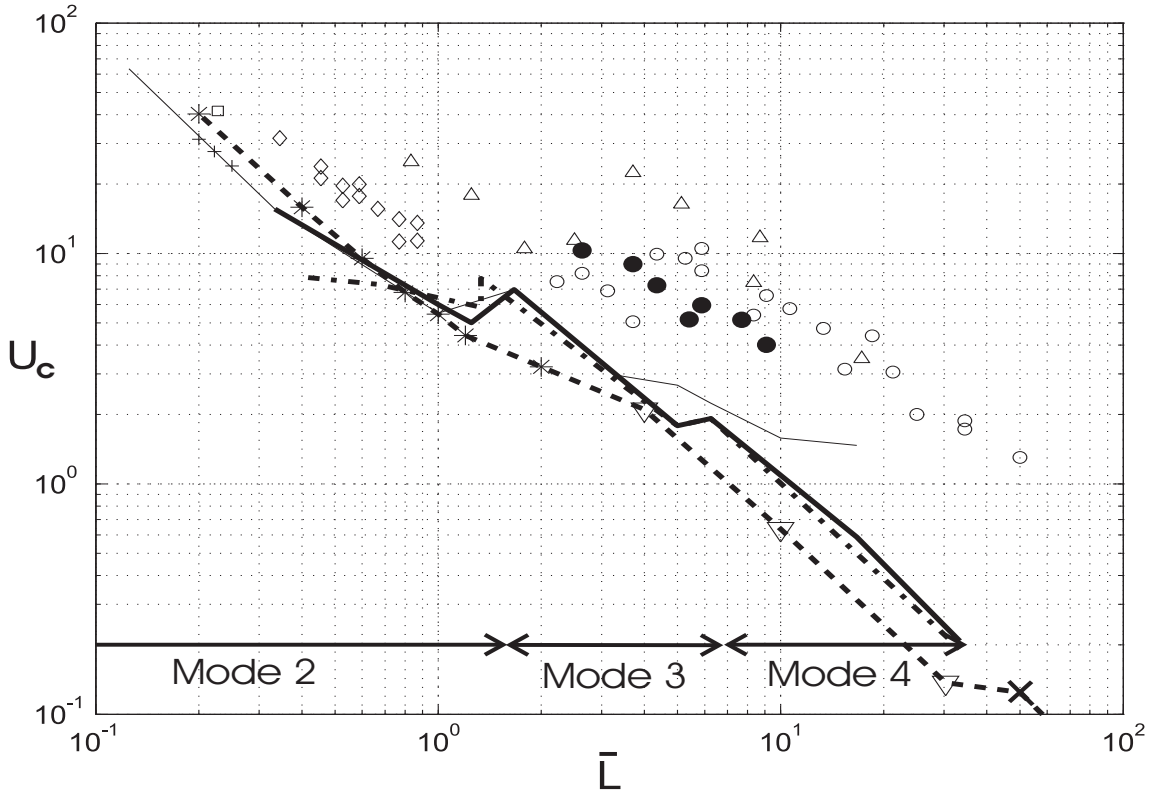

Figure C.1: Plot of U_c at different $\bar{L}$, including data from several published studies, adapted from Watanabe *et al.* (2002b). Experimental Data: From Watanabe *et al.* (2002b) ∘ flag type paper, • long-type paper, △ elastic sheet; ◊ Huang (1995); + Kornecki *et al.* (1976); Theoretical Models: − (thick) Watanabe *et al.* (2002b) with $C_D = 0$ (boundaries at the bottom of the graph show the predominant eigenmodes in the form of the critical mode calculated by this model); − (thin) Huang (1995); −. Guo and Païdoussis (2000); □ Kornecki *et al.* (1976); −− Present numerical model, different data-point markings on this line signify different predominant eigenmodes in form of the critical mode: ∗ second eigenmode, ▽ third eigenmode, × fourth eigenmode.